

2002

Sound propagation and scattering in bubbly liquids

<https://hdl.handle.net/2144/1369>

Boston University

BOSTON UNIVERSITY
COLLEGE OF ENGINEERING

Dissertation

SOUND PROPAGATION AND SCATTERING IN BUBBLY LIQUIDS

by

PRESTON SCOT WILSON

B. S., University of Texas at Austin, 1990
M. S., University of Texas at Austin, 1994

Submitted in partial fulfillment of the
requirements for the degree of
Doctor of Philosophy

2002

© Copyright by
PRESTON SCOT WILSON
2002

Approved by

Advisor:

Ronald A. Roy, Ph.D.
Associate Professor, Aerospace and Mechanical Engineering

Second Reader:

William M. Carey, Ph.D.
Professor, Aerospace and Mechanical Engineering

Third Reader:

Michael S. Howe, Ph.D.
Professor, Aerospace and Mechanical Engineering

Fourth Reader:

J. Gregory McDaniel, Ph.D.
Assistant Professor, Aerospace and Mechanical Engineering

Acknowledgments

I have wondered in the past if after years of toiling primarily alone, a disgruntled and weary graduate student has ever submitted a thesis or dissertation with a blank acknowledgments page. The completion of such a work can be an alienating experience; the long, endless hours in the lab or behind the computer, the rest of the world going about their merry way. Herein lies the the spirit of this section. It is a place to leave permanent acknowledgement to all of those who put up with that graduate student during those trying times. Such is certainly the case with this graduate student. First and foremost deserving of thanks, for her unending support and her fearless resolve, is my wonderful wife and *raison d'être*, Lila. Without her, in just about every way, this would not have been possible. Thank you Lila!

To my dissertation advisor, Dr. Ronald A. Roy, I owe much gratitude. His support throughout this project has been influential to its success, and I feel most certain the guidance he has offered will continue to be appreciated for many years to come. The same can be said for Dr. William M. Carey, to whom many thanks are given for his sage words and teachings, and for his insightful perspective. I thank Dr. Michael S. Howe for his guidance during this work, and for the learning experience afforded to me during my tenure as his teaching assistant. I also thank Dr. J. Gregory McDaniel for his interest and support during this project, and for his support dating back to my matriculation at Boston University. Thanks are due to Dr. Glynn Holt and Dr. Robin Cleveland, for their useful advice, at times their equipment, and at other times, their lab space.

Next, I would like to acknowledge the support of my fellow graduate students. We were all in it together. It seems like there were two eras. From the beginning and in no particular order thanks go to Patrick Edson, Jinlan Huang, Ibrahim Hallaj, Andrew Gephart, Mario Zampolli, Gary Dewar, Trevor Wood and Dimitar Gueorguiev. We went through the classes and the Qualifiers together. It is the second era where thanks are due specifically for help with this dissertation. I thank Eun-Joo Park for her tireless

efforts with apparatus building, bubble counting and void fraction measurement, and for her participation in the field experiments. Last but certainly not least, I thank Ryan McCormick for his help with many aspects of this work, and more importantly for his friendship. Thanks to you all.

Finally, I would like to thank my parents Helen and Mickey Wilson for helping to see me through yet another degree. Their support has always been there for me, in many more ways than I will ever be able to acknowledge. Thank you Mom and Dad.

The funding for this research was generously provided by the U.S. Navy Office of Naval Research Ocean Acoustics Program and by Boston University.

January 2002

SOUND PROPAGATION AND SCATTERING IN BUBBLY LIQUIDS

(Order No.)

PRESTON SCOT WILSON

Boston University, College of Engineering, 2002
Major Professor: Ronald A. Roy, Associate Professor
of Aerospace and Mechanical Engineering

ABSTRACT

In the ocean, natural and artificial processes generate clouds of bubbles which scatter and attenuate sound. Measurements have shown that at the individual bubble resonance frequency, sound propagation in this medium is highly attenuated and dispersive. Theory to explain this behavior exists in the literature, and is adequate away from resonance. However, due to excessive attenuation near resonance, little experimental data exists for comparison.

An impedance tube was developed specifically for exploring this regime. Using the instrument, unique phase speed and attenuation measurements were made for void fractions ranging from 6.2×10^{-5} to 2.7×10^{-3} and bubble sizes centered around 0.62 mm in radius. Improved measurement speed, accuracy and precision is possible with the new instrument, and both instantaneous and time-averaged measurements were obtained. Behavior at resonance was observed to be sensitive to the bubble population statistics and agreed with existing theory, within the uncertainty of the bubble population parameters.

Scattering from acoustically compact bubble clouds can be predicted from classical scattering theory by using an effective medium description of the bubbly fluid interior. Experimental verification was previously obtained up to the lowest resonance frequency. A novel bubble production technique has been employed to obtain unique scattering measurements with a bubbly-liquid-filled latex tube in a large indoor tank. The effective scattering model described these measurements up to three times the lowest resonance frequency of the structure.

Contents

List of Tables	xii
List of Figures	xiv
1 Introduction	1
1.1 Motivation and Background	1
1.1.1 Origin of Oceanic Bubbles	3
1.1.2 Brief Problem Description	4
1.2 Review of the Literature	5
1.2.1 Preliminary Topics	5
1.2.2 Theory of Sound Propagation in Bubbly Fluids	7
Low Frequency Propagation	9
The Effect of Bubble Dynamics	11
1.2.3 Theory of Scattering from Acoustically Compact Bubble Clouds	13
1.2.4 Experiments in Sound Propagation and Scattering in Bubbly Fluids	14
Low Frequency Propagation	14
The Effect of Bubble Dynamics—Broadband Propagation	15
Scattering from Bubble Clouds	17
1.3 Recapitulation	18
1.3.1 Primary Contributions	19
1.3.2 Road Map of Dissertation	19

2	Exploration of Propagation and Scattering Theory	25
2.1	Acoustic Propagation in Bubbly Liquids, Revisited	25
2.1.1	Comparison Of Results	27
2.1.2	From Wave Number to Phase Speed and Attenuation	29
2.2	Effect of Bubble Population Parameters on Propagation	29
2.2.1	General Behavior	30
2.2.2	Effect of Void Fraction	31
2.2.3	Effect of Bubble Size	32
2.2.4	The Addition of Multiple Bubble Sizes	33
2.3	Theory of Scattering from a Bubbly-Liquid-Filled Compliant Cylinder . . .	35
2.3.1	Scattering of Continuous Waves	36
2.3.2	Scattering of Finite Duration Waves	40
2.4	The Effect of Bubble Population Parameters on Scattering	41
2.4.1	General Behavior	41
2.4.2	Effect of the Shell	42
2.4.3	Effect of Void Fraction	43
2.4.4	Effect of Cloud Size	44
2.4.5	Effect of Bubble Resonance	44
2.5	Summary	46
3	Development of a Water-Filled Impedance Tube	62
3.1	Introduction	63
3.2	Basic Impedance Tube Techniques	64
3.2.1	Standing Wave Method	64
3.2.2	Transfer Function Method	67
	Extension of TFM for a Single Sensor	75
3.3	Adaption of Two-Sensor Technique for Use In Water	75
3.4	Theory of Propagation and Resonance In Finite Elastic Waveguides with Real Terminations	77

3.4.1	Review of Plane Wave Propagation in Rigid Tubes	77
3.4.2	Theory of Sound Propagation in Elastic Waveguides	80
	Particle Displacement Profiles and Phase Speed	80
3.4.3	Effective Plane Wave, Combined Source-Tube Propagation Model	85
3.5	Prototype Impedance Tube	86
3.5.1	Apparatus	87
3.5.2	Procedures	89
3.6	Preliminary Results	90
3.6.1	Verification of EPWM	90
3.6.2	Verification of Impedance Measurement Technique	96
	Water-Filled Transmission Line	97
	Xanthan Gel	98
3.6.3	Bubble Production and Characterization	101
3.7	Second Generation Impedance Tube System	103
3.7.1	Theory of Cross-Calibration	104
3.7.2	Second Generation Apparatus	106
3.7.3	Cross-Calibration and Operational Procedure	107
3.7.4	Verification of Impedance Tube System	109
3.7.5	Additional Verification with Single Sensor Method	110
3.8	Measurement Error Analysis	111
3.8.1	Errors in the Transfer Function Measurement	112
3.8.2	Errors Propagated Through Measured Quantities	114
3.8.3	Total Uncertainty in Impedance Measurement	116
3.9	Comparison to Other Systems	117
4	Characterization of Bubbly Liquid by Impedance Tube	146
4.1	Bubble Production	146
4.2	Determination of Bubble Size Distribution	148
4.3	Determination of Void Fraction	151

4.4	Impedance Measurement	156
4.4.1	Time-Averaged Measurement Procedure	157
4.4.2	Instantaneous Measurement Procedure	160
4.4.3	Inversion Procedure	162
4.5	Results and Comparison to Theory	164
4.5.1	Bubble Population Data Reduction	164
4.5.2	Time-Averaged Results	166
4.5.3	Discussion of Time-Averaged Results	171
	Elastic Waveguide Effects	171
	Signal and Noise Issues	174
	Bubble Population Parameters and Void Fraction	176
4.5.4	Instantaneous Results	177
4.5.5	Discussion of Instantaneous Results	180
5	Scattering from a Bubbly Cylinder	217
5.1	Description of the Experiment	218
5.2	Mass Production of Microbubbles	219
5.3	Experimental Results and Model Comparison	222
5.4	Measurement Uncertainty and Ping-to-Ping Variability	224
5.5	Discussion	227
6	Summary and Conclusions	244
6.1	Development of a Water-Filled Impedance Tube System	244
6.2	Propagation Measurements Near Resonance	245
6.3	Scattering Measurements	247
A	Experimental Verification of Wood's Equation	249
B	High Mechanical Input Impedance Hydrophones	257
C	Initial Cross-Calibration Procedure	269

D Single Needle Bubble Population Statistics	272
E Matlab Scripts	286
Bibliography	302
Vita	312

List of Tables

1.1	Representative sound speeds for air bubbles in sea water at atmospheric pressure, calculated from Eq. 1.10 and Eq. 1.12 using: $\rho_\ell = 1021 \text{ kg/m}^3$, $c_\ell = 1500 \text{ m/s}$, $\rho_g = 1.21 \text{ kg/m}^3$, $P_\infty = 101.3 \text{ kPa}$ and $c_g = \sqrt{P_\infty/\rho_g}$, the isothermal value. [†] The $\chi = 0$ value was not calculated but merely included for comparison.	21
2.1	Values of the physical parameters used in Section 2.2.	47
2.2	Values used to construct the bubble size distributions presented in Fig. 2.6, and the limits of integration and void fraction χ subsequently used for Fig. 2.7. All values are in millimeters except those for void fraction χ which is unitless.	47
2.3	Unless otherwise stated, the above values were used in the scattering calculations of Section 2.4. The latex material properties, shown in the rightmost column, were obtained from the literature [85, p. V-5]. Dissipation within the latex material was neglected.	47
3.1	The aluminum/water waveguide parameters used in the calculations shown Fig. 3.5 are tabulated.	119
3.2	Physical parameters of the prototype impedance tube are shown.	119
3.3	The table contains the values used to make Fig. 3.29.	119
3.4	The table contains the values used to make Fig. 3.31.	119
3.5	Average measurement error for the second generation impedance tube. . . .	119

- 4.1 The table contains the results and the error analysis for the void fraction measurements. †For Case 1, χ was estimated from optical measurements. . . 182
- 4.2 The table contains the parameters used to produce the Figs. 4.28.–4.30. All the physical parameters listed in Table 2.1, except c_ℓ were also used. The presence of the asterisk (*) in a cell indicates that parameter was fitted. . . 182

List of Figures

1.1	Eq. 1.10, is plotted for air bubbles in sea water with $c_\ell = 1500$ m/s, $\rho_\ell = 1021$ kg/m ³ , $c_g = 289.3$ m/s, and $\rho_g = 1.21$ kg/m ³	21
1.2	Experimental verification of Wood's Equation (Eq. 1.10) is shown. See Appendix A for a detailed description.	22
1.3	Comparison of Commander and Prosperetti's theoretical attenuation with Silberman's data for $\beta = 0.0377\%$ and bubble radii 0.994 mm (diamonds) and 1.07 mm (triangles and circles). Figure adapted from [33].	22
1.4	Comparison of theoretical phase speed of Foldy (curve 1) and Feuillade (curve 2) with Silberman's data for $\beta = 0.22\%$ and bubble radii 1.83 mm (circles), 2.07 mm (squares) and 2.44 mm (triangles), after [73]. The horizontal dotted line represents the speed of sound in pure water for experimental temperature.	23
1.5	Comparison of Commander and Prosperetti's theoretical phase velocity with Cheyne <i>et al.</i> data for $\beta = 1\%$ and bubble radii 1.11 mm. Both interferometer (\circ) and hydrophone (\times) data is shown, after [32].	23
1.6	The target strength of a bubble cloud from the Lake Seneca experiment is shown. The figure was adapted from Gephart [29].	24
2.1	Phase speed (upper) and attenuation (lower) for propagation in a monodisperse bubbly fluid is shown as a function of frequency for bubble radius $\bar{a} = 1.0$ mm and void fraction $\chi = 10^{-3}$	48

2.2	The curves of Fig. 2.1 are replotted on linear axes to emphasize the behavior at resonance and below. (bubble radius $\bar{a} = 1.0$ mm, void fraction $\chi = 10^{-3}$)	49
2.3	The effect of void fraction is demonstrated. Phase speed (upper) and attenuation (lower) is shown for bubble radius $\bar{a} = 0.62$ mm and three void fractions.	50
2.4	The effect of bubble size is demonstrated. Phase speed (upper) and attenuation (lower) is shown for void fraction $\chi = 10^{-4}$ and three bubble radii, which represent $\pm 10\%$ change in radius.	51
2.5	The effect of a discrete distribution of bubble sizes is demonstrated. Phase speed (upper) and attenuation (lower) is shown for void fraction $\chi = 10^{-4}$ and bubble size distribution $\varphi(a) = \sum_1^3 \delta(a - \bar{a}_j)$. The \bar{a}_j 's are the same as in Fig. 2.4.	52
2.6	The three bubble size distributions $\varphi(a)$ used in Fig. 2.7 are shown. Details are given in the text and Table 2.2.	53
2.7	Phase speed (upper) and attenuation (lower) is shown as a function of frequency for void fraction $\chi = 10^{-4}$ and three bubble size distributions of different standard deviation s . The legend applies to the upper and lower plots. Further details are given in the text and Table 2.2.	54
2.8	The sensitivity to distribution width is demonstrated. Phase speed (upper) and attenuation (lower) is shown for void fraction $\chi = 10^{-4}$ and three standard deviations s . The legend applies to both plots. Further details are given in the text and Table 2.2-(b).	55
2.9	A schematic diagram of the bubbly-liquid-filled cylinder is shown, along with the incident plane wave $P_i(t)$.	56
2.10	Scattering from a bubbly-liquid-filled compliant cylinder is presented. Inclusion of three modes in the sum is required for these conditions.	57

2.11	The effect the shell and the effect of void fraction are shown. Solid lines are for the shell, dashed lines are for no shell. The shell/no shell cases are almost indistinguishable in the high void fraction case.	58
2.12	The effect of void fraction is shown. The small blips around 18 kHz do not appear to be numerical artifacts. They do, however, become narrower as $\Delta f \rightarrow 0$ in the calculations and are artificially wide at the resolution shown in the present figure.	59
2.13	The effect of cloud size is shown. The inner radius b has been varied for a constant shell thickness of 1 mm.	60
2.14	Bubble resonance effects are shown for two bubble sizes. The associated phase speed V and attenuation A is shown in the upper two plots. The corresponding scattering strength is shown in the lower plot. The legend applies to all three plots. The scattering for the Wood limit case is also shown for comparison.	61
3.1	A schematic of standing wave method is shown.	120
3.2	Schematic of transfer function method is shown. Acoustic pressure sensors are placed at positions 1 and 2.	120
3.3	A schematic of the combined source-tube system is shown.	121
3.4	Geometry used in development of the elastic waveguide propagation model. A liquid cylinder is surrounded by an elastic solid cylinder of inner radius b , and an outer radius d . The system is symmetric about the z -axis.	121
3.5	Dispersion curves for an elastic waveguide are shown with solid lines. They were calculated using Eq. 3.72 and the physical parameters listed in Table 3.1. Rigid waveguide curves for the same parameters are shown approximately with the dashed lines.	122
3.6	A schematic of the prototype experimental apparatus is shown.	122
3.7	A photograph of horizontal laboratory deployment is shown.	123
3.8	A schematic of vertical deployment is shown.	123

3.9	Typical waveforms from the time-of-flight sound speed measurements are shown. Dashed vertical lines indicate corresponding parts of waveforms and hence the time increment. The corresponding length was 1.502 m, for a round trip of 3.004 m.	124
3.10	Measured waveguide phase speed c_{ph} is compared to the theoretical prediction from Eq. 3.72. The values are normalized by c_0 , the intrinsic sound speed in water for the experimental temperature.	125
3.11	Measured acoustic pressure profiles are shown for three frequencies. The abscissa represents radial position within the tube, normalized by the inner radius b . The acoustic pressure at each position is normalized by the acoustic pressure at the center.	125
3.12	The measured acoustic pressure profile at 40 kHz is shown. The abscissa represents radial position within the tube, normalized by the inner radius b . The acoustic pressure is plotted in dB referenced to the pressure at the center $p(0)$	126
3.13	The measured acoustic pressure profile inside a thin-walled aluminum waveguide is shown. Comparison with Fig. 3.11 shows the importance of wall thickness and material strength.	126
3.14	Calculated particle displacements for the two lowest order modes in the impedance tube are shown.	127
3.15	In part (a) the source free resonance predictions from Eq. 3.73 are shown along with the measurements. In part (b), the combined source + tube model given by Eq. 3.74 is compared with measurement. For both cases, the model parameters are given in the text.	128
3.16	System frequency response: Measurement (open circles) and Eq. 3.75 (solid line). See text for parameters.	129
3.17	The measured standing wave field inside the impedance tube is shown. . . .	130
3.18	A subset of the measured standing wave field is shown in waterfall.	131

3.19	The standing wave pattern for four frequencies: Measurement (open circles) and Eq. 3.80 (solid line). See text for parameters.	132
3.20	Verification measurement of an approximate pressure release surface, showing real and imaginary parts of the measured complex reflection coefficient. Compare to the value predicted by Eq. 3.81, $R = -0.9994 + j0$, which for clarity is not shown on the plot. Note increasing deviation from expected values as frequency decreases.	133
3.21	Ground truth/verification measurement of a water-filled transmission line showing magnitude and phase of the measured complex reflection coefficient at the interface. The theoretical curve is Eq. 3.82. See text for explanation of “x-cal. error.”	134
3.22	Measured magnitude and phase of the reflection coefficient of a near bubble-free Xanthan gel. Shaded areas represent frequency range of cross-calibration error. Note similarity to Fig. 3.21.	134
3.23	The optical bubble size distribution of Xanthan gel mixtures for Fig. 3.24 is shown.	135
3.24	Measured magnitude and phase of the reflection coefficient of Xanthan gel with $VF_2 > VF_1$. Shaded areas represent frequency range of cross-calibration error.	135
3.25	Measured magnitude and phase of the reflection coefficient for the open tube, as compared to predicted results from Eqs. 3.83, 3.84, 3.85 and 3.86. Shaded areas represent frequency range of cross-calibration error.	136
3.26	The input impedance $z/\rho c = i \tan(kd - i\alpha)$ of a calibration termination is shown for $\alpha = 0.02, 0.04$ and 0.08 . In the upper plot, a null appears in the frequency band, and the three plots differ near 7 kHz. In the lower plot, no null exists and the three plots are very similar.	137
3.27	The dimensions of the second generation impedance tube are shown.	138
3.28	The impedance tube system is shown in schematic.	138

3.29	The measured (dots) and calculated (solid lines) impedance z of a pressure release terminated transmission line is shown. This plot serves as the ground truth verification for the second generation impedance tube system.	139
3.30	For additional verification, the measured (dots) and calculated (solid lines) impedance z of a pressure release terminated transmission line is shown for a second length, $d_0 = 8.40$ cm.	140
3.31	A final system verification using the single sensor method is shown. Again, the measured (dots) and calculated (solid lines) impedance z of a pressure release terminated transmission line is presented, but the frequency range was 2–5 kHz.	141
3.32	Maximum bias error in the measurement of the transfer function y for a transmission line is shown. The normalized error in magnitude (Eq. 3.96) is shown using the left scale, and the absolute error in the phase angle (Eq. 3.97) is shown using the right scale.	141
3.33	Random error in the measurement of the transfer function y for a transmission line is presented. The normalized error in magnitude (Eq. 3.98) is shown using the left scale, and the absolute error in the phase angle (Eq. 3.99) is shown using the right scale.	142
3.34	The envelope of maximum error due to uncertainties in the measured inputs to Eq. 3.93 is shown. The error in impedance magnitude is shown in the upper plot and phase error is shown in the lower plot. The phase error at 8.6 kHz increased to a maximum absolute value of 80 degrees, but the plot was scaled to show the error at 5.75 kHz clearly.	142
3.35	Relative error due to uncertainty of the measured inputs to Eq. 3.93.	143
3.36	Phase and magnitude of the reflection coefficient measured from an water-air interface using the second generation impedance tube.	144

3.37	Accuracy and precision of three impedance tube systems as expressed in the measurement of the reflection coefficient of an water-air interface. The 1947 and 1983 data were obtained from [47] and [86], respectively.	145
4.1	A schematic diagram of the air delivery system is shown	183
4.2	A schematic diagram of the bubble injection manifold is shown. Part a) is a cross-sectional view showing the injection manifold mounted between the impedance tube and the sample holder. Two needles are shown making bubbles. Part b) shows a top view of the injection manifold separated from the impedance tube and the sample holder. All twelve needles are in place, forming an inner circle of four and an outer circle of eight.	183
4.3	The photograph shows the four equal length conduits, made of 3.175 mm diameter copper tubing, which connect the air delivery system to the air injection manifold, insuring an even distribution of air to the plenum. Six 30 gauge needles are shown extending 1.27 cm into the inner diameter of the tube. The scale is 15 cm in length.	184
4.4	A schematic diagram of the bubble size measurement system is shown with the air injection manifold producing bubbles. The height h of the water column is the same as that inside the sample holder during impedance measurements.	184
4.5	A typical image obtained with the bubble size measurement system is shown in a). These bubbles are of a size large enough to exhibit the oblate spheroid shape. The same image after processing is shown in b). Each bubble is outlined and assigned a number and the size data is stored in a file.	185
4.6	The bubble size distribution is shown for the image in Fig. 4.5-b and 19 others like it, based on the oblate spheroid analysis of Eq. 4.2. A total of 210 bubbles were analyzed in this example.	186
4.7	An enlarged image of one of the bubbles from Fig. 4.5 is shown in a). Uncertainty due to pixelation is shown in b).	186

4.8	A schematic diagram of the void fraction resonator is shown.	187
4.9	A photograph is shown of the void fraction resonator with the bubble injection manifold mounted at the bottom of the tube. The scale is 15 cm in length.	188
4.10	The void fraction resonator is shown with the hydrophone positioning system attached.	189
4.11	The acoustic pressure field measured inside the void fraction resonator is shown for bubbles produced by an airflow of 108ml/min at 21.85 kPa. . . .	190
4.12	The bubble size distribution is shown for the axial scan measurements of Fig. 4.11. The approximate resonance frequency calculated by Eq. 1.15 is 3.1 kHz.	190
4.13	A single spectrum obtained from the void fraction resonator at $x = 7.5$ cm is shown. This corresponds to a slice out of Fig. 4.11 at $x = 7.5$ cm. The resonance peaks are identified, and the region of bubble generated broadband noise is shown. Above about 2.3 kHz, the spectrum level decreases due to absorption associated with bubble resonance.	191
4.14	The four standing wave patterns corresponding to the resonance frequencies identified in Fig. 4.13 are shown, along with the sound speed obtained from Eq. 4.5. Measurements are shown with open circles and predictions are shown with solid lines.	192
4.15	Phase speed V and attenuation coefficient A obtained from the void fraction resonator are shown in this figure. Measurements with error bars are shown with open circles and predictions are shown with solid lines.	193
4.16	A photo of the impedance tube system is shown without the bifilar microscope. The Ling V-203 electrodynamic source appears in the photo, but the Kildare TP-400 was actually used for the measurements in this section.	194

4.17	Time lines for the instantaneous impedance measurements are shown. Impedance was measured every 15 seconds at times indicated by the symbol “x”. The video recorded continuously, as indicated with the thin horizontal arrow. Individual frames were acquired from the video for six second blocks every minute.	195
4.18	Bubble population parameters are shown for Case 1, a single needle. . . .	196
4.19	Measured and predicted phase speed V and attenuation A for Case 1, using the population parameters from Fig. 4.18.	197
4.20	The measured data for Case 1 is shown again, but the predicted phase speed V and attenuation A was obtained by adjusting bubble radius.	198
4.21	The phase speed V and attenuation A data points from Fig. 4.20 are shown with dots, and the range of measurement uncertainty is shown using dashed lines. Note that the phase speed is plotted on a linear scale, in order to make the error range visible.	199
4.22	Bubble population parameters are shown for Case 2, a single needle installed in the BIM.	200
4.23	The measured data for Case 2 is shown, along with the predicted phase speed V and attenuation A obtained by fitting.	201
4.24	A running average of bubble radius versus time for Case 2 bubbles is shown.	201
4.25	Bubble population parameters are shown for Cases 3, 4 and 5. In all three cases, the bubbles were produced by four needles installed in the BIM. . . .	202
4.26	The measured data for Case 3 is shown, along with the predicted phase speed V and attenuation A obtained by fitting.	203
4.27	The measured data for Case 4 is shown, along with the predicted phase speed V and attenuation A obtained by fitting.	204
4.28	The measured data for Case 5 is shown, along with the predicted phase speed V and attenuation A obtained by fitting.	205

4.29	Bubble population parameters are shown for Case 3–5, four needles installed in the BIM.	206
4.30	The measured data for Case 6 is shown, along with the predicted phase speed V and attenuation A obtained by fitting.	207
4.31	Predicted phase speeds in an elastic waveguide are shown for supersonic regime bubbly fluid.	208
4.32	The measured coherence function γ^2 is shown for three calibration measurements and a ground truth measurement.	208
4.33	The results of the SNR experiment are presented. Phase speed V and attenuation A was measured for five SNRs. The coherence function γ^2 is also shown. The legend applies to all three plots and represents relative change in drive level.	209
4.34	The measured coherence function γ^2 is shown for Case 6.	209
4.35	Mean bubble radius a_0 and standard deviation s are shown as a function of time. The thick horizontal lines represent the global means, $\langle a_0 \rangle$ and $\langle s \rangle$, and the thin horizontal lines represent two standard deviations above and below the global means.	210
4.36	Minimum and maximum bubble radius is shown as a function of time.	211
4.37	Number of bubbles n and optically estimated void fraction χ are shown as a function of time.	212
4.38	Phase speed V and attenuation A is shown for each of the 16 measurements acquired during the instantaneous experiment.	213
4.39	Calculated phase speed V and attenuation A from the instantaneous experiment are shown. Refer to the text for details. Note: For comparison, the plots' scales were kept the same as in Fig. 4.38, except the A scale was shifted up 2 dB/cm.	214
4.40	Measured and calculated maximum attenuation is shown as a function of time, normalized by the global mean.	215

4.41	Measured and calculated frequency of maximum attenuation is shown as a function of time, normalized by the global mean.	216
5.1	Schematic diagram showing a side view of the experimental setup and coordinate axes. The latex tube appears in cross-section, with its length normal to the page.	230
5.2	Schematic view of the latex tube deployment from a position behind the projector (projector and hydrophone omitted for clarity). The bubbly liquid is generated at BFG and circulated via the supply lines labeled SL. The latex tube is held in place by wire support lines. The letter X marks the acoustic axis, which is normal to the page.	231
5.3	Six video frames from the laser alignment system are shown, verifying experimental geometry. See text for details. In the grainy video stills, the tank water looks cloudy, but it was actually clean and clear. A circular viewing port is visible in the tank wall behind the latex tube in b), c) and d).232	
5.4	A schematic of the transmit and receive electronics used during the scattering experiment is shown. The projector is labeled “P”, the hydrophone receiver is labeled “R” and “A/D” stands for analog-to-digital conversion. .	232
5.5	A schematic diagram of the bubbly fluid generator is shown. The primary and secondary circuits flow through pumps 1 and 2, respectively. Here “test section” is used to indicate either the latex tube during scattering experiments, or an imaging cell during bubble sizing.	233
5.6	Sound speeds measured in the VF resonator for two experimental cases are shown as a function of time.	234
5.7	A typical measurement showing the incident and scattered waveforms is presented. Various features are identified on the plot. This case is for a frequency of 12 kHz and the highest non-unity void fraction case. The receive gate is plotted at 10 times its actual amplitude, for clarity.	235

5.8	Measured scattering from bubbly cylinders (open circles) is shown for three different void fractions χ . Predictions are shown (solid lines) for a CW plane wave fluid cylinder model.	236
5.9	The effect of the shell on scattering strength is shown. At low void fractions (lower curve) the shell adds a dB or two to the scattering strength. At higher void fractions, the effect of the shell is barely discernible at the scale shown. The shell (solid line) and no shell (dashed line) cases almost overlay each other.	237
5.10	A typical pair of measurements, specifically the case corresponding to $\text{VF} = 1.3 \times 10^{-3}$, at 11.2 kHz. Upper plot: measured incident pulse, $p_{\text{inc}}(t)$. Lower plot: measured reflection $p_{\text{sc}}(t)$ shown with a solid line, and predicted reflection $p_{\text{sc,p}}(t)$ shown with open circles.	238
5.11	Measured (open circles) and predicted (solid lines) peak echo level versus frequency for scattering from the bubbly-liquid-filled latex tube at five different VFs.	239
5.12	One hundred consecutive incident and scattered pings are shown for the 15 kHz and void fraction $\chi \approx 0.0012$ case.	240
5.13	The variation in incident and scattered rms acoustic pressure is shown for the 15 kHz data from Fig. 5.12.	241
5.14	The variation in echo level is shown for the 15 kHz data from Fig. 5.12. The mean echo level $\langle EL \rangle$ is shown with a thick solid line, and $\langle EL \rangle \pm \sigma$ are shown with dashed lines.	242
5.15	The standard deviation of echo level, $\sigma[EL]$, is shown as a function of frequency for three void fractions χ and an air filled tube. The small arrow at 15 kHz indicates the data point corresponding to the standard deviation σ from Fig. 5.14.	243
A.1	A schematic diagram of the demonstration apparatus is shown.	254

A.2	A single spectra from the 0.4% void fraction case is shown in (a) where the individual modes have been identified. A waterfall plot of all the experimental spectra is shown in (b). Sound speeds obtained from these spectra are shown in Fig. A.3.	255
A.3	Experimental verification of Wood's Equation.	256
A.4	Ruggles data from Fig. 5.2.2 of [129] is shown along with the predictions of Eq. 2.1 for two best fit void fractions, $\chi = 1.625\%$ and $\chi = 2.28\%$. The dashed horizontal lines represent the Wood limit sound speed at the same void fractions. Ruggles reported $\chi = 2.01\%$ and $\chi = 2.98\%$ for the upper and lower data, respectively.	256
B.1	a) Cross-sectional view of original custom hydrophone, BU-250-10, which proved too great an impedance mismatch with the tube wall. b) Redesigned high mechanical-input-impedance hydrophone, BU-2502.	260
B.2	a) Frequency response before (solid line) and after (dotted line) installation of original custom hydrophone. Note frequency shifts throughout range, and severely reduced response from 1500–4000 Hz. b) Frequency response before (solid line) and after (dotted line) installation of high impedance hydrophone.	261
B.3	A facsimile of the mechanical drawing used to make the high mechanical input impedance hydrophone BU-2502 is shown. This is part 1 of a 3 part drawing.	262
B.4	A facsimile of the mechanical drawing used to make the high mechanical input impedance hydrophone BU-2502 is shown. This is part 2 of a 3 part drawing.	263
B.5	A facsimile of the mechanical drawing used to make the high mechanical input impedance hydrophone BU-2502 is shown. This is part 3 of a 3 part drawing.	264

B.6	A measurement of the electrical input impedance of the BU-2502 hydrophone, Serial Number 1 is shown.	265
B.7	A measurement of the electrical input impedance of the BU-2502 hydrophone, Serial Number 2 is shown.	266
B.8	Sensitivity of three hydrophones used in this work. The curve for the 8103 was not measured in house, but represents the data provided by the supplier.	267
B.9	Measured charge sensitivity of BU 250-10 hydrophones, Mark IV and V. . .	268
C.1	The hydrophone cross-calibration function H_c , obtained in the reverse fash- ion described in the text.	271
D.1	A photograph of the single needle bubble experiment apparatus is shown. .	273
D.2	A different view of the single needle bubble experiment apparatus is shown.	273
D.3	A typical unprocessed image from the single needle bubble experiment is shown. This is frame 01:02:24.	274
D.4	A typical surface of minimization used for fitting the bubble size distribution parameters is shown. This goes along with Fig. D.5. Although X^2 was actually minimized, the plot is shown for $1/X^2$ because visualization is easier in this format.	274
D.5	Minute 1 statistics are shown. For archival purposes, the data file name is included in the upper plot title.	275
D.6	Minute 2	275
D.7	Minute 3	276
D.8	Minute 4	276
D.9	Minute 5	277
D.10	Minute 6	277
D.11	Minute 7	278
D.12	Minute 8	278
D.13	Minute 9	279

D.14 Minute 10	279
D.15 Minute 11	280
D.16 Minute 12	280
D.17 Minute 13	281
D.18 Minute 14	281
D.19 Minute 15	282
D.20 Minute 16	282

Chapter 1

Introduction

There is geometry in the humming of the strings. There is music in the spacing of the spheres.

Pythagoras, 5th Century, B.C.

1.1 Motivation and Background

The interaction of sound and bubbles has been studied in modern science for at least 92 years, and has been part of human consciousness for many hundreds of years, perhaps longer. It is a scientifically interesting and complex problem with a long and diverse history, yet our understanding of the phenomenon is still incomplete. Part of the intrigue comes from the fact that minute parameter changes in a bubbly fluid can have large and unexpected effects. Consider for instance a column of water contained within a rigid tube. The addition of just a small number of bubbles, representing as little as 0.1% by volume, can transform the once simple medium into a highly dispersive and nonlinear one, with a sound speed less than 20% of the host medium. That corresponds to a 4 parts in 5 sound speed change for a 1 part in 10,000 density change.

The early scientific work on the acoustics of bubbles was motivated primarily by the desire to unravel certain man-made and natural curiosities. In 1910, a paper was published

by Mallock [1] which sought to explain the fact that when struck, a drinking glass filled with a “frothy liquid” produces a dull sound. Perhaps inspired by his former laboratory assistant,¹ Lord Rayleigh published a paper in 1917 which described the sound produced by water boiling in a tea kettle [3]. A few years later, in 1933, Minnaert was interested in understanding the sounds produced by running water, such as the flowing stream and the crashing of ocean waves [4]. The latter two studies both introduced relationships between the size of a bubble and its period of oscillation. Both works considered water as the host medium, but Rayleigh considered steam bubbles, while Minnaert considered air bubbles.

These topics were academically captivating in their time, but now the acoustics of bubbly fluids has a number of important practical applications beyond the babbling brook and the boiling tea kettle. These include a variety of industrial processes utilizing multi-phase flow [5], micro-fluidic manipulation [6], and the design of nuclear reactor containment systems [7]. In the ocean, various acoustic techniques are used in conjunction with oceanic bubble populations to make measurements relevant to meteorology, chemical oceanography, marine fluid dynamics, and marine biology [8]. By shrouding propellers and hulls with man-made bubble screens, unwanted noise produced by ships and submarines is quieted [9]. In shallow water, the presence of bubbles and bubble clouds produced by breaking waves greatly hinders the performance of sonar. This is especially true for mine hunting operations. In such cases, the scattering of sound from bubble clouds is an important consideration.

Another important application is in the understanding of ambient noise in the ocean. Since at least 1962 and the publication of the Wenz curves [10], the role of individual bubbles has been acknowledged. Mid-frequency noise scales well with wind speed above 500 Hz, and can often be attributed to the oscillation of individual bubbles and surface agitation [11, 12]. Through 1984, the wind dependency of ambient noise below 500 Hz was attributed to a variety of processes, including the coupling of wind turbulence into surface

¹Arnulph Mallock worked for Lord Rayleigh in the 1870’s and conducted experiments in the hydraulic laboratory at Terling, Lord Rayleigh’s estate [2].

waves, pressure deviations due to surface motions, nonlinear wave-wave interaction, spray and cavitation [13]. Then in 1985, at the fall meeting of the Acoustical Society of America, the following idea was put forth: The collective oscillation of bubble clouds produced by wind driven breaking waves could be responsible for the wind dependency of ambient noise around and below 500 Hz. This hypothesis was put forth independently by both Carey [14] and Prosperetti [15]. Since that time, the noise produced by the collective oscillation of bubble clouds, both artificial and those generated by breaking waves, has been studied by Carey *et al.* [16, 17, 18], Prosperetti *et al.* [19, 20], Kolaini *et al.* [21, 22], and Nicholas *et al.* [23], among others.

1.1.1 Origin of Oceanic Bubbles

Where do these ocean bubbles and bubble clouds come from, and how ubiquitous are they? As recently as 1965, a standard textbook in underwater acoustics stated that large numbers of bubbles did not occur regularly in the ocean, except in the wakes of ships [24, p. 86]. It is now well known that the upper layers of the ocean can contain as many as 10^5 to 5×10^6 bubbles per cubic meter, even in calm seas [8]. Supersaturation of sea water by spring warming, snow, rain, and wave breaking are all known to produce bubbles at or near the surface [25]. In addition, marine plant photosynthesis, marine mammal life processes, decomposition of organic material, and geological processes contribute to the continual presence of bubbles throughout the ocean [8]. Perhaps the most acoustically relevant bubbles are those produced by spilling and plunging breakers, which can form into plumes and clouds [26]. These bubble clouds can migrate, via turbulence [27] and Langmuir currents [28], into a variety of spacial distributions and be transported to depths as great as 30 meters. These bubble clouds can cause attenuation as great as 60 dB per meter [8], and persist for minutes at a time [26]. Recent measurements have shown that an artificial bubble cloud² can have a monopole target strength as high as -2.6 dB [29]. In addition to these naturally occurring bubbles, highly organized and extraordinarily

²Experimental cloud volume: 222 liters, void fraction: 0.006, depth: 90 m.

persistent bubbles are also found in the wakes of ships.

So in general, the near surface ocean environment can support a background of small, widely dispersed bubbles which primarily refract and attenuate sound. Superimposed on this background, one finds complex structures composed of groups of bubbles. These bubble clouds are created by wave action, can evolve spatially and temporally, and primarily scatter and attenuate sound.

1.1.2 Brief Problem Description

Bubbles and bubble clouds exist in the upper layers of the ocean. Sound propagation in shallow water waveguides, and deep water acoustic backscattering from near surface regions, are strongly affected by the presence of bubbles suspended in the water column. To first order, these effects manifest themselves as significant, frequency-dependent variations in sound speed, attenuation and scattering [30, 31]. Sound speed dispersion in clean suspensions of bubbles is well understood, except near the individual bubble resonance frequency, where experimental data is rare [32, for example]. The attenuation of sound in such bubbly mixtures is not well understood, particularly at and slightly above the bubble resonance frequency [33]. Furthermore, when considering small bubbles stabilized by layers of surface-active material, this deficiency is broadband; it applies to frequencies below, near and above the bubble resonance region [34, 35, 36, 37, 38]. Scattering from the sea surface has been studied extensively, but scattering from natural bubble clouds is not well understood. Even the idealized case of scattering from well characterized clouds in well characterized environments is almost completely unexamined.

The immediate purpose of this work is to increase our understanding of the basic physics of sound propagation and scattering in bubbly fluids through a carefully conducted laboratory investigation, primarily using air bubbles in pure water. The greater purpose is toward the achievement of a much longer term goal: complete understanding of the propagation and scattering of sound in the near surface and shallow water ocean environment.

1.2 Review of the Literature

There is a vast literature on the topic of acoustic bubbles. One of the most well known monographs on the subject, Timothy Leighton's *The Acoustic Bubble* contains references to over 1,400 cited works [39]. The present review will focus on theory and experiment in linear sound propagation through bubbly fluids, specifically air bubbles in water. In addition, a brief review of theory and experiment in sound scattering from artificial bubble clouds is presented.

1.2.1 Preliminary Topics

To begin, consider a single spherical gas bubble suspended in a liquid medium. At equilibrium, the hydrostatic pressure of the surrounding water is balanced by the gas pressure inside the bubble and the bubble has an equilibrium radius \bar{a} . If the gas behaves as an ideal gas, it is governed by the relation

$$PV^\nu = \text{constant}, \quad (1.1)$$

where P is the pressure, V is the volume and ν is the polytropic index. For an adiabatic process, $\nu = \gamma$, where γ is the ratio of specific heats of the gas. For an isothermal process, $\nu = 1$.

If the bubble radius is perturbed a small amount, equilibrium is lost and oscillation occurs. The alternating compression and expansion of the undriven bubble is due to the transfer of energy between an effective inertia provided by the locally surrounding liquid, and the compressibility of the gas inside the bubble. At this stage, lossless conditions are assumed, but viscous, thermal and acoustic dissipative effects will eventually be included. It can be shown that the effective stiffness of the bubble is given by $12\pi\bar{a}\nu P_\infty$, where P_∞ is the hydrostatic pressure and the effect of surface tension has also been neglected. Since the bubble acts like a small pulsating sphere and radiates sound uniformly in all directions,

the effective mass is given by the low frequency limiting value of the radiation reactance. This low frequency limit is called the radiation mass and is given by $4\pi\bar{a}^3\rho_\ell$, where ρ_ℓ is the liquid density. This limiting value is acceptable because the resonance size of a gas bubble is always much smaller than the wavelength in the water at resonance frequency. The resonance frequency is then given by the square root of the stiffness to mass ratio, or

$$\omega_0 = \frac{1}{\bar{a}} \sqrt{\frac{3\nu P_\infty}{\rho_\ell}} \quad (\text{radians/sec}), \quad (1.2)$$

where \bar{a} is the equilibrium bubble radius, ν is the polytropic index, P_∞ is the hydrostatic pressure and ρ_ℓ is the density of the surrounding liquid.

This relation was first derived by Minnaert [4] in 1933, although he used a different methodology. Minnaert was considering bubbles in the size range 3–6 mm, and concluded that the period of oscillation would be small compared to the time required for the heat of compression to be conducted away. Since the bubble was considered to be undergoing an adiabatic process, the polytropic index ν was taken to be the ratio of specific heats γ . It turns out that the adiabatic and negligible surface tension assumptions made by Minnaert were reasonable for the bubble sizes he was considering, but it is instructive to consider a more accurate description.

As pointed out by Leighton [39], because of the high thermal conductivity and specific heat capacity of the surrounding liquid, the gas in direct contact with the bubble wall can be considered isothermal. The gas at the very center of the bubble behaves adiabatically. Therefore, the polytropic index for the bubble as a whole can take on a range of intermediate values depending on the bubble's size relative to the size of the thermal boundary layer. The ratio of the bubble equilibrium radius to the length of thermal boundary layer l_{th} is given by

$$\frac{\bar{a}}{l_{\text{th}}} = \frac{\bar{a}\sqrt{2\omega}}{\sqrt{D_g}}, \quad (1.3)$$

where D_g is the thermal diffusivity of the gas and ω is the frequency of excitation. For

sufficiently high frequencies, the bubble is much larger than l_{th} and it behaves adiabatically. For sufficiently low frequencies, the bubble is much smaller than l_{th} and it behaves isothermally. The value of D_g for air at room temperature is $2.08 \times 10^{-5} \text{ m}^2/\text{s}$, therefore, \bar{a} is about 90 times l_{th} for Minnaert's bubbles, confirming the adiabatic assumption.

By virtue of the surface separating the liquid and the gas inside the bubble, a surface tension arises at the bubble wall. The effect of surface tension is to increase the pressure inside a bubble to a value greater than the hydrostatic pressure P_∞ . The pressure inside the bubble at equilibrium is given by

$$P_{\text{b,e}} = P_\infty + \frac{2\sigma}{\bar{a}}, \quad (1.4)$$

where σ is the surface tension, which is a property of the two materials in contact. The term $2\sigma/\bar{a}$ is known as the Laplace pressure. For air and water, $\sigma = 0.0725 \text{ N/m}$, therefore the Laplace pressure can be considered negligible when $\bar{a} \gtrsim 0.1 \text{ mm}$, as far as the natural frequency is concerned. At this bubble size, the Laplace pressure is less than 1.5% of $P_{\text{b,e}}$ and gets smaller as the bubble size increases. With these preliminary topics in mind, the discussion will now turn to the propagation of sound through a collection of bubbles. In such a case, the incident acoustic pressure is the source of perturbation.

1.2.2 Theory of Sound Propagation in Bubbly Fluids

With apparently no predecessors, Mallock [1] in 1910 applied mixture theory to what he termed “frothy liquids,” under the assumption that the gas bubbles were of such number and separation that the medium could be considered homogenous. He obtained an expression for the mixture sound speed which, under certain conditions, is still valid 92 years later. In 1930, Wood [40] began with a thermodynamic argument and confirmed Mallock's work, but cast the results in a more useful form, and specifically considered air bubbles in water. From this humble beginning, much progress has been made. In this section, basic equations pertinent to sound propagation in bubbly liquid will be developed, based on the

work of Carey [41], and Carey and Roy [42].

The following assumptions and definitions are used. The bubbly fluid is composed solely of spherical gas bubbles suspended in liquid under the influence of small amplitude pressure fluctuations. The subscripts ℓ and g refer to the liquid and gas phases, respectively. Effective quantities pertaining to the mixture are denoted with the subscript m . Mass is conserved such that the mixture mass is the sum of the liquid and gas masses, and there is no relative translational motion between the two phases. This means the bubbles are small enough that buoyancy does not cause them to rise significantly over the acoustic time scale, which is $1/f$, the inverse of frequency. Many of the bubbles found in the upper layers of the ocean are included in this category.

Under such circumstances the volume fraction of the gas phase, known as the void fraction χ is given by

$$\chi = V_g/V_m, \tag{1.5}$$

where V_g is the volume of the gas phase and V_m is the total volume of the mixture, given by $V_m = V_g + V_\ell$. The effective mixture density is

$$\rho_m = (1 - \chi)\rho_\ell + \chi\rho_g, \tag{1.6}$$

where ρ_ℓ is the density of the liquid and ρ_g is the density of the gas. The mixture compressibility κ_m can be shown to be

$$\kappa_m = (1 - \chi)\kappa_\ell + \chi\kappa_b, \tag{1.7}$$

where κ_ℓ is the compressibility of the liquid and κ_b is the compressibility due to the gas in the bubbles. In general, the speed of sound c is defined

$$c^2 = \frac{1}{\rho\kappa}. \tag{1.8}$$

Further definition of κ_b and the way it is eventually included in Eq. 1.8 depends in part upon the conditions that prevail during the compression phase. For air bubbles in water at frequencies well below individual bubble resonance, the process can be considered isothermal, as mentioned in Section 1.2.1 and shown rigorously by Hsieh and Plesset [43]. The response of an individual bubble is dominated by the compressibility of the gas within the bubble, hence $\kappa_b = (\kappa_g)_{\text{isothermal}}$. As the excitation frequency increases, the dynamics of the bubble become important and $\kappa_b \rightarrow \kappa_b(f) \neq \kappa_g$. Well above resonance, the bubbles behave adiabatically. In between, the polytropic index that governs the compression and expansion of the gas inside the bubbles is frequency dependent, as shown by Prosperetti [44] and must be accounted for. We first consider the low frequency case where the excitation frequency is well below the resonance frequency of any individual bubble.

Low Frequency Propagation

Substitution of Eqs. 1.6 and 1.7 into Eq. 1.8 results in an equation for the mixture sound speed,

$$\frac{1}{c_m^2} = [(1 - \chi)\rho_\ell + \chi\rho_g] [(1 - \chi)\kappa_\ell + \chi\kappa_g], \quad (1.9)$$

which is equivalent to Wood's 1930 equation [40]. For bubbles well below resonance size, where surface tension and dissipative effects are negligible, Eq. 1.8 can be used to relate the above result to the density and sound speeds of the the two mixture components.

After manipulation this results in the equivalent relation

$$\frac{1}{c_{mlf}^2} = \frac{(1 - \chi)^2}{c_\ell^2} + \frac{\chi^2}{c_g^2} + \chi(1 - \chi) \frac{\rho_g^2 c_g^2 + \rho_\ell^2 c_\ell^2}{\rho_\ell \rho_g c_\ell^2 c_g^2}, \quad (1.10)$$

where c_{mlf} is the low frequency mixture sound speed and c_g is the isothermal sound speed in the gas. Note that as the mixture approaches pure liquid, $\chi \rightarrow 0$ and $c_{mlf} \rightarrow c_\ell$. Alternatively, as $\chi \rightarrow 1$, $c_{mlf} \rightarrow c_g$. It is noted that upon approach to $\chi = 1$, a change to the adiabatic speed of sound in air would be required. The bubbly liquid sound speed

given by Eq. 1.9 or 1.10 is known as Wood's low frequency sound speed or the Wood limit sound speed. The behavior of Eq. 1.10 for air bubbles in sea water is shown in Fig. 1.1.

Because of the great difference in density and sound speed between air and water, Eq. 1.10 can be approximated by a much simpler expression for a limited range of χ . For air bubbles in water, in the range $0.002 < \chi < 0.94$, the first two terms on the right-hand side of Eq. 1.10 are much smaller than the third term. Neglecting them and noting that $\rho_g^2 c_g^2 \ll \rho_l^2 c_l^2$ results in

$$c_{mlf}^2 \simeq \frac{1}{\rho_l \kappa_g \chi (1 - \chi)}. \quad (1.11)$$

The compressibility of the gas is given by $\kappa_g = 1/P_\infty$ for this isothermal case, where P_∞ is the local hydrostatic pressure and the Laplace pressure due to surface tension has been neglected. Substitution into Eq. 1.11 results in a simple approximate expression for the low frequency mixture sound speed

$$c_{mlf} \simeq \sqrt{\frac{P_\infty}{\rho_l \chi (1 - \chi)}}, \quad \{0.002 < \chi < 0.94, \text{ error} < 1.2\%\}. \quad (1.12)$$

A comparison between Eq. 1.10 and Eq. 1.12 is shown in Table 1.1 for air bubbles in sea water at atmospheric pressure. A minimum occurs at $\chi = 0.5$, and the mixture sound speed is lower than the intrinsic sound speeds in air or water across much of the void fraction range. This remarkable result can be qualitatively explained in the following manner: The addition of bubbles greatly increases the mixture compressibility yet effects the density much less. The high compressibility coupled with high density leads to low sound speed, as seen in Eq. 1.8. Another interesting result is that in this model, the bubble size does not play a role at low frequencies. The primary environmental variable is the void fraction. Extensions to Eq. 1.12 accounting for relative motion between the phases, i.e. bubbly fluid flows, have been provided by Crespo [45] and Ruggles *et al.* [46].

The Effect of Bubble Dynamics

There is a simple and heuristic way to approximately account for the effects of bubble dynamics by using a compressibility argument and modeling the individual bubble response as that of a simple harmonic oscillator, thereby extending Eq. 1.9 for use at all frequencies. For sufficiently small pressure fluctuations given by $P(t) = P_\infty + p(t)$, an isolated spherical bubble exhibits radially symmetric oscillations of the form $a(t) = \bar{a} + \xi(t)$. For harmonic excitation, $p(t) = P_a e^{i\omega t}$ and $\xi(t) = \xi_0 e^{i\omega t}$.

The effect of bubble dynamics for a distribution of bubble sizes can be accounted for by evaluating κ_b in Eq. 1.7 in the following way. If we take a control volume approach, the gas volume $V_g = \frac{4}{3}\pi V_m \int_0^\infty \wp(a) a^3 da$, where V_m is the total volume, and $\wp(a) da$ is number of bubbles per unit volume with equilibrium radius between a and $a + da$. Then the compressibility becomes

$$\kappa_b = \frac{-1}{V} \frac{\partial V}{\partial P} = -4\pi \int_0^\infty \wp(a) a^2 \left(\frac{\partial a}{\partial P} \right) da. \quad (1.13)$$

The partial derivative in the integrand can be evaluated approximately for small signal conditions using the linear oscillator model, where $\xi(t)$ is governed by

$$\frac{d^2 \xi}{dt^2} + 2\delta \frac{d\xi}{dt} + \omega_0^2 \xi = \frac{-P_a e^{i\omega t}}{\rho_\ell \bar{a}}. \quad (1.14)$$

The term δ represents a frequency and equilibrium radius dependent dissipation term, as of yet unspecified, and ω_0 is given by Minnaert's [4] relation

$$\omega_0 = \frac{1}{\bar{a}} \sqrt{\frac{3\gamma P_\infty}{\rho_\ell}}. \quad (1.15)$$

The steady state solution of Eq. 1.14 then yields

$$a(t) = \bar{a} + \xi(t) = \bar{a} + \text{Re} \left[\frac{-P_a e^{i\omega t}}{\rho_\ell \bar{a} \omega_0^2 \left(1 - \frac{\omega^2}{\omega_0^2} + i \frac{2\delta(\omega, \bar{a}) \omega}{\omega_0^2} \right)} \right], \quad (1.16)$$

where Re indicates the real part of the bracketed term. Consequently, $\partial a/\partial P$ can be evaluated by noting that $\partial a/\partial P \rightarrow \partial \xi/\partial p$, which results in

$$\frac{\partial \xi}{\partial p} = \frac{\partial}{\partial p} \left[\frac{-p(t)}{\rho_\ell \bar{a} \omega^2 \left(1 - \frac{\omega^2}{\omega_0^2} + i \frac{2\delta(\omega, a)\omega}{\omega_0^2} \right)} \right] = \frac{-\bar{a}}{3P_\infty \left(1 - \frac{\omega^2}{\omega_0^2} + i \frac{2\delta(\omega, a)\omega}{\omega_0^2} \right)}, \quad (1.17)$$

and use of Eq. 1.15 has been made to form the last equality. Eq. 1.13 is then substituted into the mixture compressibility Eq. 1.7, which allows evaluation of Eq. 1.9 without restriction in frequency. Additional manipulation yields the following approximate expression for the mixture sound speed in terms of a frequency dependent bubble response term F_b ,

$$\frac{1}{c_m^2} = \frac{(1 - \chi)^2}{c_\ell^2} + \frac{\chi^2}{c_g^2} F_b + \frac{\chi(1 - \chi)\rho_\ell}{P_\infty} F_b, \quad (1.18)$$

where

$$F_b = \frac{1}{\int_0^\infty \wp(a) a^3 da} \int_0^\infty \frac{\wp(a) a^3 da}{1 - \frac{\omega^2}{\omega_0^2} + i \frac{2\delta(\omega, a)\omega}{\omega_0^2}}. \quad (1.19)$$

For $\omega \ll \omega_0$, F_b approaches unity, and Eq. 1.18 reduces to the previous low frequency expression Eq. 1.10.

A similar approach and result has been reported by Meyer and Skudrzyk [47, 48]. Similar results have also been obtained via alternative approaches. In the 1940's, Foldy [49] and Carstensen and Foldy [50] utilized a scattering approach where the bubble dynamics are manifested in the frequency dependent scattering strength of independent bubbles summed over the bubble size distribution. From the basic conservation equations in terms of averaged quantities, Whitfield and Howe [51] obtained a similar expression for the wave number that accounts for frequency dependent bubble damping.

Finally, based on the linearized effective conservation equations of Caffisch *et al.* [52], and van Wijngaarden [53], along with the bubble dynamics of Prosperetti *et al.* [54] and Keller [55], Commander and Prosperetti [33] derived a wave number for the effective medium which accounts for bubble damping in the form of viscous, thermal, and acoustic

re-radiation components. The latter two terms have been incorporated in a frequency dependent manner.³ An equilibrium bubble size and frequency dependent polytropic index has also been incorporated, which plays an important role in this bubble size range. The addition of these details results in a bubble resonance frequency that differs somewhat from Eq. 1.15. Recall that in Wood’s equation, the polytropic index is taken to be unity for isothermal behavior. For the Minnaert resonance frequency (Eq. 1.15), lossless and adiabatic behavior was assumed, and the polytropic index was taken to be the ratio of specific heats γ , which is 1.4 for air. For a bubble of 0.5 mm radius, the polytropic index near resonance is actually about 1.2 [56]. Additional attention will be given to these issues in Section 2.1.

1.2.3 Theory of Scattering from Acoustically Compact Bubble Clouds

As mentioned before, it was postulated that the collective oscillation of bubble clouds could possibly account for increased wind dependent low-frequency ambient noise in the ocean [14, 15]. Subsequent work by Roy *et al.* [57] showed that when insonified by low frequencies, bubble clouds behave to first order like compressible spheres, characterized by cloud size and free gas volume, as opposed to the number density and size of individual bubbles. It was also shown [42, 58] that that the general scattering formulation for a given compressible body can be taken from the classical literature, such as Anderson [59], Morse and Ingard [60] or Rzhevkin [61]. The compressibility of the scatterer is obtained from the low frequency void fraction dependent sound speed (Eq. 1.12, for example) and the scattered field can thus be predicted. Near surface bubble clouds have been modeled as acoustically compact scatterers near a pressure release plane by Crum *et al.* [62] and Roy *et al.* [63]. These theoretical developments and the related experimental work (The Lake Seneca Experiment) up to 1995 were comprehensively archived by Schindall [56].

³For radii between $3\mu\text{m}$ – 3 mm (a size range prevalent in the upper layers of the ocean) thermal damping is dominant [19].

1.2.4 Experiments in Sound Propagation and Scattering in Bubbly Fluids

While the theoretical literature on this subject is vast, the experimental literature is not. One finds reference to the same few papers again and again. In fact, most theoretical papers appear with no comparison to measurement at all. A brief overview of some of the best measurements of phase speed and attenuation will be presented here, followed by a short discussion of scattering measurements.

Low Frequency Propagation

One of the most enduring works is that of Silberman [64], published in 1957. He measured the phase speed of bubbly fluid in a vertical steel pipe using a standing wave technique. Hypodermic needles produced bubbles with radius of order 1 mm. The pipe was excited at the lower end by a modified telephone speaker. The distance between neighboring pressure nodes, obtained via scanned hydrophone, gave the half-wavelength, from which the phase speed was determined by $c = f\lambda$, after corrections for elastic waveguide effects and hydrostatic head gradient were applied. Phase speeds were measured for frequencies 90–3000 Hz, and for void fractions about 0.001–0.1. Comparison was made with the simplified Wood’s Eq. 1.12 and in Silberman’s words, agreement was “satisfactory,” showing little dispersion below 1/10 resonance frequency.

At nearly the same time, similar work was being performed by Karplus [7], using the same type of apparatus and procedure. A degree of linear dispersion was found, which was later attributed to the presence of detergent in the system. When the results were extrapolated to zero frequency, excellent agreement was found with Wood’s Eq. 1.12.

These examples are typical and other corroborations exist, such as in works by Campbell and Pitcher [65], Ruggles *et al.* [46], Gibson [66], and recently Costigan and Whalley [67]. As an introductory exercise, this author conducted a simple set of experiments for comparison with Wood’s Eq. 1.10 and also found excellent agreement [68]. Results from

this experiment are shown in Fig. 1.2 and the experiment is described in Appendix A. These results are typical and are representative of the others mentioned above. Although Fig. 1.2 only shows data for a maximum void fraction of 2.5%, experimental verification is common in the literature up to 50–60%. There is at least one instance where Wood’s Equation was verified up to 85%, published by Semenov and Kosterin [69]. Therefore, Wood’s Eq. 1.12 is generally excepted as a good approximation for clean water, in the low frequency limit, below about half of the individual bubble resonance frequency. It is an approximation though, because there is a small amount of dispersion, as has been observed by Ruggles [46] and Karplus [7]. It is on the order of a few percent, but of course increases as the frequency increases. This will be discussed further in Section 4.3, because it can play an important role if one wishes to use the low frequency sound speed as a measure of void fraction.

The Effect of Bubble Dynamics—Broadband Propagation

In this section, four modern papers will be discussed. The first two present highly developed theories with few limitations, yet both rely on decades-old data for comparison. It is clear from all four that additional experimental data is desperately needed for corroboration.

In addition to the development of their model, Commander and Prosperetti [33] review several experimental works for comparison. In their opinion, the premier experimental results available at the time were still those of Silberman [64]. Some of the others included are Fox *et al.* [70], Kol’tsova *et al.* [71], and Macpherson [72]. Several other experimental works are mentioned (including contemporary ones) but are not deemed useful for comparison due to insufficient control over, or reporting of, the necessary model parameters.

The performance of this model is best summed up in the words of the authors:

“The data concern the phase speed, attenuation, and transmission coefficient through a layer of bubbly fluid. It is found that the model works very

well up to volume fractions of 1%–2% provided that bubble resonances play a negligible role. Such is the case in a mixture of many bubble sizes or, when only one or a few sizes are present, away from the resonance frequency regions for these sizes. In the presence of resonance effects, the accuracy of the model is severely impaired.”

A typical result for attenuation is shown in Fig. 1.3, which is a comparison with Silberman’s data [64] for 0.0377% volume fraction and bubble radius around 1 mm. Although the log scale obfuscates it, the measurement near resonance is less than one third of the prediction. The poor performance close to resonance is attributed to the incorrect representation of multiple scattering processes between bubbles.

In an attempt to address this issue, Feuillade [73] has developed a model that “includes all orders of multiple scattering.” The validity of this model has been challenged within the community, but it is included here because it represents one of the most recently published results. Again, comparison is made to decades-old data; that of Silberman [64] and Fox *et al.* [70]. The need for more data, especially near resonance frequency, is made poignantly clear in Fig. 1.4. Even a few quality data points around resonance would help confirm the validity of any of these models. Based on comparison with limited data, this model’s performance appears quite similar to that of Commander and Prosperetti, and no conclusions can be drawn.

Another publication is worth mentioning here, because it appears to almost perfectly describe Silberman’s data for both attenuation and phase speed. This model by Varadan *et al.* [74] utilizes a Monte-Carlo numerical simulation to account for multiple scattering. After seeing this paper, one might think that the issue is closed because the agreement between experiment and model is so good. There is a problem, though. Silberman’s paper contains seven plots of phase speed and attenuation, for as many different void fractions and several bubble sizes each. There is apparently only one case shown in Varadan *et al.*, and it contains eight data points on the phase speed curve and another seven on the

attenuation plot. The particular case they are comparing to is never mentioned! The reader is not informed of the void fraction or the bubble size, or the figure from which Silberman's data was taken! Why were the other cases not compared? Did the model describe them poorly? This glaring omission relegates the work to nothing more than a curiosity.

The final work discussed contains the present state-of-the-art measurement of phase speed in a bubbly liquid.⁴ Using a fiber optic laser interferometer and a vertical standing wave tube, Cheyne, Stebbings and Roy [32] obtained measurements above and below resonance, but none within a 1500 Hz band immediately surrounding resonance, as shown in Fig. 1.5. They compare their data to the model of Commander and Prosperetti [33] with good agreement, but the region of greatest interest was unobtainable due to excessive attenuation for frequencies near ω_0 .

The description of real bubbly fluids is inherently a statistical endeavor. For air bubbles in water, it is not practical to know the position, velocity, size and shape of every bubble for all time. This has been addressed in theoretical developments by Foldy [49] and by Howe [75], for instance. In the current formulation it is addressed by accounting for the bubble size distribution with a probability density function, such as $\varphi(a)$ in Eq. 1.13. There have been a number of experimental studies performed in the ocean, where the time evolution of scattering from and propagation through bubble clouds has been investigated, [76] for example. In laboratory experiments focused on observing the propagation parameters, time-averaged data is typically presented. This author has found no experimental work in which the acoustic and bubble population parameters were both observed in detail as a function of time.

Scattering from Bubble Clouds

There is a large literature on the topic of sea surface scatter and a good deal of evidence that suggests bubble clouds produced by breaking waves play a significant role [77, 78]. If

⁴For unknown reasons, Feuillade did not consider this data for comparison, despite its availability.

one considers scattering from well characterized clouds in well characterized environments, where experimental uncertainty is minimized, there may be only one precedent, The Lake Seneca Experiment [29, 42, 56, 57, 58, 62, 63]. In the most recent work, Gephart [29] uncovered a systematic experimental error that brought theory and measurement into agreement for the monopole component of the scattered field, but considerable higher order detail remains unexplained. The target strength of a typical Lake Seneca bubble cloud is shown in Fig. 1.6, along with the compressible sphere scattering prediction. Good agreement was found with the theory up to the the first resonance frequency. Above the first resonance frequency, the cloud was no longer acoustically compact, and the simple “effective monopole” model was not expected to describe the data.

1.3 Recapitulation

It is appropriate to reiterate the main points discussed thus far. Several theories exist which describe sound propagation in bubbly fluids at and near the resonance frequency, but there has been very little reliable data to compare with these theories. Therefore, inconsistencies about behavior at resonance among the various theories are unresolved and the range of validity of these theories is not known. In the present work, the acoustics of bubbly fluids is viewed as two sides of the same coin. If propagation through bubbly fluids is the first side, then the second side is scattering from assemblages of bubbly fluid. For excitation frequencies much lower than the individual bubble resonance frequency, classical scattering theory has been used, along with an effective medium description of the bubbly interior, to predict the lowest resonance frequency of an artificial bubble cloud, and the target strength of the cloud up to the lowest resonance frequency. Extensive measurements of scattering from the sea surface have been performed, but beyond the Lake Seneca experiment, no other experimental data on scattering from well characterized bubble clouds in well characterized environments has been found. These are the motivating issues of this work.

1.3.1 Primary Contributions

There are three primary contributions reported and discussed herein:

1. A new experimental instrument, in the form of an improved water-filled impedance tube, has been developed. The purpose of the instrument is to measure sound speed and absorption in bubbly fluids, below, at and above the resonance frequency of the individual bubbles. The speed, accuracy and precision of this instrument is unprecedented for a water-filled impedance tube.
2. Unique measurements of phase speed and attenuation in bubbly liquid across the resonance regime have been obtained with this instrument. Never before has the impedance tube technique been applied to bubbly liquid. Both time-averaged and instantaneous measurements have been obtained. Existing theory satisfactorily describes these measurements, but knowledge of the bubble population parameters is insufficient to allow absolute verification.
3. New scattering experiments employing a bubbly-liquid-filled compliant cylinder have been performed. These experiments have shown that bubble clouds with a known geometry can be described by classical scattering formulations using a Wood's limit effective medium description of the bubbly interior at higher frequencies than previously shown. The range of validity of this approach has been extended to about three times the lowest resonance frequency of the cloud.

1.3.2 Road Map of Dissertation

The present chapter provides the motivation and background material, and outlines the primary direction of the work. A concise literature review is also included. The theory of sound propagation in bubbly fluids and the theory of scattering from a bubbly-liquid-filled compliant cylinder is discussed in Chapter 2. Chapter 3 documents the development, implementation, and verification of the new experimental apparatus, a water-filled impedance

tube. Included in Chapter 3 are discussions of basic impedance tube theory, adaptation of an airborne theory for use in water and theory of propagation in realistic elastic waveguides. The measurement procedure and the results of the propagation experiments are described in Chapter 4, along with comparison to existing theory. In Chapter 5, the experimental observation of scattering from a bubbly-liquid-filled compliant cylinder is reported. Finally, several appendices are included which contain supporting information and the work concludes with the bibliography.

–	Eq. 1.10	Eq. 1.12
χ	c_{mlf} (m/s)	c_{mlf} (m/s)
0	1500 [†]	1500
0.002	220.54	222.95
0.02	71.071	71.148
0.2	24.896	24.902
0.5	19.909	19.922

Table 1.1: Representative sound speeds for air bubbles in sea water at atmospheric pressure, calculated from Eq. 1.10 and Eq. 1.12 using: $\rho_\ell = 1021 \text{ kg/m}^3$, $c_\ell = 1500 \text{ m/s}$, $\rho_g = 1.21 \text{ kg/m}^3$, $P_\infty = 101.3 \text{ kPa}$ and $c_g = \sqrt{P_\infty/\rho_g}$, the isothermal value. [†]The $\chi = 0$ value was not calculated but merely included for comparison.

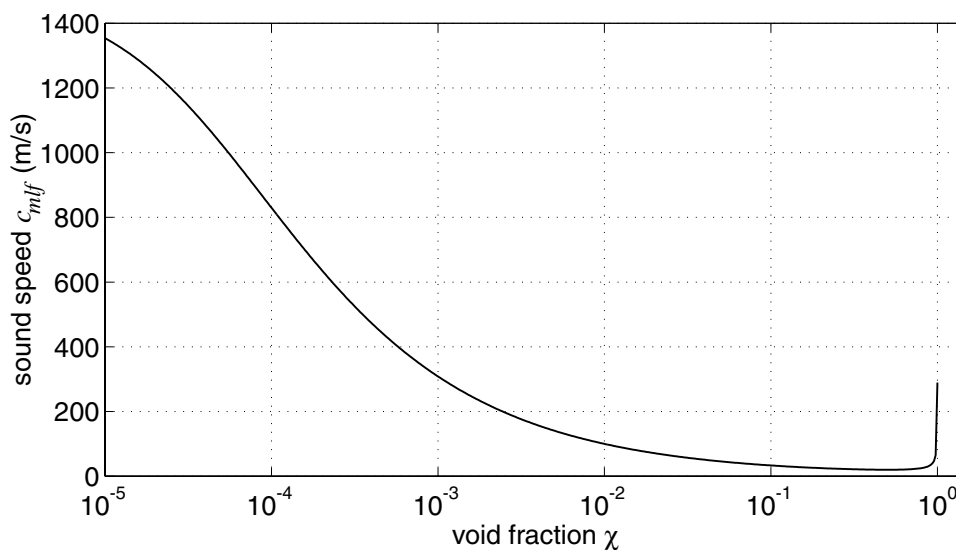


Figure 1.1: Eq. 1.10, is plotted for air bubbles in sea water with $c_\ell = 1500 \text{ m/s}$, $\rho_\ell = 1021 \text{ kg/m}^3$, $c_g = 289.3 \text{ m/s}$, and $\rho_g = 1.21 \text{ kg/m}^3$.

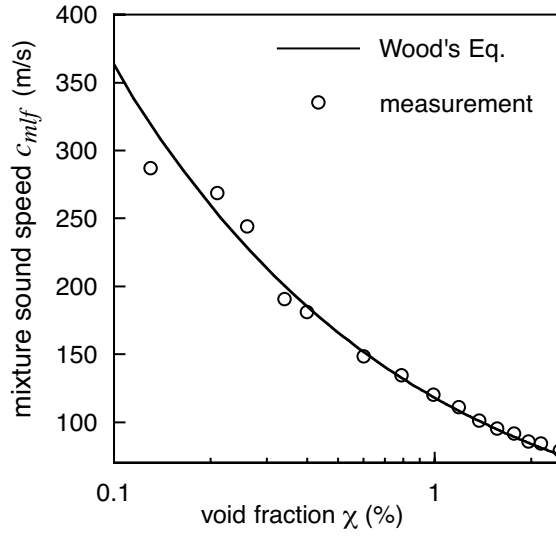


Figure 1.2: Experimental verification of Wood's Equation (Eq. 1.10) is shown. See Appendix A for a detailed description.

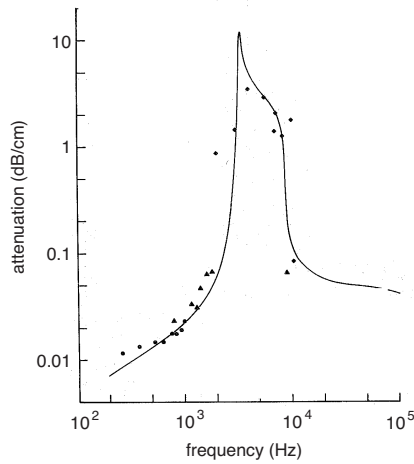


Figure 1.3: Comparison of Commander and Prosperetti's theoretical attenuation with Silberman's data for $\beta = 0.0377\%$ and bubble radii 0.994 mm (diamonds) and 1.07 mm (triangles and circles). Figure adapted from [33].

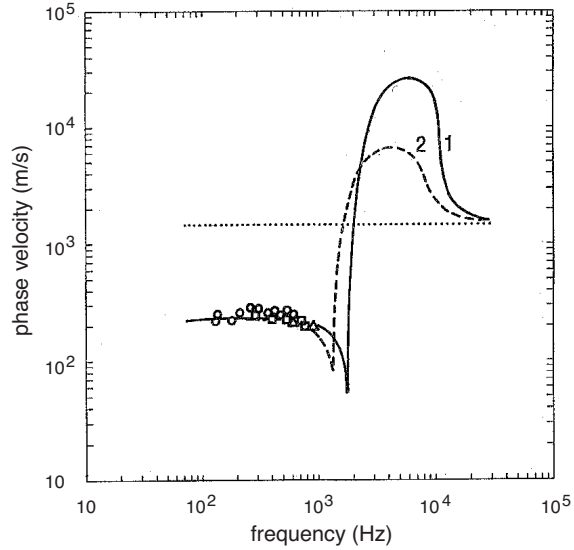


Figure 1.4: Comparison of theoretical phase speed of Foldy (curve 1) and Feuillede (curve 2) with Silberman's data for $\beta = 0.22\%$ and bubble radii 1.83 mm (circles), 2.07 mm (squares) and 2.44 mm (triangles), after [73]. The horizontal dotted line represents the speed of sound in pure water for experimental temperature.

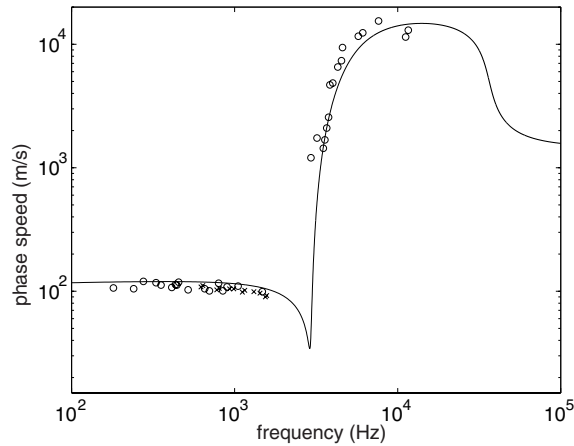


Figure 1.5: Comparison of Commander and Prosperetti's theoretical phase velocity with Cheyne *et al.* data for $\beta = 1\%$ and bubble radii 1.11 mm. Both interferometer (\circ) and hydrophone (\times) data is shown, after [32].

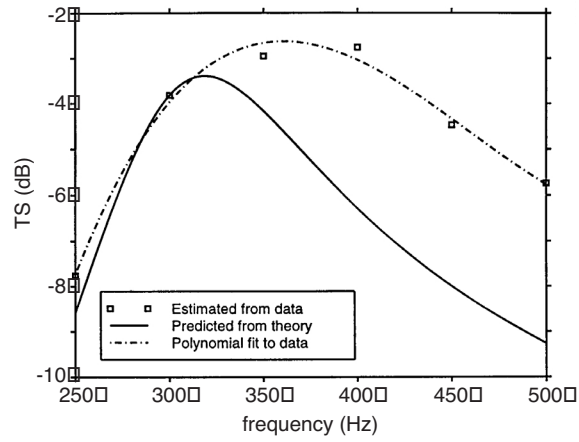


Figure 1.6: The target strength of a bubble cloud from the Lake Seneca experiment is shown. The figure was adapted from Gephart [29].

Chapter 2

Exploration of Propagation and Scattering Theory

This section will be devoted to the theoretical description of sound propagation in bubbly liquids, and the theoretical description of scattering from a bubbly-liquid-filled compliant tube. The heuristic development of a broadband equation for sound speed was shown in Section 1.2.2, but the damping term was left undefined. For air bubbles in pure water, three damping mechanisms are at work. 1) Energy is lost via thermal conduction between the gas and the host liquid. 2) Work is performed against viscous forces at the bubble wall. 3) Energy is radiated away from the bubble in the form of acoustic waves. These dissipative effects are accounted for in the following discussion. In the ocean, the presence of natural and man made surface-active materials may accumulate on the bubble wall. The energy flow in and out of a bubble can be altered by surfactants, but these effects are ignored in the present work.

2.1 Acoustic Propagation in Bubbly Liquids, Revisited

In 1989, Commander and Prosperetti [33] brought together results previously published by other authors and composed a model for sound propagation in bubbly liquid which

accounted for energy dissipation in a detailed way. The first component was the equations of motion published by Caffisch *et al.* [52] and van Wijngaarden [53]. The second component was a precise description of the internal dynamics of the bubbles put forth by Prosperetti, Crum and Commander [54] and Keller [55]. The basic form of their equation for the bubbly liquid complex sound speed is similar to that of Foldy [49], Whitfield and Howe [51] and Eq. 1.18, and their treatment of bubble damping is similar to that in [51]. Complete derivation of the Commander and Prosperetti result is a significant endeavor and therefore beyond the present scope. It was even beyond the scope of [33], which gave an overview of the derivation. The final result is shown below and the interested reader is referred to [33] and the various original works cited therein.

Consider a host liquid with sound speed c_ℓ , density ρ_ℓ , surface tension μ , viscosity σ and equilibrium pressure P_∞ . This liquid contains bubbles composed of a gas with thermal diffusivity D_g and ratio of specific heats γ . The complex mixture sound speed c_m is given by

$$\frac{c_\ell^2}{c_m^2} = 1 + 4\pi c_\ell^2 \int_0^\infty \frac{a\wp(a)da}{\omega_0^2 - \omega^2 + 2ib\omega}, \quad (2.1)$$

where ω is the circular excitation frequency and $\wp(a)da$ is the number of bubbles per unit volume with equilibrium radius between a and $a + da$. The damping coefficient is defined by

$$b = \frac{2\mu}{\rho_\ell a^2} + \frac{P_{b,e}}{2\rho_\ell a^2 \omega} \text{Im}\Phi + \frac{\omega^2 a}{2c_\ell}, \quad (2.2)$$

where the three terms are due to viscous, thermal and acoustic dissipation effects, respectively and $\text{Im}\Phi$ is the imaginary part of

$$\Phi = \frac{3\gamma}{1 - 3(\gamma - 1)iX[(i/X)^{1/2} \coth(i/X)^{1/2} - 1]}. \quad (2.3)$$

The bubble resonance frequency is

$$\omega_0^2 = \frac{P_{b,e}}{\rho_\ell a^2} \left(\text{Re}\Phi - \frac{2\sigma}{aP_{b,e}} \right), \quad (2.4)$$

where $\text{Re}\Phi$ is the real part of Φ . The definition

$$X = D_g/\omega a^2, \quad (2.5)$$

has been used and the quantity $P_{b,e}$ represents the equilibrium pressure in the bubbles

$$P_{b,e} = P_\infty + \frac{2\sigma}{a}, \quad (2.6)$$

where P_∞ is the hydrostatic pressure in the liquid. The wave number for propagation within the bubbly mixture can then be written from Eq. 2.1 as

$$k_m^2 = \frac{\omega^2}{c_l^2} + 4\pi\omega^2 \int_0^\infty \frac{a\wp(a)da}{\omega_0^2 - \omega^2 + 2ib\omega}. \quad (2.7)$$

It can be seen from Eq. 2.4 that the bubble resonance frequency becomes a function of frequency. The polytropic index ν is not explicitly apparent, but it becomes a function of frequency and bubble size. The polytropic index is contained in Eq. 2.3, and is given by

$$\nu = \frac{1}{3}\text{Re}\Phi. \quad (2.8)$$

2.1.1 Comparison Of Results

The two results for broadband sound speed, Eqs. 2.1 and 1.18 were obtained in different ways, but the results appear quite similar. It turns out that under some reasonable assumptions they are equivalent, as will be shown below.

Begin by evaluating Commander and Prosperetti's Eq. 2.1 for a monodisperse¹ bubble population given by

$$\wp = n\delta(a - \bar{a}), \quad (2.9)$$

¹The adjective monodisperse is deeply rooted in the literature, despite being somewhat self-contradictory. In this work, monodisperse will refer to either a delta function distribution, or a very narrow distribution with a single peak.

with n bubbles per unit volume and equilibrium radius \bar{a} , which results in

$$\frac{c_\ell^2}{c_m^2} = 1 + \frac{4\pi c_\ell^2 n \bar{a}}{\omega_0^2 - \omega^2 + 2ib\omega}. \quad (2.10)$$

Now consider the broadband equation derived in Chapter 1. Evaluation of Eq. 1.19 for the bubble population given by Eq. 2.9 results in

$$F_b = \frac{1}{1 - \frac{\omega^2}{\omega_0^2} + i\frac{2\delta\omega}{\omega_0^2}}. \quad (2.11)$$

Impose a low void fraction assumption $\chi \ll 1$, such that $(1 - \chi)^2 \approx 1$ and $\chi^2 \approx 0$, which transforms Eq. 1.18 into

$$\frac{1}{c_m^2} = \frac{1}{c_\ell^2} + \frac{\chi(1 - \chi)\rho_\ell}{P_\infty} \frac{\omega_0^2}{\omega_0^2 - \omega^2 + 2i\delta\omega}. \quad (2.12)$$

Using $\omega_0^2 = 3\gamma P_\infty / \rho_\ell \bar{a}^2$, Eq. 2.12 becomes

$$\frac{1}{c_m^2} = \frac{1}{c_\ell^2} + \frac{3\gamma\chi}{\bar{a}^2} \frac{1}{\omega_0^2 - \omega^2 + 2i\delta\omega}, \quad (2.13)$$

by again noting that $1 - \chi \approx 1$ for $\chi \ll 1$. Using the definition of void fraction from Eq. 1.5 obtain the equivalent statement,

$$\chi = \frac{4}{3}\pi\bar{a}^3 n. \quad (2.14)$$

Making one last assumption, $\nu \approx 1$ instead of γ , we find that

$$\frac{3\nu\chi}{\bar{a}^2} = 4\pi\bar{a}n, \quad (2.15)$$

which upon substitution into Eq. 2.13 yields

$$\frac{1}{c_m^2} = \frac{1}{c_\ell^2} + \frac{4\pi\bar{a}n}{\omega_0^2 - \omega^2 + 2i\delta\omega}, \quad (2.16)$$

the same expression shown in Eq. 2.10. This is a very interesting result. Even though the polytropic index ν was taken to be unity, which is a low frequency assumption, we arrive upon a result which is equivalent to one that was rigorously derived. Apparently, all the higher order effects can be expressed within the frequency dependent damping term and resonance frequency. This indicates that the use of the energy loss paradigm of the damped harmonic oscillator is a versatile and powerful way to model energy dissipation in bubbly fluids.

2.1.2 From Wave Number to Phase Speed and Attenuation

So far, broadband propagation in bubbly fluids has been described in terms of complex wave numbers. It is often more useful to express results in terms of phase speed and attenuation. Begin by setting $c_\ell/c_m = u - iv$ and noting that $k_m = \omega/c_m$. For progressive plane wave propagation with wave number k_m one finds

$$\exp(i\omega t - ik_m x) = \exp\left(-\frac{\omega v}{c_\ell} x\right) \exp\left[i\omega\left(t - \frac{u}{c_\ell} x\right)\right]. \quad (2.17)$$

Therefore, the phase velocity V is given by

$$V = c_\ell/u, \quad (2.18)$$

and the attenuation coefficient A in dB/unit length is given by

$$A = 20(\log_{10} e)(\omega v/c_\ell). \quad (2.19)$$

2.2 Effect of Bubble Population Parameters on Propagation

Small changes in bubble population parameters, such as mean bubble size, bubble size distribution, and void fraction can have large effects on the phase speed and attenuation in bubbly fluids. In this section these effects will be investigated using Eq. 2.1. The

calculations will be done for air bubbles in pure water. The physical parameters used throughout section 2.2, unless otherwise stated, are given in Table 2.1.

2.2.1 General Behavior

To begin with, consider a monodisperse bubble population composed of just one bubble size, given by

$$\wp(a) = n\delta(a - \bar{a}). \quad (2.20)$$

As shown before, substitution into Eq. 2.1 yields

$$\frac{1}{c_m^2} = \frac{1}{c_\ell^2} + \frac{4\pi\bar{a}n}{\omega_0^2 - \omega^2 + 2i\delta\omega}. \quad (2.21)$$

Now set $\bar{a} = 1$ mm and choose n such that the void fraction is $\chi = 10^{-3}$, as given by Eq. 2.14. The general propagation effects are exemplified well by such a bubble population. The phase speed and attenuation is then obtained from Eqs. 2.21 by using 2.18 and 2.19, respectively. The results are shown for a range of frequencies from well below to well above resonance in Fig. 2.1. At low frequencies, below about 1 kHz, the sound speed appears non-dispersive, and the attenuation is very low. Above 1 kHz, the attenuation begins to rise sharply, and the phase speed begins to fall. The medium is now extremely dispersive. Extrema are reached just above 3 kHz, where the phase speed is only about 90 m/s and the attenuation is approximately 20 dB/cm. This is the region associated with bubble resonance. Just above resonance, the phase speed rises and goes supersonic relative the host medium at 3.538 kHz. The supersonic region continues, accompanied by somewhat reduced attenuation until phase speed peaks at more than 30 km/s before falling. Another region of high dispersion is encountered around 12 kHz. The dispersion then lessens and the phase speed asymptotically approaches the speed of sound in the bubble free host medium, again accompanied by low attenuation.

It is interesting to compare some of these results to the simple calculations given by

Wood’s and Minnaert’s equations, Eqs. 1.10 and 1.15, respectively. The Wood limit sound speed is 337.5 m/s, which corresponds well with sub-1 kHz part of the phase speed curve in Fig. 2.1. The Minnaert resonance frequency is 3.286 kHz, which also appears to match the frequency of the extrema in Fig. 2.1. Upon closer inspection, one finds the Wood and Minnaert values are just a little different than those obtained from Eq. 2.21. The curves are replotted using linear axes and a reduced frequency range in Fig. 2.2. The Wood limit sound speed is shown in the top plot for comparison, where a small amount of dispersion is visible, even below 1 kHz. It is interesting to note that at the lowest frequencies the sound speed does not merely flatten out but actually falls off. The Minnaert frequency, shown on both plots, corresponds well with the maximum attenuation but is just higher than the minimum phase speed.

Low frequency dispersion has been noted in the experimental literature. In the early works, it was either obfuscated by scatter in the data [64], or attributed to experimental error, such as the use of detergent contaminated water [7]. A careful experimental and theoretical study of low frequency dispersion was conducted by Ruggles [46] in 1986, who was able to predict its effects as presented through phase speed. Ruggles’ model did not, however, explain the accompanying attenuation quite as well. In 1989, Commander and Prosperetti [33] chose not to compare Ruggles’ low frequency sound speed data to their model because in their opinion, the experimental parameters were not well controlled. This comparison has been performed for some of Ruggles’ data in Appendix A. The dispersion is actually well described by Eq. 2.1 but at a different void fraction than that reported by Ruggles. Low frequency dispersion will be discussed further in Chapter 4.

2.2.2 Effect of Void Fraction

Changes in void fraction influence the mean phase speed, and also affect the the level of dispersion and attenuation. The delta function bubble size distribution of Eq. 2.20 is again considered. Here the bubble size is $\bar{a} = 0.62$ mm, which was chosen for similarity to the bubbles used in the experimental section, Chapter 4. Phase speed and attenuation

obtained from Eqs. 2.21, 2.18 and 2.19 is shown in Fig. 2.3 for three void fractions. In these plots the frequency range is restricted to the resonance regime in order to highlight the behavior there. In the high void fraction case, $\chi = 10^{-3}$, we see the same sharp dispersion that was seen previously in Fig. 2.1, but as void fraction decreases, so does the dispersion. Minimum phase speed is 300 m/s for $\chi = 10^{-4}$, and only about 800 m/s for $\chi = 10^{-5}$. The maximum phase speed is about 20,000 m/s for $\chi = 10^{-4}$, and only about 4000 m/s for $\chi = 10^{-5}$. The frequency range over which propagation is supersonic (relative to the bubble free host medium) is also greatly reduced as void fraction decreases, spanning about 4 kHz and 0.5 kHz for $\chi = 10^{-5}$ and $\chi = 10^{-4}$, respectively. Peak attenuation, as seen in the lower plot, is reduced from 30 dB/cm down to about 2.5 dB/cm. Similarly, the frequency range of the high attenuation region decreases with void fraction. A general conclusion is beginning to emerge. Increasing the void fraction lowers the average phase speed, and increases dispersion and attenuation.

2.2.3 Effect of Bubble Size

The effect of bubble size is simpler to describe than the effect of void fraction, and can be understood to first order by examination of Minnaert's Eq. 1.15. As has been seen previously, two prominent features are associated with the bubble resonance frequency; the minimum phase speed and the maximum attenuation both occur near the bubble resonance. According to Minnaert's equation, the bubble resonance frequency is inversely proportional to the bubble equilibrium radius, therefore we expect these extrema features to scale the same way. Indeed such is the case, as can be seen in Fig. 2.4, where phase speed and attenuation are plotted for three bubble sizes. Again, the delta function distribution of Eq. 2.20 is used, with a void fraction $\chi = 10^{-4}$, along with Eqs. 2.21, 2.19 and 2.18. Both curves appear to shift along the frequency axis as bubble size is varied. A small increase in peak attenuation is seen as bubble size decreases, while the minimum phase speed actually goes up slightly. The later effect is not prominent on the logarithmically scaled axis, but is indeed present. The behavior of the attenuation in this range is governed by thermal

dissipation, which is inversely proportional to the radius squared.

Note that the effects shown in Fig. 2.4 are caused by only a 10% variation in bubble radius, or specifically, $\pm 62\mu\text{m}$. The experimental ability to discern the difference between acoustic signals of 5.3 and 5.8 kHz (the frequencies of peak attenuation for the two smaller bubble sizes shown in Fig. 2.4) is often greater than our ability to discern the difference in the two corresponding bubble sizes. If one were only interested in the size of a few bubbles this would not be the case; high magnification optical methods would provide sufficient resolution. However, when one cares to measure the sizes of hundreds of bubbles, not motionless but in a flow, the statement bears much more significance. This issue will be discussed further in Chapter 4.

2.2.4 The Addition of Multiple Bubble Sizes

In this section, the presence of multiple bubble sizes is explored. To begin, a discrete distribution of bubble sizes is considered. Such a distribution is given by

$$\wp(a) = \sum_{j=1}^N n_j \delta(a - \bar{a}_j), \quad (2.22)$$

which when substituted into Eq. 2.1 yields

$$\frac{1}{c_m^2} = \frac{1}{c_\ell^2} + \sum_{j=1}^N \frac{4\pi\bar{a}_j n_j}{\omega_0^2 - \omega^2 + 2i\delta\omega}. \quad (2.23)$$

The phase speed and attenuation produced by this collection of discrete bubble sizes is shown in Fig. 2.5 for the same three bubble sizes as shown in Fig. 2.4. Here $n_1 = n_2 = n_3$ and the overall void fraction is $\chi = 10^{-4}$. Several important features are evident in this plot. There are now three local minima in the phase speed curve and three local maxima in the attenuation curve, each corresponding to the resonance of one of the three discrete bubble sizes. In each case, the extrema are less pronounced than in the corresponding case with only a single bubble size present. The presence of more than one bubble size

tends to diminish the effects that either size would have alone. Note that the maximum attenuation in Fig. 2.5 is only 6 dB/cm, which occurs at the resonance frequency of the smallest bubble size. Note also that the maximum attenuation for this bubble size alone is 20 dB, as shown in Fig. 2.4. The frequency range of the dispersive region is diminished as well. The phase speed is supersonic for only 2.5 kHz compared to well over 5 kHz for any of the single size cases.

Continuous bubble size distributions will now be considered. Foreshadowing what will be discussed in the experimental part of this work, the normal distribution will be explored. The probability density function of a normally distributed random variable is defined by [79]

$$\varphi(a) = \frac{C}{s\sqrt{2\pi}} \exp \left[-\frac{(a - a_0)^2}{2s^2} \right], \quad (2.24)$$

where a_0 and s represent the mean value and the standard deviation of the distribution, respectively. Here, a_0 is taken to be the mean bubble radius, and C is used as a scaling parameter such that the void fraction χ is given by

$$\chi = \frac{4\pi}{3} \int_{a_{\min}}^{a_{\max}} \varphi(a) a^3 da. \quad (2.25)$$

The purpose is to show the effect of increasing the standard deviation of the distribution, that is, the effect of widening the distribution. The frequency range of the calculations will again be narrowed in order to emphasize the resonance regime. Changing the mean bubble radius a_0 has the same effect here as in Fig. 2.4, and will not be discussed again.

Three distributions, (a), (b), and (c) are shown in Fig. 2.6, constructed using the variates given in Table 2.2. With $\varphi(a)$ thus described, Eq. 2.1 was evaluated numerically using an adaptive Simpson quadrature technique [80], and the integration limits given in Table 2.2. The results are presented in Fig. 2.7. Distribution (a) is the same delta function distribution seen before. The effect of widening the distribution can easily be seen. For both phase speed and attenuation, the extrema of (b) and (c) are less pronounced than the

extrema of (a). The frequency range in which high dispersion is present is also dependent upon the width of the distribution. Now comparing just cases (a) and (b): They are quite similar except directly around the resonance region. Indeed, propagation in the resonance region bears the most sensitivity to the details of the bubble size distribution.

In order to exemplify this point, the values used to produce case (b) will again be used, but this time, the standard deviation s will be the only parameter that is varied, and to a much lesser degree. The results are shown in Fig. 2.8 for $s = 0.02, 0.03,$ and 0.04 mm, which represents a range of plus and minus 33 percent. The peak attenuation varies about 1.8 dB/cm and the minimum phase speed varies by about 100 m/s. At first glance, this does not appear to be significant, but do not forget that the units for attenuation are dB/cm.

2.3 Theory of Scattering from a Bubbly-Liquid-Filled Compliant Cylinder

The prediction of acoustic scattering from naturally occurring bubble clouds in the ocean is difficult because all of the important parameters that affect the scattering strength are usually unknown. This includes the shape of the cloud, the void fraction, and the distribution of bubble sizes. These parameters are not constant but vary with position inside the cloud and with time. This led to the study of artificial bubble clouds, and the current focus is on clouds with well characterized geometry. The most convenient shape to work with was that of a long cylinder. The geometry can be realized theoretically and experimental realization is readily obtained by pumping bubbly fluid through a thin walled compliant tube. The theoretical description of scattering from such a structure is examined in this section.

2.3.1 Scattering of Continuous Waves

The scattering of continuous plane waves travelling in an infinite fluid medium and normally incident upon an infinitely long cylindrical tube filled with bubbly liquid is considered. A coordinate system is chosen such that the incident wave vector is along the x -axis, and the center of the tube is coincident with the z -axis. The receiver is located in the x - y plane, with radial position r and θ , where $\theta = 0$ represents forward scattering. The outer and inner radii of the tube are given by a and b , respectively. The outer fluid and the bubbly liquid inside the shell are labeled by 1 and 3, respectively, and the shell material is labeled by 2. A schematic of the system is shown in Fig. 2.9. If the excitation frequency is kept well below any bubble's resonance frequency, the bubbly fluid is modeled as a lossless effective medium with sound speed and density dependent upon VF, as given by Wood's Eq. 1.10 and Eq. 1.6, respectively. The fluid properties ($i = 1, 3$) are thus given by sound speeds c_i and densities ρ_i , with propagation constants $k_i = \omega/c_i$. For the shell material with Lamé constants λ and μ , the longitudinal and transverse sound speeds inside the shell material are given by $c_l^2 = (\lambda + 2\mu)/\rho_2$ and $c_t^2 = \mu/\rho_2$ with $k_l = \omega/c_l$ and $k_t = \omega/c_t$. [81]

The material properties thus described, Doolittle and Überall's classical scattering formulation [82] for an elastic fluid-filled shell of infinite length is used to predict the scattered field. For a cylindrical coordinate system with $x = r \cos \theta$ and $y = r \sin \theta$, the acoustic pressure field in the outer fluid, medium 1, is written as the sum of incident and scattered waves, $P = P_i + P_{sc}$, where P_i is the incident plane wave pressure given by

$$P_i = P_0 \sum_{n=0}^{\infty} i^n \epsilon_n J_n(k_1 r) \cos n\theta, \quad (2.26)$$

and the scattered pressure is

$$P_{sc} = P_0 \sum_{n=0}^{\infty} i^n \epsilon_n b_n H_n^{(1)}(k_1 r) \cos n\theta = P_0 S(f, r, \theta), \quad (2.27)$$

where P_{sc} is the pressure amplitude of the scattered wave, P_0 is pressure amplitude of the incident wave, $\epsilon_0 = 1$, $\epsilon_{n \geq 1} = 2$, $H_n^{(1)}$ is an n^{th} order Hankel function of the first kind, b_n are unknown coefficients (which depend upon a and b , and shell and internal fluid material properties), and the time factor $\exp(-i\omega t)$ is suppressed. Radial displacements are written as

$$(S_{i,\text{sc}})_r = (1/\rho_1\omega^2)(\partial P_{i,\text{sc}}/\partial r). \quad (2.28)$$

In medium 2, a displacement vector \mathbf{S} is expressed in terms of a scalar displacement potential Φ and a vector displacement potential Ψ , given by

$$\mathbf{S} = -\nabla\Phi + \nabla \times \Psi. \quad (2.29)$$

In the usual manner, Φ and Ψ satisfy the ordinary wave equations

$$\nabla^2\Phi = \frac{1}{c_l^2} \frac{\partial^2\Phi}{\partial t^2}, \quad (2.30)$$

and

$$\nabla^2\Psi = \frac{1}{c_t^2} \frac{\partial^2\Psi}{\partial t^2}. \quad (2.31)$$

Because the model is infinite in z , we take $\Psi_r = \Psi_\theta = 0$, which leads to $S_z = 0$. Then accounting for symmetry in θ the solutions of Eq. 2.30 and 2.31 are

$$\Phi = P_0 \sum_{n=0}^{\infty} i^n \epsilon_n [c_n J_n(k_l r) + d_n N_n(k_l r)] \cos n\theta, \quad (2.32)$$

and

$$\Psi_z = P_0 \sum_{n=0}^{\infty} i^n \epsilon_n [e_n J_n(k_t r) + f_n N_n(k_t r)] \sin n\theta. \quad (2.33)$$

The bubbly fluid, medium 3, supports a compressional wave which must remain regular

at the origin and is thus given by

$$P_3 = P_0 \sum_{n=0}^{\infty} i^n \epsilon_n g_n J_n(k_3 r) \cos n\theta. \quad (2.34)$$

The boundary conditions to be satisfied at $r = a$ and $r = b$ are: 1) The fluid pressure equals the normal component of stress in the shell. 2) The normal component of displacement is continuous. 3) The tangential components of shear stress vanish. These stress components are expressed in terms of displacements in the usual way [83, p. 288] which leads to six linear equations with six unknown coefficients b_n, \dots, g_n from Eqs. 2.27, 2.32, 2.33 and 2.34. Finally, Cramer's rule is used to find the coefficients for each value of n . The results for b_n , which yields P_{sc} are given below:

$$b_n = \frac{1}{D} \begin{vmatrix} \beta_1 & \alpha_{12} & \alpha_{13} & \alpha_{14} & \alpha_{15} & 0 \\ \beta_2 & \alpha_{22} & \alpha_{23} & \alpha_{24} & \alpha_{25} & 0 \\ 0 & \alpha_{32} & \alpha_{33} & \alpha_{34} & \alpha_{35} & 0 \\ 0 & \alpha_{42} & \alpha_{43} & \alpha_{44} & \alpha_{45} & \alpha_{46} \\ 0 & \alpha_{52} & \alpha_{53} & \alpha_{54} & \alpha_{55} & \alpha_{56} \\ 0 & \alpha_{62} & \alpha_{63} & \alpha_{64} & \alpha_{65} & 0 \end{vmatrix}, \quad (2.35)$$

where D is given by

$$D = \begin{vmatrix} \alpha_{11} & \alpha_{12} & \alpha_{13} & \alpha_{14} & \alpha_{15} & 0 \\ \alpha_{21} & \alpha_{22} & \alpha_{23} & \alpha_{24} & \alpha_{25} & 0 \\ 0 & \alpha_{32} & \alpha_{33} & \alpha_{34} & \alpha_{35} & 0 \\ 0 & \alpha_{42} & \alpha_{43} & \alpha_{44} & \alpha_{45} & \alpha_{46} \\ 0 & \alpha_{52} & \alpha_{53} & \alpha_{54} & \alpha_{55} & \alpha_{56} \\ 0 & \alpha_{62} & \alpha_{63} & \alpha_{64} & \alpha_{65} & 0 \end{vmatrix}, \quad (2.36)$$

In order to find c_n, d_n, \dots , the 2nd, 3rd, \dots column of D is replaced with $(\beta_1 \beta_2 0000)$ and

then inserted in the R.H.S. of Eq. 2.35. The α_{ij} 's are listed using $x_i = ak_i$ and $y_i = bk_i$

$$\begin{aligned}
\beta_1 &= (x_1/k_1)^2 J_n(x_1), \\
\beta_2 &= x_1 J'_n(x_1); \\
\alpha_{11} &= -(x_1/k_1)^2 H_n^{(1)}(x_1), \\
\alpha_{12} &= 2\mu x_l^2 J_n''(x_l) - \lambda x_l^2 J_n(x_l), \\
\alpha_{13} &= 2\mu x_l^2 N_n''(x_l) - \lambda x_l^2 N_n(x_l), \\
\alpha_{14} &= 2\mu n[J_n(x_t) - x_t J'_n(x_t)], \\
\alpha_{15} &= 2\mu n[N_n(x_t) - x_t N'_n(x_t)]; \\
\alpha_{21} &= -x_1 H_n^{(1)'}(x_1), \\
\alpha_{22} &= -\rho_1 \omega^2 x_l J'_n(x_l), \\
\alpha_{23} &= -\rho_1 \omega^2 x_l N'_n(x_l), \\
\alpha_{24} &= \rho_1 \omega^2 n J_n(x_t), \\
\alpha_{25} &= \rho_1 \omega^2 n N_n(x_t); \\
\alpha_{32} &= 2n[x_l J'_n(x_l) - J_n(x_l)], \\
\alpha_{33} &= 2n[x_l N'_n(x_l) - N_n(x_l)], \\
\alpha_{34} &= -x_t^2 J_n''(x_t) + x_t J'_n(x_t) - n^2 J_n(x_t), \\
\alpha_{35} &= -x_t^2 N_n''(x_t) + x_t N'_n(x_t) - n^2 N_n(x_t); \\
\alpha_{42} &= 2\mu y_l^2 J_n''(y_l) - \lambda y_l^2 J_n(y_l), \\
\alpha_{43} &= 2\mu y_l^2 N_n''(y_l) - \lambda y_l^2 N_n(y_l), \\
\alpha_{44} &= 2\mu n[J_n(y_t) - y_t J'_n(y_t)], \\
\alpha_{45} &= 2\mu n[N_n(y_t) - y_t N'_n(y_t)], \\
\alpha_{46} &= -(y_3/k_3)^2 J_n(y_3); \\
\alpha_{52} &= -\rho_3 \omega^2 y_l J'_n(y_l), \\
\alpha_{53} &= -\rho_3 \omega^2 y_l N'_n(y_l),
\end{aligned}$$

$$\begin{aligned}
\alpha_{54} &= \rho_3 \omega^2 n J_n(y_t), \\
\alpha_{55} &= \rho_3 \omega^2 n N_n(y_t), \\
\alpha_{56} &= -y_3 J'_n(y_3); \\
\alpha_{62} &= 2n[y_t J'_n(y_t) - J_n(y_t)], \\
\alpha_{63} &= 2n[y_t N'_n(y_t) - N_n(y_t)], \\
\alpha_{64} &= -y_t^2 J''_n(y_t) + y_t J'_n(y_t) - n^2 J_n(y_t), \\
\alpha_{65} &= -y_t^2 N''_n(y_t) + y_t N'_n(y_t) - n^2 N_n(y_t).
\end{aligned}$$

2.3.2 Scattering of Finite Duration Waves

If short pulses are of interest instead of continuous waves, the finite length of the incident pulse must be accounted for. To obtain a prediction for the scattered echo in such a case, the measured incident pulse $p_{\text{inc}}(t_n)$ can be convolved with the predicted scattering response given by Eq. 2.27. Time domain convolution is equivalent to multiplication in the frequency domain, so P_0 is replaced with the fast Fourier transform $\text{FFT}[p_{\text{inc}}(t_n)] = P_{\text{inc}}(f_n)$. The predicted time domain scattered pulse is then obtained with the inverse FFT,

$$p_{\text{sc,p}}(t_n) = \text{IFFT}[P_{\text{inc}}(f_n)S(f_n, r, \theta)]. \quad (2.37)$$

The scattering function $S(f_n, r, \theta)$ had a time dependency $\exp(-i\omega t)$, therefore, for a discrete incident waveform vector p_{inc} of length N , the discrete Fourier transform implied above is a length N vector P_{inc} , with elements

$$P_{\text{inc}}(f_n) = \sum_{t_n=1}^N p_{\text{inc}}(t_n) \exp[-2\pi i(f_n - 1)(t_n - 1)/N], \quad 1 \leq f_n \leq N, \quad (2.38)$$

and the inverse transform is given by

$$p_{\text{inc}}(t_n) = \frac{1}{N} \sum_{f_n=1}^N P_{\text{inc}}(f_n) \exp[2\pi i(f_n - 1)(t_n - 1)/N], \quad 1 \leq t_n \leq N. \quad (2.39)$$

2.4 The Effect of Bubble Population Parameters on Scattering

In the present section, the effects of varying the bubble population parameters will be explored. In Sections 2.1 and 2.2, the focus was on propagation in the presence of individual bubble resonance. In the present section, the primary focus is on Wood limit behavior of the bubbly fluid, which leads to resonance behavior of the overall structure. The inclusion of bubble resonance effects will be briefly introduced at the section's end.

2.4.1 General Behavior

To demonstrate the basic behavior of the scattering function and to foreshadow later experimental results, a latex rubber material is chosen for the shell and the backscatter direction is considered. The results will be presented in terms of an echo level given by

$$EL = 20 \log_{10} \frac{P_{sc}}{P_0}, \quad (2.40)$$

where P_{sc} and P_0 are taken from Eq. 2.27. The echo level form is chosen over a target strength form in order to eventually facilitate direct model comparison to measurements. The geometric and material parameters used in the calculations are given in Table 2.3 and the results are shown in Fig. 2.10. The scattering function is a multimode expansion. The contribution of the first three modes is shown in Fig. 2.10. If one were to add a plot for the sum of four modes, it would be indistinguishable from the sum of three modes curve that is shown in the figure. Specifically, adding the fourth mode results in a maximum deviation from the previous sum of only 0.002 dB. Therefore the sum will be carried out over the first three modes for all the calculations shown in this section.

Consider now the solid curve in Fig. 2.10, which essentially represents the full solution for these parameters. One can see by comparison with the curve for the 1st mode alone, that the peak between 5 and 10 kHz is due to the first mode. This peak is commonly

called the monopole resonance peak and is due to the uniform volume mode expansion of the cylinder in the radial direction. Below this frequency the scattering strength drops precipitously. Above, the response falls off less sharply and another peak is reached between 15 and 20 kHz. This peak is due to dipole mode oscillations, and shows a strong θ dependence. In the present case, the backscatter direction, shell motion parallel to the x -axis is maximized, producing this peak. As the frequency increases, the response falls sharply, about 15 dB, before briefly flattening out towards 25 kHz. Of course, as the frequency continues to increase, more and more modes present themselves and the resonance structure becomes rich, but this regime is beyond the scope of the present study.

2.4.2 Effect of the Shell

The long-term goal is the understanding of scattering from oceanic bubble clouds, which have no confinement shell. Ideally, an artificial cloud would be created with a well characterized shape in the absence of any confining structure, but this is difficult to realize in practice, hence the use of a thin-walled compliant tube. However, it will be shown that the compressibility provided by the bubbly liquid dominates the scattering response and the effect of a latex shell of the given dimensions plays a minimal role. This fact also justifies approximating the latex as a lossless material, at least for the frequencies considered here. The effect is void fraction dependent, though. The shell plays an increasingly important role as void fraction decreases, and as void fraction $\chi \rightarrow 0$, the shell becomes the only source of contrast.

This situation is demonstrated in Fig. 2.11. Scattering strength given by Eq. 2.27 in terms of echo level (Eq. 2.40) is plotted as a function of frequency for three void fractions. For each void fraction, two cases are shown. The solid lines represent the bubbly-liquid-filled shell with parameters given in Table 2.3 (except void fraction), while the dashed lines are for a fluid cylinder of identical inner radius a with no shell and the same remaining parameters. The case of the fluid cylinder can be considered on its own, for instance as

discussed by Stanton [84], or equivalently as a limiting case of the shelled cylinder, where the shell's shear speed goes to zero while its compressional speed is set to that of the surrounding fluid.

In Fig. 2.11 for the lowest void fraction case, $\chi = 10^{-5}$, the difference between the shell and no shell case is at most about 3.5 dB at 5 kHz, and as little as 2 dB at 25 kHz. For the middle void fraction case, $\chi = 10^{-4}$, the difference is at most 0.4 dB. Finally, for the high void fraction case $\chi = 10^{-3}$, the effect of the shell increases the echo level by at most 0.025 dB. It therefore appears that the presence of this particular shell should not impede the study of geometrically well characterized bubble clouds. It adds at most a small, almost constant increase of contrast over an unconfined cloud at void fractions above $\chi = 10^{-4}$.

2.4.3 Effect of Void Fraction

At a void fraction of $\chi = 0$, there are no air bubbles present and therefore no contrast except that due to the shell. As void fraction increases, the inner fluid contrast increases, primarily due to an increase in compressibility. This manifests itself in two ways. The increased contrast causes the overall echo level to increase across the frequency range. The increased compressibility additionally causes resonances to decrease in frequency and appear closer together. The first effect is shown in Fig. 2.11 for three void fractions spanning two orders of magnitude, from $\chi = 10^{-5}$ to $\chi = 10^{-3}$, which results in a peak echo level increase of about 30 dB. The second effect is more apparent for a reduced range of void fractions, as shown in Fig. 2.12. Again, scattering strength given by Eq. 2.27 in terms of echo level (Eq. 2.40) is plotted as a function of frequency for three void fractions using the parameters in Table 2.3 (except void fraction). As the void fraction changes from $\chi = 0.0008$, to $\chi = 0.001$, then to $\chi = 0.0012$, the lowest order resonance frequency changes from about 9, to 8, and then to 7 kHz.

2.4.4 Effect of Cloud Size

Increasing the diameter of the cylindrical bubble cloud has an effect similar to increasing the void fraction. The added size increases the contrasting volume, and therefore increases the echo level. The increased compressibility provided by the additional volume causes the resonance frequency to decrease. This effect is shown in Fig. 2.13, where scattering strength given by Eq. 2.27 in terms of echo level (Eq. 2.40) is plotted as a function of frequency for three tube sizes, using the parameters in Table 2.3 (except a and b). In these calculations, the shell thickness was maintained constant, while the inner radius was varied. It is clear from the figure that the scattering strength is fairly sensitive to the radius of the tube. Considering the 6.35 mm and 3.00 mm radii cases, a decrease in radius of 3.35 mm results in a doubling of the lowest order resonance frequency, from about 8 kHz to 16 kHz. Relative to the wavelength in the host medium, this represents an increase in size of only 3%.

2.4.5 Effect of Bubble Resonance

If the frequency of excitation includes the bubble resonance regime, then the Wood limit description of the bubbly liquid interior is no longer valid. Although this situation was not encountered during the experiments that are described in Chapter 5, it is discussed here for illustrative purposes. In the present section, the scattering strength is calculated just as it was in the previous sections, except here, the sound speed inside the tube is calculated using the broadband expression, Eq. 2.21, and a delta function bubble size distribution. The complex sound speed was calculated using the physical parameters given in Table 2.1 and two bubble sizes, $\bar{a} = 0.2$ mm and $\bar{a} = 0.5$ mm. The scattering strength was then calculated using Eq. 2.27 with the parameters from Table 2.3 (except c_1) and plotted as an echo level using Eq. 2.40. The results are shown in Fig. 2.14. The figure consists of three frames. In the upper frame, the bubbly fluid phase speed is shown for the two bubble sizes; in the middle frame, the accompanying attenuation is shown.

The lower frame shows the resulting scattering strengths for the two resonance regime cases and for comparison, a third case in which the bubble size is much smaller and the Wood limit behavior is still in effect. Consider the case for bubbles with radius $\bar{a} = 0.5$ mm, shown with the coarse dashed line. Here the individual bubble resonance frequency is about 6.5 kHz, and the reduced sound speed just below resonance causes an increase in contrast and therefore a corresponding peak in scattering strength at 5 kHz. As the frequency goes through resonance, the attenuation increases rapidly, causing a decrease in the scattering strength. The acoustic energy is now being absorbed instead of reflected or re-radiated. Above resonance frequency the phase speed is high, which would normally cause high contrast and therefore high scattering strength, but the attenuation overrides this and keeps the scattering strength low.

Now consider the case where $\bar{a} = 0.2$ mm. Up until approximately 7 kHz, the behavior is the same as for the Wood limit case, then attenuation starts to reduce the scattering strength. Between 10 and 15 kHz, the phase speed is decreasing as it was in the previous case, but this time, it is not accompanied by an increase in scattering strength. This is because the effect is taking place at a frequency that is above the monopole resonance of the structure. The strong volume oscillations associated with the lowest order resonance are not present in this frequency range. What happens next is not at all expected. Although the attenuation is higher for this case than it was in the previous case, the accompanying scattering strength is not lower than in the previous case. The ups and downs in the scattering function are smoothed out, as one might expect of a dynamic response in the presence of damping, but the comparative levels are not simply explained. Perhaps at these conditions, the acoustic energy is reflected without entering the structure, or the scattering strength is increased in a direction other than the backscatter direction shown here. It is clear that interesting effects are at work, but more detailed investigation is beyond the scope of the present work.

2.5 Summary

In this section the theory of sound propagation in bubbly fluids was explored in order to demonstrate the effect of bubble population parameters. Phase speed and attenuation was found to be quite sensitive to the bubble population statistics. A similar exercise was conducted for the scattering of sound from bubbly-liquid-filled latex tubes. Such a structure was investigated because it serves as a canonical model for investigation of bubble clouds with well characterized geometry. The scattering strength of such structures was also found to be sensitive to bubble population parameters and the size of the scatterer. The remainder of this work will be focused on experiments that were conducted in order to validate the theory explored here.

$c_\ell = 1481 \text{ m/s}$	$D = 2.08 \times 10^{-5} \text{ m}^2/\text{s}$
$\rho_\ell = 998 \text{ kg/m}^3$	$P_\infty = 101.3 \text{ kPa}$
$\sigma = 0.0725 \text{ N/m}$	$\mu = 0.00102 \text{ Pa}\cdot\text{s}$
$\gamma = 1.4$	

Table 2.1: Values of the physical parameters used in Section 2.2.

–	a_0	s	a_{\min}	a_{\max}	χ
(a)	0.62	$s \rightarrow 0$	$-\infty$	$+\infty$	10^{-4}
(b)	0.62	0.03	0.50	0.75	10^{-4}
(c)	0.62	0.10	0.30	0.95	10^{-4}

Table 2.2: Values used to construct the bubble size distributions presented in Fig. 2.6, and the limits of integration and void fraction χ subsequently used for Fig. 2.7. All values are in millimeters except those for void fraction χ which is unitless.

$r = 1.75 \text{ m}$	$\lambda = 1.95 \times 10^9 \text{ kg/m} \cdot \text{s}^2$
$\theta = \pi \text{ rad}$	$\mu = 4.30 \times 10^5 \text{ kg/m} \cdot \text{s}^2$
$c_1 = 1481 \text{ m/s}$	$c_l = 1418 \text{ m/s}$
$\rho_1 = 998 \text{ kg/m}^3$	$c_t = 21.05 \text{ m/s}$
$a = 8.02 \text{ mm}$	$\rho_2 = 970 \text{ kg/m}^3$
$b = 6.35 \text{ mm}$	$\chi = 10^{-3}$

Table 2.3: Unless otherwise stated, the above values were used in the scattering calculations of Section 2.4. The latex material properties, shown in the rightmost column, were obtained from the literature [85, p. V-5]. Dissipation within the latex material was neglected.

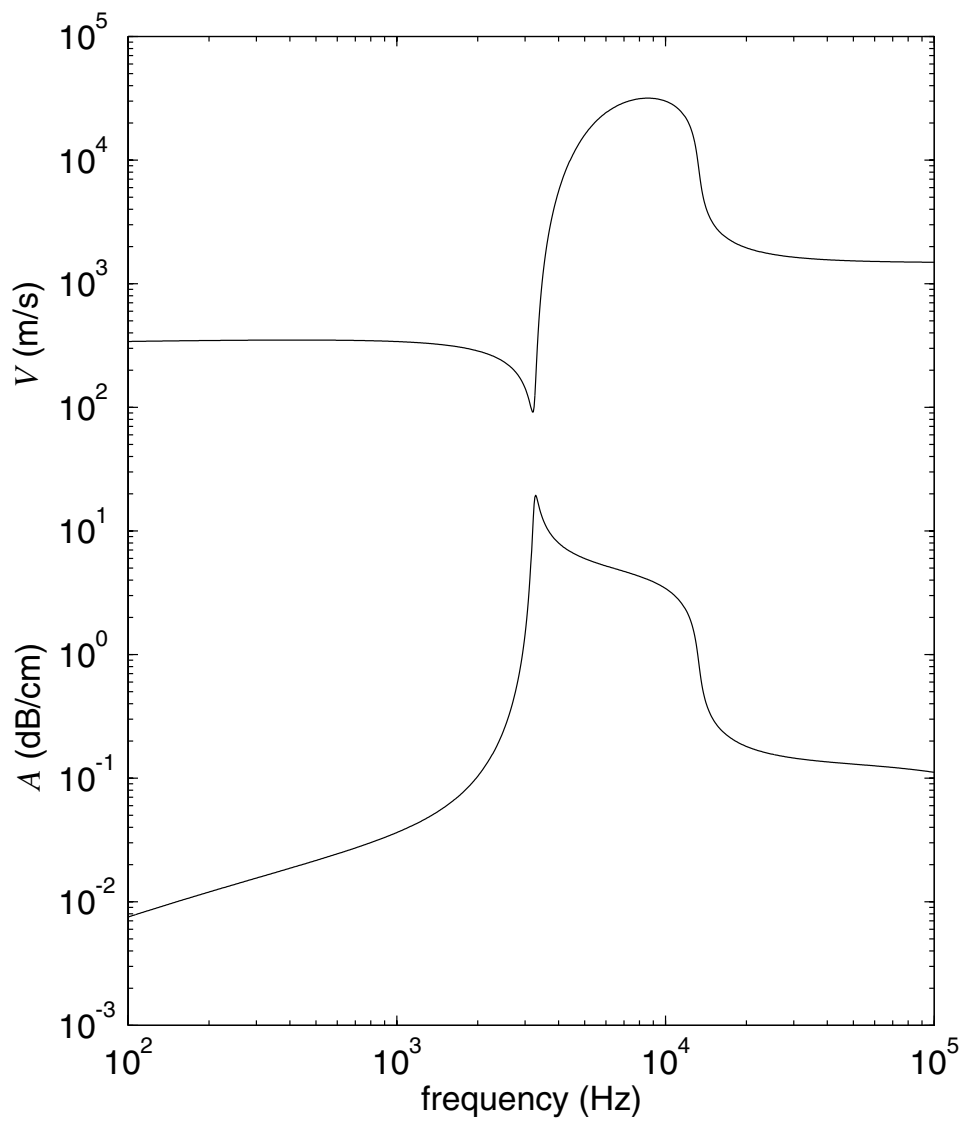


Figure 2.1: Phase speed (upper) and attenuation (lower) for propagation in a monodisperse bubbly fluid is shown as a function of frequency for bubble radius $\bar{a} = 1.0$ mm and void fraction $\chi = 10^{-3}$.

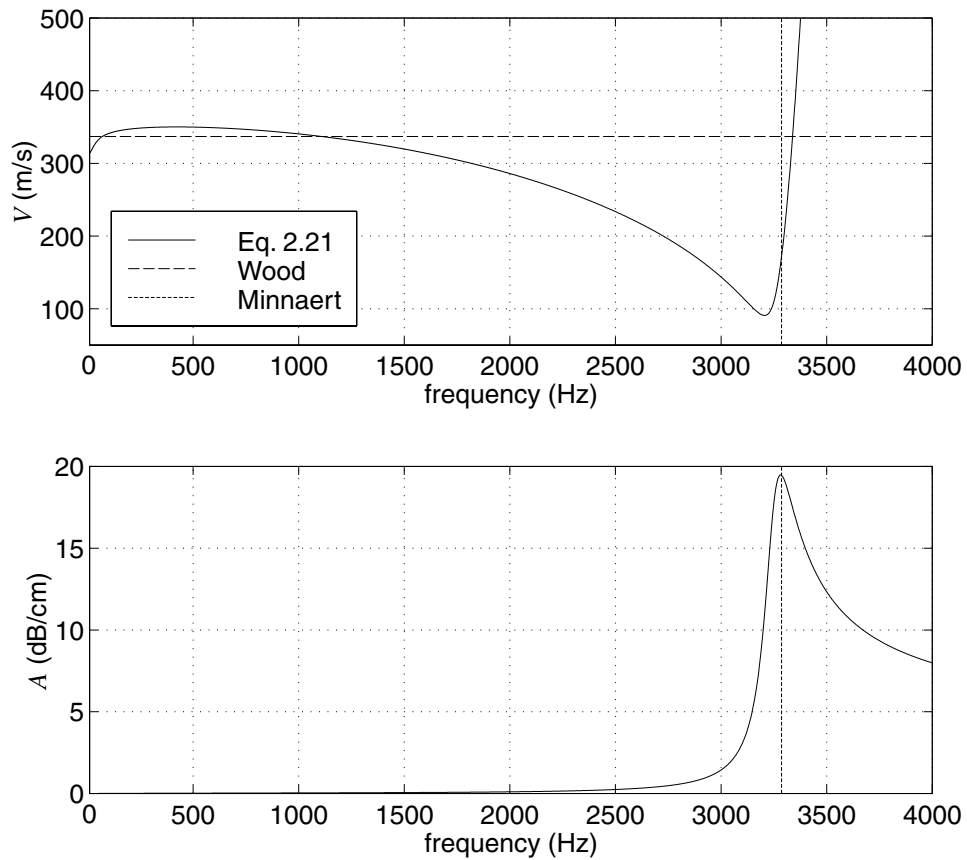


Figure 2.2: The curves of Fig. 2.1 are replotted on linear axes to emphasize the behavior at resonance and below. (bubble radius $\bar{a} = 1.0$ mm, void fraction $\chi = 10^{-3}$)

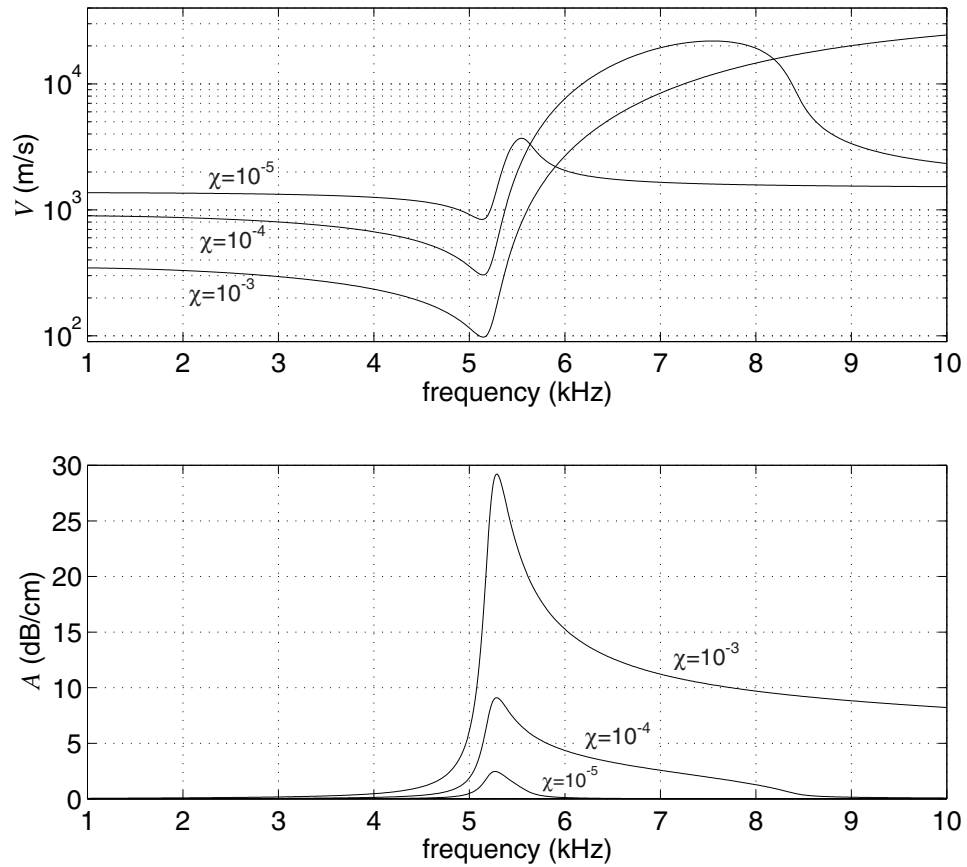


Figure 2.3: The effect of void fraction is demonstrated. Phase speed (upper) and attenuation (lower) is shown for bubble radius $\bar{a} = 0.62$ mm and three void fractions.

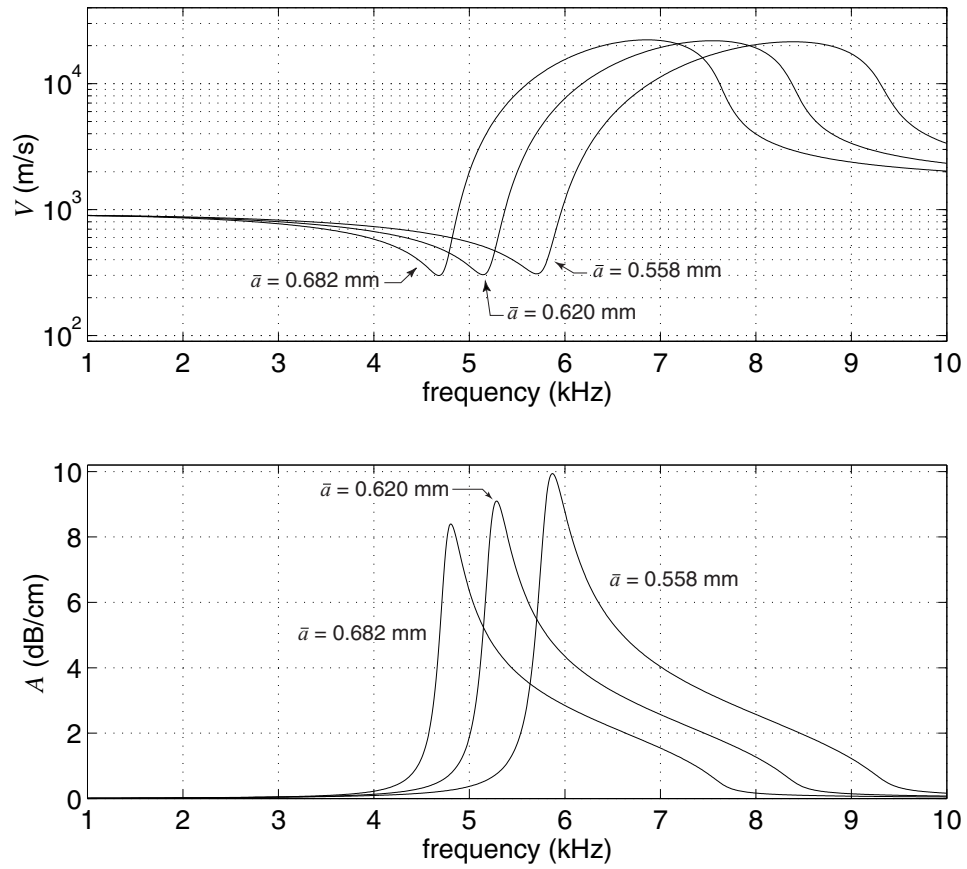


Figure 2.4: The effect of bubble size is demonstrated. Phase speed (upper) and attenuation (lower) is shown for void fraction $\chi = 10^{-4}$ and three bubble radii, which represent $\pm 10\%$ change in radius.

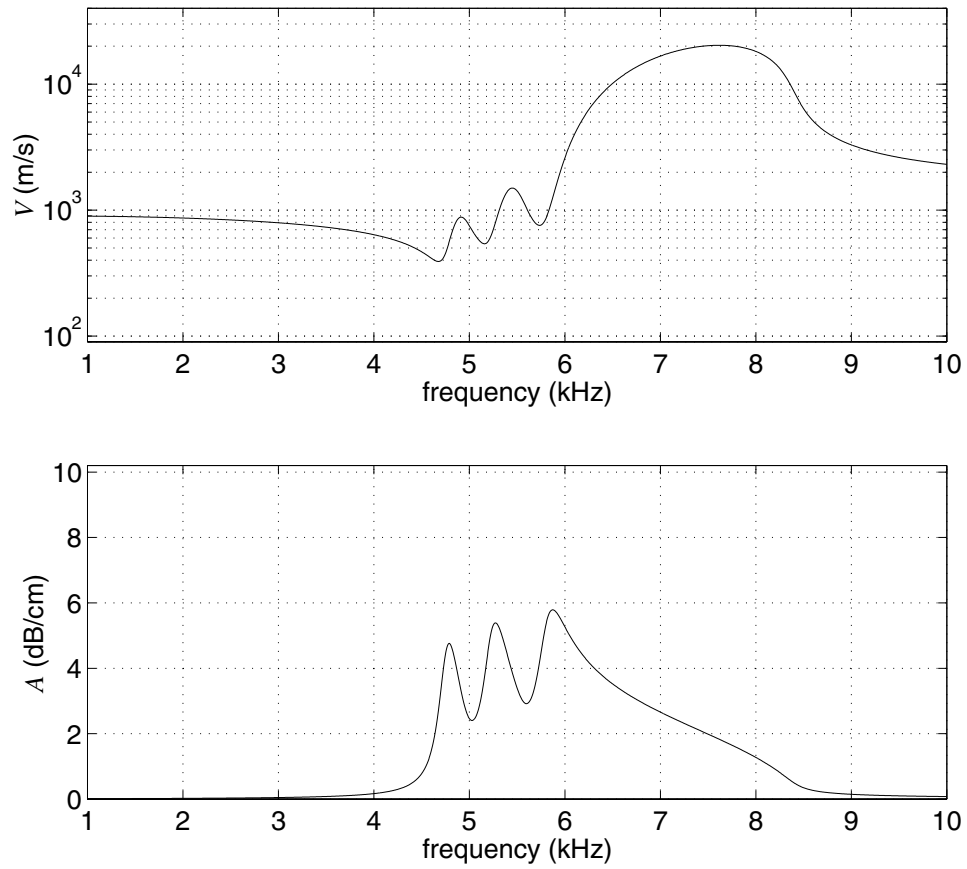


Figure 2.5: The effect of a discrete distribution of bubble sizes is demonstrated. Phase speed (upper) and attenuation (lower) is shown for void fraction $\chi = 10^{-4}$ and bubble size distribution $\varphi(a) = \sum_1^3 \delta(a - \bar{a}_j)$. The \bar{a}_j 's are the same as in Fig. 2.4.

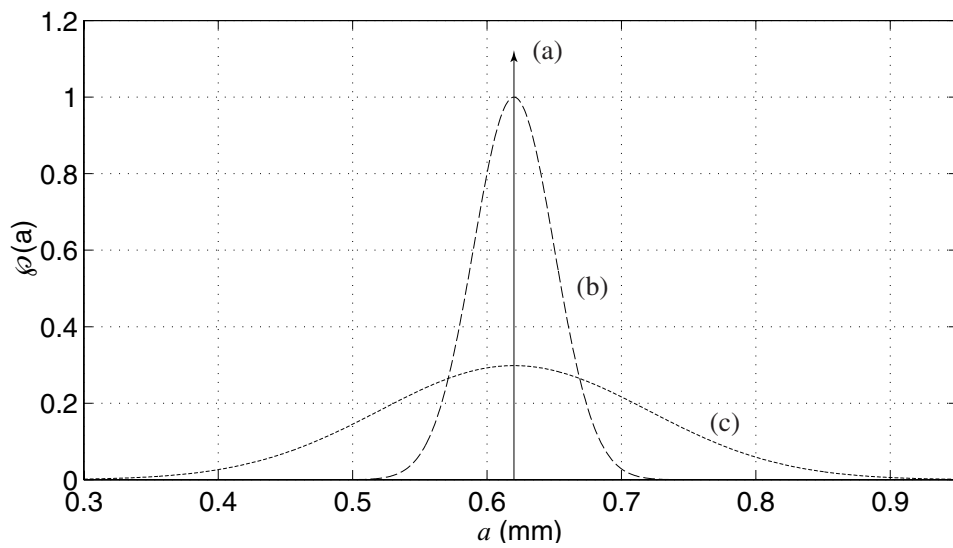


Figure 2.6: The three bubble size distributions $\varphi(a)$ used in Fig. 2.7 are shown. Details are given in the text and Table 2.2.

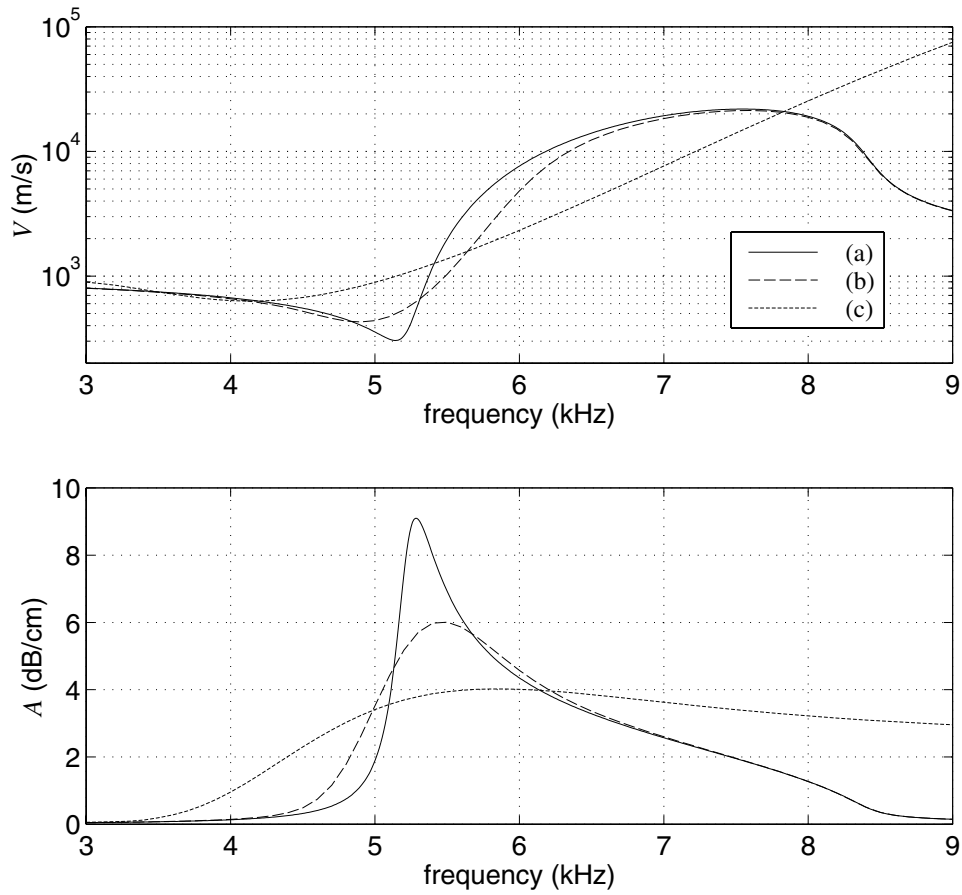


Figure 2.7: Phase speed (upper) and attenuation (lower) is shown as a function of frequency for void fraction $\chi = 10^{-4}$ and three bubble size distributions of different standard deviation s . The legend applies to the upper and lower plots. Further details are given in the text and Table 2.2.

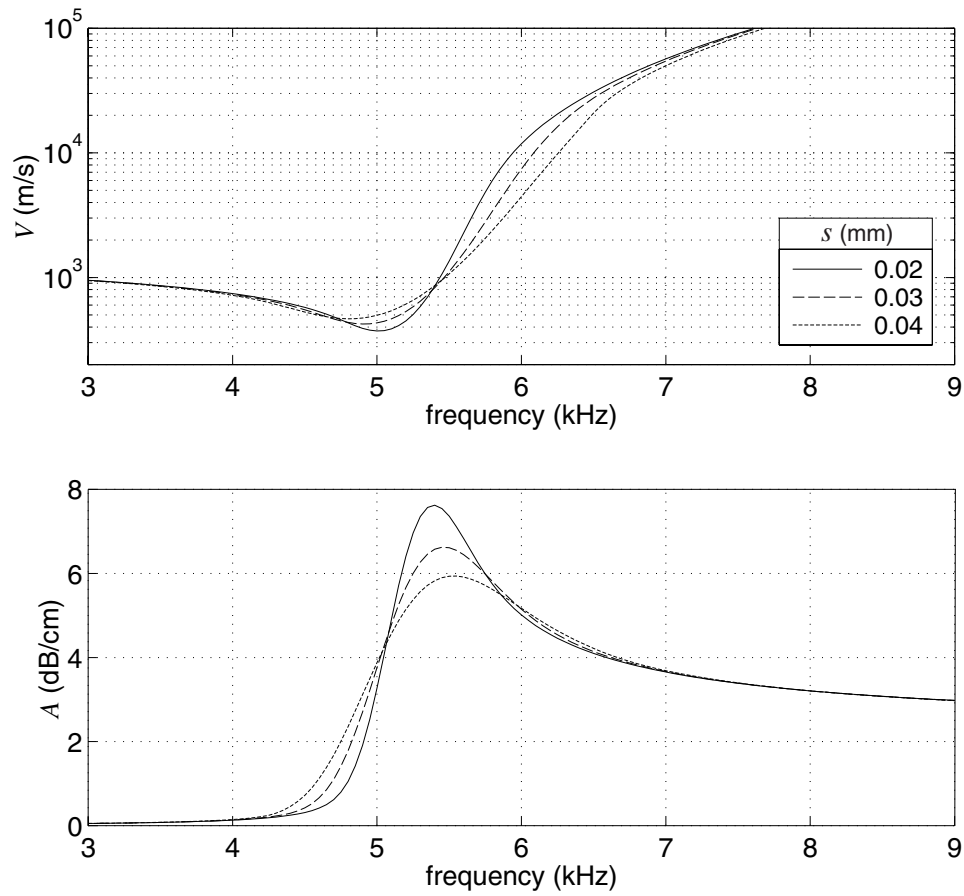


Figure 2.8: The sensitivity to distribution width is demonstrated. Phase speed (upper) and attenuation (lower) is shown for void fraction $\chi = 10^{-4}$ and three standard deviations s . The legend applies to both plots. Further details are given in the text and Table 2.2-(b).

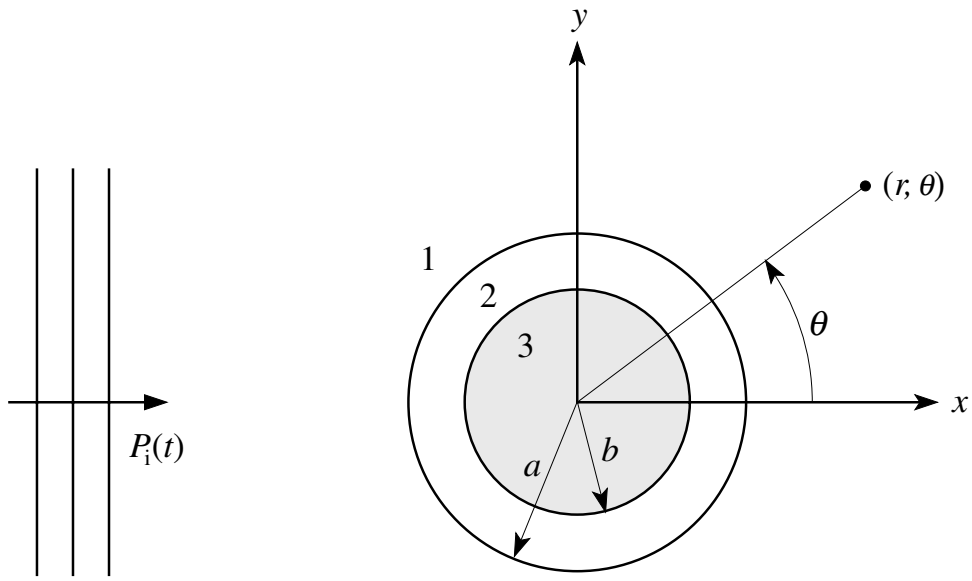


Figure 2.9: A schematic diagram of the bubbly-liquid-filled cylinder is shown, along with the incident plane wave $P_i(t)$.

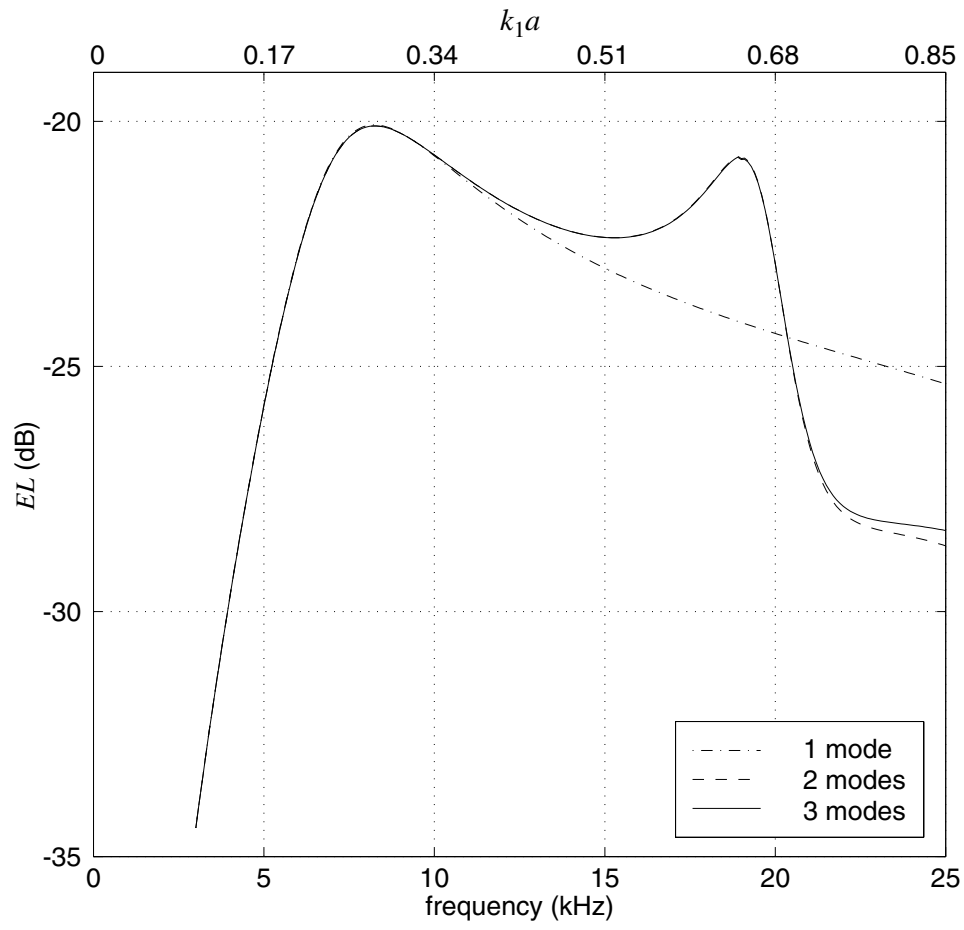


Figure 2.10: Scattering from a bubbly-liquid-filled compliant cylinder is presented. Inclusion of three modes in the sum is required for these conditions.

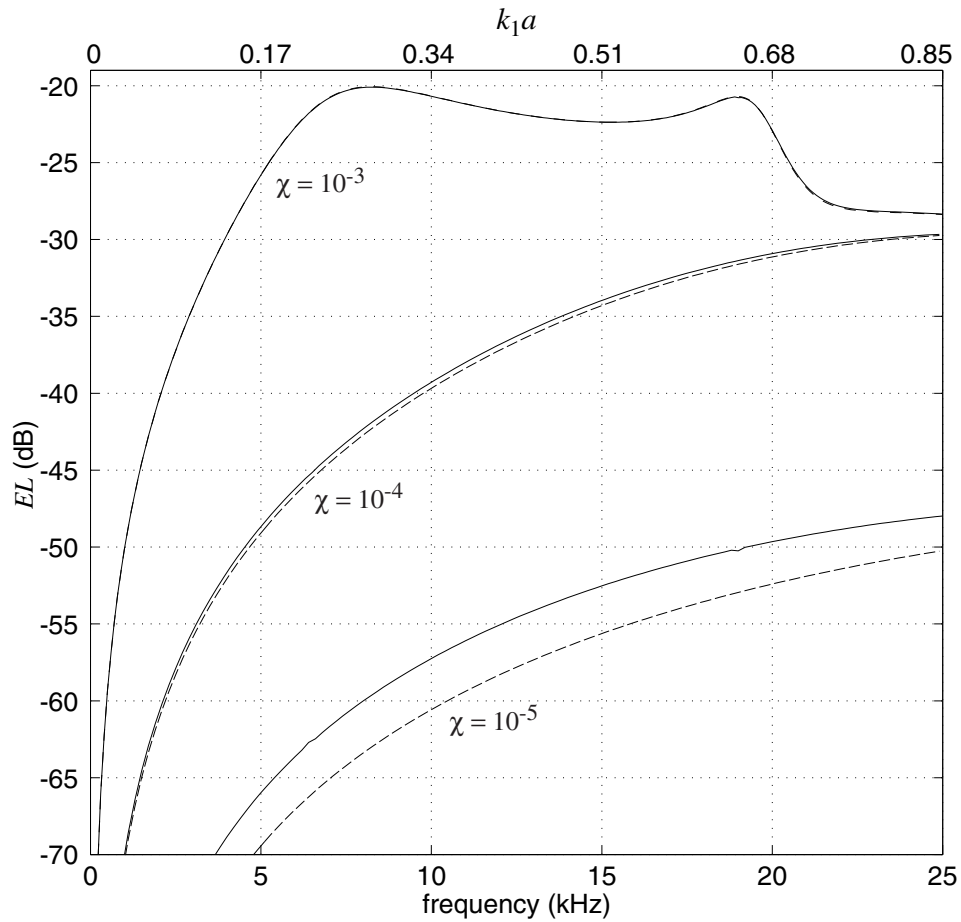


Figure 2.11: The effect the shell and the effect of void fraction are shown. Solid lines are for the shell, dashed lines are for no shell. The shell/no shell cases are almost indistinguishable in the high void fraction case.

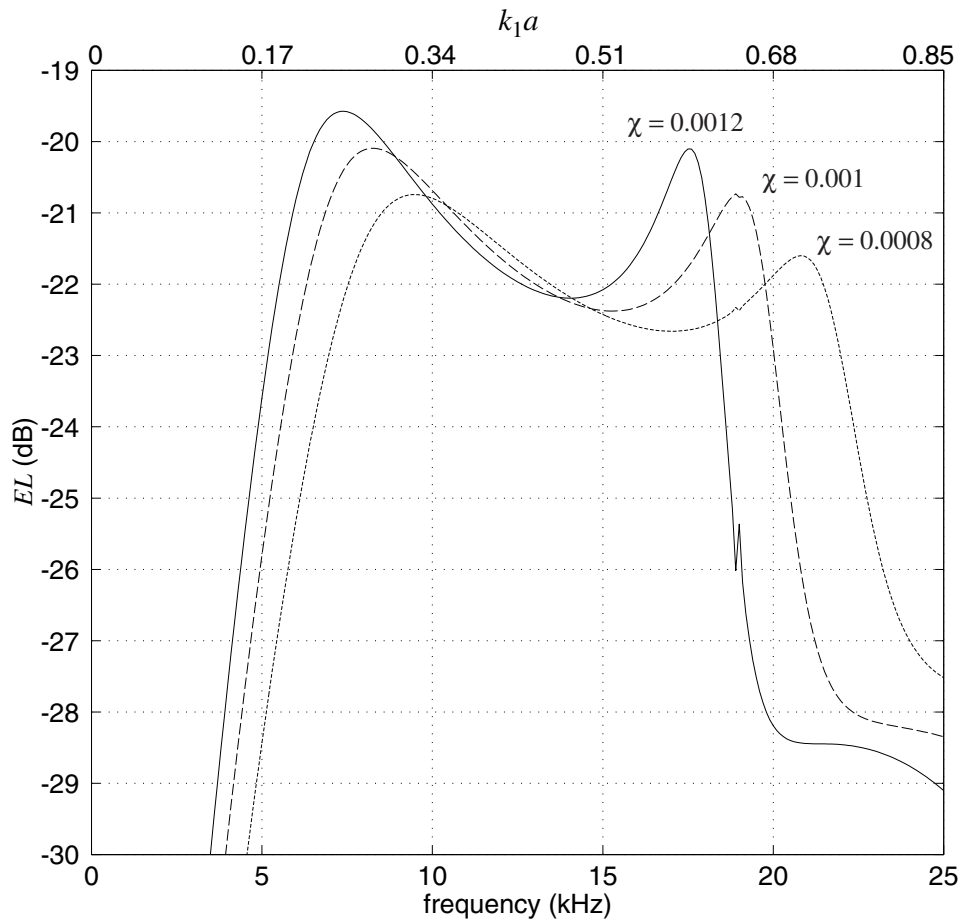


Figure 2.12: The effect of void fraction is shown. The small blips around 18 kHz do not appear to be numerical artifacts. They do, however, become narrower as $\Delta f \rightarrow 0$ in the calculations and are artificially wide at the resolution shown in the present figure.

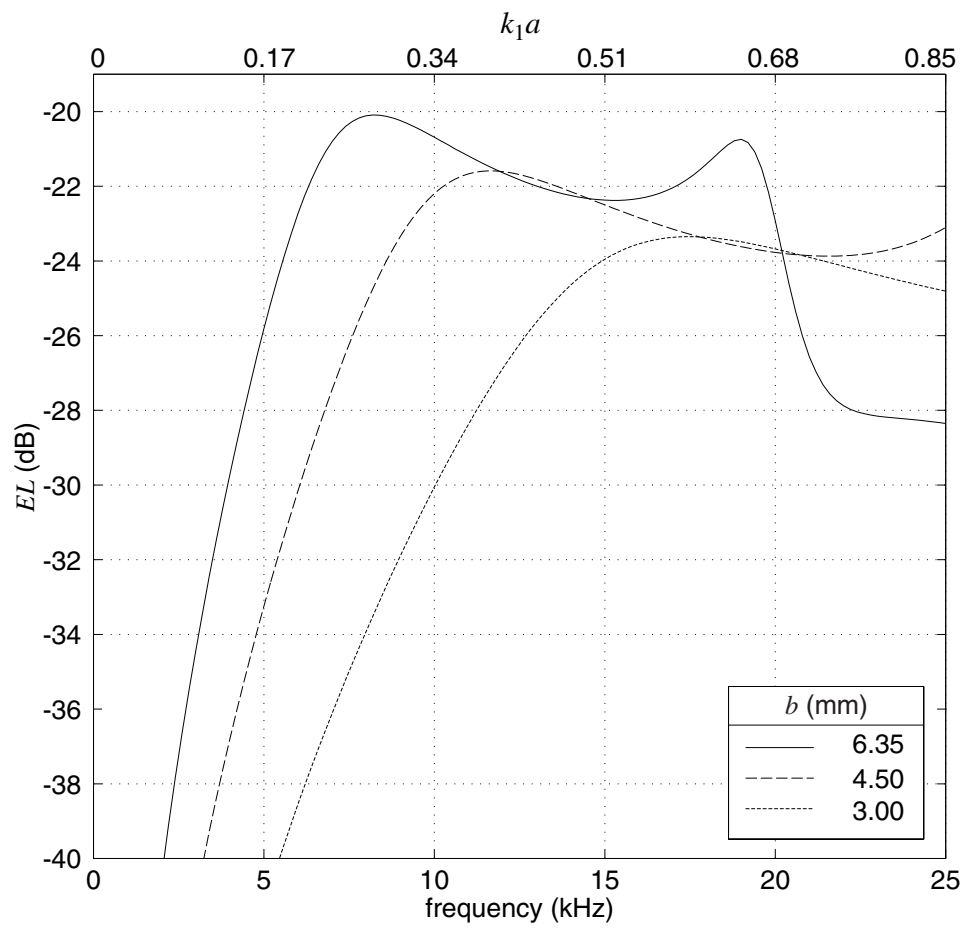


Figure 2.13: The effect of cloud size is shown. The inner radius b has been varied for a constant shell thickness of 1 mm.

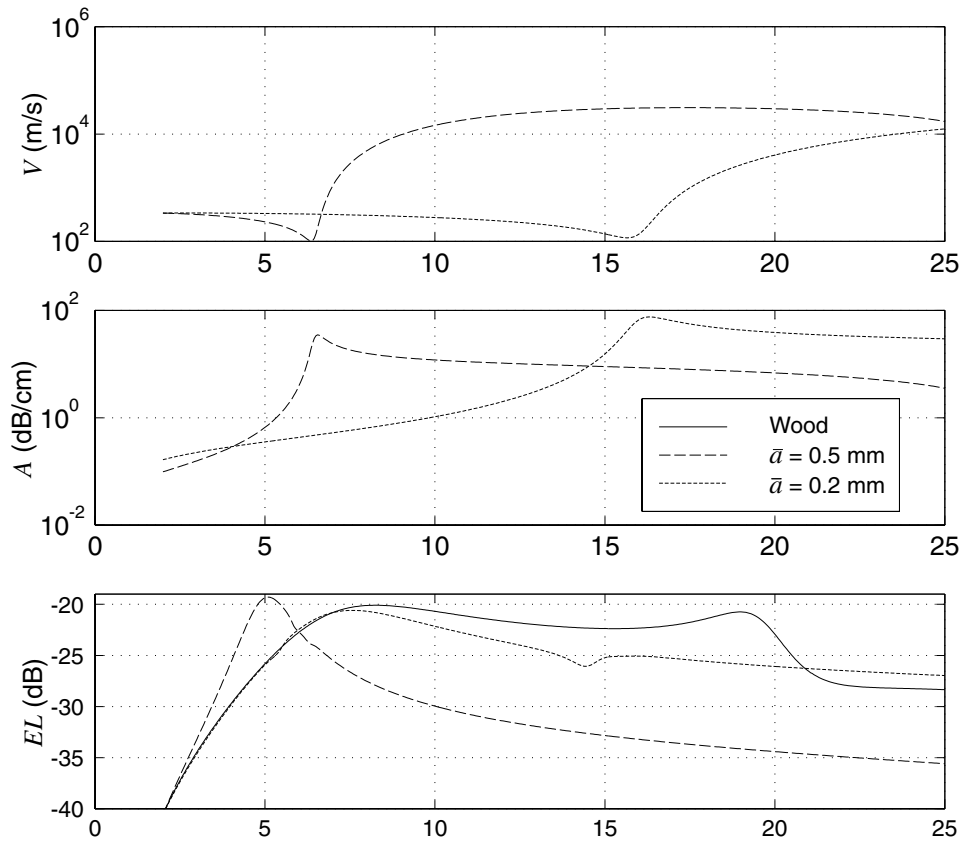


Figure 2.14: Bubble resonance effects are shown for two bubble sizes. The associated phase speed V and attenuation A is shown in the upper two plots. The corresponding scattering strength is shown in the lower plot. The legend applies to all three plots. The scattering for the Wood limit case is also shown for comparison.

Chapter 3

Development of a Water-Filled Impedance Tube

A common theme of previous experimental investigations of bubbly fluid was that the primary propagation occurred within the bubbly fluid itself. This presents problems near resonance frequency and at high void fractions, where attenuation as high as 60 dB/cm is insurmountable. Standing wave techniques fail because standing waves cannot develop at all. Direct propagation techniques fail because acoustic energy is absorbed before the far field of the transducer is reached. Hence, there is a scarcity of data under these conditions. The present technique does not overcome the attenuation, but merely avoids it. Instead of measuring propagation directly in the medium of interest, sound waves confined in a waveguide are reflected off the medium, which is contained in a section of the waveguide called the “sample holder.” In this work, a standard air impedance tube technique has been adapted for use in water. By using a two sensor, FFT based processing algorithm, the complex, frequency dependent acoustic impedance of the sample medium can be measured across a range of frequencies spanning bubble resonance in seconds. From this, the broadband sound speed and attenuation can be derived, hence characterizing plane wave propagation within the sample medium. Excess attenuation at resonance

never plays a role within the impedance tube itself, only in the sample holder. The present chapter documents the development of a water-filled impedance tube for use in the measurement of bubbly liquid propagation parameters in the vicinity of the individual bubble resonance frequency.

3.1 Introduction

To the author's knowledge, the impedance tube technique has not been applied to bubbly liquids. Perhaps this is because water-filled impedance tubes are not commercially available, and recent instruments described in the open literature have met with limited success [86, 87, 88]. One problem that applies to both recent and older works ([89, 90, 91] for example) is that reference measurements are not presented. The reader is presented with a variety of measured material properties, and usually, there is no theoretical value for comparison, nor any reference measurements to verify the accuracy of the technique. Typically one finds statements of the sort: "in the range to be expected for this type of material." Thus, the development of a new instrument was deemed necessary.

There is one body of work that constitutes a notable exception, which was most helpful during the early part of the present study, and is an interesting story in its own right. Please indulge in a short diversion. In their efforts to develop an echo reducing coating for the U-Boats, a group of German scientists including Walter Kuhl, Erwin Meyer, Hermann Oberst, Eugen Skudrzyk and Konrad Tamm developed an impedance tube apparatus for the measurement of the acoustic properties of materials in water. Their impedance tube was instrumental in the development of the coating, which was successful and installed on German U-Boats during World War II. After the war, much of their research was unclassified and published by the U. S. Navy [47], and subsequently in the open technical literature [92, 48]. A typical result from this work is the predicted and measured acoustic input impedance of metal disk with a slot [47, p. 439].

Another successful and convincing technique for the measurement of acoustic proper-

ties in water was recently published, which is similar to the impedance tube technique. It is called broadband time-domain reflectometry (BTDR), and it has been applied to the study of the medical ultrasound contrast agent Albunex [93]. BTDR is a high frequency technique in which freely propagating (not confined in a waveguide) ultrasound pulses are sent through a “witness plate,” which is in contact with the fluid of interest. The waveform reflected from a reference fluid is compared to the waveform reflected from the fluid of interest. From this the phase speed and attenuation are obtained. Plane wave propagation is assumed throughout. Measured attenuation as high as 5000 dB/cm was reported in the megahertz range. BTDR was deemed unpractical for the present study because the wavelengths of interest would require an unacceptably large apparatus and an unacceptably large volume of bubbly fluid.

3.2 Basic Impedance Tube Techniques

Impedance tubes for characterizing materials in air have been in use for almost 100 years and several variations exist; a review by Beranek mentions six of these [94]. Most acoustics texts develop impedance tube theory to a fairly sophisticated degree, such as Pierce [95] and Kinsler and Frey [96]. Two methods have emerged as superior and have achieved standard status: the standing wave method, and the transfer function method.

3.2.1 Standing Wave Method

The standing wave method (SWM) [97] is the older and perhaps more straight forward of the two methods. Although it was not used in the present work, a description of it is included for illustrative purposes. A sound source is placed at one end of a circular or rectangular cross-section rigid-walled waveguide whose length is many times greater than its diameter. The sample, which must be flat, is placed at the other end, terminating the tube in a sealed manner. Once the source is activated, a standing wave pattern develops in the tube. A microphone is scanned down the length of the tube, starting at

the sample end. The location and level of the first extrema is recorded along with several subsequent maxima and minima. From these data, the normal incidence sound absorption coefficient and the specific acoustic impedance of the sample can be calculated. This is done one frequency at a time, with a complete spatial scan for each frequency. Since the technique relies upon the presence of only plane waves, there is a maximum frequency of operation for a given tube size. Once the cutoff frequency for the lowest order transverse mode is approached, the method fails, due to the presence of additional modes. This is a hallmark of any impedance tube method. The theory behind the standing wave method of impedance measurement is developed below, following Blackstock [98].

Consider the impedance tube system shown in Fig. 3.1. Assume the walls are rigid and the wavelength inside the tube is greater than twice the tube diameter. Then only plane waves can propagate in the tube. From $0 < x < \ell$, the characteristic impedance is $z_1 = \rho_1 c_1$, and from $x > \ell$, $z_2 = \rho_2 c_2$. Assume lossless conditions and time harmonic excitation, then let the acoustic pressure and velocity be

$$\begin{aligned} p(x, t) &= P(x)e^{i\omega t} \\ u(x, t) &= U(x)e^{i\omega t}, \end{aligned}$$

where P and U can be complex quantities.

Let $P = P^+ + P^-$, where the superscripts $+$ and $-$ represent forward and backward traveling waves. Define the reflection coefficient R

$$R = \frac{P^-}{P^+}. \quad (3.1)$$

Solving Helmholtz's equation for acoustic pressure inside the tube for $0 < x < \ell$, where $k = \omega/c_1$ results in

$$P = Ae^{-ikx} + Be^{ikx} \quad (3.2)$$

and since $p = \pm z_1 u$ for $\begin{pmatrix} \text{forward} \\ \text{backward} \end{pmatrix}$ traveling waves,

$$U = \frac{A}{z_1} e^{-ikx} - \frac{B}{z_1} e^{ikx}. \quad (3.3)$$

Rewrite Eqs. 3.2 and 3.3 in terms of the distance from the interface $d = \ell - x$:

$$P = A e^{-ik\ell} e^{ikd} + B e^{ik\ell} e^{-ikd} = P^+ e^{ikd} + P^- e^{-ikd} \quad (3.4)$$

Combining Eqs. 3.1 and 3.4 results in

$$P = P^+ \left(e^{ikd} + R e^{-ikd} \right) \quad (3.5)$$

and

$$U = \left(\frac{P^+}{z_1} \right) \left(e^{ikd} - R e^{-ikd} \right)$$

The impedance at any point in the tube can now be written

$$z(d) = \frac{P(d)}{U(d)} = z_1 \frac{e^{ikd} + R e^{-ikd}}{e^{ikd} - R e^{-ikd}},$$

and when $d = 0$ the impedance of the termination is given:

$$z_2 = z_1 \frac{1 + R}{1 - R}. \quad (3.6)$$

Unless $z_2 = z_1$, a standing wave field will develop in the region $0 < x < \ell$. The standing wave ratio is defined as

$$\text{SWR} = \frac{|P_{\max}|}{|P_{\min}|},$$

where the max and min values are any two neighboring extrema within the tube. It can be shown from Eq. 3.5 that

$$\text{SWR} = \frac{1 + |R|}{1 - |R|},$$

therefore the magnitude of the reflection coefficient is

$$|R| = \frac{\text{SWR} - 1}{\text{SWR} + 1}.$$

The phase can be found from the following. Let $R = |R|e^{i\phi}$, then from Eq. 3.5

$$P = P^+ \left[e^{ikd} + |R|e^{i(\phi-kd)} \right].$$

It can be shown that if a pressure maximum occurs nearest the termination, $kd_{\max} = \phi/2$. If a minimum occurs first, $kd_{\min} = \phi/2 - \pi/2$. Therefore, if the extrema nearest the termination is a pressure maximum,

$$R = \frac{\text{SWR} - 1}{\text{SWR} + 1} e^{i2kd_{\max}}, \quad (3.7)$$

and if a minimum,

$$R = -\frac{\text{SWR} - 1}{\text{SWR} + 1} e^{i2kd_{\min}}. \quad (3.8)$$

The impedance of the termination can now be found from either Eq. 3.7 or 3.8 combined with Eq. 3.6.

3.2.2 Transfer Function Method

The two-sensor transfer function method (TFM) [99] was developed to exploit the power of modern spectral analysis processing, and thereby increase the speed and accuracy of impedance measurements. The speed of the TFM is the primary benefit over the SWM, especially when considering the dynamic nature of bubbly fluids whose properties may be nonstationary in both time and space.

The physical system is the same as in the SWM, except two acoustic pressure sensors are wall-mounted at known locations near the sample end of the tube, replacing the single spatially scanned microphone of the SWM. A broadband signal is generated and

the pressure signals are sampled and processed. The incident and reflected waves are decomposed in the frequency domain. Calculations are performed which yield the complex frequency dependent specific acoustic impedance, in terms of the host medium's characteristic impedance. Again, the technique is entirely dependent on the existence of solely plane waves in the tube. The theory of the TFM will be developed in two ways. In the first derivation, a physically intuitive approach will be taken in which harmonic excitation is assumed. In the second derivation, a more generalized approach is taken, which allows for arbitrary excitation but concludes with an equivalent result.

TFM with Harmonic Excitation

The following definitions are recalled: the specific acoustic impedance is given by $z = p/u$, where p is the acoustic pressure at a point and u is the particle velocity at the same point. For plane progressive waves, this ratio is equivalent to the quantity ρc , which is the characteristic impedance of a material. Consider the impedance tube system shown in Fig. 3.2. For $d > 0$, the tube is filled with a fluid of known sound speed c_1 and density ρ_1 . The finite length termination contains the material under test, with unknown sound speed c_2 and density ρ_2 . The two sections are separated by an imaginary interface. In practice, the interface can be made of a very thin material, which renders it acoustically transparent at the frequencies usable in the tube.

An expression for the reflection coefficient R of the interface at $d = 0$ will be derived. If desired, the specific acoustic impedance at the interface, z_2 , could then be obtained from R using Eq. 3.6, where $z_1 = \rho_1 c_1$. Note that because the termination in this case has a finite length, the impedance obtained from the measurement as described thus far would yield the specific acoustic impedance due to the termination as a whole, which is not the same as the characteristic impedance of the test material. The way to obtain a measurement of the characteristic impedance $\rho_2 c_2$ from this specific acoustic impedance is described at the end of this section. Note also, that the specific acoustic impedance at the interface can be considered the input impedance of the termination by invoking the

electrical circuit analogy.

Assume the walls are rigid and the wavelength inside the tube is greater than twice the tube diameter, thus only plane waves can propagate in the tube. Assume lossless conditions, no mean flow, and a sensor separation distance s . Sensor 1 is positioned a distance ℓ from the interface. Let $p_1(t)$ and $p_2(t)$ be the acoustic pressures at positions 1 and 2, respectively. In general, the acoustic pressure at any position $d > 0$ is given by

$$p(d, t) = P^+ \left(e^{ik_1 d} + R e^{-ik_1 d} \right) e^{i\omega t}, \quad (3.9)$$

where $k_1 = \omega/c_1$, that is for the fluid within the impedance tube, not the material under test. The amplitude of the right-going wave, and its phase relative to the left-going wave is given by the complex quantity P^+ and the reflection coefficient of the interface is R , which can also be complex. At positions 1 and 2, the acoustic pressure is

$$p_1(t) = P^+ \left(e^{ik_1 \ell} + R e^{-ik_1 \ell} \right) e^{i\omega t}, \quad (3.10)$$

$$p_2(t) = P^+ \left(e^{ik_1(\ell-s)} + R e^{-ik_1(\ell-s)} \right) e^{i\omega t}. \quad (3.11)$$

Note that measurable acoustic pressures would be given by the real parts of Eqs. 3.10 and 3.11. Eliminate P^+ between 3.10 and 3.11 and then divide through by p_1 to obtain

$$\frac{1}{e^{ik_1 \ell} + R e^{-ik_1 \ell}} = \frac{p_2(t)/p_1(t)}{e^{ik_1(\ell-s)} + R e^{-ik_1(\ell-s)}}. \quad (3.12)$$

Now let $H_{12} = p_2(t)/p_1(t)$, which is a complex quantity,¹ and rearrange 3.12 to get

$$R = \frac{H_{12} e^{ik_1 \ell} - e^{ik_1(\ell-s)}}{e^{-ik_1(\ell-s)} - H_{12} e^{-ik_1 \ell}}. \quad (3.13)$$

Multiply the RHS of 3.13 by

$$\frac{e^{-ik_1 \ell} e^{i2k_1 \ell}}{e^{ik_1 \ell}} \quad (3.14)$$

¹ H_{12} contains the amplitude ratio and phase difference between $p_2(t)$ and $p_1(t)$ at frequency ω .

and obtain

$$R = \frac{H_{12} - e^{-ik_1 s}}{e^{ik_1 s} - H_{12}} e^{i2k_1 \ell}, \quad (3.15)$$

which is the reflection coefficient at the interface.

The impedance of the test section could be obtained from Eqs. 3.15 and 3.6. This impedance is equivalent to the characteristic impedance of the test material *only if the waves in the test section are plane progressive waves traveling in the $-d$ direction*, i.e. if the test section is very long, or terminated with a perfect absorber. For a short termination which contains standing waves, a model would be required to relate the input impedance of the termination to the characteristic impedance of the test material. For the bubbly liquid experiments described in Chapter 4, the high attenuation present in the individual bubble resonance regime will be relied upon to make the sample holder effectively infinite in length. Therefore, the impedance at the interface will be equivalent to the specific acoustic impedance of the bubbly liquid.

Generalized Derivation

The theory behind the transfer function method of impedance measurement is developed below for stationary random excitation, following Chung and Blaser [100]. Consider the impedance tube system discussed previously in Fig. 3.2. Assume the walls are rigid and the wavelength inside the tube is greater than twice the tube diameter, thus only plane waves can propagate in the tube. Assume lossless conditions, no mean flow, and a sensor separation distance s . Let $p_1(t)$ and $p_2(t)$ be the stationary random acoustic pressures at the first and second sensor positions, written as the sum of incident and reflected components

$$p_1(t) = p_{1i}(t) + p_{1r}(t), \quad (3.16)$$

and

$$p_2(t) = p_{2i}(t) + p_{2r}(t). \quad (3.17)$$

The following convolution integrals are defined,

$$p_{1r}(t) = \int_0^{\infty} r_1(\tau) p_{1i}(t - \tau) d\tau, \quad (3.18)$$

$$p_{2r}(t) = \int_0^{\infty} r_2(\tau) p_{2i}(t - \tau) d\tau, \quad (3.19)$$

$$p_{2i}(t) = \int_0^{\infty} h_i(\tau) p_{1i}(t - \tau) d\tau, \quad (3.20)$$

$$p_{2r}(t) = \int_0^{\infty} h_r(\tau) p_{1r}(t - \tau) d\tau, \quad (3.21)$$

$$p_2(t) = \int_0^{\infty} h_{12}(\tau) p_1(t - \tau) d\tau, \quad (3.22)$$

where r_1 and r_2 are the impulse responses corresponding to the reflected wave evaluated at positions 1 and 2, h_i and h_r are the impulse responses corresponding to the incident and reflected waves evaluated between positions 1 and 2, and h_{12} is the impulse response corresponding to the combined incident and reflected waves evaluated between positions 1 and 2.

Combining Eqs. 3.16, 3.17, and 3.22 results in

$$p_{2i}(t) + p_{2r}(t) = \int_0^{\infty} h_{12}(\tau) [p_{1i}(t - \tau) + p_{1r}(t - \tau)] d\tau. \quad (3.23)$$

Then using Eqs. 3.20 and 3.21, Eq. 3.23 becomes

$$\int_0^{\infty} p_{1i}(t - \tau) [h_{12}(\tau) - h_i(\tau)] d\tau = \int_0^{\infty} p_{1r}(t - \tau) [h_r(\tau) - h_{12}(\tau)] d\tau. \quad (3.24)$$

Multiplying both sides by $p_{1i}(t - \alpha)$ and taking expected values,² Eq. 3.24 becomes:

$$\begin{aligned} & \int_0^{\infty} E \{ p_{1i}(t - \tau) p_{1i}(t - \alpha) \} [h_{12}(\tau) - h_i(\tau)] d\tau \\ & = \int_0^{\infty} E \{ p_{1r}(t - \tau) p_{1i}(t - \alpha) \} [h_r(\tau) - h_{12}(\tau)] d\tau. \end{aligned} \quad (3.25)$$

²For contextual definition of expected value, see [101].

Now,

$$E \{p_{1i}(t - \tau)p_{1i}(t - \alpha)\} = R_{1i1i}(\alpha - \tau) \quad (3.26)$$

and

$$E \{p_{1r}(t - \tau)p_{1i}(t - \alpha)\} = R_{1i1r}(\alpha - \tau), \quad (3.27)$$

where R_{1i1i} and R_{1i1r} are the auto- and cross-correlations functions, respectively. Substitution of Eqs. 3.26 and 3.27 into Eq. 3.25, and subsequent Fourier transformation results in:

$$\begin{aligned} & \int_{-\infty}^{\infty} \int_0^{\infty} R_{1i1i}(\alpha - \tau) [h_{12}(\tau) - h_i(\tau)] e^{-i2\pi f\alpha} d\tau d\alpha \\ &= \int_{-\infty}^{\infty} \int_0^{\infty} R_{1i1r}(\alpha - \tau) [h_r(\tau) - h_{12}(\tau)] e^{-i2\pi f\alpha} d\tau d\alpha. \end{aligned} \quad (3.28)$$

Let $\alpha - \tau = \eta$ and $d\alpha = d\eta$, then Eq. 3.28 becomes

$$\begin{aligned} & \int_{-\infty}^{\infty} R_{1i1i}(\eta) e^{-i2\pi f\eta} d\eta \int_0^{\infty} [h_{12}(\tau) - h_i(\tau)] e^{-i2\pi f\tau} d\tau \\ &= \int_{-\infty}^{\infty} R_{1i1r}(\eta) e^{-i2\pi f\eta} d\eta \int_0^{\infty} [h_r(\tau) - h_{12}(\tau)] e^{-i2\pi f\tau} d\tau, \end{aligned} \quad (3.29)$$

or

$$\frac{S_{1i1r}(f)}{S_{1i1i}(f)} = \frac{\int_0^{\infty} [h_{12}(\tau) - h_i(\tau)] e^{-i2\pi f\tau} d\tau}{\int_0^{\infty} [h_r(\tau) - h_{12}(\tau)] e^{-i2\pi f\tau} d\tau}, \quad (3.30)$$

where $S_{1i1i}(f)$ is the Fourier transform of $R_{1i1i}(\eta)$, and is therefore the auto-spectral density of the incident pressure component at position 1. Similarly, $S_{1i1r}(f)$ is the cross-spectral density between the incident and reflected pressure components at position 1. By definition,

$$\frac{S_{1i1r}(f)}{S_{1i1i}(f)} = R_1(f), \quad (3.31)$$

the complex reflection coefficient at position 1. It can be shown that $R_1(f)$ is the Fourier

transform of $r_1(\eta)$,

$$R_1(f) = \int_0^\infty r_1(\eta) e^{-i2\pi f\eta} d\eta = \frac{S_{1i1r}(f)}{S_{1i1i}(f)}, \quad (3.32)$$

and similarly,

$$H_i(f) = \int_0^\infty h_i(\tau) e^{-i2\pi f\tau} d\tau = \frac{S_{1i2i}(f)}{S_{1i1i}(f)}, \quad (3.33)$$

$$H_r(f) = \int_0^\infty h_r(\tau) e^{-i2\pi f\tau} d\tau = \frac{S_{1r2r}(f)}{S_{1r1r}(f)}, \quad (3.34)$$

and

$$H_{12}(f) = \int_0^\infty h_{12}(\tau) e^{-i2\pi f\tau} d\tau = \frac{S_{12}(f)}{S_{11}(f)}, \quad (3.35)$$

where H_i , H_r , and H_{12} , are the acoustical transfer functions corresponding to their associated impulse responses h_i , h_r , and h_{12} .

Now from Eqs. 3.30 to 3.35, the complex reflection coefficient at position 1 can be written:

$$R_1(f) = \frac{H_{12}(f) - H_i(f)}{H_r(f) - H_{12}(f)}. \quad (3.36)$$

We must now relate R_1 to the reflection coefficient at the interface. It can be shown, through analysis similar to that in Eqs. 3.16–3.36, that

$$\frac{R_1(f)}{R_2(f)} = \frac{H_i(f)}{H_r(f)}. \quad (3.37)$$

From which follows, based on the plane wave and no mean flow assumptions:

$$H_i(f) = e^{-iks}, \quad (3.38)$$

and

$$H_r(f) = e^{+iks}, \quad (3.39)$$

where k is the wave number and s is the distance between positions 1 and 2. Similarly,

$$\frac{R_1}{R} = \frac{H'_i}{H'_r} = \frac{e^{-ik\ell}}{e^{+ik\ell}}, \quad (3.40)$$

where R is the complex reflection coefficient at the interface and ℓ is the distance from position 1 to the sample interface. Combining Eqs. 3.36, 3.38, 3.39 and 3.40 results in

$$R(f) = \frac{H_{12}(f) - e^{-iks}}{e^{iks} - H_{12}(f)} e^{+i2k\ell}, \quad (3.41)$$

which is the complex, frequency dependent reflection coefficient at the interface.

There is a singularity in Eq. 3.41, when the denominator vanishes. The behavior of this singularity can best be examined by investigating Eq. 3.36, which becomes singular when $H_r - H_{12} = 0$. It can be shown that this condition occurs when $ks = m\pi$, or $s = m\frac{\lambda}{2}$, for $m = 1, 2, 3 \dots$. This corresponds to frequencies where positions 1 and 2 are integer multiples of a half wavelength. Therefore, the sensor spacing must be

$$s \leq c/2f_{\max}, \quad (3.42)$$

where f_{\max} is the maximum frequency of interest and c is the speed of sound in the tube.

From Eq. 3.41 a number of acoustic quantities can be deduced, as discussed in [99]. The specific acoustic impedance of the sample can be determined from Eqs. 3.41 and 3.6, and is given by

$$\frac{z_2}{z_1} = i \frac{H_{12} \sin k\ell - \sin k(\ell - s)}{\cos k(\ell - s) - H_{12} \cos k\ell}, \quad (3.43)$$

Up to this point, the two pressure sensors have been considered ideal; it has been assumed that the two sensors exhibit identical responses to a given input. Since no two real sensors have this characteristic, some kind of procedure must be undertaken in practice to correct for the mismatch. A sensor switching technique is given in the standard [99] which requires a “non-reflecting” termination. This is not practically realizable in a water-

filled impedance tube. Two different methods have been employed in the present work to overcome this difficulty and will be discussed in subsequent sections.

Extension of TFM for a Single Sensor

A simple modification of procedure and a single additional measurement allows the TFM to be performed with a single sensor [102]. The excitation signal is used as a reference for a measurement at the first position. The same sensor is moved to the second position and another measurement is made, thereby eliminating the need to account for the different responses of two sensors. The transfer function H_{12} in Eq. 3.41 is replaced with

$$H_{12} = \frac{S_{1s}}{S_{11}} \frac{S_{s2}}{S_{ss}} = H_{1s}H_{s2}, \quad (3.44)$$

where H_{1s} is the transfer function between the hydrophone signal at position 1 and the source excitation signal, and H_{s2} is the transfer function between the source excitation signal and the hydrophone signal at position 2.

3.3 Adaption of Two-Sensor Technique for Use In Water

The TFM, as described in [99] is a powerful and useful technique and has become the workhorse method for determining acoustic properties of materials in air. The noise control and architectural industries have adopted it fully. So much so in fact that Brüel and Kjær produces an off-the-shelf measurement system based on this technique. There is certainly a need for those working in underwater acoustics to measure the acoustic properties of underwater materials. Several attempts have been made to adapt TFM for use underwater, with various degrees of success [86, 87, 88].

The primary difficulty is loss of the rigid boundary condition at the tube wall. In an air-filled tube, the impedance difference between air and almost any other solid material is sufficient to render the tube wall effectively rigid. In such a system, plane waves exist

alone within the tube, from DC up to a cutoff frequency associated with the lowest order transverse mode. In a water-filled tube, the difference in impedance between water and most solid materials is not nearly as great.³ What results with a water-filled tube is an elastic waveguide which can support a higher order mode at all frequencies. The presence of more than just plane waves renders TFM unusable. Investigation of elastic wave guide theory revealed the following: if proper dimensions and materials are used, the extent of the elastic waveguide behavior can be reduced to a low level, and some simple modifications of standard TFM can be implemented to overcome this diminished difficulty. The theory validating this statement is developed in Section 3.4.

In addition, the presence of real sensors in the waveguide or in the waveguide walls can cause difficulties. With the air-filled tube, most sensors appear rigid and do not perturb the acoustic field or boundary conditions in a significant manner. This is not the case with a water-filled tube. Preliminary results indicated that high mechanical-input-impedance hydrophones and mounting arrangements were necessary. Since these were not available commercially, they were designed and constructed specifically for this application. Appendix B is devoted to further discussion of this topic. The end result: with the present hydrophone design, the acoustic pressure can be measured at the specified location, without influence from spurious wall motions, and without affecting the boundary conditions of the waveguide or perturbing the acoustic field inside the waveguide.

There is one additional difficulty in adapting TFM for use in water. Ideally, the two sensors used in the method would be identical in both amplitude and phase response. No two real sensors have this characteristic. To overcome this, a cross-calibration procedure is employed in [99], which requires a non-reflecting termination, and the switching of sensors. Such a termination is physically difficult to realize with a water-filled tube, and the sensor switching procedure is also difficult to conduct with a water-filled tube. The single sensor method has been mentioned, and it is useful for samples that are stable

³For example, the impedance of steel is about 113,252 times greater than air, but only 32 times greater than water. This leads to a plane wave reflection coefficient between air and steel of 0.999982, and 0.9389 for steel and water; significantly less rigid!

in time. However, in order to make real time measurements with time-varying samples, the two-sensor method is required, and therefore a practical cross-calibration method was needed. Initially a revised cross-calibration procedure was implemented, which proved to be only partially effective. A number of measurements which relied upon this technique will be presented, therefore, the initial cross-calibration technique is detailed in Appendix C. Ultimately, another cross-calibration was found in the literature and was adopted for the measurements presented in Chapter 4. The final procedure is detailed in Section 3.7.1.

3.4 Theory of Propagation and Resonance In Finite Elastic Waveguides with Real Terminations

In this section, the theoretical background is developed for using the TFM with a water-filled impedance tube. First, a review of propagation in rigid walled waveguides will be presented. This will provide a set of equations that predict the spatial and frequency domain behavior of such a system. Next, an introduction to propagation in elastic waveguides will be presented. This will provide the elastic waveguide phase speed. It will then be shown in Section 3.6 that the present impedance tube waveguide can be described using these rigid waveguide equations, but with an *effective* sound speed based on the elastic waveguide analysis.

3.4.1 Review of Plane Wave Propagation in Rigid Tubes

Consider a circular cylindrical tube of diameter d , filled with a liquid with density ρ and sound speed c , driven at $x = 0$ with a rigid piston, such that the particle velocity is $u(0, t) = u_0 e^{i\omega t}$. The tube is terminated at $x = \ell$ such that $p(\ell, t) = 0$. Assume that the tube walls are rigid and limit the frequency to enforce $\lambda > 2d$. Under these conditions, the one dimensional wave equation for acoustic pressure,

$$\frac{\partial^2 p}{\partial x^2} - \frac{1}{c^2} \frac{\partial^2 p}{\partial t^2} = 0, \quad (3.45)$$

is valid within the tube. Eq. 3.45 is satisfied by

$$p(x, t) = \left[A e^{ik(\ell-x)} + B e^{-ik(\ell-x)} \right] e^{i\omega t}, \quad (3.46)$$

where A and B are to be determined from the boundary conditions. Since $u(x, t) = -\frac{1}{\rho} \int \partial p / \partial x dt$, the particle velocity within the tube is

$$u(x, t) = \frac{1}{\rho c} \left[A e^{ik(\ell-x)} - B e^{-ik(\ell-x)} \right] e^{i\omega t}. \quad (3.47)$$

Applying to Eq. 3.46 the boundary condition at $x = 0$ results in $A + B = 0$, and applying the boundary condition at $x = \ell$ we find $A = \frac{\rho c u_0}{2 \cos k\ell}$ and hence $B = -\frac{\rho c u_0}{2 \cos k\ell}$. Substituting into Eq. 3.46, the acoustic pressure anywhere in the tube is

$$p(x, t) = i \rho c u_0 \frac{\sin[k(\ell - x)]}{\cos k\ell} e^{i\omega t}. \quad (3.48)$$

Similarly, the particle velocity is

$$u(x, t) = u_0 \frac{\cos[k(\ell - x)]}{\cos k\ell} e^{i\omega t}, \quad (3.49)$$

and since $z = p/u$, the specific acoustic impedance at any point in the tube is obtained from dividing Eq. 3.48 by Eq. 3.49, or

$$z(x) = i \rho c \tan[k(\ell - x)]. \quad (3.50)$$

In Eq. 3.48, the acoustic pressure becomes unbounded when $\cos k\ell = 0$ or when $k\ell = \pi/2, 3\pi/2, 5\pi/2, \dots$, therefore the resonance frequencies are

$$f_n = \frac{c}{2\ell} (n + 1/2), n = 0, 1, 2, 3, \dots, \quad (3.51)$$

for the driven/pressure release tube. Note that Eq. 3.51 is only valid for a frequency

independent prescribed velocity. A real source driven with a constant voltage amplifier may not provide this condition. A more realistic model must include the response of the source and the tube.

Dynamics of the Combined Source-Tube System

The resonance frequencies of the combined source-tube system will be developed below, following Kinsler and Frey [96]. Let the source be modeled as a simple harmonic oscillator, as shown in Fig. 3.3, with stiffness s , mass m , and resistance R_m , excited by an external force f . The mechanical input impedance Z_{md} of the driver is

$$Z_{md} = R_m + i(\omega m - s/\omega). \quad (3.52)$$

Define the mechanical input impedance of the tube as $Z_{m0} = z_0 S$, where z_0 is the specific acoustic impedance of the tube at $x = 0$, and S is the cross-sectional area of the tube. Then from Eq. 3.50,

$$Z_{m0} = i\rho c S \tan k\ell. \quad (3.53)$$

The input impedance seen by the applied force is the series sum of Eqs. 3.52 and 3.53, and resonance occurs when

$$\text{Im}\{Z_{md} + Z_{m0}\} = 0 \quad (3.54)$$

Combining Eqs. 3.52 and 3.53 with 3.54 results in

$$\omega m - s/\omega + \rho c S \tan k\ell = 0, \quad (3.55)$$

which can be solved graphically or numerically for the combined system resonances.

3.4.2 Theory of Sound Propagation in Elastic Waveguides

By the middle of the nineteenth century, it was realized that the sound speed within a fluid-filled elastic waveguide was lower than that in the unbounded fluid. Early work, summarized by Wood in [103], provided thin and thick wall approximations for the speed of sound at low frequencies. In 1948, Jacobi employed improved approximations for thin wall stress and strain, and thus predicted a dispersive behavior for the plane-wave mode [104]. By 1956, Lin and Morgan, still employing a thin wall assumption but considering transverse shear and rotary inertia, predicted a higher order mode would exist at all frequencies [105]. All the qualitative components of elastic waveguide propagation were now in place; a slower, dispersive plane-wave-like mode, and at least one higher order mode present at all frequencies. Del Grosso [106], using the exact longitudinal and shear wave equations for arbitrary wall thickness, obtained an analytic dispersion relation for the axisymmetric lossless case. Based on Del Grosso, Lafleur and Shields [107] offered some simplifications, rendering the system of equations easier to use but without loss of generality. The present work utilizes the results of Lafleur and Shields, but acknowledges the contribution of Del Grosso.

Particle Displacement Profiles and Phase Speed

In this section, the problem for particle displacement and phase speed in a system with the geometry shown in Fig. 3.4 is discussed. The problem will be set up in order to clarify the model being used but then for brevity, the solution will merely be presented, the details of execution being available elsewhere. Excitation is assumed to be harmonic with frequency ω .

Following Del Grosso [106], for a finite wall thickness elastic solid tube enclosing an inviscid liquid cylinder and itself surrounded by empty space, a displacement vector \mathbf{S} expressed in terms of a scalar displacement potential Φ and a vector displacement potential

Ψ is used as

$$\mathbf{S} = \nabla\Phi + \nabla \times \Psi. \quad (3.56)$$

In the usual manner, Φ and Ψ satisfy the ordinary wave equations

$$\nabla^2\Phi = \frac{1}{c_l^2} \frac{\partial^2\Phi}{\partial t^2}, \quad (3.57)$$

and

$$\nabla^2\Psi = \frac{1}{c_t^2} \frac{\partial^2\Psi}{\partial t^2}, \quad (3.58)$$

where c_l and c_t are the local longitudinal (compressional) and transverse (shear) wave speeds respectively. The vector form of the linear elastic equations of motion for an isotropic homogenous material obeying Hooke's law is

$$\rho \frac{\partial^2\mathbf{S}}{\partial t^2} = (\lambda + 2\mu) \text{grad } \Delta - 2\mu \text{curl } \mathbf{\Omega}, \quad (3.59)$$

where λ and μ are Lamé's constants, the rotation $\mathbf{\Omega} = \frac{1}{2} \text{curl } \mathbf{S}$ and the dilatation $\Delta = \text{div } \mathbf{S}$ [83].

In cylindrical coordinates, and for the axially symmetric case where $\mathbf{S}_\theta = 0$ and $\frac{\partial}{\partial \theta} = 0$, the displacement \mathbf{S} is composed only of radial S_r and axial S_z components:

$$S_r = \frac{\partial\Phi}{\partial r} - \frac{\partial\Psi_\theta}{\partial z}, \quad S_z = \frac{\partial\Phi}{\partial z} + \frac{1}{r} \frac{\partial}{\partial r}(r\Psi_\theta). \quad (3.60)$$

In order to establish the boundary conditions, the appropriate stress components are needed. These are

$$\sigma_{rr} = \lambda \left[\frac{1}{r} \frac{\partial}{\partial r}(rS_r) + \frac{\partial S_z}{\partial z} \right] + 2\mu \frac{\partial S_r}{\partial r}, \quad (3.61)$$

and

$$\sigma_{rz} = \mu \left[\frac{\partial S_r}{\partial z} + \frac{\partial S_z}{\partial r} \right], \quad (3.62)$$

where $\mu = \rho_W c_t^2$ and $\lambda = \frac{2\nu}{1-2\nu} \rho_W c_t^2$. Regarding material properties of the wall, ρ_W is the

density, c_t is the intrinsic transverse (shear) sound speed and ν is the ratio of Poisson.

There are six boundary conditions to satisfy: the vanishing of tangential stress, the continuity of radial displacement, and the equality of acoustic pressure p and radial stress, all taken at the radial boundaries, b and d . The latter four are combined into two statements of normal impedance equality at the radial boundaries, for a total of four boundary conditions. In the present case, the impedance condition at $r = d$ degenerates to a pressure release condition. These are

$$\begin{aligned}
\sigma_{rz} &= 0 \quad \text{at } r = b, \\
\sigma_{rz} &= 0 \quad \text{at } r = d, \\
\frac{-\sigma_{rr}}{S_r} &= \frac{p}{S_r} \quad \text{at } r = b, \\
\frac{-\sigma_{rr}}{S_r} &= \frac{p}{S_r} = 0 \quad \text{at } r = d.
\end{aligned} \tag{3.63}$$

Now following Lafleur and Shields [107] and their simplified notation, the above problem yields the following solution for particle displacement in the liquid,

$$S_z^L(r, z, t) = i\phi_0 q_{0m} J_0(rX_{0m}/b) e^{i(q_{0m}z - \omega t)}, \tag{3.64}$$

$$S_r^L(r, z, t) = -(\phi_0 X_{0m}/b) J_1(rX_{0m}/b) e^{i(q_{0m}z - \omega t)}, \tag{3.65}$$

and in the wall,

$$\begin{aligned}
S_z^W(r, z, t) &= \{iq_{0m}[AJ_0(rP_m) + BY_0(rP_m)] \\
&\quad + T_m[CJ_0(rT_m) + DY_0(rT_m)]\} e^{i(q_{0m}z - \omega t)},
\end{aligned} \tag{3.66}$$

$$\begin{aligned}
S_r^W(r, z, t) &= \{-P_m[AJ_1(rP_m) + BY_1(rP_m)] \\
&\quad - iq_{0m}[CJ_1(rT_m) + DY_1(rT_m)]\} e^{i(q_{0m}z - \omega t)}.
\end{aligned} \tag{3.67}$$

In these expressions, the following definitions apply,

$$X_{0m} = b\sqrt{k_1^2 - q_{0m}^2}, \quad P_m = \sqrt{k_l^2 - q_{0m}^2}, \quad T_m = \sqrt{k_t^2 - q_{0m}^2},$$

$$q_{0m} = \omega/c_{0m}, \quad k_l = \omega/c_l, \quad k_t = \omega/c_t, \quad k_1 = \omega/c_1,$$

where c_1 is the intrinsic speed of sound in the liquid, c_l is the longitudinal (compressional) wave speed in the tube wall, c_t is the transverse (shear) wave speed in the tube wall, and c_{0m} is the phase speed of the m th axisymmetric wave in the system. J_n and Y_n are the n th order Bessel functions of the first and second kind respectively.

The constants ϕ_0 , A , B , C , and D are obtained from the boundary conditions. Del Grosso [106] shows that the latter four satisfy the following equations:

$$\begin{aligned} A \left(E_m J_0(dP_m) + \frac{P_m}{d} J_1(dP_m) \right) + B \left(E_m Y_0(dP_m) + \frac{P_m}{d} Y_1(dP_m) \right) \\ + C \left(-iq_{0m} T_m J_0(dT_m) + i \frac{q_{0m}}{d} J_1(dT_m) \right) \\ + D \left(-iq_{0m} T_m Y_0(dT_m) + i \frac{q_{0m}}{d} Y_1(dT_m) \right) = 0, \end{aligned} \quad (3.68)$$

and

$$\begin{aligned} A [iq_{0m} P_m J_1(dP_m)] + B [iq_{0m} P_m Y_1(dP_m)] \\ + C [-E_m J_1(dT_m)] + D [-E_m Y_1(dT_m)] = 0, \end{aligned} \quad (3.69)$$

and

$$\begin{aligned} A [iq_{0m} P_m J_1(bP_m)] + B [iq_{0m} P_m Y_1(bP_m)] \\ + C [-E_m J_1(bT_m)] + D [-E_m Y_1(bT_m)] = 0, \end{aligned} \quad (3.70)$$

and

$$A \left(E_m J_0(bP_m) + \frac{1 + Q_m b}{b} P_m J_1(bP_m) \right)$$

$$\begin{aligned}
& +B \left(E_m Y_0(bP_m) + \frac{1 + Q_m b}{b} Y_1(bP_m) \right) \\
& +C \left(-iq_{0m} T_m J_0(bT_m) + i \frac{q_{0m}}{d} (1 + Q_m b) J_1(bT_m) \right) \\
& +D \left(-iq_{0m} T_m Y_0(bT_m) + i \frac{q_{0m}}{d} (1 + Q_m b) Y_1(bT_m) \right) = 0, \tag{3.71}
\end{aligned}$$

where the following definitions have been used,

$$E_m = q_{0m}^2 - k_t^2/2, \quad Q_m = \frac{\rho_L \omega^2 b J_0(X_{0m})}{2\rho_W c_t^2 X_{0m} J_1(X_{0m})},$$

and where ρ_W and ρ_L are the densities of the tube wall and the liquid, respectively.

Nonzero values for the four constants, A , B , C , and D are found by requiring the determinant of their coefficients to vanish, which results in a characteristic equation relating q_{0m} to ω ,

$$\begin{aligned}
& 1 + [L_{11}(P_m)L_{00}(T_m)] \left(\frac{\pi^2 q_{0m}^2 b d P_m^2 T_m^2}{8E_m^2} \right) + [L_{11}(T_m)L_{00}(P_m)] \left(\frac{\pi^2 b d E_m^2}{8q_{0m}^2} \right) \\
& + [L_{10}(P_m)L_{01}(T_m) + L_{01}(P_m)L_{10}(T_m)] \left(\frac{\pi^2 b d P_m T_m}{8} \right) \\
& + [bL_{11}(P_m)L_{10}(T_m) + d(1 + Q_m b)L_{11}(P_m)L_{01}(T_m)] \left(\frac{\pi^2 P_m^2 T_m}{8E_m} - \frac{\pi^2 P_m^2 q_{0m}^2 T_m}{8E_m^2} \right) \\
& + [bL_{11}(T_m)L_{10}(P_m) + d(1 + Q_m b)L_{11}(T_m)L_{01}(P_m)] \left(\frac{\pi^2 P_m E_m}{8q_{0m}^2} - \frac{\pi^2 P_m}{8} \right) \\
& + [(1 + Q_m b)L_{11}(T_m)L_{11}(P_m)] \left(\frac{\pi^2 P_m^2}{8q_{0m}^2} + \frac{\pi^2 P_m^2 q_{0m}^2}{8E_m^2} - \frac{\pi^2 P_m^2}{4E_m} \right) = 0, \tag{3.72}
\end{aligned}$$

where $L_{mn}(\xi) = J_m(d\xi)Y_n(b\xi) - J_n(b\xi)Y_m(d\xi)$.

In these equations, the use of the subscript $0m$ identifies the mode of the traveling wave. The leading 0 indicates all these modes are axisymmetric. At any given frequency, Eq. 3.72 has multiple real solutions, q_{0m} , for $m = 0, 1, \dots, M_\omega$, each being the wave number of the m th mode at that frequency.⁴ The number of possible modes M_ω is frequency

⁴Despite having parts which contain complex quantities, e.g. P_m and T_m , it can be shown that each of

dependent, and it has been shown [107] at least two modes can exist at all frequencies. The parameters which affect the phase speed are summarized here: b , d , c_t , c_l , c_1 , ρ_W , and ρ_L . Since all of these are known, the values for q_{0m} can be determined numerically using a zero finding routine. The phase speed for the m th mode, at frequency ω , is then obtained from $c_{0m} = \omega/q_{0m}$. Note that defining a source or termination boundary condition is not required for the determination of phase speed. They would be required to quantify the field inside the cylinder, though.

To illustrate the dispersion encountered in an elastic waveguide, calculations were performed for an aluminum tube with the properties listed in Table 3.1. The results are shown in Fig. 3.5. The figure also includes the family of curves that would arise if the walls were rigid. Five modes are shown for c_{0m} , $m = 0, 1, 2, 3$ and 4. Notice the 0th mode shows a modest amount of dispersion and a reduced phase speed relative to the rigid case. Also note that the next higher mode indeed exists down to zero frequency.

3.4.3 Effective Plane Wave, Combined Source-Tube Propagation Model

In order to describe the acoustics of our real impedance tube, we join together the results of sections 3.4.1 and 3.4.2, and call the result the Effective Plane Wave, Combined Source-Tube Propagation Model (EPWM). For the resonances of the source-free system, solve Eq. 3.51,

$$f_n = \frac{c_{\text{eff}}}{2\ell} (n + 1/2), n = 0, 1, 2, 3, \dots, \quad (3.73)$$

or for the resonances of the combined source-tube system, solve Eq. 3.55,

$$\omega m - s/\omega + \rho c_{\text{eff}} S \tan k\ell = 0, \quad (3.74)$$

and for the spatial or frequency response of the system, use Eq. 3.48

$$p(x, t) = i\rho c_{\text{eff}} u_0 \frac{\sin[k(\ell - x)]}{\cos k\ell} e^{i\omega t}, \quad (3.75)$$

the terms in Eq. 3.72 are always real.

where c_{eff} is calculated from Eq. 3.76 and $k = \omega/c_{\text{eff}}$. $c_{00}(\omega)$ is the phase speed of the lowest order mode predicted by Eq. 3.72, which for the conditions of this experiment will be shown to display negligible dispersion over the frequency range of interest. Even so, we take the average over the frequency range,

$$c_{\text{eff}} = \langle c_{00}(\omega) \rangle = \frac{1}{(\omega_2 - \omega_1)} \int_{\omega_1}^{\omega_2} c_{00}(\omega) d\omega. \quad (3.76)$$

The validity of this model will be investigated experimentally in Section 3.6.1.

It has been shown that the waves traveling within the real impedance tube are not truly planar, but the expected deviation from plane behavior is small. In addition, a higher order mode may exist at all frequencies, but because its radial distribution is unmatched to a piston source, it is not effectively excited and thus is expected to have a very low amplitude. If an effective plane wave model can accurately predict the behavior of this system, we hypothesize that the TFM will work within that same system. Restated simply, the waves are not truly plane, but they are “plane enough” and TFM will work. In the next section we will present evidence in support of this statement.

3.5 Prototype Impedance Tube

In this section, the first generation instrument is described. This prototype was created as an engineering and verification test bed. First, the waveguide geometry required verification, in order to ensure that propagation inside was suitably plane. This required a waveguide of greater length than would be necessary for impedance tube measurements alone. Second, the custom made acoustic sensors needed to be tested to ensure that they were insensitive to wall motions, yet did not perturb the acoustic field inside the waveguide. Third, the implementation of the TFM and the sensor cross-calibration techniques required verification.

3.5.1 Apparatus

The instrument described herein was designed to measure the complex, frequency dependent acoustic impedance of fluid and solid materials, in the frequency range of roughly 100 Hz to 10 kHz. Guidelines laid out in the ASTM Standard [99, section 6], which is for an air-filled impedance tube, were followed precisely, but some details had to be adapted for use in water. For example, ribbed plywood is suggested for use as a wall material, in order to provide the rigid boundary condition. This is not sufficient for a water-filled waveguide and a different material was used. A schematic of the prototype apparatus is shown in Fig. 3.6.

The waveguide tube was made out of type 304L seamless stainless steel tubing, with an internal diameter of 5.08 cm, wall thickness of 2.54 cm, and length 151.5 cm. These dimensions were arrived upon after careful consideration of the elastic waveguide problem discussed in Section 3.4, and they minimize the elastic waveguide effects, as will be shown in Section 3.6. The tube is supported by custom made cradles, of design pertinent to the mode of deployment, each incorporating vibration isolation in the form of rubber sheets or blocks. The three deployment modes were:

1. Floor mounted, in laboratory, with tube positioned vertically.
2. Floor mounted, in laboratory with tube positioned horizontally, as shown in Fig. 3.7.
3. Suspended in water. Both horizontal and vertical positions are possible.

The fluid of interest was contained in the sample holder, as shown in Fig. 3.6, which has construction identical to that of the waveguide tube itself and is made of the same material. The sample holder is mounted to the tube using flanges (withheld from Fig. 3.6 for clarity) and sealed to the tube with an o-ring. An acoustically transparent mylar membrane (thickness = 0.15 mm) separates the two fluids.⁵

⁵Additional sample holders, like the one shown in Fig. 3.7 may also be used and will be discussed in Section 3.6.3.

During normal operation (while making impedance measurements) the excitation signal was generated with the internal source of a Hewlett-Packard HP 89410A Vector Signal Analyzer. During preliminary testing, a Wavetek Model 39 Waveform Generator was also used to generate monochromatic CW signals and short pulses. In all cases the excitation signals were further amplified with a Krohn-Hite Model 7500 Wideband Power Amplifier.

During most operations, the sound source was a Kildare Model TP-400/A, which is a specially housed Tonpiltz type projector that was custom built for this application.⁶ The housing serves as a mount to the waveguide tube, and hermetically seals the projector from the external environment. The Tonpiltz floats inside the housing on large o-rings, mechanically isolating it from the housing and waveguide walls. The o-ring supporting the radiating face also prevents the water inside the waveguide from entering the housing. A small accelerometer, PCB Model 352A10,⁷ is embedded inside the piston of the TP-400/A, so that absolute velocity of the radiating face can be monitored. The response of the TP-400 falls off below 5 kHz. If significant low frequency energy was required, an electromechanical shaker, Ling Dynamic Systems model V-203, was used. A custom made piston/tube interface, of the same type used with the TP-400, was used with the V-203.

During normal operation, the two custom built piezoelectric hydrophones described in Appendix B were mounted in the walls of the waveguide tube, 10.16 cm and 12.7 cm from the sample interface. These hydrophones possess a high mechanical input impedance, to minimize perturbation of the field inside the waveguide. Their positions within the tube are specified in the ASTM Standard [99] and are related to the waveguide internal diameter and the maximum frequency of operation. During preliminary testing, Brüel and Kjær Model 8103 and Dapco 1mm needle hydrophones⁸ were used to probe the field inside the waveguide. In all cases, hydrophone signals are conditioned by a multi-channel Brüel and Kjær Nexus 2692 charge amplifier, which provides charge conversion, band-pass filtering, and pre-amplification. During certain preliminary work, additional low and band-pass

⁶Kildare Corporation; One Spar Yard Road; New London, CT 06320; 860-443-7768

⁷PCB Piezotronics, Inc.; 3425 Walden Ave.; Depew, NY 14043; 716-684-0001

⁸Dapco Industries; Ridgefield, CT 06877; 203-438-9696

filtering was provided by a bank of Krohn-Hite Model 34A analog filters.

During impedance measurements, the suitably amplified and filtered hydrophone signals were digitized and processed by the HP 89410A. The calculations described in Section 3.2.2 and in Appendix C were performed on the HP 89410A in realtime. Results were immediately displayed on the analyzer and subsequently saved to disc or transferred to a computer via GPIB. The HP 89410A was controlled manually, but automated operation is also possible over GPIB.

3.5.2 Procedures

A laboratory impedance measurement session is conducted with the waveguide tube in the vertical position. Water, processed by a Barnstead Nanopure filtering system, is degassed using an aspirator pump and carefully introduced into the bottom of the waveguide with flexible tubing. The system is then left to thermally equilibrate. The waveguide is degassed to remove any air bubbles that may have been entrained during the filling process. The tube is then precisely filled to the top using a syringe, again carefully ensuring no bubbles get entrained. This process will be referred to as “filling the tube with standard water,” or as the “standard filling procedure.” All measurements reported herein have been conducted using this standard filling procedure. The importance of a bubble free waveguide can not be overemphasized. The presence of just one bubble somewhere in the waveguide can completely ruin the results. The temperature of the water in the waveguide is then measured. Previously tabulated experimental results then relate the measured temperature to an effective waveguide sound speed, which is input into the HP 89410A’s processing routine. The cross-calibration procedure described in Appendix C is then performed.

Next, the sample holder is filled with the fluid of interest and mounted to the end of the waveguide tube. This must be done underwater, which is the only way to ensure that no bubbles or pockets of air get caught anywhere in the apparatus. This is accomplished with a small container attached to the end of the tube, as shown in Fig. 3.8. The container

is partially filled with processed water and the sample holder is installed while submerged, making sure no air bubbles remain attached anywhere on the apparatus.

The instrument is now ready to perform the measurement. Execution is performed automatically via a program loaded on the HP 89410A. A typical run is described: The frequency range of interest is input, the source activated, and the acquisition parameters set. The HP 89410A sweeps through the frequency range while performing the acquisition, then processes and displays the data on screen. Usually a number of averages are desired to overcome uncorrelated ambient noise and vibration. If so, the process is repeated the required number of times and the display is continually updated with the running average. Finally, the averaged data is stored to disc or transferred to PC.

3.6 Preliminary Results

A number of measurements were performed using the prototype apparatus and procedure described in Section 3.5. These preliminary results are described below.

3.6.1 Verification of EPWM

It was proposed in Section 3.4.3 that the waves traveling in this impedance tube are not truly planar, but if they can be described with a plane wave model, they are “plane enough” for the TFM to work. A non-dispersive, reduced sound speed, combined source-tube propagation model (EPWM) was developed to investigate this hypothesis. The assumptions going into this model, and the model itself, is compared with a series of experiments discussed below. In all cases, measurements were made while the high mechanical input impedance hydrophones were installed in the tube wall.

Waveguide Phase Speed

The first assumption of the EPWM model is that despite elastic waveguide effects, the sound speed inside the tube can be approximated as non-dispersive. The results from

Section 3.4.2 predict only about 0.5% dispersion in the frequency range of interest. An experiment was conducted to verify this. The tube was positioned vertically, and filled with standard water.⁹ Time-of-flight measurements were conducted inside the tube using a single 8103 hydrophone mounted just under the surface of the water, at the open end of the tube. Short pulses of a few cycles, depending on frequency, were sent down the tube. They bounced back and forth between the hard boundary at the source and the soft boundary at the open end. The waveforms were well preserved and the time between similar features of subsequent pulses was easily extracted. Typical waveforms for three frequencies are shown in Fig. 3.9. The results at several frequencies are favorably compared with theory (Eq. 3.72) in Fig. 3.10. The overall variation from 3 kHz to 15 kHz is less than 0.5%, as predicted, and the speeds are just a few percent below the intrinsic medium sound speed. The parameters used in the calculation are given in Table 3.2.

For comparison, calculations were also performed for a similar sized aluminum tube, with inner diameter 4.73 cm and wall thickness 0.49 cm. This tube has a phase speed that varies more than 4% over the same frequency range, and is reduced to around 85% of the free space sound speed.

Radial Profiles

To investigate the planar nature of the field inside the waveguide, radial pressure profiles were made at a variety of frequencies. This information does not enter into the EPWM model but is offered for illustrative purposes. The tube was positioned vertically, and filled with standard water. A Dapco needle hydrophone was scanned across the open end of the tube, just below the water surface, and rms pressure measurements were recorded as a function of position. The results are shown in Fig. 3.11. In a truly plane wave, there would be no radial dependence. Measurements show 1% deviation between the center of the tube and the wall at 5 kHz, less than 2% at 10 kHz, and almost 5% at 15 khz. In order to illustrate the high frequency field, the radial profile at 40 kHz is shown in

⁹See Section 3.5.2 for description of “standard water.”

Fig. 3.12. The transverse modes are fully established at this frequency and the Bessel function dependence of the sound field is clearly visible.

In order to demonstrate the importance of the thick walls used in this design, some additional measurements were made in an aluminum tube with a similar inner diameter, but a much thinner wall. It was the same aluminum tube mentioned in the previous section, and had an inner diameter of 4.73 cm, a wall thickness of 0.49 cm, and a length of 1.5 m. The same procedure was used as with the impedance tube waveguide. The results are shown in Fig. 3.13 for the same three frequencies. As can be seen in the figure, the aluminum waveguide shows about 3 times as much radial variation as does the impedance tube waveguide.

The presence of the second mode, which is predicted from elastic waveguide theory, would render the impedance tube technique unusable. Using a flat piston should cause very little excitation of this mode. The lowest order mode is nearly plane, and the next higher order mode is curved. In addition, the piston imparts no radial motion, further reducing the coupling into the higher order mode. In order to investigate this, one could use a long waveguide and observe propagating acoustic pulses separated by a significant distance. The two modes, which travel at different speeds, would separate and their relative amplitudes could be measured. The impedance tube is not long enough to do this and no evidence of the higher order mode was ever directly observed. In order to further reinforce the absence of the higher order mode, the longitudinal and radial particle displacements inside the wave guide were calculated using Eqs. 3.64 and 3.65, respectively. In order to make comparison between the two components, the particle displacement is normalized by the longitudinal amplitude at the center of the waveguide using

$$A_0 \equiv S_z^L(0, 0, 0) = iq_{0m}\phi_0. \quad (3.77)$$

Therefore, the normalized longitudinal particle displacement is given by,

$$A_z^L/A_0 = J_0(rX_{0m}/b), \quad (3.78)$$

and the normalized radial particle component is

$$A_r^L/A_0 = \frac{iX_{0m}}{q_{0m}b} J_1(rX_{0m}/b). \quad (3.79)$$

The results are shown in Fig. 3.14 for mode 0,0 and 0,1 for a frequency of 7.5 kHz, which is in the middle of the range of interest. The parameters used in the calculation are given in Table 3.2. One can clearly see that the lowest order mode (0,0) is close to plane, with very little radial particle displacement. The 0,1 mode has a strong radial component and deviates from plane by as much as 15%. A flat piston should indeed impart very little energy into the 0,1 mode.

Resonances

EPWM model predictions of resonance in the system are now compared to measurements. This is first done without consideration of the source (Eq. 3.73), and then the source is included (Eq. 3.74). For this experiment, the source was an electromechanical shaker, Ling Dynamic Systems model V-203. It was chosen because the values of its dynamic parameters were available. The tube was positioned vertically, and filled with standard water. A B&K 8103 hydrophone was placed with its tip just under the water surface, at the open end of the tube. This is a very good approximation of a pressure release boundary condition because the 8103 takes up only about 3.5% of the surface, and its tip is impedance matched with water. The HP89410A was used to perform a frequency response measurement. Moving the 8103 up and down a few centimeters, while observing the spectrum, revealed little change. This indicates that the presence of the 8103 was not perturbing the measurement. Model parameters common to both calculations are:

$c_{\text{eff}} = 1463$ m/s, which is the average value over the frequency range of interest, predicted by Eq. 3.72 for the measured water temperature, and measured length of the water column $\ell = 1.50$ m. Results are shown in Fig. 3.15. In part a), the source is not considered, and the predictions are from Eq. 3.73. In part b), the source is considered, and the predictions are from a numerical solution of Eq. 3.74, with the following additional parameters: measured piston mass $m = 0.187$ kg; measured driver stiffness $s = 3500$ N/m; tabulated water density $\rho = 998$ kg/m³; measured cross-sectional area $S = 2.02 \times 10^{-3}$ m². As postulated, it is clear that the dynamics of the source must be considered in order to make accurate resonance predictions. An interesting result is that the acoustics of the tube dictate the slope of the curve, but the dynamics of the source set the absolute value of the resonances.

Frequency Response

It is often considered easier to predict the resonance frequencies of a system than to predict the entire frequency response. With knowledge of the piston velocity, EPWM is capable of predicting the frequency response of the system, including the correct absolute value. The Kildare TP-400/A is used, with its calibrated accelerometer providing the absolute piston velocity. The only fitted parameter is the attenuation. For this preliminary stage, attenuation was accounted for by adding a small constant imaginary part to the wave number in Eq. 3.75. The value was adjusted in order to match the predicted and measured peak resonance levels at an arbitrarily chosen frequency. With no attenuation, the model predicts a physically unrealistic infinite response at resonance. The real part of the wave number was given by Eq. 3.72, so that $k = \omega/c_{\text{eff}} - 0.09i$. Except for the source, the measurement procedure and the other parameters were the same as in the previous section. The acoustic center of the hydrophone was positioned at $x = 1.4852$ m. The results are shown in Fig. 3.16. Good agreement is found across the frequency range, except directly at the resonances from 3 to 7 kHz. This indicates that the attenuation is frequency dependent. Further investigation would be required for complete understanding, but this did not appear to effect the remainder of the measurements. Moreover, the impact

of this phenomenon is certainly reduced during impedance measurements because only the short distance between the sensors and the sample interface is involved. The relative level of attenuation is reduced over the shorter path length. In addition, the inner surface of the prototype tube was fairly rough. The inner surface of the second generation tube was made smooth, which should further reduce the attenuation.

Standing Wave Patterns

In this section, we compare the predicted spatial distribution of the acoustic field inside the waveguide to measurement. The tube was positioned vertically and filled with standard water. An 8103 hydrophone, positioned in the radial center of the tube, was scanned along the length of the tube, starting at the open end and proceeding down.¹⁰ A frequency spectrum was obtained at each position. The measurements at each position were then assembled into a single map of the frequency and position dependent field inside the waveguide. The resulting map is shown in Fig. 3.17. To orient the reader, the single spectrum that was shown in Fig. 3.16 would be represented by a slice out of the left-most part of the map in Fig. 3.17. The parallel horizontal white lines are the resonance frequencies. The curved dark lines are the nulls. In this form, all the data can be seen at once, but it is difficult to get a good physical understanding of the standing wave field in this format. A waterfall plot of the data is presented in Fig. 3.18, which does promote increased physical insight. This is just a frequency subset, so that the details of the individual modes can be seen. The plane wave “organ pipe” modes can now be clearly seen. The first mode is a quarter wavelength long, just below 500 Hz. The second mode occurs at about 800 Hz and is a half wavelength. The fourth mode, at about 1800 Hz, is one wavelength long, etc. This method of presentation provides physical insight but

¹⁰In order to minimize perturbation of the field by the ever increasing presence of the hydrophone and most importantly its cable, a stainless steel sheath was used. This sheath was a hollow tube with outer diameter of 8.00 mm and wall thickness 1.00 mm. One end of the tube was machined to accept the housing of the 8103. During the measurements, the sheath tube is filled with water and degassed. This technique successfully eliminates most of the perturbations caused by the presence of the hydrophone. Monitoring a second 8103 positioned at the open end reveals a small amount of perturbation as the sheathed 8103 is scanned down the tube and this effect is somewhat frequency dependent.

comparison to theory requires a different format.

To compare to theory, slices were taken out of the map in the spacial dimension. Because of the sheath effect described in Footnote 10, comparison to theory required a normalization. The measured results at any given frequency were normalized to the maximum pressure at that frequency, and in the predictions, only the spatial part of Eq. 3.75 was used:

$$p(x, t) = \frac{\sin[k(\ell - x)]}{\cos k\ell}, \quad (3.80)$$

where $k = \omega/c_{\text{eff}}$, and c_{eff} is the sound speed predicted by Eq. 3.76 for the experimental temperature (1450 m/s), and $\ell = 1.50$ m. Note that $(\ell - x)$ is the distance from the open end of the tube. Results are shown in Fig. 3.19 for a variety of frequencies and excellent agreement is found in all cases.

Conclusion: These results show that the effective plane-wave model is indeed capable of describing the acoustics of this real impedance tube. The dispersion is negligible, the radial field dependence is negligible, and the higher order mode is negligible. It appears that plane waves are travelling in the tube, and the pressure can be measured without perturbing the field. *We therefore conclude that the TFM can be successfully implemented with this water-filled impedance tube.*

3.6.2 Verification of Impedance Measurement Technique

The next step was to make actual reflection coefficient measurements with known terminations and to compare these “ground truth” measurements with the predicted values. This was accomplished with the following: a pressure release termination, a water-filled transmission line, two samples of bubbly fluid, and finally the radiation impedance of the open tube itself.

In these measurements, the frequency range is reduced to 5–10 kHz, due to limitations of the Kildare TP-400/A source. Since this is a resonant Tonpiltz type source, its efficiency decreases away from resonance, hence little source level is available below 5 kHz. It has

been shown in previous work [88] that the water-filled TFM technique is particularly sensitive to low signal-to-noise ratios, and that fact is well corroborated here. The results were generally poor below 5 kHz.

Pressure Release Surface

An approximate pressure release surface was obtained in the usual way, which is to have the tube positioned vertically and filled with standard water. No sample holder was used, just the end of the tube, filled carefully to the top. The Appendix C cross-calibration was performed, and then immediately, a forward measurement was performed. The predicted value was obtained by rearranging Eq. 3.6,

$$R = \frac{z_2 - z_1}{z_2 + z_1} = \frac{428 - 1.48 \times 10^6}{428 + 1.48 \times 10^6} = -0.9994, \quad (3.81)$$

where tabulated values for water and air have been used [96]. Typical results are presented in Fig. 3.20. Effect of decreasing source level can be seen at low frequencies.

Water-Filled Transmission Line

The above result was encouraging, but it is not really an independent verification. The simple addition of a water-filled transmission line made possible an independent verification of the complex, frequency dependent quantities. This situation was modeled by rearranging Eq. 3.6 and substituting for z_2 the input impedance of a pressure release terminated transmission line (Eq. 3.50),

$$R = \frac{z_2 - z_1}{z_2 + z_1} = \frac{iz_1 \tan kd - z_1}{iz_1 \tan kd + z_1} = \frac{i \tan kd - 1}{i \tan kd + 1}. \quad (3.82)$$

Following the procedures in Section 3.5.2, with standard water in the sample holder, the reflection coefficient at the interface between the impedance tube and the sample holder was measured. Results are shown in Fig. 3.21. The difficulty associated with

the Appendix C cross-calibration procedure is now apparent. One may notice that this difficulty did not arise in the pressure release case (Fig. 3.20). The reason for this is simple. The problem is automatically solved during the cross-calibration, since it uses a pressure release termination, too. The shaded areas labeled “x-cal. error” in Fig. 3.21 represent the frequency ranges of difficulty. This issue is discussed fully in Appendix C, but a brief explanation is given here. The cross-calibration procedure fails at and near the frequencies where half-wavelengths exist between the open end of the tube and each sensor. At each offending frequency, there is a null at the corresponding sensor, providing no information from which to cross-calibrate, and therefore the cross-calibration function suffers a near-singularity. As a partial solution for these measurements, the cross-calibration function was smoothed by hand near these two frequencies, but since actual cross-calibration data is not available, the measurements suffer. Despite these difficulties, the results appear to be good.

Xanthan Gel

The following step was to fill the sample holder with a Xanthan gel [108], which could be produced with a varying amount of monodisperse bubbles. Since the bubble free gel has similar properties to water, this should give results similar to those of Fig. 3.21. Results for a near bubble free gel (qualitatively called VF₀) are shown in Fig. 3.22. The near unity magnitude and linear progression of phase angle indicates similar transmission line behavior. The zero crossing of phase is shifted relative to the water-filled case due to a difference in sound speed, which is to be expected. It would be appropriate to make a quantitative comparison, but an independent measurement of sound speed in Xanthan gel was not available. Further, it should be noted that a completely bubble free gel sample was unobtainable.¹¹ Some of the blips in the data are most likely due to the presence of unwanted bubbles, but no further quantification is available.

¹¹It proved very difficult not to entrain air when the gel was transferred into the sample holder. It was determined later that the gel could be created in the sample holder, thereby eliminating the problem.

The next two cases are for Xanthan gel mixtures with bubbles. The bubble size distribution of these samples¹² is shown in Fig. 3.23. The distribution is fairly wide but a sharp peak occurs around 96 μm . The absolute values of the void fractions are not known but qualitatively by visual comparison $\text{VF}_2 > \text{VF}_1 \gg \text{VF}_0$. Micrographs of portions of each sample, and the measured complex reflection coefficient from these samples is shown in Fig. 3.24.

What is expected from these samples? Approximate void fractions were calculated from the micrographs by counting bubbles and measuring bubble radii. These estimates yield $\text{VF}_1 \approx 1.5\%$ and $\text{VF}_2 \approx 31\%$. From Eq. 1.15, the resonance frequency of 96 μm radius bubbles is about 34 kHz. The maximum frequency of excitation is 9 kHz, so these bubbles should be in the low-frequency Wood limit regime. From Eq. 1.12, we expect the sound speeds to be $c_1 \approx 90$ m/s and $c_2 \approx 24$ m/s. Consequently we expect $|R_1| \approx 0.85$ and $|R_2| \approx 0.99$, with a phase of $\angle R = 180^\circ$ for both cases. The measurements seem to bear this out quite well.

The same hand-smoothed cross-calibration was used for these measurements, but the cross-calibration errors are not as apparent as in the transmission line cases. This is again because the terminations in the measurements and the calibration were similar.

Radiation Impedance of an Open Tube

One of the most famous analytical results in all of acoustics may be the radiation impedance of an open tube reported by Levine and Schwinger in 1948 [109]. The reflection coefficient for the plane wave component of the velocity potential in a rigid, unflanged tube of *zero wall thickness* is given by $R_0 = -|R_0|e^{2ikl}$, where

$$|R_0| = \exp \left\{ -\frac{2ka}{\pi} \int_0^{ka} \frac{\tan^{-1}(-J_1(x)/N_1(x))}{x[(ka)^2 - x^2]^{\frac{1}{2}}} dx \right\}, \quad (3.83)$$

¹²See Section 3.6.3 for description of bubble size measurement used here.

and

$$\begin{aligned} \frac{l}{a} = & \frac{1}{\pi} \int_0^{ka} \frac{\ln \left\{ \pi J_1(x) [(J_1(x))^2 + (N_1(x))^2]^{\frac{1}{2}} \right\}}{x[(ka)^2 - x^2]^{\frac{1}{2}}} dx \\ & + \frac{1}{\pi} \int_0^{\infty} \frac{\ln[1/(2I_1(x)K_1(x))]}{x[x^2 + (ka)^2]^{\frac{1}{2}}} dx. \end{aligned} \quad (3.84)$$

Here a is the radius of the tube and k is the wave number in the unconfined medium. First-order cylinder functions of real and imaginary argument are designated by J_1 , N_1 and I_1 , K_1 respectively. This result serves as a good ground truth test for the impedance tube instrument, but as mentioned, it is for a vanishingly thin wall.

Another result available in the literature is for a tube with an *infinite flange*. Lord Rayleigh [110] provided an approximate result for this case, but Norris and Sheng [111] improved upon it. Their result is in the form of an infinite series, but a rational function approximation has been provided, which is good for low frequencies ($0 < ka < 3.8$). The infinite flange reflection coefficient is $R_{\infty}(ka) = -|R_{\infty}(ka)|e^{i2kL}$, using the following approximations:

$$|R_{\infty}| = \frac{1 + \alpha ka + \beta(ka)^2}{1 + \alpha ka + (1 + \beta)(ka)^2}, \quad (3.85)$$

where $(\alpha, \beta) = (0.323, -0.077)$ and

$$L(ka)/a = \frac{0.82159 - 0.49(ka)^2}{1 - 0.46(ka)^3}. \quad (3.86)$$

Again, a is the radius of the tube and k is the wave number in the unconfined medium. The tube wall and the flange are both considered rigid.

These two results serve as good bounding cases for instrument verification and an experiment was conducted. The entire apparatus shown in Fig. 3.6, except for the power amplifier, the computer, and the HP89410A was made submersible and deployed in a large fresh water pond.¹³ Measurements of the complex, frequency dependent reflection

¹³Location was Dodge Pond, a U.S. Navy open water test facility in New London, CT.

coefficient of the open ended tube were obtained. The results are shown in Fig. 3.25, along with the bounding predictions of Eqs. 3.83, 3.84, 3.85 and 3.86.

In this case, the original unsmoothed cross-calibration was used, and the results of doing so are visible. Despite this, it is clear that the measurement falls where expected, somewhere between an infinitely thin wall and an infinite flange, but asymptotic to the latter, as the wavelength becomes smaller relative to the wall thickness. It should be noted that in both models the intrinsic medium sound speed applies to the entire domain. In our experiment, the elastic waveguide effect invalidates this assumption by a few percent and is not accounted for. Also, the elastic waveguide model does not account for external fluid loading. No attempt was made to address this theoretically. Instead of using a calculated waveguide sound speed, an in-situ measured waveguide sound speed was utilized to perform the complex reflectivity calculations.

3.6.3 Bubble Production and Characterization

Generation and characterization of bubbly fluid samples is of paramount importance to the success of this work. Partial reproduction of the ocean bubble environment is desired, which requires bubbly fluid samples with void fractions in the range 10^{-5} to 10^{-1} , composed of bubbles with radii in the range 10–100 μm [8]. Further, the meaningful comparison of experiment and theory is only possible with an accurate assessment of bubble cloud properties, primarily overall void fraction and bubble size distribution. In the present section preliminary work in these areas, which served as a test bed for ideas, is discussed.

Spinning Bubble Machine

Small bubbles are somewhat difficult to create. Achieving a degree of control over size is even more difficult. Based on a short paper [112] in a conference proceedings, an interesting bubble generation technique was investigated, centered around the following fact. Air bubbles exiting a small hole in a flat plate, in the presence of tangential flow,

will exhibit a radius inversely proportional to the flow velocity. Chiba and Takahashi, adapting a cylindrical geometry, realized a 1 to 10 variation in measured bubble radius by varying the rotation rate of a submerged cylindrical frit in the presence of a differential pressure across the frit wall. A version of their apparatus was reproduced and testing revealed promising results.

Bubbles in the size range from 10–100 μm radius were generated using a porous ceramic cylindrical frit¹⁴ and by varying the rate of rotation from 1200 to 0 RPM. Another factor of ten radius increase is available at zero rotation rate by increasing the differential pressure by a factor of two. The spinning bubble machine is shown in Fig. 3.7, terminating the impedance tube. One problem with this device is that large bubbles tend to leave the frit where it is secured to the axle with epoxy. These large bubbles “short-circuit” the air flow and reduce the number of small bubbles, lowering the effectiveness of the technique. The spinning bubble machine was ultimately not used for the impedance tube measurements discussed in Chapter 4. The technique was modified and adapted to create large volumes of small bubbles, and used for the scattering experiments discussed in Chapter 5.

Optical Bubble Size Characterization

The bubble size characterizations reported in this chapter were performed using a Leica stereo microscope with an integrated CCD camera, shown in one possible operating position in Fig. 3.7. Images were monitored with a Sony display, acquired using a Macintosh Quadra 840A/V, and processed with NIH Image software,¹⁵ which was configured to automatically process images for individual bubble area in the form of raw pixel count. A calibration then related pixel size to absolute units of area. A shape assumption was made: The bubbles appeared to be oblate spheroidal, from which effective spherical radius was extrapolated.

¹⁴Porosity 45%, maximum pore size 2.5 μm ; Supplier: Soilmoisture, 810 S. Kellogg Ave., Goleta, CA 93117; (805) 964-3525.

¹⁵NIH Image is freeware available from the National Institutes of Health website: <http://rsb.info.nih.gov/nih-image/>.

Fluid Static Void Fraction Technique

The only preliminary void fraction measurement scheme investigated was a fluid static technique, which was used in the measurements described in Appendix A. Bubbly fluid was introduced into a vertical cylindrical water column of known bubble-free height ℓ . A small float attached to a mechanical pointer indicated the change in the column height $\Delta\ell$ via fiducial marks, from which void fraction was directly obtained using

$$\beta = \frac{\Delta\ell}{\ell + \Delta\ell}, \quad (3.87)$$

for the constant cross-section column. Although this method is a direct measurement of void fraction, its accuracy is diminished at low void fractions due to diminishing $\Delta\ell$, and its precision deteriorates at high void fractions due to the turbulent air-water interface produced at high airflow rates.

3.7 Second Generation Impedance Tube System

Hopefully the success of the preliminary measurements has convinced the reader that the water-filled impedance tube has been practically realized. It was shown that with proper design, the elastic waveguide effects were minimized. This rendered an effective plane wave theory adequate to describe propagation in the tube. Therefore, standardized techniques produced accurate impedance measurements of bubbly fluids. The cross-calibration problem was subsequently solved using an existing technique [113]. In addition, a number of papers were found in the literature which reported error analyses for the TFM technique [114, 115, 116, 117, 118]. Using these works and the experience gained with the prototype device, a second generation impedance tube system was built, which is discussed below.

3.7.1 Theory of Cross-Calibration

In order to compensate for the complex response inequality between the two sensors, the TFM standard document [99] prescribes a cross-calibration procedure which requires a “non-reflecting” termination and the switching of the two sensors. A practical termination for use in water was not found. Furthermore, for a water-filled tube, and for operation underwater, the switching procedure is cumbersome and can be physically difficult to accomplish. The initial technique was not sufficient, as discussed in Appendix C. A technique known as the two-sensor-three-calibration (TMTC) procedure was found in the literature [113] and it was adopted.

The quantity of interest is the sample impedance, which is obtained from a transfer function measurement and Eq. 3.43, repeated here for convenience,

$$\frac{z_2}{z_1} = i \frac{H_{12} \sin k\ell - \sin k(\ell - s)}{\cos k(\ell - s) - H_{12} \cos k\ell}. \quad (3.88)$$

where $H_{12}(f) = \bar{H}_{12}(f)/H_c(f)$. \bar{H}_{12} is the actual measurement made during an impedance run, and H_c is the cross-calibration factor obtained from the standard cross-calibration procedure. This procedure described in the standard [99] results in an accurate absolute measurement, requiring no further calibration.

Instead of obtaining $H_c(f)$ in the forward manner,¹⁶ we obtain it in a reverse manner utilizing three different known impedance terminations. In fact, the TMTC method is actually more general than standard TFM in that it does not rely upon a deterministic plane wave interpretation of the energy within the impedance tube. Instead, it assumes that the signals s_1 and s_2 received by the two sensors are linear functions of the termination impedance and uniquely determined by the acoustic pressure p and velocity u at the termination location in the following way:

$$s_1 = \alpha p + \beta \rho c u, \quad (3.89)$$

¹⁶“Forward manner” indicates without comparison to some known impedance.

$$s_2 = \gamma p + \delta \rho c u, \quad (3.90)$$

where α, β, γ , and δ are unknown parameters that depend upon the geometry of the system, the response of each sensor, and the density ρ and sound speed c within the impedance tube. Note that in this formulation, the sensor positions are reversed with respect to Eq. 3.88. This is done only for mathematical convenience in the expressions that follow and Eq. 3.88 can also be written for the switched case. Utilizing the definition of specific acoustic impedance $z = p/u$ and defining y as the ratio of the two signals, the result is

$$y = \frac{s_2}{s_1} = \frac{\gamma z + \delta \rho c}{\alpha z + \beta \rho c}, \quad (3.91)$$

which yields

$$\frac{z}{\rho c} = \frac{-\beta y + \delta}{\alpha y - \gamma} = \frac{Ay + B}{y - y_0}, \quad (3.92)$$

where $A = -\beta/\alpha$, $B = \delta/\alpha$ and $y_0 = \gamma/\alpha$. Note the similarity to Eq. 3.88.

The values of the three unknown coefficients are obtained by the measurement of three known terminations. In the present work, the terminations are pressure release terminated transmission lines, i.e., water-filled tubes of three different lengths, with impedances $Z', Z'',$ and Z''' , each given by $Z^{(i)} = z/\rho c = i \tan k d_i$, where k is the propagation constant and d_i is the length of the termination. The lengths d_i are chosen such that both resonance and anti-resonance of the termination are avoided for the frequency range of interest. This way, precise knowledge of the loss mechanism is not required. See Fig. 3.26 for a demonstration of this effect. One measures the transfer function $y^{(i)}$ for each of the known terminations $Z^{(i)}$. Subsequently, measurement of the transfer function y for any unknown termination yields its impedance in terms of the three calibration transfer functions:

$$\frac{z}{\rho c} = \frac{Z' Z''' (y' - y''')(y - y'') + Z' Z'' (y'' - y')(y - y''') + Z''' Z'' (y''' - y'')(y - y')}{Z''' (y'' - y')(y''' - y) + Z' (y''' - y'')(y' - y) + Z'' (y' - y''')(y'' - y)}. \quad (3.93)$$

Recall that the sensors are switched in this formulation, therefore $y = H_{21}$, not H_{12} . In practice, the only difference is that the cables are switched at the signal analyzer inputs. This result has been attained without reliance on any particular assumption about the fields at each sensor, except that they are linearly and uniquely related to the impedance at the plane of interest. This is fulfilled as long as the waves are one-dimensional, but sensor perturbations are allowed. If one assumes no sensor perturbations, it is shown from first principles in [113] that Eq. 3.92 is indeed equivalent to Eq. 3.88. This technique overcomes the difficulty that was encountered in the Appendix C technique. If a null exists at one of the sensors at a certain frequency in one calibration, it will be not be present in the other two calibration measurements. In such a way the denominator of Eq. 3.93 remains non-zero and continuous cross-calibration information is obtained at all frequencies of interest.

3.7.2 Second Generation Apparatus

The prototype impedance tube was longer than necessary so that propagation measurements could be performed in it. As discussed in the standard [99], the overall length should be minimized in order to reduce the effects of attenuation and noise, yet the prescribed distance between the sensors should be maintained according to Eq. 3.42. The distance from the source to the nearest sensor should be greater than one tube diameter. This minimizes the effect of any higher order modes which could be generated due to source inhomogeneities, such as a non-planar piston. For the same reason, the distance from the termination reference plane to the nearest sensor should also be greater than one tube diameter. The tube was redesigned with these parameters in place, but the inner and outer diameters used in the prototype tube were kept nominally the same, since these are the dimensions which minimized elastic waveguide effects. The inside surface of the tube and the sample holder were machined smooth and made concentric to one another. The dimensions of the second generation tube are shown in Fig. 3.27. The sample holder and the impedance tube are bolted together using flanges and eight 3/8"–16 UNC bolts. An

O-ring seal is used between the two sections. If the fluid of interest is different than the liquid inside the impedance tube, a thin mylar membrane is sandwiched between the two sections. If the fluid of interest is the same throughout, no membrane is needed.

A supporting structure was fabricated out of stamped steel structural members. This framework supported the tube and also provided mounting space for secondary equipment. A schematic of the system is shown in Fig. 3.28. It was found that sub-millimeter water level accuracy was needed for accurate calibration, therefore the water level in the tube was measured using a bifilar measuring microscope. A bubble level was mounted on the tube flange or at the top of the tube to insure a horizontal water surface. The feet of the framework could be adjusted to maintain a level orientation. The temperature of the system was monitored using a thermocouple and a digital multimeter. The thermocouple bead was attached to the outside wall of the impedance tube, as shown in the figure. Water could be removed from the system through a 4 mm I.D. Tygon drain tube attached to a fitting just above the source. The calibration lengths were actually set by removing a specified mass of water. A small pinch valve controlled the flow into a milligram balance. The outlet of the Tygon drain tube was kept under water, to insure accuracy and repeatability. As in the prototype apparatus, the custom made hydrophones described in Appendix B were mounted in the wall of the impedance tube at the positions labeled 1 and 2. The signal generation, and data acquisition and control were unchanged from the prototype apparatus, except for the addition of a more powerful Crown CE-1000 power amplifier. The B&K 8103 was used at the top of the tube for a variety of monitoring purposes.

3.7.3 Cross-Calibration and Operational Procedure

In this section, the cross-calibration and standard operational procedures will be discussed. The calibration is rather sensitive to the speed of sound in the tube, and therefore sensitive to temperature. Normally, a calibration is performed at the beginning of each work day. If the temperature changes by about 0.5 °C, a new calibration must be performed. The

tube is filled with pure, degassed water, preferably the night before. This insures temperature equilibrium, and the dissolution of any air trapped between the sample holder and the tube, around the source piston or around the phones. The water level is obtained to approximately 0.05 mm accuracy by using the bifilar microscope to measure the distance from the water surface to the top of the tube. The sound source is driven with 5–9 kHz periodic chirps or 5–9 kHz band-limited pseudo-random noise. The chirps are useful for single short-time measurements, and the noise is useful for time-averaged measurements. The transfer function between the two wall-mounted phones is measured, and from the position of nulls and peaks, the in-situ sound speed can be calculated based on the water level. This transfer function is also saved for use as a ground truth measurement. Typically, in the range 5–9 kHz, using the 14 cm sample holder, a single peak and two nulls are present, and average sound speed is used, with variation between them of the order 0.3%. This variation is in agreement with that predicted from Eq. 3.72. This average sound speed c_{eff} is subsequently used in the calibration and operational calculations.

The system is now ready for the three calibration measurements to be performed. The lengths are selected to avoid any extrema, as previously mentioned, and typical lengths are 1.5, 2.5 and 3.5 cm. The appropriate volume of water is removed by monitoring the milligram balance and then a transfer function is measured for each length. The excitation used during the calibration is the same excitation that will be used during the actual measurement. In order to minimize bias error in the transfer function estimate, the resolution bandwidth should be maximized. Typically, 1601 or 801 frequency points are acquired, which results in resolution bandwidths of 5 Hz or 2.5 Hz, respectively. The transfer functions are saved, along with the measured coherence function, for further processing and inspection. Once the transfer functions for the three calibration impedances have been measured, the apparatus is ready for operational measurements.

An efficient way to verify that the calibration was done correctly is to use the first transfer function measurement as a ground truth test case. This corresponds to a fourth length of fluid, which can be considered a pressure release terminated transmission line. The

length of this termination is known from the microscope measurement. The impedance of this or any subsequent measurement is then calculated using the three calibration measurements and Eq. 3.93.

If a membrane is used to separate the fluids, the length of the calibration terminations must be set in a different way, because the membrane would prevent the fluid from flowing out of the drain. The mass removal system can still be used, but the fluid must be taken out of the top of the tube with a pipette, for example.

3.7.4 Verification of Impedance Tube System

The pressure release terminated transmission line has a complex, frequency dependent input impedance. Short lengths are used as calibration terminations, because no extrema are encountered. A longer length does contain extrema. Such a termination serves as a difficult test for any impedance tube, including commercially available air tubes, because its value can vary over several orders of magnitude. This termination has been chosen to verify the operation of the impedance tube system because it is a rigorous test, and also because a good model is available for comparison. Recall that acoustic losses do not impact the calibration, but they will be present in the ground truth measurement. The thermal and viscous losses in the tube will be modeled with a complex wave number given by

$$k^2 = \frac{\omega^2}{c^2} \left(1 + \frac{\epsilon(1-i)\sqrt{2}}{R} \sqrt{\frac{c}{\omega}} \right), \quad (3.94)$$

where R is the inner radius of the tube, and ϵ is a function of the heat conductivity and viscosity of the water inside the tube [113]. Typical values for water are of order $\epsilon = 10^{-4}\sqrt{\text{m}}$. With the wave number thus described, the impedance looking into the pressure release terminated transmission line is given by

$$\frac{z}{\rho c} = i \tan kd_0, \quad (3.95)$$

where ρc is the specific acoustic impedance of the water that fills the tube, and d is the length of the transmission line. A ground truth measurement is shown in Fig. 3.29, compared with the prediction given by Eqs. 3.94 and 3.95, using a fitted value of $\epsilon = 5 \times 10^{-5} \sqrt{m}$. The remaining parameters used in the calculations are given in Table 3.3. Pseudo-random noise excitation was used, with a Hann window and a resolution bandwidth of 5 Hz. To the author’s knowledge, results like these are unique. Rarely is there seen this level of precision between neighboring frequency bins and such good agreement with theory. This statement is true for air-filled impedance tubes and especially true for the water-filled case. For additional verification, a different ground truth case is shown in Fig. 3.30, where the termination length d_0 was 8.40 cm.

3.7.5 Additional Verification with Single Sensor Method

The skeptical reader may consider the preceding verifications to be unconvincing because the calibration and the verification both use the same type of termination. This concern is understandable, although not warranted. The impedance presented by the 13.98 cm ground truth transmission line could not be more different from the three calibration impedances, due to the complete lack of any extrema in the calibration responses. In any case, an additional measurement obtained from the single sensor method is presented in Fig. 3.31. The theoretical calculation is the same as in the previous section but with the parameters in Table 3.4. Note that this measurement has absolutely no calibration whatsoever and is obtained directly from Eqs. 3.44 and 3.43. It serves to further validate this impedance tube system, and also demonstrates an increased frequency range. As the frequency goes down, the optimum spacing between the two sensor positions increases. The wall-mounted sensors are optimized for the 5–9 kHz range and are too close together for lower frequencies. Therefore, a sheathed 8103 was inserted into the open end of the impedance tube and scanned between two more optimal positions. These results are very good as well, especially in the magnitude. There is some fluctuation in the phase that was not present in the calibrated measurements, and the phase transition is not captured

quite as well. These small deviations may be caused by the presence of the hydrophone sheath throughout the sample holder and the impedance tube. Certainly, this is not an optimal situation. If the single sensor method were to be pursued in full, the sensor would have to be mounted from the source end of the tube. The measurements presented in Figs. 3.29, 3.30 and 3.31 indicate that the second generation impedance tube system is capable of performing precise and accurate measurements. These are perhaps even state-of-the-art measurements, at least in the open literature. There are impedance tube systems in U. S. Navy facilities which may rival the present system, but results from those systems are not readily available for comparison.

3.8 Measurement Error Analysis

In this section the error and uncertainty in the measured impedance obtained by the second generation system will be discussed. As mentioned previously, the literature contains a number of papers on this very topic [114, 115, 118]. This discussion will follow that given by Bodén and Åbom [115]. Exact formulations for the prediction of errors do not exist for the measurement of impedance using the transfer function technique, although approximations do exist. Another issue that makes the absolute quantification of errors in impedance measurement difficult is the absence of any absolute reference standard. By absolute reference standard, something like the platinum-iridium bar kept as the reference standard for the meter is inferred. Typically in the literature one finds comparisons between different measurement techniques, and sometimes comparison to theory, as has been done here, but there is no absolute standard to compare to. In any case, the errors can be divided into two major classes: errors associated with the measurement of the transfer function y , and errors associated with the other measured quantities used in the subsequent calculations, such as speed of sound and various lengths.

3.8.1 Errors in the Transfer Function Measurement

Measurement of the transfer function is subject to bias errors and also random errors, if a non-deterministic signal is used for excitation. In this work, pseudo-random noise and deterministic periodic chirps have been used. The errors discussed in this section do not include the amplitude or phase error in the actual voltage measurement. Those errors will be included later.

Bias Errors

Estimation of the transfer function is subject to a number of bias errors, including those caused by noise, nonlinearities, and lack of sufficient spectral resolution. As long as the measured coherence function γ^2 is kept near unity, these errors are minimized [119]. As mentioned previously, when using a highly reflective termination nulls in the measured acoustic field can be present at certain frequencies, thereby lowering the coherence function. In such a case, it is useful to have an estimate of the error. As long as the coherence function is greater than approximately 0.5, resolution bias error will dominate. An approximate expression for the maximum normalized bias error ϵ_b is [115]:

$$|\epsilon_b[|y|]| \lesssim \frac{8\pi^2 \Delta f^2 |R_\ell| \ell^2}{3c_1^2 (1 - |R_\ell|)^2}, \quad (3.96)$$

where $|y|$ is the magnitude of the measured transfer function y , Δf is the frequency resolution of the measurement, $|R_\ell|$ is the magnitude of the measured termination reflection coefficient, ℓ is the distance from the termination to the furthest sensor, c_1 is the speed of sound inside the impedance tube, and the bars around ϵ_b indicate the absolute value. For the phase of the transfer function, the maximum bias error β is

$$|\beta[\varphi]| \lesssim |\epsilon_b[|y|]|, \quad (3.97)$$

in units of radians, where φ is the phase angle of y in radians, and $|\epsilon_b[|y|]|$ is given by Eq. 3.96. Again, the bars around β indicate the absolute value. The error estimate for phase angle is based upon geometric arguments in the complex plane, and is only valid for $|\epsilon_b| \ll 1$. Once the calculation is made, the units can be changed to degrees if desired. As one can see, the bias error is dependent upon the type of termination being measured. The typical maximum bias error attained in this work is shown in Fig. 3.32, where the termination was a pressure release terminated transmission line of 14 cm length, with a measured impedance like that shown in Fig. 3.29. Note that these estimates are for the maximum bias error, as found at frequencies where the coherence function is low. Away from these frequencies where the coherence function is near unity, the bias error will usually be much smaller than the other errors [119].

Random Errors

Measurements made with random excitation are susceptible to random errors. The error depends on the number of averages and the measured coherence function, not on the nature of the termination. The normalized random error e_r in the transfer function estimate is given approximately by [119]

$$\epsilon_r[|y|] \approx \left[\frac{1 - \gamma^2}{2n\gamma^2} \right]^{1/2}, \quad (3.98)$$

where γ^2 is the measured coherence function and n is the number of averages. The variation in phase due to random error is given by

$$\sigma[\varphi] \approx \epsilon_r[|y|], \quad (3.99)$$

where σ is the standard deviation in radians, φ is the phase angle in radians of the measured transfer function y , and $\epsilon_r[|y|]$ is given by Eq. 3.98. This error estimate for phase angle is based upon the same geometric argument in the complex plane, and is only

valid for $|\epsilon_r| \ll 1$. The random error estimated for the measurement of a 14 cm length pressure release terminated transmission line is shown in Fig. 3.33, where n was 100 and γ^2 was the measured coherence function. Notice that the error is small except for at three sharp peaks near 5.5, 6.1 and 8.25 kHz. At these frequencies, the coherence function has sharp notches due to acoustic pressure nulls at the measurement positions. Increasing the number of averages does little to lower these errors when the coherence function is low. Increasing the signal level, or using coherent averaging does decrease the error.

3.8.2 Errors Propagated Through Measured Quantities

Examination of Eq. 3.93 reveals the other measured quantities that can influence error in the measurement of impedance. The lengths d_i of the calibration terminations, the speed of sound c , both alone and within the wave number k , and the density are inputs to the calculation. Except for the ρc on the left hand side, these errors effect the measurement of impedance differently than the errors discussed in the previous section. Examination of the equivalent Eq. 3.88 reveals that except for the ρc , everything else appears as the argument of an exponential function. Therefore, errors in c and d_i cause both the magnitude and the phase of the measured impedance to be shifted in frequency relative to their correct values. Depending on the application, it is often perfectly acceptable to render error in the quantity ρc inconsequential by considering a normalized result $z/\rho c$, which has been done in this work. Therefore, this discussion will be focused on the effects of c and d_i as they present in the argument of exponential.

In this work, the speed of sound was obtained by using the frequency of nulls that appeared at the positions of the wall-mounted hydrophones. The holes for the hydrophones were machined with an accuracy of ± 0.025 mm, but a greater uncertainty lies in the position of the acoustic center of the hydrophone. The active element was 6.35 mm in diameter, and it was positioned with 0.025 mm accuracy, but due to near field diffraction the acoustic center of the hydrophone changes with frequency. The uncertainty in the location of the acoustic center was conservatively estimated to be ± 0.5 mm, based upon

the results of Bodén and Åbom [115]. The resolution of the frequency measurement was minimized during the sound speed measurement and was no greater than $\Delta f = 0.5$ Hz. Combining these uncertainties in $c = \lambda f$ one finds an uncertainty in measured sound speed c of ± 0.22 %.

The calibration termination lengths d_i were obtained through calculation based on the mass of the water removed from the sample holder in a very carefully constructed apparatus that used a milligram balance. The volume was calculated from a temperature dependent density table [120] and the length of water column removed was then calculated from the measured diameter of the tube. Finally, d_i was obtained by subtracting the removed length from the measured length of the sample holder. The dimensions of the precision machined sample holder were known to an accuracy of 0.025 mm. The combined uncertainties of the various contributing factors lead to an uncertainty in d_i of ± 0.09 %.

The uncertainty in c and d_i express themselves in a complicated way through Eq. 3.93, which is best explored by direct calculation using measured data and by varying the quantities by the uncertainties discussed above. The maximum error was calculated and its envelope is shown in Fig. 3.34. It is clear that the uncertainties are manifested most severely around the resonance and antiresonance of the termination, near 5.75 and 8.6 kHz, respectively. It is also clear that the error increases with frequency. There is very little error away from these frequencies. This plot of maximum error is somewhat deceiving because the curves are actually shifting in frequency relative to one another and not changing very much in value otherwise. To demonstrate, the calculated impedances themselves are shown in Fig. 3.35. The solid curve shows the actual measurement using the measured values of c and d_i . The dashed curves to the left and right represent the maximum deviation as obtained from the uncertainties in c and d_i , which amount to shifting the solid curve through a range of approximately 12 Hz.

Another way to envision these two measures of error is the following: Fig. 3.34 represents the maximum absolute error. If the absolute value of impedance at a given frequency is the quantity of interest, the maximum error at that frequency is shown in Fig 3.34. Al-

ternatively, if one wanted to know the maximum impedance of this termination, then the relative error could be taken from Fig. 3.35. Here it is seen that the uncertainty in the maximum impedance is really only 2.9 dB, and the frequency of that maximum impedance is known within a 12 Hz range of frequencies.

3.8.3 Total Uncertainty in Impedance Measurement

It has been shown that the uncertainty in the measured impedance is a complicated function of the frequency and the type of termination. The maximum uncertainty for a variety of errors has been given independently. Ultimately, the total error in a measurement is the desired quantity. It is not possible to give a general analytical result, but a worst case scenario can be examined and a maximum total error can be estimated by assuming that all of the constituent errors present themselves at their maximums. In this case, it is more realistic to consider the relative error, such as that presented in Fig. 3.35. Therefore, using Figs. 3.32, 3.33 and 3.35 as a guide, the maximum relative error in magnitude and then phase will be calculated. At this time, the actual voltage measurement uncertainty inherent in the spectrum analyzer will be included.

For the magnitude:

1. From Fig. 3.32, the maximum error is 9 % at 5.0 kHz which is equivalent to 0.75 dB.
2. From Fig. 3.33 the maximum error is 6 % at 5.5 kHz which is equivalent to 0.51 dB.
3. From Fig. 3.35 the maximum error is 2.9 dB.
4. According to a recent factory calibration the magnitude error between channels for the analyzer used in this work is less than 0.07 dB

Therefore the maximum total error in magnitude is 4.23 dB.

For the phase:

1. From Fig. 3.32, the maximum error is 5.25 degrees.

2. From Fig. 3.33, the maximum error is 3.4 degrees.
3. From Fig. 3.35, the relative error is negligible. The uncertainty is related to the frequency at which the transition from +90 to -90 occurs.
4. According to a recent factory calibration the phase error between channels for the analyzer used in this work is less than 0.36 degrees.

Therefore the maximum total error in phase is 9.01 degrees.

It is unlikely that a single measurement point would exhibit the maximum error. To present another possibility, the total average error was considered. Contributions due to bias, random and calculation input uncertainty were added up. The average error for each component was calculated by summing the discrete error values at each frequency and dividing by the total number of bins. This was done for the single error curve shown in Fig. 3.33 and for the difference between the envelope curves shown in Fig. 3.34, but the only the maximum is available for the bias error. In order to estimate the average *bias* error, the ratio between the average and the maximum *random* error was used. This ratio was applied to the maximum bias error to obtain an estimate of the average bias error. The individual magnitude contributions were converted to dB, and the phase contributions were left in units of degrees. The errors inherent in the actual voltage measurement are again taken from a recent factory calibration. Since the errors reported in the calibration were maximum values, a conservative approach was to take half the maximum error as the average error. The results are given in Table 3.5, and the totals are also stated here: the total average error in magnitude was 0.190 dB and the total average error in phase was 0.42 degrees.

3.9 Comparison to Other Systems

The reflection coefficient measured from an water-air interface was used to compare the performance of the second generation impedance tube to the performance of other water-

filled impedance tubes. The water-filled transmission line would also have been a useful termination for comparison, but no such measurements were found in the literature. The only other types of measurements found were of various slabs of material: wire mesh, perforated metal, compliant materials, etc., which would have been difficult to reproduce exactly. Therefore, the water-air interface was chosen as the most reliable means to compare different systems. Even in this case, only two other water-air interface measurements were found [47, 86], from 1947 and 1983, respectively.

The reflection coefficient obtained using the present system is shown in Fig. 3.36. Near the 9 kHz frequency range, the measurement begins to suffer from non-optimum spacing, which causes the deviations seen in both phase and magnitude. The plots were scaled to emphasize behavior very near the expected values (very close to unity for magnitude and 180 degrees for phase). Therefore, the deviations near 9 kHz go off the plot slightly. In order to compare this measurement to the two others that were found in the literature, the phase and magnitude values were averaged across the 5–9 kHz frequency range to obtain mean values. The standard deviations were then obtained to create error bars. This was done in the 5–9 kHz frequency range for both phase and magnitude measurements from [86, p. 91], and only for the phase from [47, p. 429], which did not report the magnitude. These three representative results are compared in Fig. 3.37. It is clear that for this particular case, the present impedance tube produces the most accurate and precise measurement. The increase in precision is most likely attributable to the availability of more advanced electronics for signal excitation, control, and data acquisition, as compared to 1983 and 1947. The increased accuracy is most likely due to an increased degree of attention paid to the minimization of elastic waveguide effects, and to the design of the present pressure sensors, which have very little effect on the acoustic field in the tube.

$c_1 = 1491.5 \text{ m/s}$	$c_l = 6300 \text{ m/s}$	$\rho_L = 998 \text{ kg/m}^3$	$b = 2.381 \text{ cm}$
–	$c_t = 3173 \text{ m/s}$	$\rho_W = 2800 \text{ kg/m}^3$	$d = 2.858 \text{ cm}$

Table 3.1: The aluminum/water waveguide parameters used in the calculations shown Fig. 3.5 are tabulated.

$c_1 = 1491.0 \text{ m/s}$	$c_l = 5640 \text{ m/s}$	$\rho_L = 998 \text{ kg/m}^3$	$b = 2.54 \text{ cm}$
–	$c_t = 3070 \text{ m/s}$	$\rho_W = 7974 \text{ kg/m}^3$	$d = 5.08 \text{ cm}$

Table 3.2: Physical parameters of the prototype impedance tube are shown.

$d_1 = 3.54 \text{ cm}$	$d_3 = 1.47 \text{ cm}$	$R = 2.589 \text{ cm}$	$c = 1457.1 \text{ m/s}$
$d_2 = 2.55 \text{ cm}$	$d_0 = 13.98 \text{ cm}$	$T = 24.05 \text{ }^\circ\text{C}$	$\epsilon = 5 \times 10^{-5} \sqrt{\text{m}}$

Table 3.3: The table contains the values used to make Fig. 3.29.

$s = 3.54 \text{ cm}$	$\ell = 6.80 \text{ cm}$	$R = 2.589 \text{ cm}$	$c = 1456.1 \text{ m/s}$
–	$d_0 = 14.00 \text{ cm}$	$T = 23.90 \text{ }^\circ\text{C}$	$\epsilon = 4 \times 10^{-4} \sqrt{\text{m}}$

Table 3.4: The table contains the values used to make Fig. 3.31.

Error Type	Bias	Random	Input	HP 89410 A	Total
Fig.	3.32	3.33	3.34	–	
magnitude (dB)	0.021	0.014	0.12	0.035	0.190
phase (deg.)	0.14	0.093	0.0072	0.18	0.42

Table 3.5: Average measurement error for the second generation impedance tube.

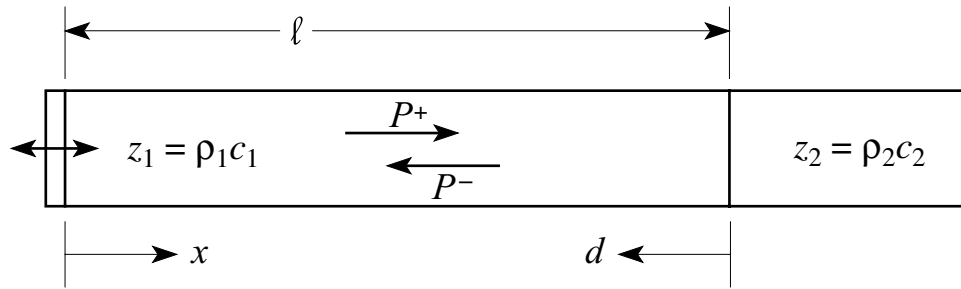


Figure 3.1: A schematic of standing wave method is shown.

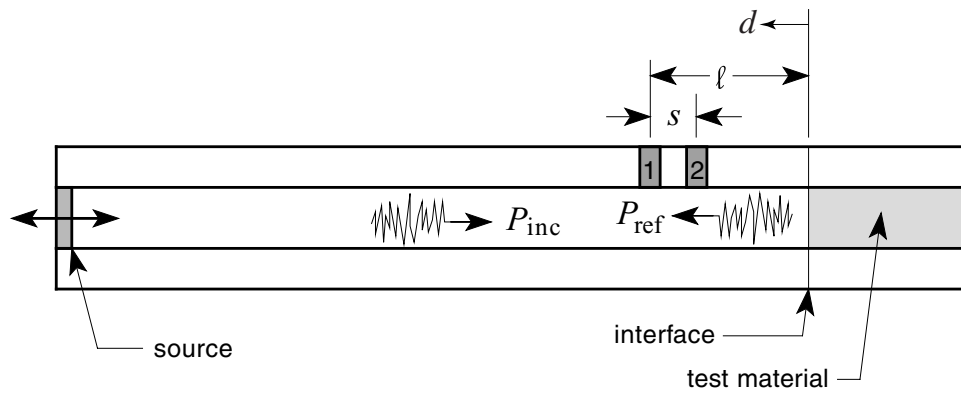


Figure 3.2: Schematic of transfer function method is shown. Acoustic pressure sensors are placed at positions 1 and 2.

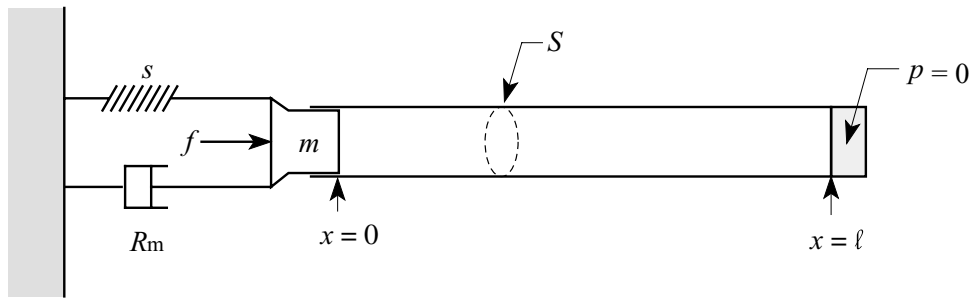


Figure 3.3: A schematic of the combined source-tube system is shown.

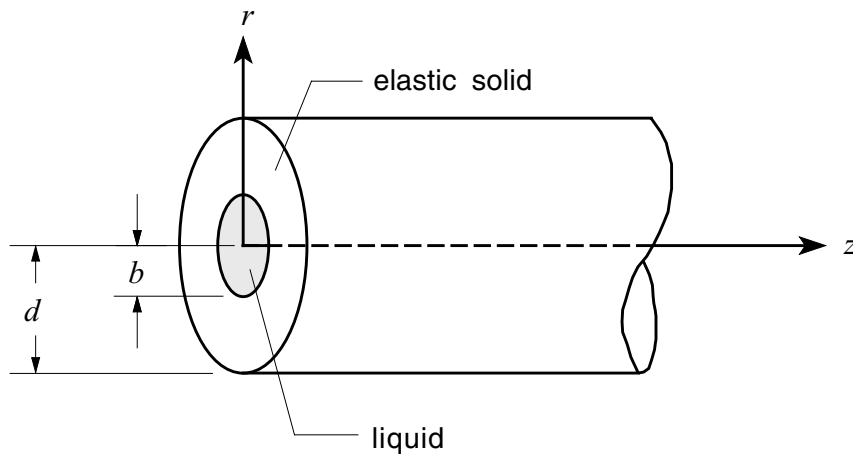


Figure 3.4: Geometry used in development of the elastic waveguide propagation model. A liquid cylinder is surrounded by an elastic solid cylinder of inner radius b , and an outer radius d . The system is symmetric about the z -axis.

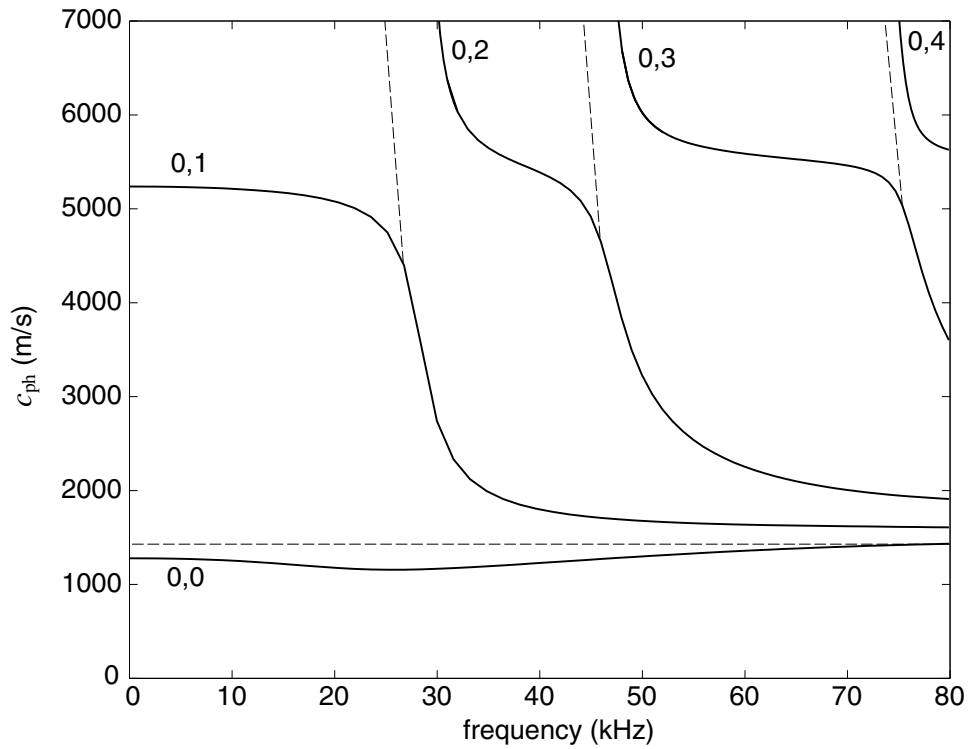


Figure 3.5: Dispersion curves for an elastic waveguide are shown with solid lines. They were calculated using Eq. 3.72 and the physical parameters listed in Table 3.1. Rigid waveguide curves for the same parameters are shown approximately with the dashed lines.

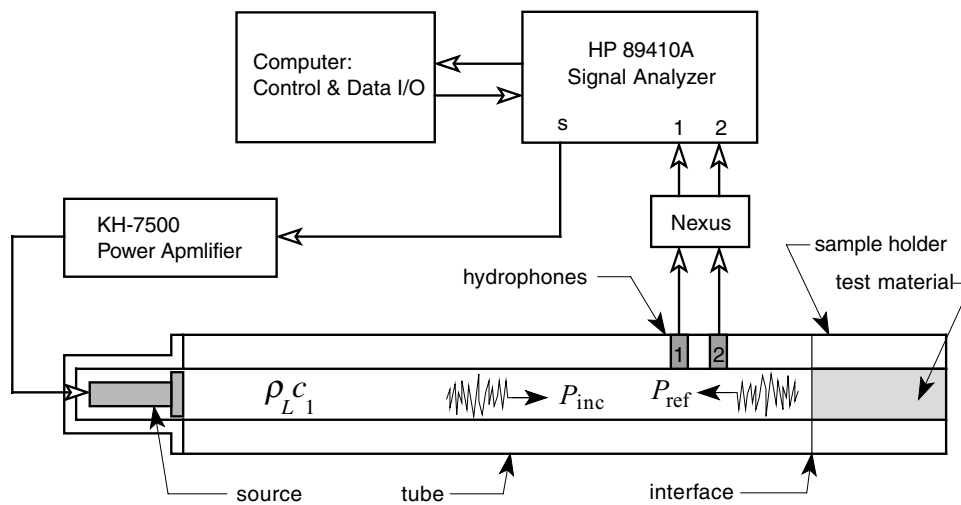


Figure 3.6: A schematic of the prototype experimental apparatus is shown.

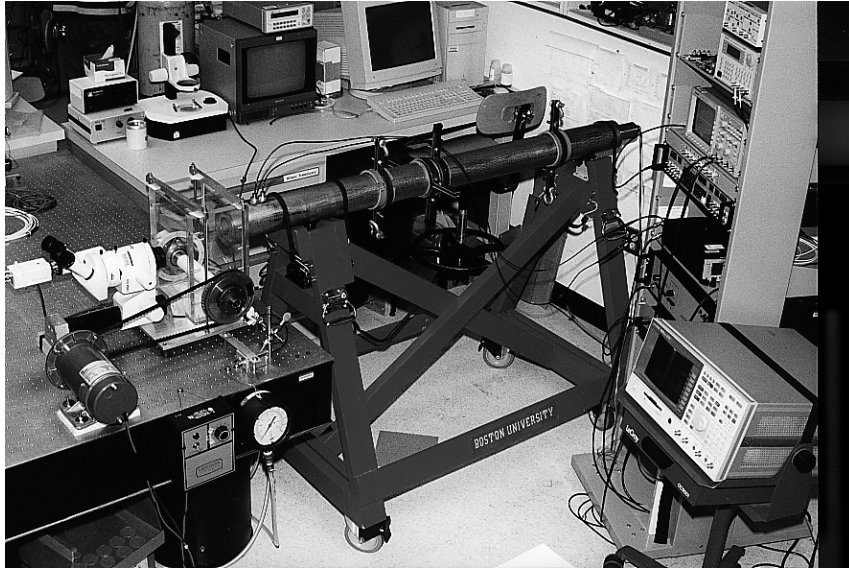


Figure 3.7: A photograph of horizontal laboratory deployment is shown.

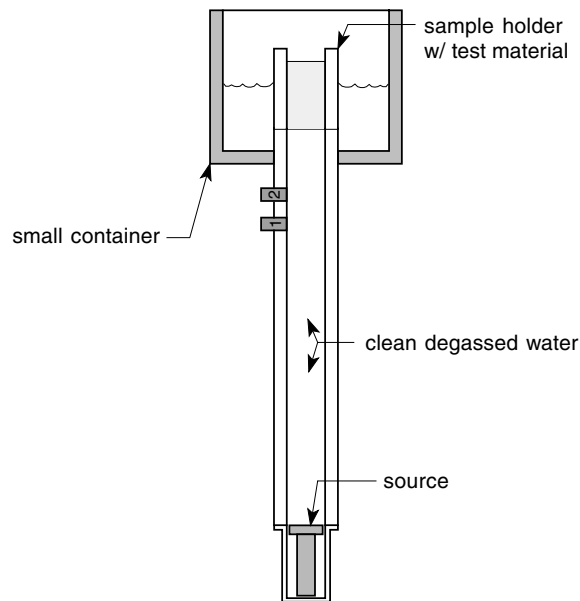


Figure 3.8: A schematic of vertical deployment is shown.

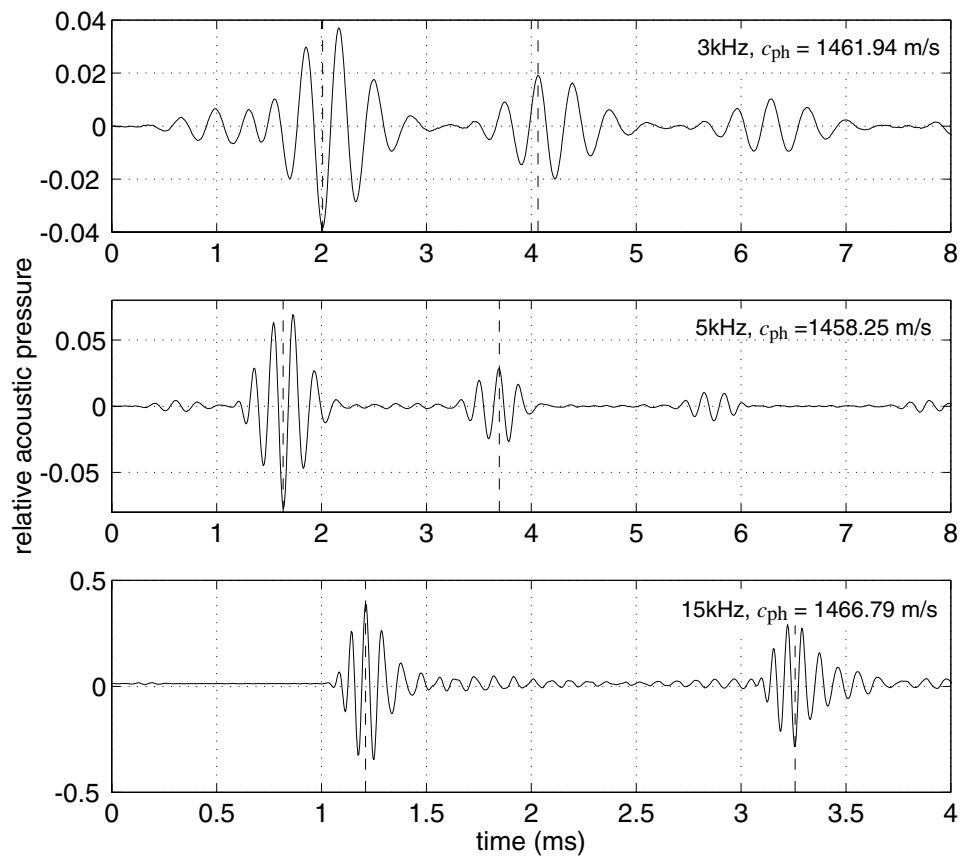


Figure 3.9: Typical waveforms from the time-of-flight sound speed measurements are shown. Dashed vertical lines indicate corresponding parts of waveforms and hence the time increment. The corresponding length was 1.502 m, for a round trip of 3.004 m.

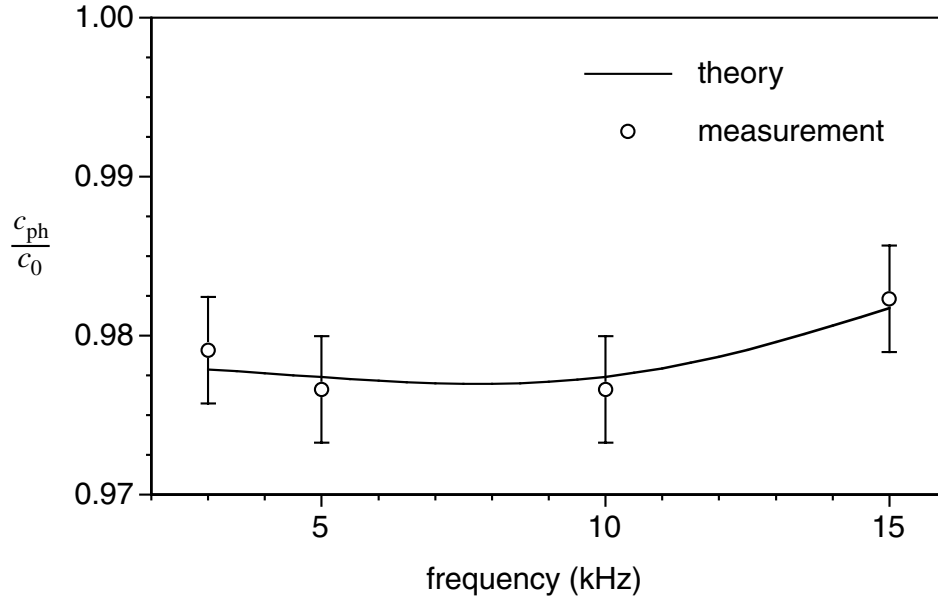


Figure 3.10: Measured waveguide phase speed c_{ph} is compared to the theoretical prediction from Eq. 3.72. The values are normalized by c_0 , the intrinsic sound speed in water for the experimental temperature.

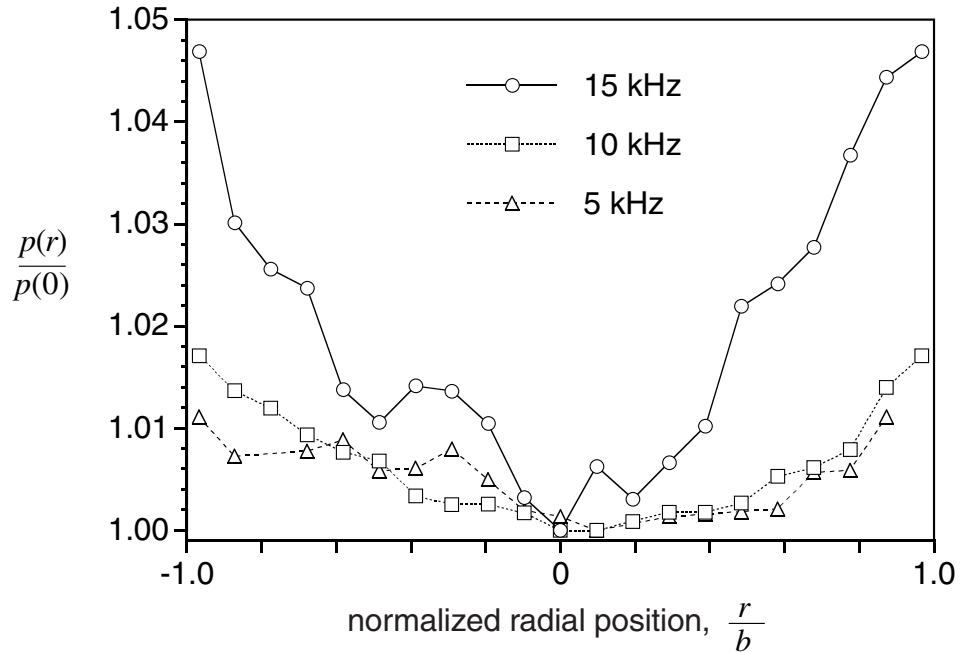


Figure 3.11: Measured acoustic pressure profiles are shown for three frequencies. The abscissa represents radial position within the tube, normalized by the inner radius b . The acoustic pressure at each position is normalized by the acoustic pressure at the center.

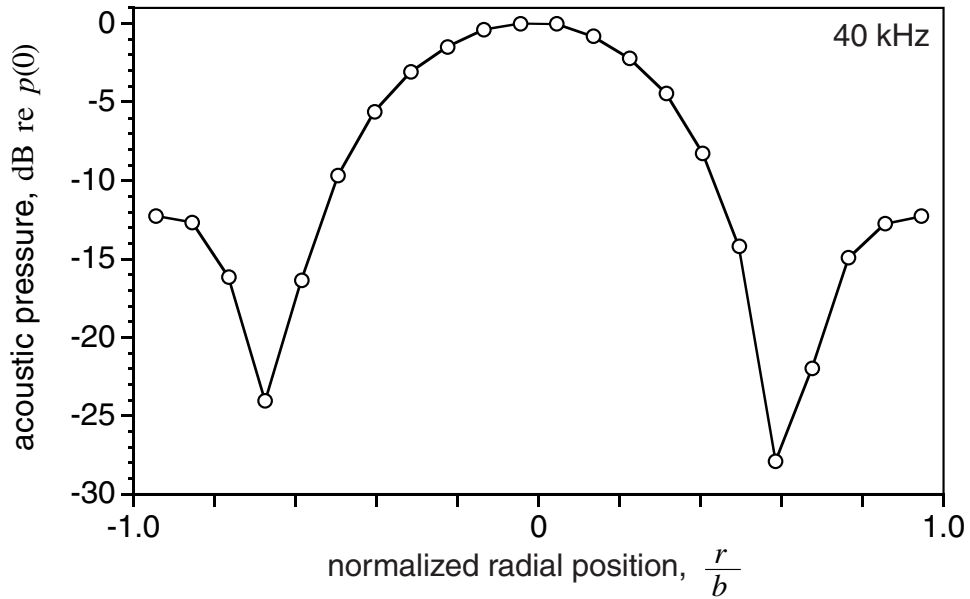


Figure 3.12: The measured acoustic pressure profile at 40 kHz is shown. The abscissa represents radial position within the tube, normalized by the inner radius b . The acoustic pressure is plotted in dB referenced to the pressure at the center $p(0)$.

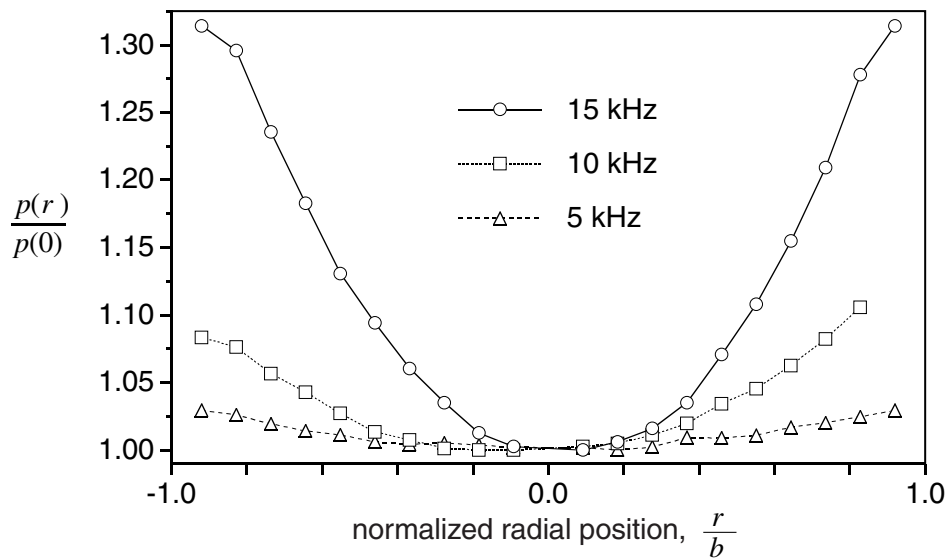


Figure 3.13: The measured acoustic pressure profile inside a thin-walled aluminum waveguide is shown. Comparison with Fig. 3.11 shows the importance of wall thickness and material strength.

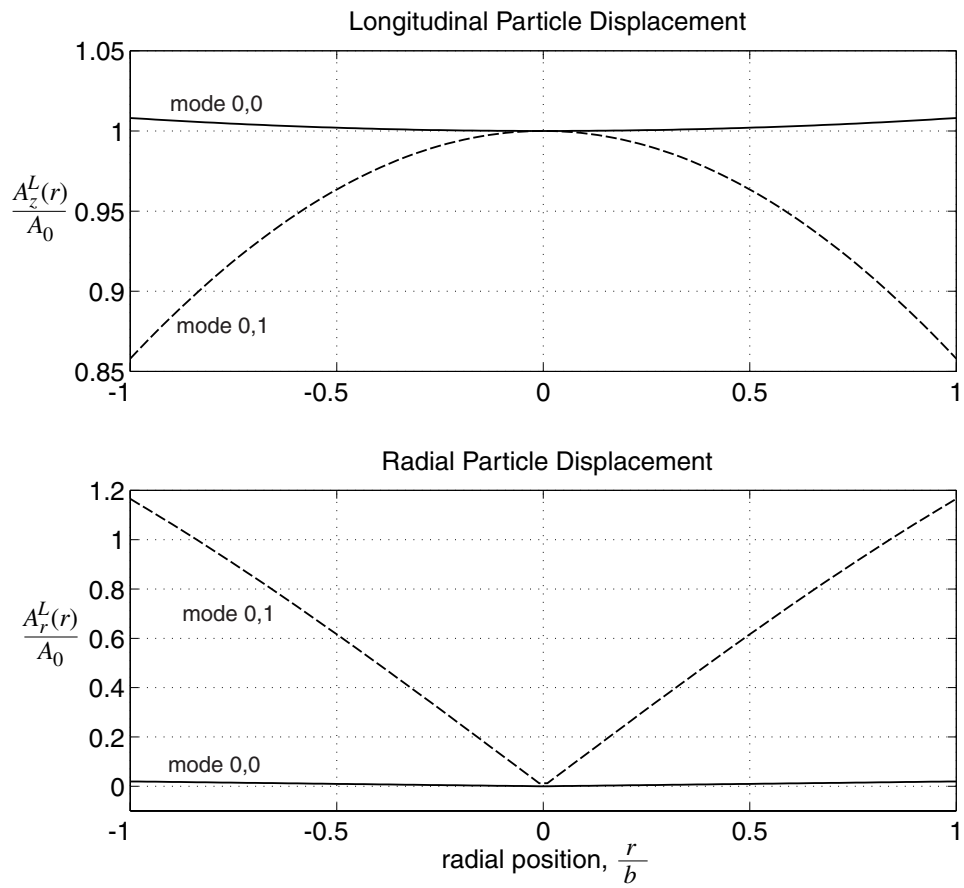


Figure 3.14: Calculated particle displacements for the two lowest order modes in the impedance tube are shown.

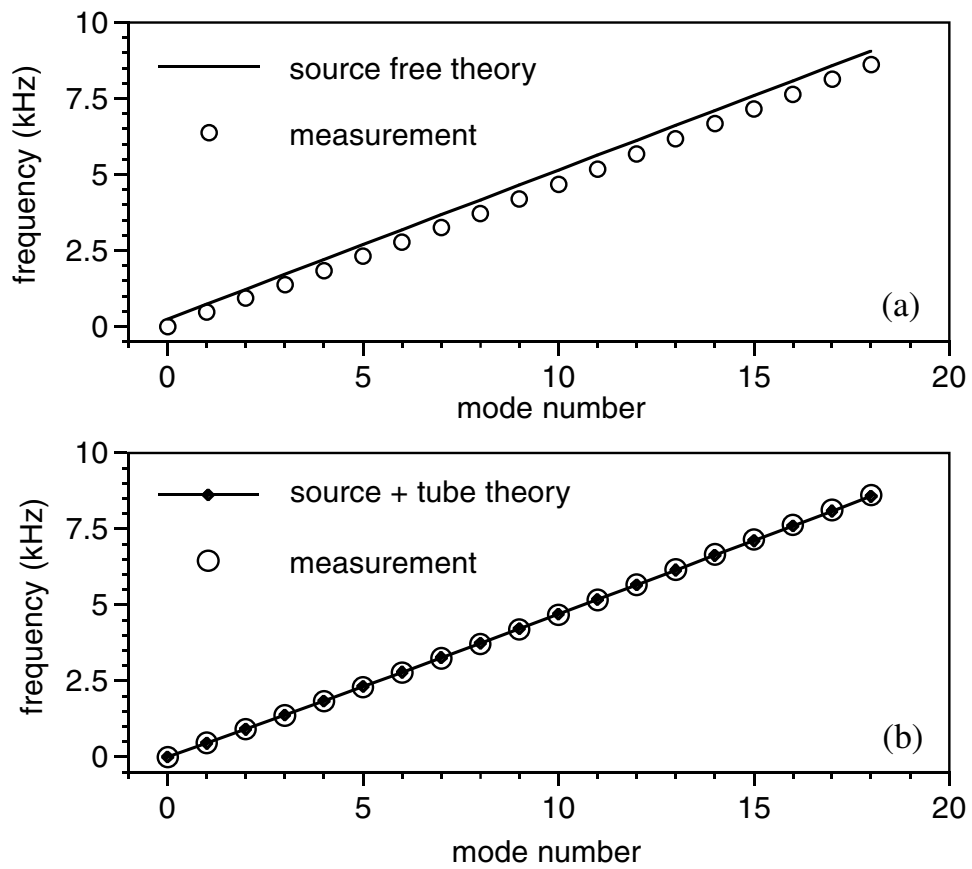


Figure 3.15: In part (a) the source free resonance predictions from Eq. 3.73 are shown along with the measurements. In part (b), the combined source + tube model given by Eq. 3.74 is compared with measurement. For both cases, the model parameters are given in the text.

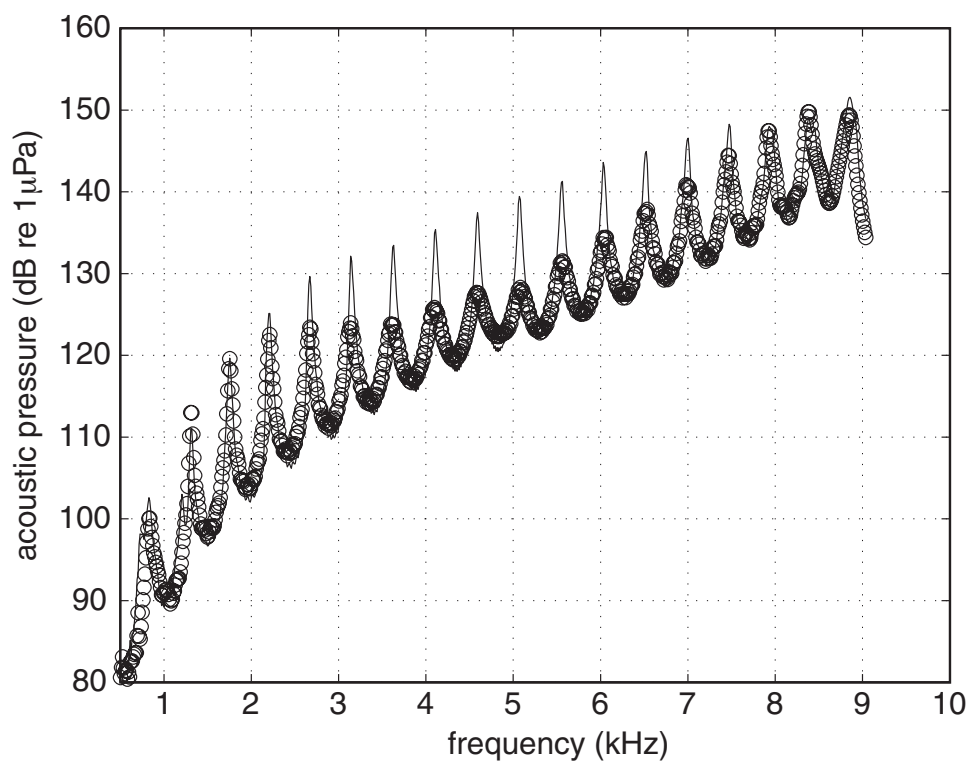


Figure 3.16: System frequency response: Measurement (open circles) and Eq. 3.75 (solid line). See text for parameters.

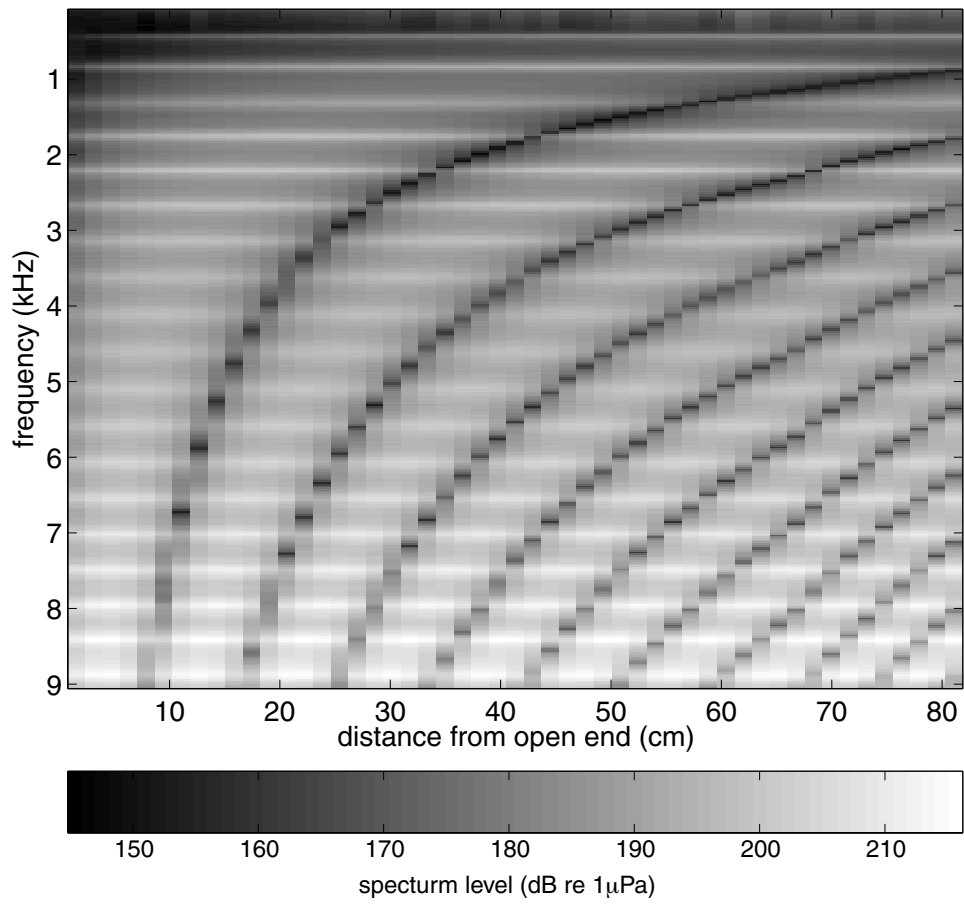


Figure 3.17: The measured standing wave field inside the impedance tube is shown.

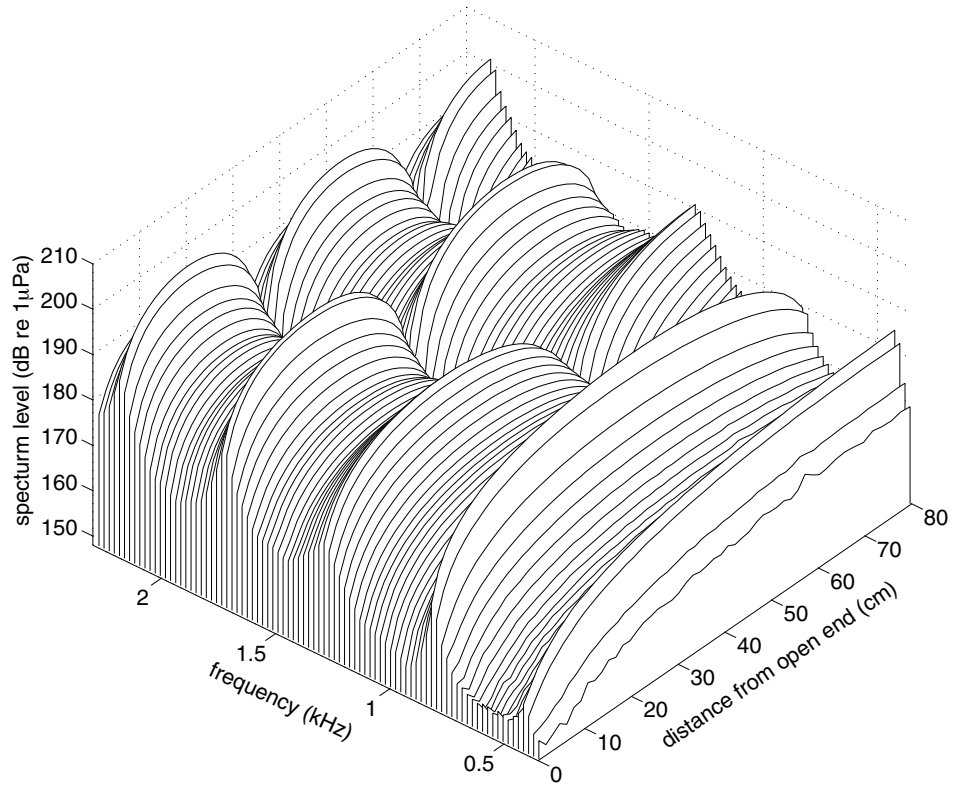


Figure 3.18: A subset of the measured standing wave field is shown in waterfall.

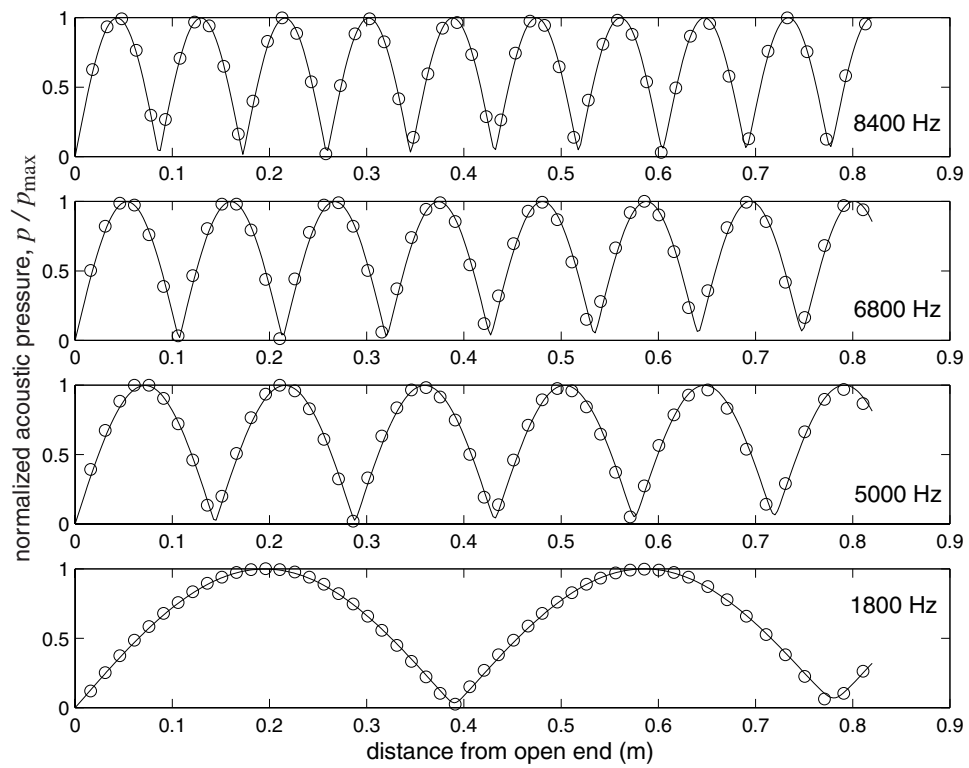


Figure 3.19: The standing wave pattern for four frequencies: Measurement (open circles) and Eq. 3.80 (solid line). See text for parameters.

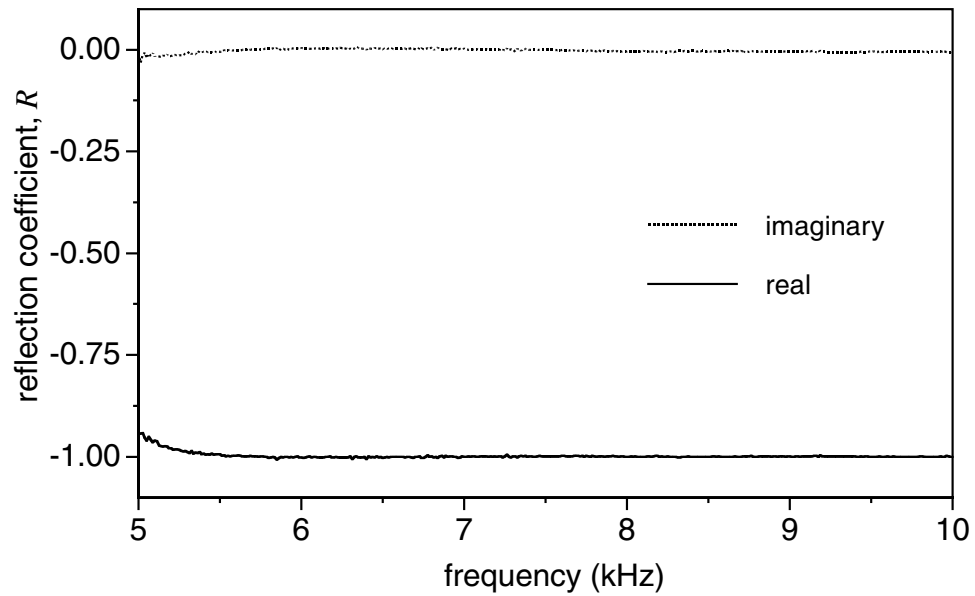


Figure 3.20: Verification measurement of an approximate pressure release surface, showing real and imaginary parts of the measured complex reflection coefficient. Compare to the value predicted by Eq. 3.81, $R = -0.9994 + j0$, which for clarity is not shown on the plot. Note increasing deviation from expected values as frequency decreases.

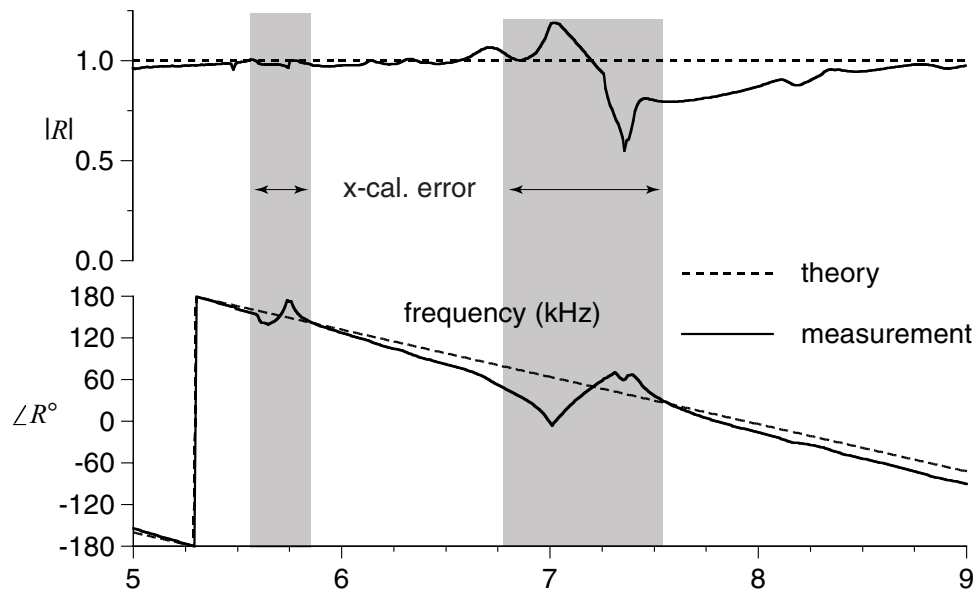


Figure 3.21: Ground truth/verification measurement of a water-filled transmission line showing magnitude and phase of the measured complex reflection coefficient at the interface. The theoretical curve is Eq. 3.82. See text for explanation of “x-cal. error.”

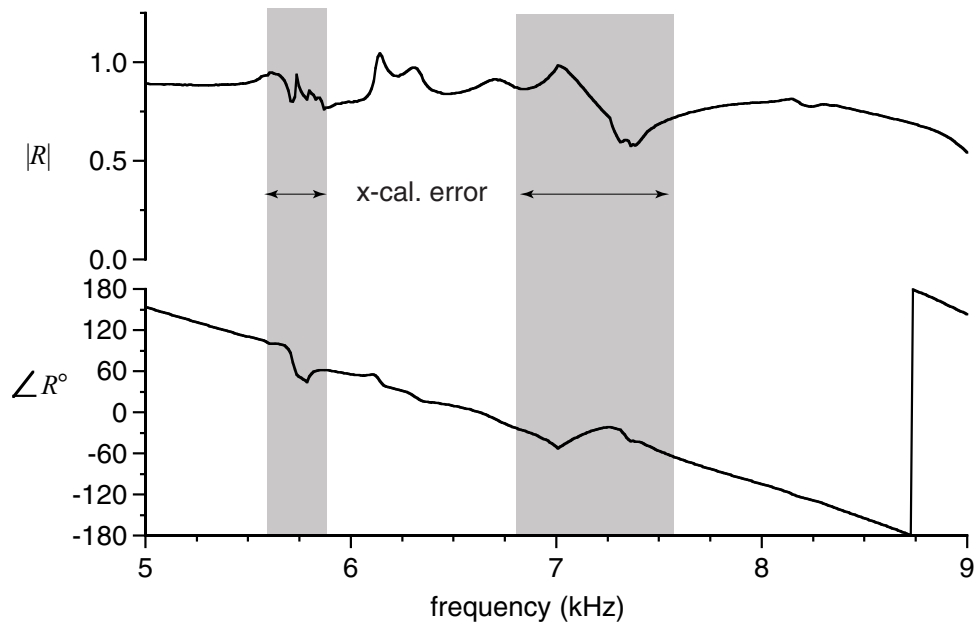


Figure 3.22: Measured magnitude and phase of the reflection coefficient of a near bubble-free Xanthan gel. Shaded areas represent frequency range of cross-calibration error. Note similarity to Fig. 3.21.

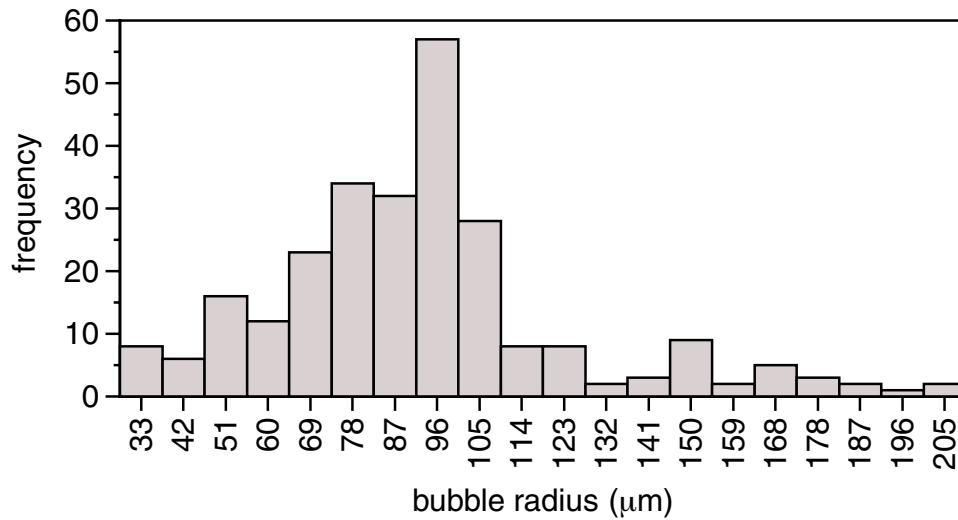


Figure 3.23: The optical bubble size distribution of Xanthan gel mixtures for Fig. 3.24 is shown.

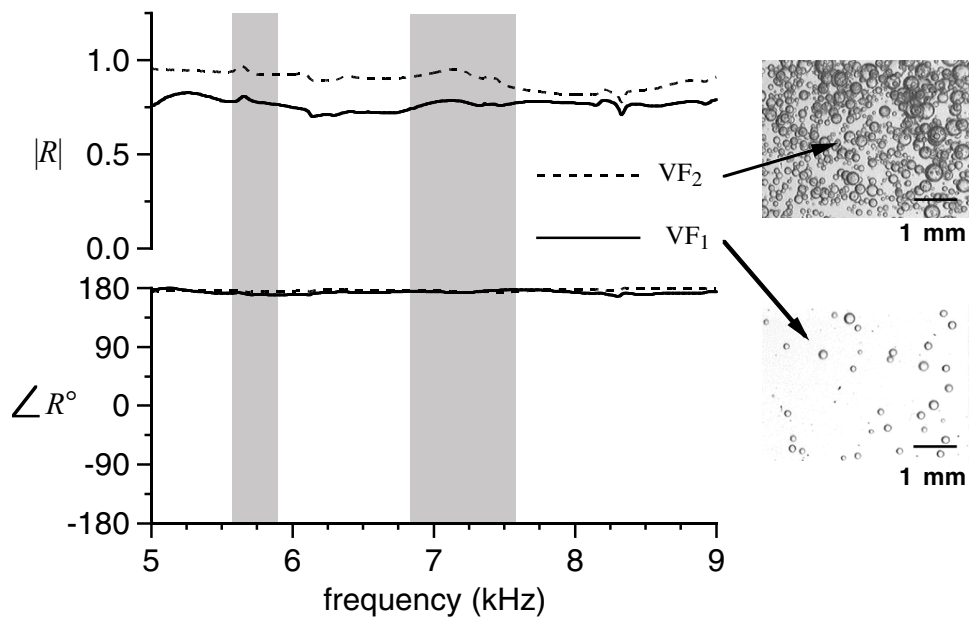


Figure 3.24: Measured magnitude and phase of the reflection coefficient of Xanthan gel with $VF_2 > VF_1$. Shaded areas represent frequency range of cross-calibration error.

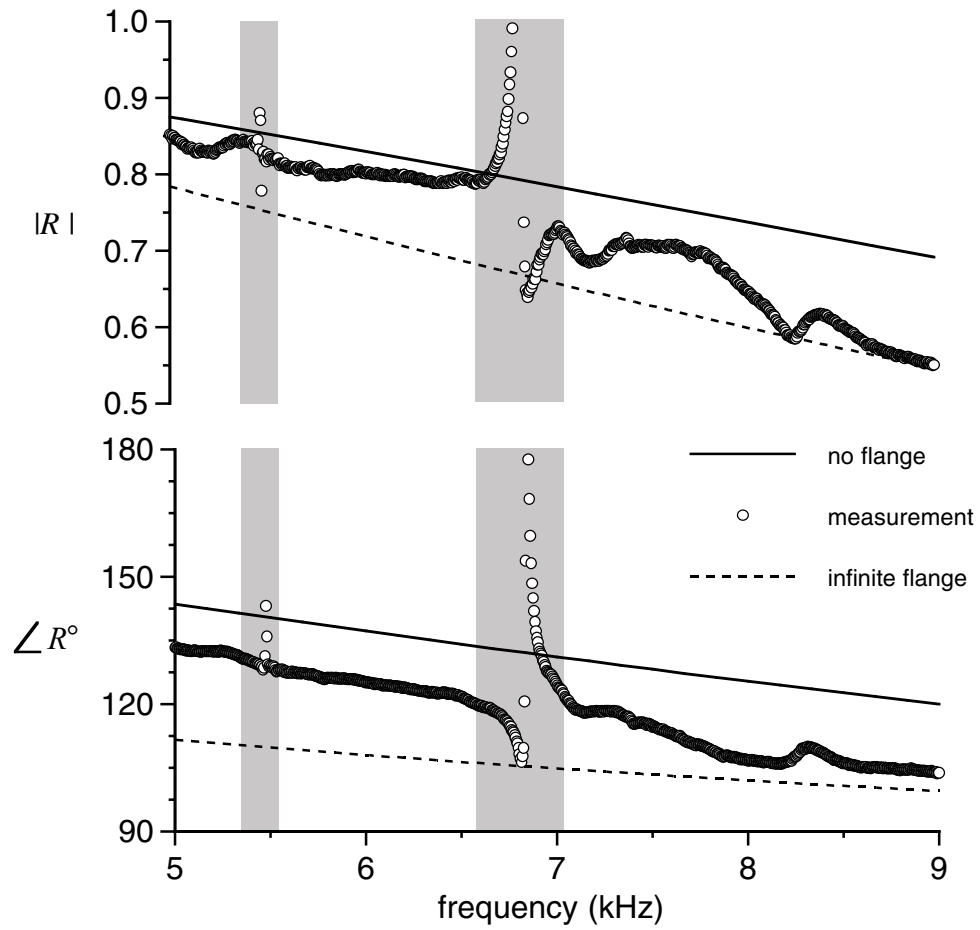


Figure 3.25: Measured magnitude and phase of the reflection coefficient for the open tube, as compared to predicted results from Eqs. 3.83, 3.84, 3.85 and 3.86. Shaded areas represent frequency range of cross-calibration error.

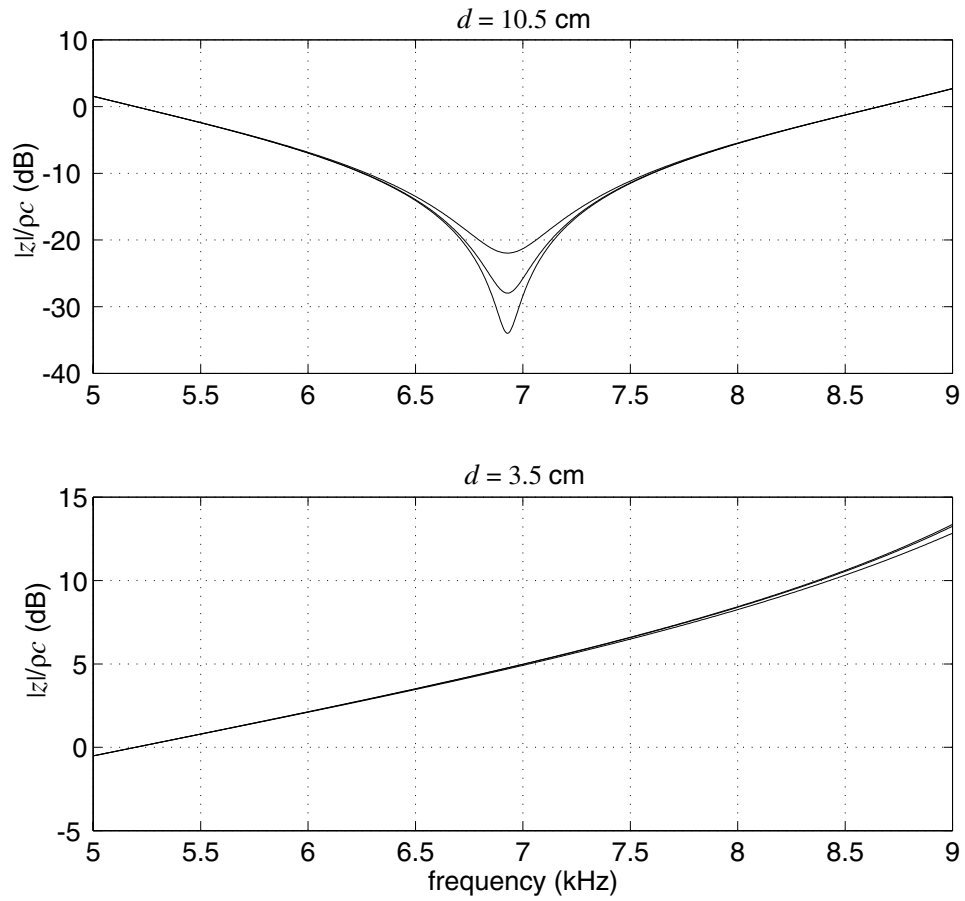


Figure 3.26: The input impedance $z/\rho c = i \tan(kd - i\alpha)$ of a calibration termination is shown for $\alpha = 0.02, 0.04$ and 0.08 . In the upper plot, a null appears in the frequency band, and the three plots differ near 7 kHz. In the lower plot, no null exists and the three plots are very similar.

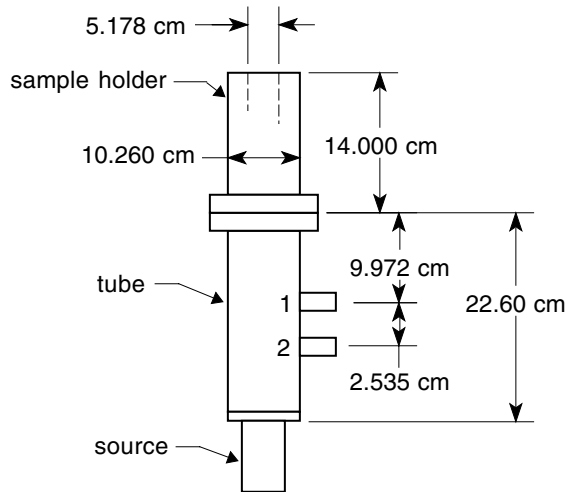


Figure 3.27: The dimensions of the second generation impedance tube are shown.

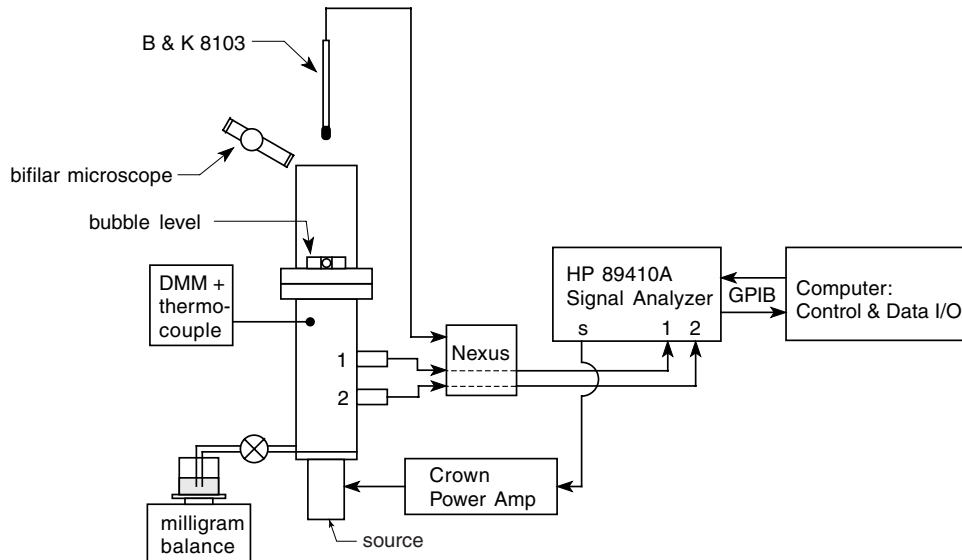


Figure 3.28: The impedance tube system is shown in schematic.

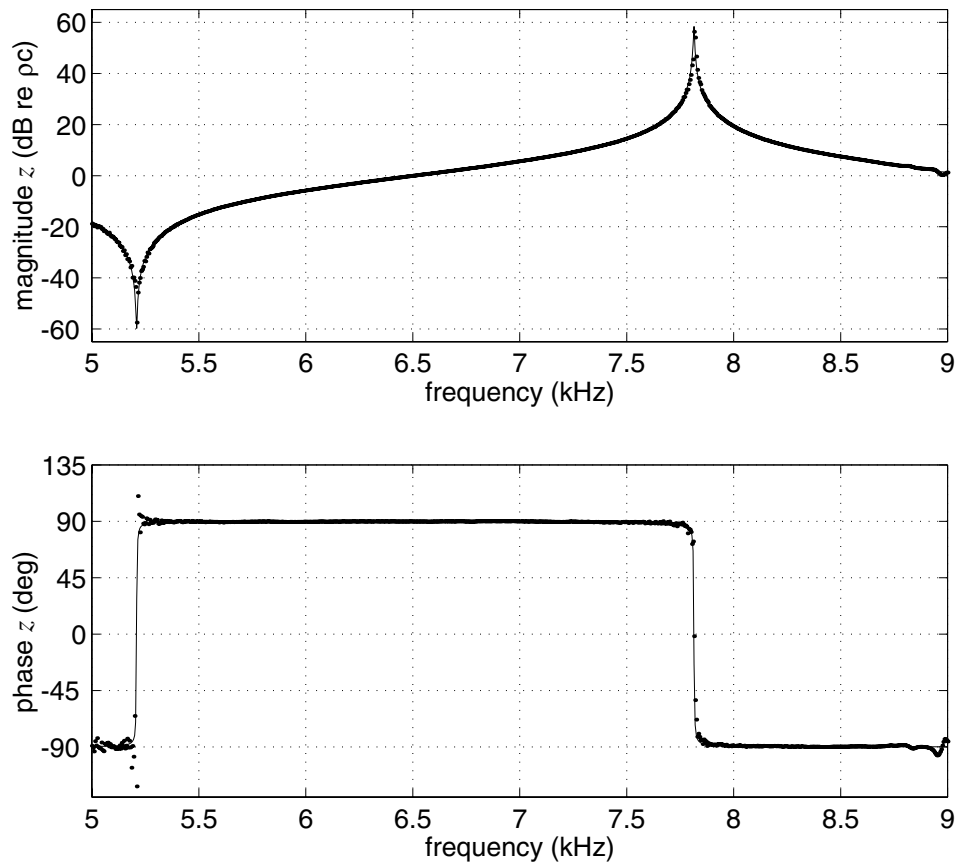


Figure 3.29: The measured (dots) and calculated (solid lines) impedance z of a pressure release terminated transmission line is shown. This plot serves as the ground truth verification for the second generation impedance tube system.

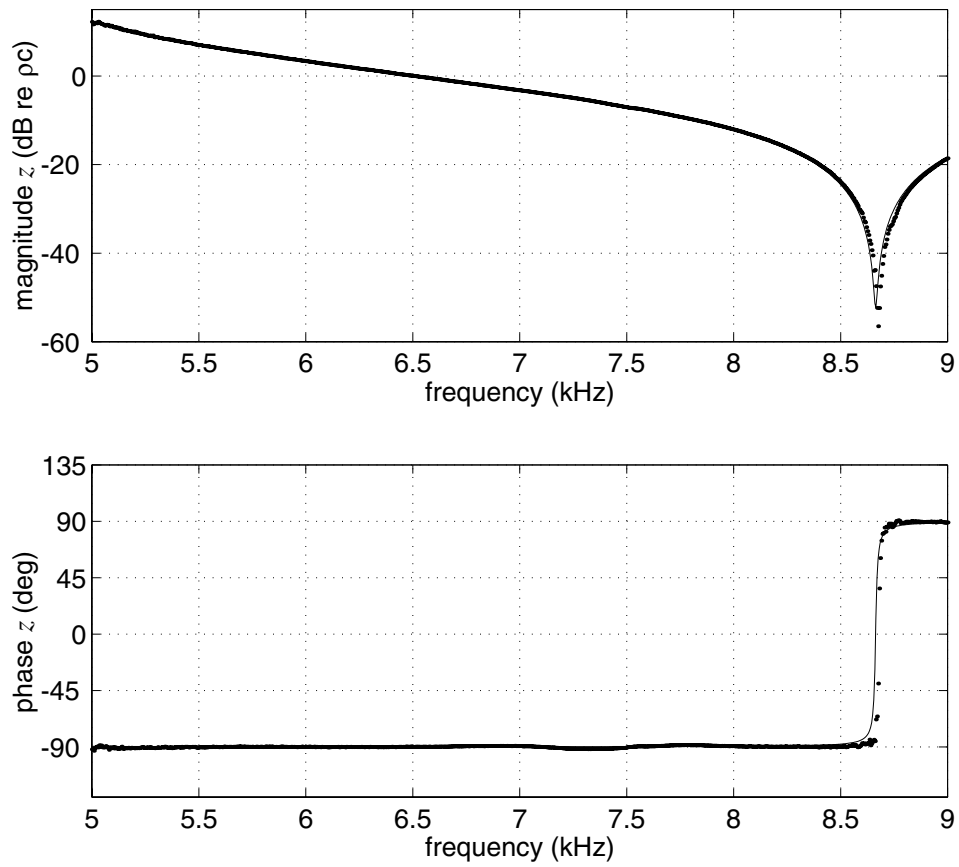


Figure 3.30: For additional verification, the measured (dots) and calculated (solid lines) impedance z of a pressure release terminated transmission line is shown for a second length, $d_0 = 8.40$ cm.

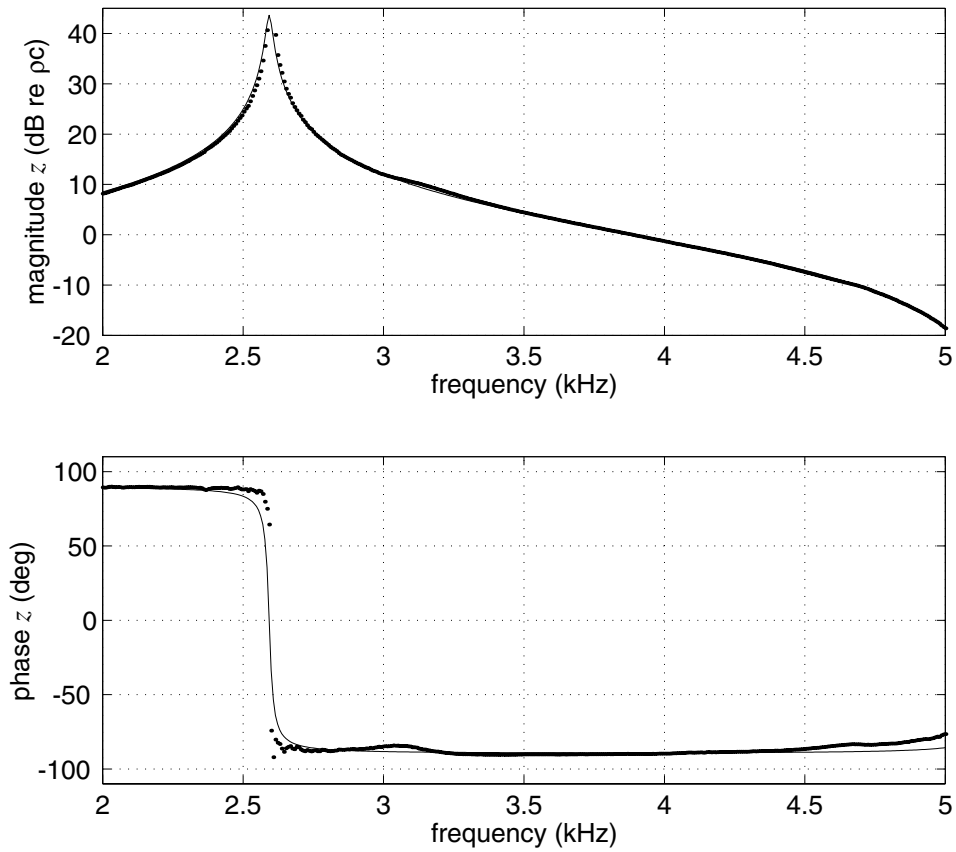


Figure 3.31: A final system verification using the single sensor method is shown. Again, the measured (dots) and calculated (solid lines) impedance z of a pressure release terminated transmission line is presented, but the frequency range was 2–5 kHz.

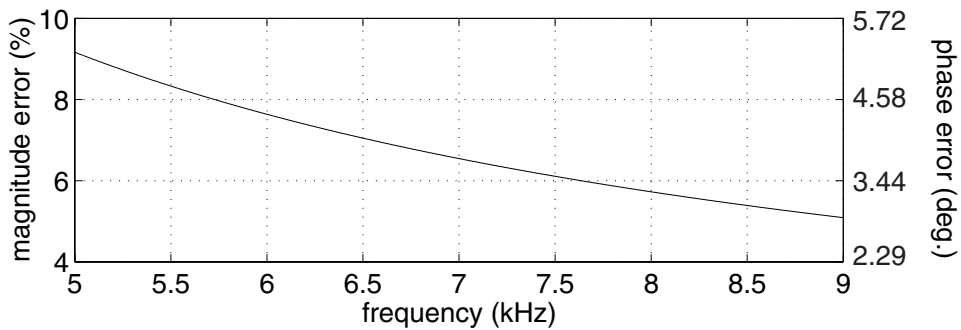


Figure 3.32: Maximum bias error in the measurement of the transfer function y for a transmission line is shown. The normalized error in magnitude (Eq. 3.96) is shown using the left scale, and the absolute error in the phase angle (Eq. 3.97) is shown using the right scale.

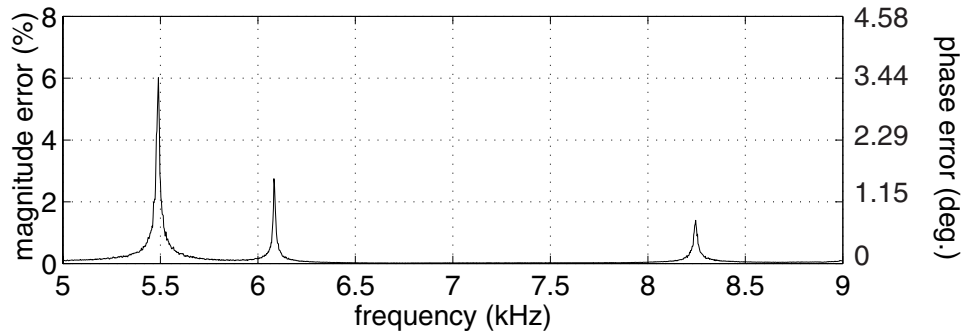


Figure 3.33: Random error in the measurement of the transfer function y for a transmission line is presented. The normalized error in magnitude (Eq. 3.98) is shown using the left scale, and the absolute error in the phase angle (Eq. 3.99) is shown using the right scale.

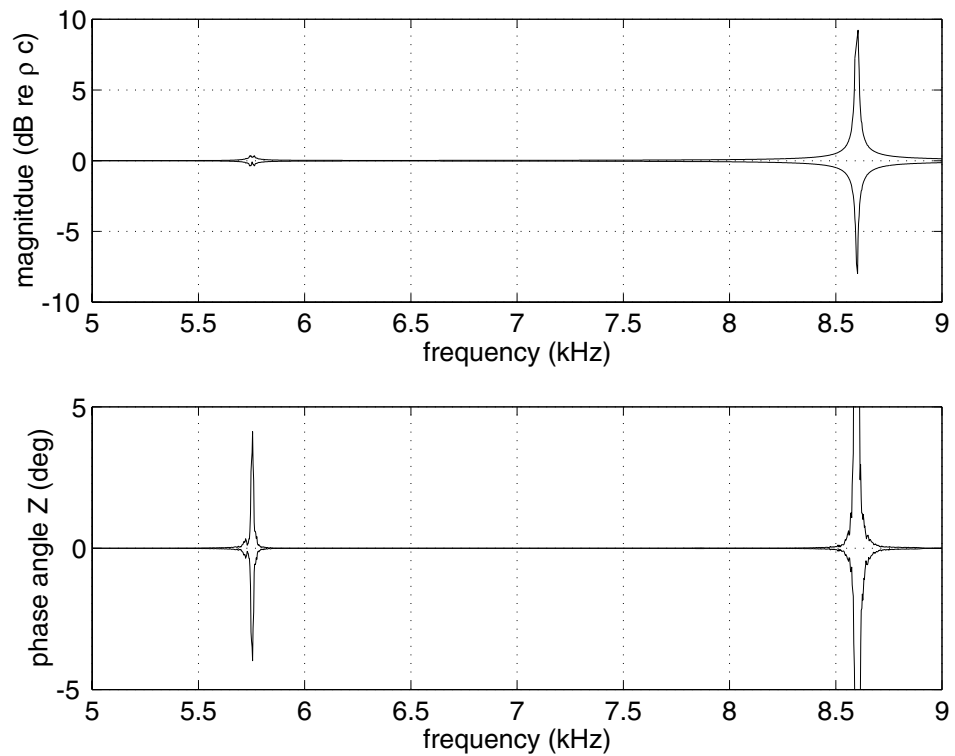


Figure 3.34: The envelope of maximum error due to uncertainties in the measured inputs to Eq. 3.93 is shown. The error in impedance magnitude is shown in the upper plot and phase error is shown in the lower plot. The phase error at 8.6 kHz increased to a maximum absolute value of 80 degrees, but the plot was scaled to show the error at 5.75 kHz clearly.

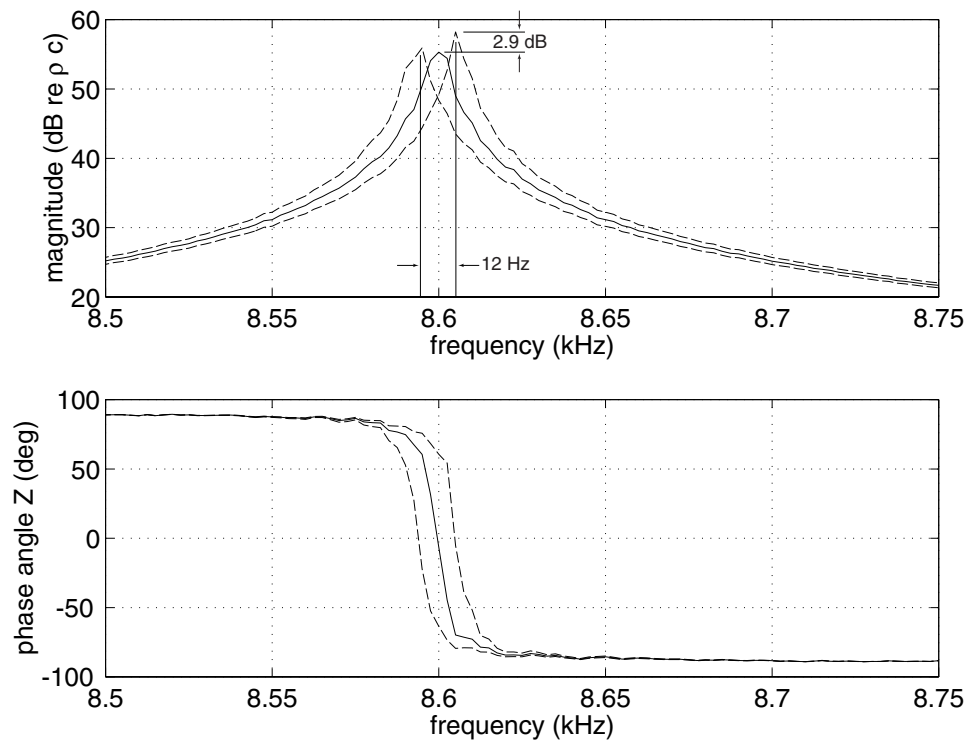


Figure 3.35: Relative error due to uncertainty of the measured inputs to Eq. 3.93.

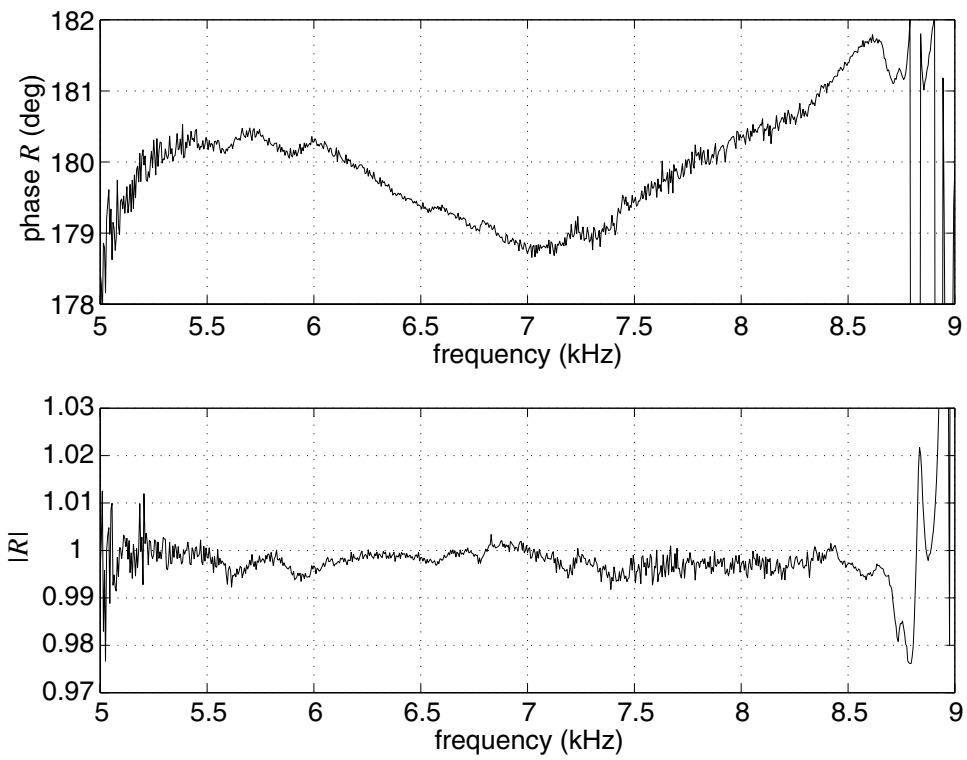


Figure 3.36: Phase and magnitude of the reflection coefficient measured from an water-air interface using the second generation impedance tube.

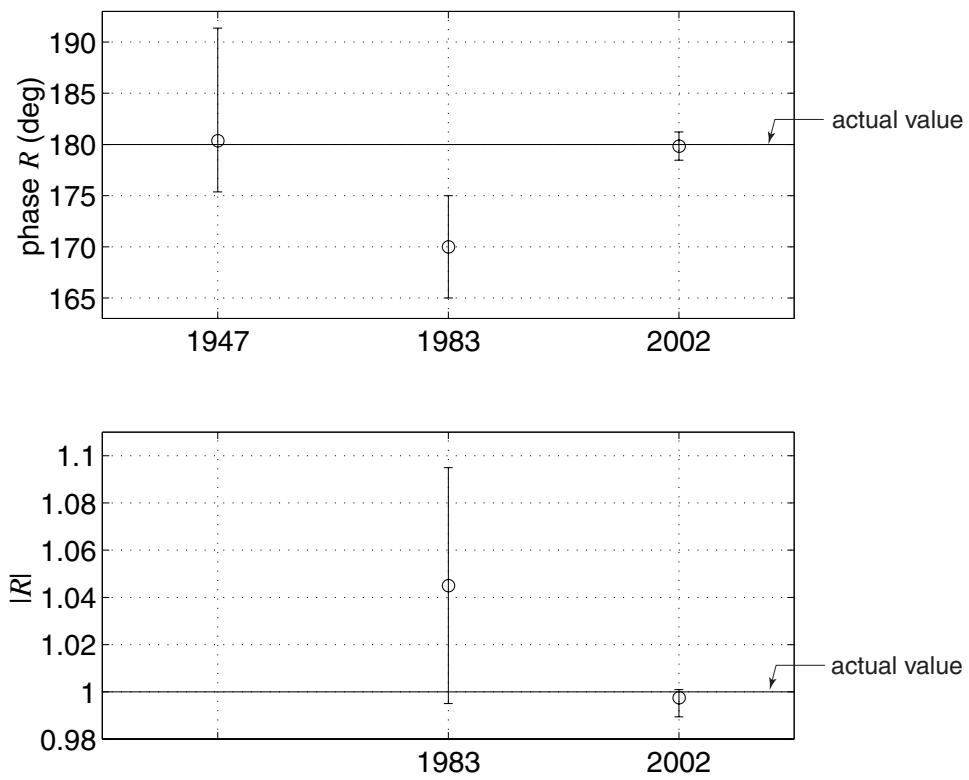


Figure 3.37: Accuracy and precision of three impedance tube systems as expressed in the measurement of the reflection coefficient of an water-air interface. The 1947 and 1983 data were obtained from [47] and [86], respectively.

Chapter 4

Characterization of Bubbly Liquid by Impedance Tube

Now that the performance of the impedance tube has been verified, a main objective of this dissertation can be discussed: measuring the propagation parameters in a bubbly liquid near resonance. As has been mentioned previously, meaningful comparison of theory and experiment in bubbly fluid sound propagation requires knowledge of the number and size of the bubbles contained within the fluid of interest. In this chapter, all the issues associated with bubble production and population characterization will be discussed, in addition to the details of the impedance measurements. Finally, this chapter will include the results and comparison to theory.

4.1 Bubble Production

The bubbly liquid considered in all of the impedance tube experiments reported in the present chapter consists of air bubbles injected into pure water¹ using 30 gauge needles. In all cases, the air is supplied from a compressed air bottle, through a primary regulator, then into a needle valve, a flow meter, and finally into the needle/s, either directly or

¹See Section 3.5.2 for a description of the water purification procedure.

through a manifold. A pressure gauge is connected in parallel between the flow meter and the needles. A schematic of this basic air delivery system is shown in Fig. 4.1. It would be possible, either theoretically or empirically, to relate the flow rate and pressure to the bubble size distribution and void fraction produced by the system, thereby allowing one to dial-in any desired bubble population. Instead, the flow rate and pressure measurements were used solely to insure that the flow conditions, and hence the bubble population, remained as constant as possible throughout any given experiment. The bubble size distribution and overall void fraction was measured directly for each case.

During the initial stages of this work, from one to four long needles (30 gauge, 0.31 mm diameter, 20.3 cm in length) were used to generate bubbles with resonance frequencies within the operating range of the impedance tube. The needles were inserted into the sample holder from the open end of the tube and they were positioned such that they released their bubbles at the measurement plane. This arrangement prevented adequate control and repeatability of the bubble population, so a bubble injection manifold (BIM) was developed. The manifold body is of the same radial dimensions and material as the impedance tube itself, but contains an internal plenum which directs the air supply into a number of needles, as shown in Fig. 4.2-a. There can be from one to twelve needles, which are directed radially from the tube walls into the fluid. All the needles lie in a plane perpendicular to the tube's longitudinal axis, which is coincident with the impedance measurement plane. For the maximum number of twelve, the needles are of such length and orientation so that two concentric rings are formed within the tube, resulting in an even distribution of injection sites throughout the plane. A schematic of this needle arrangement is shown in Fig. 4.2-b. As the bubbles rise, they typically deviate from a directly upward path. By the time they have risen a few centimeters above the needles, they are randomly distributed throughout the tube.

An effort was made to equalize the flow rate through each needle, in hopes of narrowing the bubble size distribution. This was accomplished first by making the plenum volume about 300 times greater than the volume of air that is injected when one bubble of typical

size exits each of the twelve needles. Second, the primary air supply system shown in Fig. 4.1 was connected to the air injection manifold via four equal length conduits, which enter into four ports equally spaced around the circumference of the injection manifold, as shown in Fig. 4.3.

Since changing the flow rate of air through a single needle changes the bubble size as well as the void fraction, one must add additional needles with the same per needle flow rate in order to independently increase the void fraction. Since the injection manifold can hold from one to twelve needles, twelve void fractions are available for any given bubble size distribution. Considering flow through any single needle, it is not possible to independently control the bubble size distribution. At low flow rates, the bubbles exit the needle with a fairly constant size. As the flow rate increase, there is greater size variation, therefore, the bubble size distribution becomes wider as the flow rate increases. Because of these difficulties, the bubble size distribution and the void fraction are measured for each experimental condition reported.

4.2 Determination of Bubble Size Distribution

The bubble size distribution was determined by direct photographic observation of the bubbles. Illumination was provided using a combination of direct and back lighting such that the outline of the bubbles appeared dark against a much lighter background. The bubble injection manifold was placed within a small glass aquarium filled with pure water. The bubbles were free to rise up through the water column and they were photographed using a Kodak DC265 digital camera equipped with a macro lens and a strobe. The acquisition rate was about one photograph per second. This rate was limited by the write-to-RAM speed of the camera. A machinist's scale was placed in one of the photographs, thereby providing a length reference. A schematic of the bubble size measurement system is shown in Fig. 4.4. A typical image obtained by the system is shown in Fig. 4.5-a. Both the imaging and subsequent analysis are undertaken following guidelines published by The

National Institute of Standards and Technology [121]. A Cannon model GL1 digital video camera with a high speed shutter and a high-gain ccd was also used to obtain photographic data at a higher rate. More will be said about this in Section 4.4.2.

The images were processed with the image analysis software package NIH Image.² Four steps were performed on each image in order to extract the size information. The background was not illuminated uniformly and this was removed by Image's built-in background subtraction routine. The exact structure of this operation is not readily available from the NIH Image documentation. Typically, background subtraction is achieved by fitting a polynomial to a number of background pixel values throughout the image. Image offers several options. In these images, background pixels were selected by using a one-dimensional vertical "rolling ball" technique [122, p. 177], with a radius of 50 pixels. The images were then thresholded in such a way that the bubble size was preserved. More on this in a moment. A thresholding operation reassigns black/white to every pixel, depending on whether the pixel grayscale value is above/below the threshold value.

Out-of-focus bubbles were often removed by the thresholding operation. If not, they were removed from the image by hand. At this stage, in-focus bubbles appeared with black outlines on a white background. Often the outlines were not completely closed, depending on the bubble's orientation relative to the direction of illumination. Small breaks or gaps in the outline often appeared. A "closing" operation was performed to remedy this. The closing operation consisted of repeated application of a rank filter; three times to dilate the image, and then two times to erode the image. The rank filter dilates/erodes an image by taking each pixel and turning it on/off if n or more of its eight surrounding neighbors are on/off [123, p. 136]. In this work, $n = 4$ typically gave good results. Most of the bubbles then appeared with completely closed outlines, in either spherical or spheroidal shapes. A quick check was made, and any non closed bubbles were carefully closed by hand. NIH Image was then used to outline, determine the pixelated area of, and number

²NIH Image is a public domain image processing and analysis program for the Macintosh. It was developed at the Research Services Branch of the National Institute of Mental Health, part of the National Institutes of Health, and is available at: <http://rsb.info.nih.gov/nih-image/>.

each bubble. The results of this processing, as applied to the image in Fig. 4.5-a, is shown in Fig. 4.5-b.

At this point, the processed image was compared to the original image to make sure the outlined bubbles were the same shape and size as the original bubbles. If not, the thresholding level or the closing operation would be altered through trial and error until agreement was achieved. As long as the photographic variables were well controlled during the experiment, the processing would only be set up once, and the remainder of the images could be processed accurately with the original settings.

Two different analysis methods were required depending on the average size of the bubbles in any given experiment. For bubbles with radius $a < 0.5$ mm, which remain mostly spherical, the radius was calculated from the pixelated area, assuming an effective circular shape. Specifically, NIH Image counted the number of pixels n for each bubble. The length reference l_{ref} (length/pixel) was taken from the machinist's scale and the effective radius a was calculated from

$$a = \sqrt{A/\pi} = l_{\text{ref}} \sqrt{n/\pi}. \quad (4.1)$$

Bubbles with radius $a > 0.50$ mm become somewhat flattened, with a shape well approximated by an oblate spheroid. The major and minor axes $2b$ and $2c$ appeared in the plane of the image, and were determined by NIH Image in number of pixels. The spheroidal volume is given by $V = \frac{4}{3}\pi b^2 c l_{\text{ref}}^3$. The radius a was then calculated based on an effective spherical volume

$$a = \left(\frac{3V}{4\pi} \right)^{1/3} = l_{\text{ref}} (b^2 c)^{1/3}. \quad (4.2)$$

The number of individual bubbles analyzed depended upon the experiment being done, but a typical number was 200. A typical histogram of bubble radii, obtained from the image in Fig. 4.5-b and 19 others like it, is shown in Fig. 4.6.

Two primary factors that contribute to the uncertainty of the bubble size measurement

are deviation of the actual bubble shape from the model shape, and the limited length resolution of the pixelated images. Close scrutiny of the magnified image reveals that the error due to pixelation is likely the greater of the two. This is demonstrated in Fig. 4.7. A single bubble taken from the Fig. 4.5-a is shown greatly enlarged in part a), so that individual pixels can be seen. The same bubble is again shown in part b), but a slightly larger ellipse has been overlain, and it is apparent that the shape is a good match to that of the bubble. There is some uncertainty about the boundary of the bubble, though. When the image was digitized, the pixels were assigned discrete values of brightness, therefore one can not be sure exactly where the boundary was. Motion of the bubble during the exposure also contributes to this uncertainty. Consider the minor axis of the bubble, with length $2c$. If one assumes the actual boundary lies somewhere between the outer most two pixels, then the minimum and maximum possible minor diameters are shown in the figure. For this typical bubble size, $2c_{\min} = 20$ pixels, and $2c_{\max} = 24$ pixels. Although not shown in the figure, a similar situation exists for the major axis, with $2b_{\min} = 32$ and $2b_{\max} = 36$ pixels, and for the scale value, $l_{\text{ref}} = 230 \pm 2$ pixels/cm. Using Eq. 4.2 one finds the uncertainty in the measured bubble radius for this size range is $a \pm 7.7\%$. At this point a trade-off is evident. For a given imaging system, one can increase the magnification and thereby increase the length resolution, but then the number of bubbles per image is decreased, the size of the statistical population is decreased.

4.3 Determination of Void Fraction

The void fraction was determined using a one dimensional resonator, filled with the bubbly liquid of interest, and operating below the resonance frequency of the largest bubble. In this range, known as Wood's limit, the mixture sound speed is only very weakly dependent on frequency, and is related to the void fraction by Wood's Equation, Eq. 1.10. Furthermore, a one dimensional waveguide filled with such a fluid exhibits resonance frequencies which are directly related to the mixture sound speed and the resonator's length.

Consider a rigid hollow tube of length ℓ and circular cross-section with radius a , filled with a fluid possessing sound speed c_0 , taken to be a constant for the purposes of the present discussion. The cutoff frequency of the lowest order transverse mode is given by [98]

$$f_{11}^c = \frac{\alpha'_{11} c_0}{2\pi a}, \quad (4.3)$$

where $\alpha'_{11} = 1.841$ and is the first root of $J'_1(x) = 0$. Below f_{11}^c , only plane waves can propagate within the tube. Solution of the wave equation within this tube for pressure release boundary conditions at both ends yields the eigenfunctions

$$p(x) = \sum_{n=1}^{\infty} a_n \sin \frac{n\pi x}{\ell}, \quad (4.4)$$

and eigenfrequencies

$$f_n = \frac{nc_0}{2\ell}. \quad (4.5)$$

If one plots f_n as a function of mode number n , the slope of the line is $c_0/2\ell$, and one can calculate the sound speed from a measurement of resonance frequencies.

In practice, one must excite the waveguide in some way. A tube driven by a constant velocity piston has been described previously, and has resonance frequencies given by Eq. 3.51 and repeated here,

$$f_m = \frac{c_0}{2\ell} (m + 1/2). \quad (4.6)$$

Despite having different resonance frequencies, the slope of the line is the same for both cases, $c_0/2\ell$.

It has also been shown in Section 3.4.1 that the dynamics of the source can cause the resonance frequencies to deviate from Eq. 4.6, if the mechanical input impedance of the source is of the same order of magnitude as that of the tube. For the measurements reported in this section, the excitation is provided by the bubbles breaking off the needles, which takes place very near the lower end of the tube. It is beyond the scope of the present

discussion to seek a detailed description of the source mechanism for this application. It will be shown that Eqs. 4.4 and 4.5 constitute a good model for the void fraction resonator at resonance, and that the slope of the resonance frequency curve is a good measure of sound speed inside the tube, if the sound speed is constant. For some of the bubbly fluids considered, the sound speed becomes dispersive at the higher resonance frequencies, which renders the slope of the resonance frequency versus mode number curve nonlinear. In such a case, the dispersive sound speed can still be determined directly from Eq. 4.5.

A schematic diagram of the void fraction resonator is shown in Fig. 4.8. An aluminum tube (30.13 cm length, 5.08 cm diameter, 0.635 cm wall thickness) was mounted to the top of the air injection manifold and sealed with an o-ring. The lower pressure release boundary condition was achieved by closing the tube with a thin mylar membrane which was glued to a mounting fixture. The mounting fixture interfaces with the air injection manifold, sealing the tube with an o-ring, and positions the membrane just below the needles. A photograph of the resonator tube attached to the bubble injection manifold is shown in Fig. 4.9. A Brüel and Kjær type 8103 hydrophone was typically positioned 2 cm from the open end of the tube. The phone could also be scanned along the length of the tube and positioned via 1 mm fiducial marks. The hydrophone cable was sheathed in a water-filled stainless steel tube to ensure accurate positioning, and to minimize the impedance discontinuity that would be presented by the hydrophone cable alone. A photograph of the hydrophone positioning apparatus is shown in Fig. 4.10. The hydrophone signal was conditioned using a Brüel and Kjær type 2692 low noise charge amp, which also provided band-pass filtering between 10 Hz and 10 kHz. The natural resonances of the tube were excited by the bubbles breaking off the needles, and the resulting hydrophone signal was acquired using a Hewlett Packard 89410A Vector Signal Analyzer.

In order to verify the operation of the void fraction resonator, a complete scan along the length of the tube was conducted, thereby obtaining a measurement of the acoustic field at 30 points in the tube, each separated by 1 cm. At each position, a spectrum of the bubble generated acoustic field was acquired using a Hann window, 50 spectral averages,

and a resolution bandwidth of 3.5 Hz. Bubbles were being produced using the six needles shown in Fig. 4.3. The airflow for this measurement was 108ml/min at 21.85 kPa above atmospheric pressure. The acoustic pressure field is shown in Fig. 4.11. This pressure field is similar to the one shown in Fig. 3.17, which was for a nearly non-dispersive case. Note that in the current figure the interference pattern below about 1.5 kHz is similar to the pattern in Fig. 3.17, indicating the resonance structure and the standing wave pattern. Above 1.5 kHz, the interference pattering disappears. What is the explanation for this? The bubble size distribution for this flow was obtained as described in Section 4.2 and is shown in Fig. 4.12. The resonance frequency for these bubbles should be close to 3.1 kHz, as obtained from Eq. 1.15. The absorption should be high near resonance, and Fig. 4.11 shows that the acoustic pressure diminishes monotonically by 50 dB from the source to the end of the tube, at 3 kHz. Standing waves cannot form in the presence of such attenuation. Up to approximately 1.6 kHz, the standing wave pattern is visible in Fig. 4.11. Above 1.6 kHz, the standing wave field has been replaced by a field which decreases in amplitude with increasing distance from the source.

A single resonance frequency can be used to calculate the sound speed within the tube only if the resonances are associated with known boundary conditions; for the present case, $p = 0$ at each end of the tube. Integer multiples of half-wavelengths will fit inside the tube and Eq. 4.5 can be used to obtain the sound speed. A single spectrum, taken at $x = 7.5$ cm is shown in Fig. 4.13. A number of spectral peaks can be seen. In this case, the four most prominent peaks below 1.5 kHz correspond to resonance frequencies associated with modes $n = 0, 1, 2,$ and 4 . It is not always obvious which peaks are associated with resonances. Recall that this is a driven tube, and therefore can support spectral peaks at frequencies off resonance. Also recall that at certain positions x , a resonance peak may not be present in the spectra because that x corresponds to a null in the field.

A spatial observation of the field is useful for identifying the resonances. One can pick out which frequencies result in integer numbers of half wavelengths fitting inside the tube. In order to verify that the resonator exhibited this behavior, slices were taken out

of Fig. 4.11 at the four resonance frequencies already mentioned. These spatial scans are shown in Fig. 4.14, along with the theoretical prediction of the field given by $p_n(x)/P_0 = \sin(n\pi x/\ell)$. To save time during normal operation, only a single spectrum is taken. With a little experience, one can try out different positions x inside the tube and quickly find a spectrum that will yield usable resonance frequencies.

At the void fraction used in this example, the sound speed inside the tube was so low that the elastic waveguide effect is negligible. When the void fraction is lower, the elastic waveguide effect is manifested primarily as a reduction in sound speed. The frequency range is narrow enough that dispersion is negligible. The reduced sound speed can be compensated for by using Eq. 3.72 in an iterative manner to find the associated unconfined sound speed, and therefore the true void fraction through Wood's Equation. This correction has been applied to the data where necessary.

The average of the void fractions is $\chi = 4.4 \times 10^{-3}$, obtained by applying Wood's Eq. 1.10 to the sound speeds from Fig. 4.14. The bubbles used in this experiment have resonance frequencies near 3.1 kHz, which is not much greater than the frequencies from which our sound speeds were obtained. It is interesting to compare these not-so-low frequency sound speeds to the broadband prediction based upon Eqs. 2.23 and 2.22, and the measured bubble size distribution given in Fig. 4.12. The measurements and the prediction are shown in Fig. 4.15, along with the value of sound speed given by Wood's equation for the average void fraction.

The error bars are derived from two sources of uncertainty. The water column height was perturbed due to the exiting bubbles such that its uncertainty is about ± 2 mm. The resolution bandwidth of the spectrum measurement leads to an uncertainty of ± 3.5 Hz. The uncertainty in the sound speed is then a maximum of ± 3.25 m/s, obtained by variation of $c = \lambda f$. Another source of error is the local variation of void fraction with depth. Because of the hydrostatic head, the bubbles at the bottom of this resonator are slightly more compressed than those at the top. In fact, the top/bottom pressure ratio is 0.971. This small perturbation is ignored, primarily because the sound speed derived

void fraction gives an average value within the tube when driven from below. This is the same situation that occurs within the impedance tube during the bubbly liquid impedance measurements, and therefore should be a good representation of the effective void fraction as it appears looking into the sample holder.

The resonator technique as discussed here appears to yield a good estimate of the void fraction of these bubbly liquids, at least in its performance relative to theory. For the data reported in this chapter, the void fractions determined by VF resonator were not compared to any other measure of void fraction, although the resonator technique itself was verified in preliminary work, as reported in Appendix A.

As a bonus from this data set, measurements of attenuation were derived from the standing wave patterns. The attenuation coefficient A is directly related to the slope M of the line that connects the nulls in the standing wave patterns, and is given by $A = M/2$. Although the coarse spatial sampling of the measurement reduced the number of suitable data points to only three, good agreement is found. Error bars are derived from the uncertainty in the position of the nulls, which was estimated to be ± 0.5 cm since the spatial increment is 1 cm. During normal operations, spatial scans were not performed, therefore low frequency attenuation measurements were not obtained.

4.4 Impedance Measurement

In this section two different types of experiments will be discussed. In both of these experiments, the goal was to measure the phase speed and attenuation in bubbly liquid in the resonance regime. In the original experimental design, it was assumed that the bubble population statistics and the void fraction would be stationary in time, as long as the observable air injection parameters remained constant. Preliminary results indicated that the bubble population statistics were non-stationary, and that moving the bubble injection manifold from the bubble sizing apparatus to the void fraction resonator, and finally to the impedance tube, resulted in different bubbly liquids, even when the observable flow

parameters did not change. This type of chaotic behavior exhibited by needle manifolds has been noted before, particularly in the Lake Seneca experiments [56]. In the original experimental design, long time averaged quantities would have been used in all aspects of the experiment, but the discovery of non-stationarity lead to the idea that short time measurements would be interesting.

The time averaged experiments were still performed, but since the bubble population parameters were changing, a relatively small degree of fitting was usually necessary in order to bring the measurements and theory into agreement. The second type of measurement offered a unique insight into the time varying, and inherently statistical nature of sound propagation in bubbly liquids. Instantaneous impedance measurements were obtained using 66 millisecond chirps from the signal analyzer. These were acquired once every 15 seconds for 25 minutes. Afterward, an extensive study of the statistics of bubble production from a single needle was performed using a digital video camera and high magnification. Twenty-five minutes of bubble production was observed. This resulted in 18,000 frames of digital video, and ultimately about 24,000 individual bubble images. At the present, that data set has been only partially analyzed. Segments of six second length were taken once every minute for 16 minutes and analyzed for bubble size distribution. In such a way, the acoustic sampling rate and the bubble population sampling rate were brought into agreement. In the remainder of this section the two experimental procedures will be described, and the method for obtaining plane wave propagation parameters from impedance measurements will be described.

4.4.1 Time-Averaged Measurement Procedure

In this section, the procedure for time-averaged impedance measurement will be described. The procedure was composed of four parts: cross-calibration, bubble size distribution measurement, void fraction measurement, and finally impedance measurement.

First, the cross-calibration procedure, as described in Section 3.7.3 is performed. For the calibration and the impedance measurements, pseudo-random noise was used as the

excitation over a frequency range of 5–9 kHz, with Hann windowing and a resolution bandwidth of 2.5 Hz. Second, the bubble injection manifold (BIM), shown in Figs. 4.2 and 4.3, was prepared by installing the desired number of needles. The BIM was then transferred to the size distribution apparatus, shown in Fig. 4.4. Bubble size distribution (BSD) was measured, as described in Section 4.2. The BIM was then installed in the void fraction apparatus shown in Figs. 4.8 and 4.9, and the void fraction (VF) was measured, as described in Section 4.3.

Finally, the BIM was installed between the impedance tube and the sample holder, as shown in Fig. 4.2-a. Great care was taken to prevent the trapping of bubbles during installation, or failing that, to eliminate any air bubbles from the inside of the tube. The remainder of the apparatus is shown in Fig. 3.28. The tube was filled with pure water, and the water height was set using the bifilar microscope. A transfer function measurement was taken between the two wall mounted sensors and the in-situ sound speed was calculated. At this time, one can easily tell if a bubble whose size is in the 5–9 kHz resonance range is trapped in the tube, because a measured transfer function will indicate anomalies in magnitude and phase when such a bubble is present. Two spectra were also taken at this time using the 8103 at the top of the tube, with its acoustic center positioned 1 cm below the water surface. The first spectrum was taken with the excitation signal off, in order to obtain the noise floor. The second one was taken with the excitation signal turned on. Drive level was dependent upon the experiment. The minimum drive level necessary to give good results was used. How this was determined will be discussed below. Minimizing the drive level was important, because this minimized spurious signals imparted by wall motion. Maintaining a linear bubble response throughout the frequency range was also a goal.

The bubble production was then initiated and the air flow rate and pressure were allowed to equilibrate. These flow parameters were kept constant throughout this, and the BSD and VF measurements. The impedance measurement was then conducted by obtaining 100 spectral averages of the transfer function between the two wall-mounted

sensors, using the signal analyzer. The transfer function y and the averages were processed onboard the analyzer using

$$y = \frac{G_{12}(f)}{G_{11}(f)}, \quad (4.7)$$

where G_{12} is the cross-spectrum given by

$$G_{12}(f) = \frac{1}{N} \sum_{n=1}^N S_{2,n} S_{1,n}^*, \quad (4.8)$$

G_{11} is the auto-spectrum given by

$$G_{11}(f) = \frac{1}{N} \sum_{n=1}^N S_{1,n} S_{1,n}^*, \quad (4.9)$$

and spectra S_i are given by

$$S_i(f) = \text{FFT}[W(t)p_i(t)]. \quad (4.10)$$

In the above expressions, FFT is the fast-Fourier transform, $W(t)$ is the Hann window function, $p_i(t)$ is the acoustic pressure signal at sensor position i , the $*$ indicates the complex conjugate, and N is the number of averages. Finally, the averaged transfer function y was transferred to a computer over GPIB, and the impedance was obtained off-line, from Eq. 3.93.

A comment about the averaging procedure is in order. In general, the expected value of the transfer function is given by the expected value of y in Eq. 4.7, not the quotient of the expected values as indicated by Eqs. 4.8 and 4.9. It can be shown however, that this bias error is small, and in practice, the number of averages required to suppress random errors makes this inherent bias negligible [119, p. 117]. Furthermore, the average used here is more robust against extraneous noise. In fact, it can be shown [119, p. 88] that the average used in Eq. 4.8 renders G_{12} totally immune from certain kinds of noise in $p_2(t)$. The existence of bias errors in transfer function measurements caused by input noise, inadequate spectral resolution, and nonlinear effects can be detected because these

all produce anomalies in the measured coherence function. A coherence function close to unity indicates that these effects are not present, therefore the coherence function was monitored during measurements, and often saved with the impedance data. The coherence function is given by

$$\gamma_{12}^2 = \frac{|G_{12}(f)|^2}{G_{11}(f)G_{22}(f)}, \quad 0 \leq \gamma_{12}^2 \leq 1. \quad (4.11)$$

With the bubbles and the excitation still turned on, another spectrum was taken at the top of the tube using the 8103. The three top-tube spectra were used to investigate the signal-to-noise ratio, and to ensure that the non-reflecting termination condition was being met.³ A photo of the impedance tube system as it looked for these measurements is shown in Fig. 4.16.

The above procedure was repeated for a total of six different void fractions, using one, four, and twelve needles installed in the BIM. For the case of one needle, a different bubble injection scheme was also used. A long needle was inserted from the top of the tube, down to the measurement plane. In this case, the BIM was not installed. The sample holder and the impedance tube were bolted directly together. This case was actually done first. As mentioned previously, adding additional long needles to create higher void fractions proved to be difficult because the position of each needle opening could not be maintained at the interface plane, thus the BIM was developed.

4.4.2 Instantaneous Measurement Procedure

The procedure for instantaneous impedance measurements was almost the same as that for the time-averaged measurements just described, but the order was different. Four sub-procedures were again performed, but in this order: cross-calibration, void fraction measurement, impedance measurement, and lastly, bubble size distribution measurement. The cross-calibration and void fraction measurement procedures were unchanged from the time-averaged procedure.

³See section 4.4.3 for an explanation of this condition.

The goal of this experiment was to observe the time variation of both the bubble size distribution and the propagation parameters. In order to do so, a broadband excitation signal that did not require averaging was needed. Such a signal is the periodic chirp, which is constructed to be periodic with respect to the data acquisition time window. The chirp was 66 milliseconds in length and a Hann window was used, which resulted in a resolution bandwidth of 15 Hz for a frequency range of 4–10 kHz. The data from 4–5 kHz and 9–10 kHz was not used because of the window. Since the window function lowers the amplitude at the beginning and the end of the chirp, the frequencies at the beginning and end of the chirp were greatly reduced in amplitude, and therefore unusable in the presence of normally occurring noise.

The cross-calibration was performed using the periodic chirp, then the void fraction measurements were performed. The impedance measurement procedure began as it did in the previous section but instead of taking 100 back-to-back averages, one chirp-excited impedance measurement was taken every 15 seconds for 25 minutes. This was done for a single void fraction case, using four needles. Since the void fraction used in this experiment had also been studied with the time-averaged procedure, the noise measurements with the 8103 at the top of the tube and with the wall-mounted sensors were not conducted again.

Ideally, the void fraction, bubble size distribution, and impedance of a bubbly fluid sample could all be measured at the same time in the same experiment. This was not possible with the existing apparatus. The next best thing was to sample the impedance on the same time scale as the bubble size distribution. The still camera could not operate fast enough to do this, so a digital video camera was used. The resolution of this video camera was not high enough to image many bubbles in the same frame, so high magnification was used and one or two bubbles from a single needle were imaged instead: the one just released, and in about half the frames, the one right above it. It was determined that new bubbles appeared in each frame, because when run at normal speed, the video appeared to run backwards; the bubbles appeared to be flowing back into the needle. The only way for this to occur is if new bubbles are appearing in each frame. Well after

the bubble production was initiated and the flow parameters were stabilized, video was recorded continuously for 25 minutes, but only 6 second blocks taken every 60 seconds were processed for 16 minutes at the beginning of the tape. Therefore, 6 seconds of video for each event translated into 180 frames and about 220 bubbles per event. Under such circumstances, the bubble population is sampled photographically for bubble size in $33\frac{1}{3}$ millisecond intervals, and the impedance measurements sample 66 milliseconds of the bubble population. The time scales are now much more compatible. A time line relating the impedance measurements and the size measurements is shown in Fig. 4.17. These images were all processed for bubble size, as described in Section 4.2.

4.4.3 Inversion Procedure

In this section, the method for obtaining the phase speed and attenuation from impedance measurements is described. Up to this point, results have been presented in terms of reflection coefficients or impedances, which follow directly from Eqs. 3.41, 3.43, or 3.93. In this chapter, propagation parameters are the quantities of interest. In order to obtain medium characterization from impedance measurements, a model of the termination is required, for instance, $z = i\rho c \tan kd$. In such a case, measurements taken with two different lengths d are required, and both c and k are obtained. If the sample holder is of sufficient length, such that no reflections return from the end during the measurement, the medium parameters are available directly from the impedance. In this case $z = \rho c$ and the complex sound speed is readily obtained. In practice, a tube of such length is not practical, but the attenuation provided by the bubbly fluid effectively makes a relatively short sample holder appear infinite in length. The present technique relies fully on this, and is useful down to void fraction as low as $O(10^{-5})$, where on-resonance attenuation is $O(2)$ dB/cm. The sample holder used in these experiments is 14 cm in length, and therefore, a round trip attenuation of about 56 dB is achieved, which is sufficient to render the reflected signal indistinguishable from the background noise. As void fraction increases, the attenuation also increases and attenuation rapidly extinguishes any reflections.

The medium parameters are therefore obtained in the following way: Since $z = \rho c$ for plane progressive waves, and $k = \omega/c$, the wave number k is given by

$$k = \frac{\omega\rho}{z} \quad (4.12)$$

where z is the measured impedance given by Eq. 3.93, and ρ is obtained from the mixture density relationship given by Eq. 1.6. Finally phase speed is given by

$$V = \frac{\omega}{\text{Re}[k]}, \quad (4.13)$$

and the attenuation coefficient is given by

$$A = 20 \log_{10}(e) \text{Im}[k] \quad (4.14)$$

in dB/unit length.

An assumption built in to this analysis is that only one plane wave mode exists in the sample holder. As discussed in Section 3.4.2, an elastic waveguide supports at least two modes at all frequencies, both with longitudinal and radial components. It has already been shown in Section 3.6.1 that the radial component of the plane wave mode is negligible, and it is ignored. The higher order mode has also been shown to be negligible. These assertions were made for bubble free water. Below resonance, the bubbly liquid medium is soft in comparison to pure water and the elastic waveguide effects are minimized even further. Above resonance, bubbly fluid is hard in comparison to pure water, and the elastic waveguide effects will play a different role. An inversion that properly accounts for both components of both modes does not exist, but in order to investigate this situation, some calculations using simplifying assumptions have been made. For now, these effects have been ignored, and more about this will be discussed in Section 4.5.3.

4.5 Results and Comparison to Theory

The type of spectrum resulting from the void fraction technique has already been shown. That result is typical and instead of showing more of these spectra, only the final results will be reported. The void fractions χ obtained for the experiments reported in this section are shown in Table 4.1. In addition, the phase speeds taken from each VF measurement will be displayed with the impedance tube data. Because of the different void fractions involved, and hence the different sound speeds and frequencies, the spectral measurements were specialized to each case, resulting in different resolution bandwidths, and therefore different estimated error. These error values are listed in the Table 4.1 and are smaller than the size of the data symbols used on the plots.

Case 1 is an exception. It was performed before the void fraction resonator was available. The void fraction for case 1 was estimated from the bubble size. At this low void fraction, only about 15–17 individual bubbles were in the sample holder at any given time. Using the average bubble volume and the number of bubbles, the void fraction was estimated.

4.5.1 Bubble Population Data Reduction

The bubble size distribution data in raw form is a list of bubble radii, obtained from the image analysis operation. This data must be processed before it can be input into the propagation model, in the form of a probability density function $\varphi(a)$, as previously shown in Section 2.2.4. Preliminary work indicated that a truncated normal probability density function (PDF) was a suitable statistical model for the bubbles being created by the single needle or the BIM. Four parameters describe this distribution: the minimum radius a_{\min} , the maximum radius a_{\max} , the mean a_0 and the standard deviation s . From the raw data, a_{\min} and a_{\max} were kept as inputs to the statistical model, and a fitting routine was used to obtain a_0 and s . The fitting was done in the following way. An empirical cumulative

distribution function (CDF) was created from the data,

$$P_{\text{emp}}(a) = \frac{\bar{n}(a)}{N}, \quad a_{\min} \leq a \leq a_{\max}, \quad (4.15)$$

where $\bar{n}(a)$ is the number of observations $\leq a$, and N is the total number of observations.

The model CDF is given by

$$P(a) = \text{Prob}[a(t) \leq a] = \int_{a_{\min}}^a \wp(\xi) d\xi, \quad [0 \leq P \leq 1], \quad (4.16)$$

where \wp is PDF for the normal distribution and is given by

$$\wp(a) = \frac{1}{s\sqrt{2\pi}} \exp\left[-\frac{(a - a_0)^2}{2s^2}\right], \quad a_{\min} \leq a \leq a_{\max}. \quad (4.17)$$

Model CDFs were then computed for a range of a_0 and s , and a two-dimensional minimization of the chi-squared parameter was performed, yielding the best-fit mean and standard deviation. The chi-squared parameter X^2 is given by [124]

$$X^2 = \sum_{i=1}^N \frac{(P_{\text{emp},i} - P_i)^2}{P_i}, \quad (4.18)$$

where the symbol X is used to avoid confusion with the symbol for void fraction. A typical surface of minimization is shown in Fig. D.4, which is located in Appendix D.

The fitting of statistical parameters using this empirical CDF method relied entirely on the data. If the PDF had been fitted to a histogram of the data, a choice would have been made for the histogram bin size, introducing an arbitrary adjustable parameter. Some of the distributions encountered in this work were clearly not centered on the mean, yet no suitable skew distribution was found. For instance, the log-normal distribution is indeed skew, but its tail is about three times longer than appropriate for the bubble size data. Therefore, the truncated normal distribution was used. The parameters of a non-truncated normal distribution can be calculated directly from the data using the usual

relations, $a_0 = 1/N \sum_{i=1}^N a_i$ and $s^2 = 1/(N-1) \sum_{i=1}^N (a_i - a_0)^2$, but this does not yield the correct parameters when the distribution is truncated. Hence, the empirical CDF method was used instead.

4.5.2 Time-Averaged Results

The time-averaged measurements will be presented in this section. The first case that will be shown was a preliminary case, obtained before the BIM was introduced. It is for a single 30 gauge needle, 20.3 cm in length. The needle was inserted into the top of the sample holder, and oriented such that the bubbles were being injected just at the interface between the sample holder and the impedance tube, and in the radial center of the tube. The bubble size distribution data was obtained in a similar way. The needle was inserted from the top down into the size measurement system, to the same depth as in the sample holder, 14 cm. There were only 30 bubbles analyzed in this case. The results of the bubble population analysis is shown in Fig. 4.18. In the top part of the figure, the empirical and the model CDF are shown, along with the population size N , the minimum and maximum bubble radii, and the X^2 goodness-of-fit parameter. In the bottom part of the figure, the best-fit model PDF is shown along with its parameters a_0 and s . A histogram of the bubble size data is also shown for reference, although it was not used in the analysis. From Table 4.1, the void fraction estimate was $\chi = 5.49 \times 10^{-5}$.

The phase speed and attenuation measured for this bubbly liquid is shown in Fig. 4.19, along with the theoretical predictions given by Eq. 2.1, where $\wp(a)$ is given by Eq. 2.24 and the four bubble population parameters from Fig. 4.18. A complete list of the parameters used in the production of Fig. 4.19 is given in Table 4.2. It appears that the data and the theory are quite similar, but they are shifted by about 2 kHz. Recall that the bubble size uncertainty is $\pm 7\%$, and that the size data and the acoustic data are not taken at the same time. Taking this into account by adjusting the radius so that the peak attenuation lines up yields Fig. 4.20, where the radii a_{\min} , a_0 and a_{\max} were multiplied by 1.04. The volume based void fraction estimate was then multiplied by $(1.04)^3$ yielding

$\chi = 6.2 \times 10^{-5}$. Agreement is now much better across the entire frequency range. Because of the low attenuation at this void fraction, a reduced frequency range is shown. Outside of this range, the non reflecting condition at the top of the tube was surely violated, which causes the inversion process described in Section 4.4.3 to fail.

In Section 3.8.3 the uncertainty of the impedance measurement was discussed. This uncertainty propagates through the inversion process to yield an uncertainty in the phase speed and attenuation measurements. Note that this discussion only refers to the error associated with the raw impedance measurement. Other sources of error will be discussed in Section 4.5.3. As was seen in Section 3.8.1, the reflectivity of the termination effects the amount of uncertainty in the measurement, and reflection coefficients with magnitudes close to unity cause the most error. The reflection coefficient for the case shown in Fig. 4.20 was calculated and its magnitude was found to be approximately 0.85, therefore not subject to the maximum error. Furthermore, the measured coherence function is close to unity across the entire frequency range, which results in low random error. Hence, the average error reported in Table 3.5 was applied to z in Eq. 4.12. This results in an average uncertainty of $\pm 2.2\%$ and the results are shown in Fig. 4.21.

One can see that the absolute uncertainty in phase speed appears very low at low frequencies, increases with frequency, but remains less than 650 m/s at 7 kHz. When shown on a log scale, the associated error bars would be approximately the same size as the data points themselves or smaller. This remains valid for all of the phase speed data reported in this chapter. The maximum absolute uncertainty in the attenuation measurement is approximately ± 0.12 dB/cm and occurs near resonance. Error bars for this uncertainty would be about the size of three data points near resonance, and less than the size of the data points at low attenuation. Error bars will not be shown in the remaining plots, but note that the data presented in this chapter has an inherent uncertainty associated with the impedance measurement of $\pm 2.2\%$. Also note that other, less quantifiable sources of error are discussed in Section 4.5.3.

The remainder of the cases will now be shown. These were all done using the bub-

ble injection manifold and the practices previously described for it. In general, better agreement between measurement and theory was found by fitting the bubble population statistical parameters, and to a lesser degree χ , but all well within the uncertainty of those measurements. Therefore, only the fitted results will be shown.

Case 2 was for a single 30 gauge needle 3.81 cm in length. It was installed in the BIM such that it injected bubbles into the radial center of the tube. The goal was to reproduce the results just reported, but with bubbles produced by the BIM. Unfortunately, the same bubble population was not produced by the BIM and this was attributed to the great difference in length between needles used in the two cases. The bubble population parameters for Case 2 are shown in Fig. 4.22. The measured phase speed and attenuation for Case 2 are shown in Fig. 4.23. The fitting of all four bubble population parameters was required to achieve agreement. The low frequency sound speeds obtained with the void fraction resonator are included in the figure, but the void fraction measured in the resonator did not appear to be the same as the void fraction during the impedance tube measurements. Therefore, the impedance tube data void fraction was also fitted. This large void fraction discrepancy occurred only for this single needle case. Again, the low attenuation resulted in a reduced frequency range. Although the fitted prediction agreed fairly well with the data around resonance, the degree of fitting required is more than desired.

Fitting the four bubble population statistics and the void fraction is easier than one might expect because each parameter has a fairly unique effect. The fitting was done one parameter at a time, by hand. Error between data and theory in a certain range was minimized in a least squares sense by adjusting each parameter in turn. Void fraction χ was fit using the low frequency phase speed. Mean bubble radius a_0 was fit using the frequency of peak attenuation. Standard deviation s was fit using the slope of the attenuation curve on the low frequency side of the peak attenuation. Minimum bubble radius a_{\min} was fit using the width of the attenuation peak on the low frequency side of the peak. Maximum bubble radius a_{\max} was fit using the width of the attenuation peak on

the high frequency side of the peak. This order was not necessarily followed consistently, or in a methodical manner. A little experience adjusting parameters by hand, and one can rather quickly determine the best fit values. It should be noted, no attempt was made to automatically fit all five parameters simultaneously to the absolute minimum error across the frequency range. The region around resonance was given priority. Fitting of all five parameters was not always necessary. An asterisk next to a parameter in Table 4.2 indicates that parameter was fitted.

The result in Fig. 4.23 brings up an interesting possibility. The data and prediction were brought into agreement by narrowing the distribution. Perhaps the time scale of the two measurements was incompatible. The photographs used to produce the bubble size distribution were taken approximately 15 seconds apart, and exactly 50 photographs were obtained. Therefore the bubble population was sampled for about $12\frac{1}{2}$ minutes. Each impedance measurement required 400 milliseconds and 100 averages were performed, therefore, the impedance measurement sampled the bubble population for 40 seconds. If the mean bubble size was changing by a few percent per minute during these measurements, then the photographically measured bubble size distribution would be wider than the acoustically sampled case.

Fortunately, the time order of the bubble size photographs was preserved, therefore this hypothesis was investigated using a plot of the running bubble radius average versus time. The result is shown in Fig. 4.24 for a portion of the data set. The open circles represent the running average, taken every 25 bubbles for 7.5 minutes. This bubble size data was not taken at the same time as the impedance data was taken, but suppose that it was. If the impedance data was taken between 2 minutes and 2 minutes 40 seconds, then it would have sampled just a small portion of the total bubble population. This certainly indicates that the time scales of the two measurements were out of synchronization. Since it was not possible to make the bubble size measurements and the impedance measurements at the same time, and because they are on different time scales, fitting of the predicted propagation parameters using adjustable bubble size population statistics is an appropriate

way to compare the measurements with theory.

This also explains why less fitting was required for Case 1 in Fig. 4.24. Only 30 bubbles were imaged, over approximately 4 minutes, yielding a narrow distribution of sizes. In addition, the long needle most likely contributed to this as well. A long needle has the effect of stabilizing the bubble production. The flow resistance presented by the long needle is much greater than the flow resistance presented by a short needle. The total impedance looking into an open needle is the series sum of this more-or-less constant flow resistance and the impedance associated with bubble growth, which changes with time very rapidly as bubbles break off. For the long needle, there is a large constant flow resistance and a smaller fluctuating part. For a short needle, there is a much smaller constant flow resistance and a similarly sized fluctuating part. Therefore, the flow rate into the long needle is more stable than into a short needle, resulting in a narrower size distribution for the long needle.

Four 30-gauge needles, 2.86 cm in length, were installed in the BIM for Cases 3, 4 and 5. Each represents a different void fraction, which was achieved by slightly varying the overall flow rate. The needles were spaced 90° apart around the circumference of the BIM, and were inserted 1.27 cm into the tube. A single bubble size distribution measurement obtained with four needles and the intermediate flow rate is shown in Fig. 4.25. The measured phase speed and attenuation for Cases 3, 4 and 5 are shown along with their associated predictions in Figs. 4.26, 4.27 and 4.28, respectively.

The final case that will be shown was for twelve 30-gauge needles installed in the BIM, arranged as shown in Fig. 4.2-b. The needles used to form the inner circle were 2.86 cm in length, and the remaining needles were 1.91 cm in length. Case 6 represents the highest void fraction that could be produced with a resonance frequency close to 5 kHz. Any increase in flow rate would have also resulted in an increase in bubble size, and therefore, a decrease in resonance frequency. The bubble population statistics for Case 6 are shown in Fig. 4.29. The measured phase speed and attenuation for Case 6 are shown along with their associated predictions in Figs. 4.30.

4.5.3 Discussion of Time-Averaged Results

A number of general comments about the phase speed and attenuation data will be made, and then these points will be discussed more fully. The predicted phase speeds above the resonance regime are generally higher than the measured values, even after fitting. The agreement is generally better for attenuation, and is actually quite good, except in Case 6. The low void fraction measurements display fewer rapid fluctuations than the high void fraction cases; there are strong and rapid fluctuations in the Case 6 measurements. The fitted bubble population was always narrower than the measured bubble population. The low-frequency resonator void fraction results agreed well with the measurements made in the resonance regime in that the theoretical predictions tied them together well.

Elastic Waveguide Effects

Elastic waveguide effects were mentioned in reference to the impedance data inversion procedure in Section 4.4.3. In general, it has been shown that the phase speed in an elastic waveguide is reduced relative to the fluid's unconfined sound speed and is dispersive. As the frequency increases through resonance, the medium changes from acoustically soft to acoustically hard, and the elastic waveguide effects should become more pronounced. This could explain the mismatch between measurement and theory above resonance. The effect was investigated by starting with a very simple case. Propagation in the impedance tube was investigated at a single frequency using Eq. 3.72. The frequency was 7 kHz, which would represent an above resonance region in which a super-sonic bubbly fluid phase speed is predicted. Two modes are predicted to propagate in such a waveguide, and their phase speeds were calculated for a range of void fractions. In order to use Eq. 3.72, the attenuation in the bubbly fluid was set to zero, which is far from the case, but the results are still useful for insight, if not absolutely accurate.

These results are presented in Fig. 4.31. The predicted phase speed of each of the two modes is plotted as a function of the bubbly fluid sound speed. In other words, according

to the elastic waveguide model, if the internal fluid sound speed was that given on the x -axis, then the phase speed of each mode would be that given by the solid lines labeled “elastic mode 00” and “elastic mode 01.” The leading 0 indicates these are axisymmetric modes. If the waveguide was truly rigid, the waveguide sound speed would be the same as the unconfined bubbly fluid sound speed. This case is represented by the dashed line labeled “rigid.” (The plot would be straight on a linear scale but is curved because the x -axis is represented with a log scale.) The vertical dashed line represents a transition region. Below this region, mode 00 has a phase speed close to the rigid waveguide sound speed, and nearly plane wavefronts with little radial displacement. Mode 01 has curved wavefronts (concave down) and is not excited easily by plane disturbances. Above the transition region, both modes have curved wavefronts of almost the same concave up shape and similar radial components. Within the transition region, the phase speeds of the two modes are similar. Also notice, that from just below the transition region and higher, the two elastic modes are always lower than the rigid-walled sound speed. This is a possible explanation why higher phase speeds are not measured, but it also brings up another issue.

According to the elastic waveguide theory, at some point around the transition region, the 01 mode should start to become important. Now consider the situation within the impedance tube. An incoming plane wave begins to interact with the bubbly fluid at the interface between the tube and the sample holder. Part of the energy is reflected back into the impedance tube, and the part that enters finds no suitable plane wave mode to deposit its energy. The incident energy must get divided up into two propagating modes, and possibly a great number of evanescent modes. In such a case, the inversion that is used to extract phase speed and attenuation from the impedance measurements would break down, because it assumes only a single plane progressive mode.

Further evidence in support of this is available directly from the measured results. Consider the data in Fig. 4.20, which show a measured phase speed greater than 10,000 m/s at 7 kHz. According to Fig. 4.31, the maximum phase speed for mode 00 is less than

5000 m/s and about 7000 m/s for mode 01. This is still below cutoff for the next higher order mode, so nothing should be able to propagate at 10,000 m/s. The existence of other modes must interfering in such a way that an effective single mode phase speed is obtained from the inversion.

There is at least one case in the literature where a higher order mode has been used effectively in an impedance tube measurement. Dalmont and Bruneau were able to separate the contributions of the plane wave mode and the first helical mode propagating in a tube [125]. They did this by taking advantage of the spatial distribution of the helical mode and used sensors distributed in the radial plane.

Encouraged by their results, an initial attempt was made to find a more suitable inversion using a very simple model. It was assumed that only two plane-wave-like modes could exist in the tube, with phase speeds given by Eq. 3.72. The radial components and any evanescent modes were ignored. The impedance at the interface would then be given by

$$z = \rho_2 c_0 + \rho_2 c_1, \quad (4.19)$$

where ρ_2 is the density of the bubbly fluid, and c_0 and c_1 are the complex sound speeds of mode 00 and 01, respectively, given by $c_i = 1/(u_i - v_i)$. The left hand side is the measured impedance, which has real and imaginary parts. The right hand side can also be separated into real and imaginary parts, which is given by

$$z_r + iz_i = \rho_2 \left[\frac{u_0}{u_0^2 + v_0^2} + \frac{u_1}{u_1^2 + v_1^2} \right] + i\rho_2 \left[\frac{v_1}{u_0^2 + v_0^2} + \frac{v_1}{u_1^2 + v_1^2} \right] \quad (4.20)$$

The real parts, u_0 and u_1 were calculated from the elastic waveguide model, with a guessed bubbly fluid phase speed V_{bf} used as the input. Specifically, Eq. 3.72 yields two phase speeds c_{00} and c_{01} as a function of V_{bf} , from which $u_0 = 1/c_{00}$ and $u_1 = 1/c_{01}$ were obtained. The idea was that one could iterate to find a V_{bf} that would satisfy Eq. 4.20. Then one could solve for the v_i 's and obtain the two attenuation coefficients A_i from

Eq. 2.19. Unfortunately this did not work. Satisfaction of Eq. 4.20 yielded v_i 's of opposite sign, which is not allowed because it would violate causality. It was thus concluded that Eq. 4.20 is not the proper model, and pursuing a more appropriate model was beyond the present scope.

Signal and Noise Issues

Because the measurements seemed to include more sharp and rapid fluctuations as the void fraction increased, and because the source drive level was kept fairly constant, bubble noise was thought of as a possible explanation. As the void fraction was increased, there would be more and more noise produced as the bubbles broke off the needles. Perhaps this noise was corrupting the impedance measurement, because it represents energy entering into the impedance tube from a direction not allowed. The measured coherence function can be used to investigate the signal-to-noise issue. A coherence function greater than zero but less than unity implies one or a combination of the following [124]:

1. The presence of extraneous noise in the measurements.
2. The output signal includes the result of excitation not measured by the input.
3. Some nonlinearity between sensor 1 and 2.
4. Resolution bias errors are present.

Items 3 and 4 were be ruled out because coherence functions obtained from standard measurements with a transmission line termination were always close to unity, except in narrow bands. These bands are associated with nulls in the field that happen to be co-located with one of the pressure sensors. A typical series of coherence measurements is shown in Fig. 4.32. Changing to a bubbly fluid sample does not effect the linearity of the propagation between the two sensors. It certainly does not change the resolution bandwidth of the measurement.

Items 1 and 2 are possibilities, though, and an experiment was done to investigate this. The conditions of Case 5 were again used because this case represents the onset of the fluctuations. Impedance measurements were conducted for five signal-to-noise ratios (SNR), in increments of 10 dB. The hope was that the fluctuations would be proportional to SNR. Since the SNR can not be varied directly, the drive level was incremented in steps of 10 dB where 0 dB is the typical drive level. The results are shown in Fig. 4.33. First of all, although the observable experimental conditions were repeated, the level of fluctuation is lower in the present case than it was in Case 5. This is unexplained. It *is* clear that diminishing the drive level lowers the coherence between the two sensors dramatically, as evident in the coherence plot, between 5 and 6 kHz. There is little noticeable change, however, in coherence above 6.5 kHz, where most of the fluctuations appear. The loss of coherence makes itself evident in the phase speed and attenuation measurements via the increase in scatter for the -20 and -30 dB drive levels below 6 kHz, but the level of fluctuation appears to be only weakly effected by drive level above 6 kHz.

What about the coherence function for Case 6, in which the fluctuations are the most extreme of the entire data set? The coherence function for Case 6 is shown in Fig. 4.34. Never does it fall below 0.7, which is approximately the same coherence as in the -10 dB case of Fig. 4.33, where the fluctuations are much less severe. This seems to rule out low SNR, as a cause of these fluctuations, at least from a coherence standpoint.

What else could be causing these perturbations? Perhaps it could be the needles, or more specifically, the needles and the air bubbles attached to them. Case 1 shows none of these fluctuations. It was made with a single long needle. Case 2, which is for nearly the same bubble content, shows only a hint of these fluctuations. The only difference is the presence of the BIM, and the needle size and location, but this new location is perhaps crucial. The needle is now parallel to and residing directly in the measurement plane. It presents a larger cross-section than does the long needle inserted from the top, and that frontal area is positioned completely in the plane of interest, not spread out throughout the length of the sample holder. Cases 3, 4 and 5 are for four needles in the

measurement plane and are accompanied by and increased fluctuation level. Case 6 is for twelve needles in the measurement plane, and the fluctuation level increases further. Presence of needles in the measurement place could be a possible cause of the fluctuations, but more investigation is necessary.

There is a chance that these fluctuations are real. Before a bubble detaches from its needle and rises upward, it spends some time attached to the end of the needle during the growth phase. During that time, it is certainly being interrogated by the incoming sound wave and therefore contributing to the impedance of the bubbly fluid. A multiple delta function bubble distribution could possibly account for the sharp attenuation peaks that have been referred to as fluctuations in this discussion. It is less clear why there would be several different sizes present all at the same time.

There was another interesting phenomenon uncovered during the SNR experiment. This occurred at the high drive level; the +10 dB case in Fig. 4.32 shown in black. The pertinent feature is a shift in frequency of the peak attenuation. This effect was robust and repeatable. One could go back and forth between the +10 dB and the 0 dB drive levels and observe the peak move back and forth between 5.25 and 5.75 kHz in real time. Was this a nonlinear response of the bubbly fluid? If so, this could have important consequences in real-world applications. For instance, in a surf zone mine hunting scenario, a bubble cloud could be distinguished from a moored mine because the bubble cloud would have drive level dependent scattering characteristics, compared to a mine which would not. Unfortunately, another possible explanation for this shift could not be ruled out. Increasing the drive level may have also changed the bubble production such that smaller bubbles were produced, which would also explain the shift in peak frequency. Additional investigation is required.

Bubble Population Parameters and Void Fraction

The bubble populations resulting from fitting the impedance tube data always resulted in narrower distributions than those obtained from the photographic data. This further emphasizes the idea that the time scales of observation were out of synchronization,

and further motivates the instantaneous experiments. In order to validate a broadband propagation model, knowledge of the bubble population needs to be perhaps an order of magnitude more accurate than in these experiments. Bubble population parameter measurement should be conducted in-situ with the impedance measurements. On the other hand, the low frequency void fraction measurement technique proved to be reliable and agreement was found with both the resonance regime measurements and calculations. In-situ incorporation of the void fraction measurement would be ideal, but this task could perhaps be continued off-line. Finally, increased control of bubble production would be beneficial, but if in situ population measurements are actually available, this last point is not so important.

4.5.4 Instantaneous Results

An assumption made early in this work was that the experimental bubble populations would exhibit statistics that were stationary in time. As shown in Section 4.5.2, this was found to be incorrect. The bubble statistics were not stationary on the time scale of the impedance measurements. Since the bubble population characterization and the impedance measurement could not be done at the same time, an absolute comparison between the propagation model and experimental measurement was not possible. Investigation of the variability was possible, and therefore became the goal of this experiment. In order to do this, the bubble population parameters were sampled on the same time scale as the impedance observations. Using the procedure described in Section 4.4.2, a total of 16 bubble populations were analyzed. The time line for this experiment was shown in Fig. 4.17. Using the technique given in Section 4.5.1, the bubble population statistics were obtained for each of the 16 populations. The CDF/PDF plots for the entire data set are presented in Appendix D along with additional details about the data acquisition and analysis. One can get a good qualitative indication of the amount of variation by looking at the 16 histograms presented in Appendix D. The bubble population is changing dramatically on this time scale. Although void fraction was not one of the measured

parameters, it was possible to estimate the effective void fraction of each population from the total number of bubbles in the population.

In order to get an overview of the time dependency, each of the statistical parameters and the estimated void fraction were plotted as a function of time. The results are shown in Figs. 4.35–4.37. In order to be specific about the notation used in these figures, the global mean of a variable x is given by $\langle x \rangle$, where

$$\langle x \rangle = \frac{1}{16} \sum_{i=1}^{16} x(t_i), \quad (4.21)$$

and the standard deviation of x is given by

$$\sigma = \left\{ \frac{1}{16-1} \sum_{i=1}^{16} [x(t_i) - \langle x \rangle]^2 \right\}^{\frac{1}{2}}, \quad (4.22)$$

The variation of the mean bubble radius $a_0(t)$ and the radius standard deviation $s(t)$ is shown in Fig. 4.35. It may appear that a start-up transient was captured at the beginning of the upper plot, but recall that the observable control parameters of the bubble production process had reached steady state prior to the image acquisition and were not fluctuating. The curves shown in Figs. 4.35 through 4.37 confirm that the bubble population parameters are fluctuating dramatically and rapidly. Variation greater than 2 standard deviations can occur within a minute, and there is also evidence of long term trends, specifically in the standard deviation.

The results of the impedance measurements will be presented next. Recall that a 66 millisecond impedance sweep was obtained once every 15 seconds for 25 minutes. For simplicity, each measurement event will be referred to as a “ping.” The bubble size study was done for a single needle as mentioned previously, but the impedance measurements were done with 4 needles, as in Cases 3–5, reported in Section 4.5.2. The void fraction, determined just prior to the impedance measurements using the resonator technique, was 3.9×10^{-4} . Phase speed V and attenuation A were calculated for each ping. For com-

patibility with the bubble size data, V and A for four consecutive measurements were averaged together to represent one minute of time, then the next four were averaged, and so on, until 16 minutes of measured V and A were obtained. The remaining 9 minutes of data will not be reported at this time.

As an overview of the data, the 16 curves are all plotted together in Fig. 4.38, and the overall degree of ping-to-ping variation can be seen. Another feature of interest is the region of anomalous phase speed fluctuation around 7.5–7.7 kHz. These fluctuations look similar to the ones observed previously (Fig. 4.26, for example), but these are somewhat different. Instead of being merely fluctuations, these are apparently numerical singularities, because prior to the averaging, a number of the cases showed a point or two of negative phase speed. Therefore, these must be artifacts and they are most likely caused by poor resolution bandwidth. In order to achieve a short ping, resolution bandwidth was lowered to 15 Hz, where 2.5 Hz is typical. A study of resolution bandwidth error was conducted with the impedance tube using a transmission line termination. The results will not be shown, but similar errors appeared as RBW decreased. The coherence function would have been a useful diagnostic, but unfortunately, the transfer functions were saved, instead of the cross- and auto-spectra required to calculate coherence.

The eventual goal here is the quantitative comparison of this data with predictions based upon the bubble size measurement. This will eventually be accomplished by comparing two parameters, the maximum attenuation and the frequency at which it occurs. As a precursor, the predicted phase speeds and attenuations must be calculated, and a qualitative comparison can be made by showing them plotted together, as was done with the measurements in Fig. 4.38. The calculations were carried out with Eqs. 2.1 and 2.24, the measured bubble population parameters from Figs. 4.35 and 4.36, and a void fraction $\chi = 3.9 \times 10^{-4}$. Since the variation in the void fraction was only estimated, it was kept constant. All 16 curves are shown in Fig. 4.39. Based solely on visual comparison and excluding the measured phase speed above 7.5 kHz, it appears that the level of variation is similar at most frequencies, but somewhat greater in the calculated case near resonance.

At first one may think this is counter-intuitive, because the measurements were made with four needles and we know that the distribution of sizes produced by four needles is wider than with a single needle. The effects of resonance are more pronounced for a narrow distribution, though. Perhaps a narrow distribution is more sensitive to small population changes than is a wider distribution.

In order to compare the variability of these multifaceted measurements and calculations, attention will be focused on two parameters, the maximum attenuation $A_{\max}(t)$ and the frequency at which that maximum attenuation occurs, $f_0(t)$. Since the relative variation is of interest, the results will be presented in normalized form, $A_{\max}/\langle A_{\max} \rangle$ and $f_0/\langle f_0 \rangle$, where the brackets represent the global mean as defined in Eq. 4.21, and the normalized standard deviation is given by

$$\bar{\sigma} = \left\{ \frac{1}{16-1} \sum_{i=1}^{16} \left[\frac{x(t_i)}{\langle x \rangle} - 1 \right]^2 \right\}^{\frac{1}{2}} . \quad (4.23)$$

The results are given in Fig. 4.40 and 4.41 for attenuation and frequency, respectively. When cast in this form, the variation we expect to see based on our measured bubble population statistics is very close to the variation we actually observe. For the normalized frequency parameter, we expect a $\bar{\sigma}$ variation of 0.87% and we observe 0.84%. For the normalized attenuation parameter we expect a variation of 4.9% and we observe 5.3%.

4.5.5 Discussion of Instantaneous Results

The similarity between predicted and observed variability of the peak attenuation and its frequency is quite good. Making comparisons of the variation minimized the problems relating to the uncertainty of the instantaneous bubble population, including the uncertainty in the absolute size of the bubbles. As discussed in Appendix D, the uncertainty in bubble radius for the instantaneous experiment was about 10%.

In the region around peak attenuation, the phase speed is near its minimum, hence the elastic waveguide effects are minimized. Therefore, the inversion problems that are

evident well above resonance play no role here. In addition to the inherent errors already discussed there is an additional source of bias error for this experiment. The resolution bias error was made negligible in the time-averaged experiment, as confirmed by near unity measured coherences. The short excitation time lead to a resolution bandwidth of 15 Hz, which increased the maximum estimated resolution bias errors a small amount. The level of error is still significantly smaller than the observed fluctuation, which can confidently be attributed to changes in the medium itself.

It has long been predicted from theory that propagation in bubbly fluids is sensitive to the bubble population parameters. This was investigated theoretically and again shown to be true in Chapter 2. The statistical representation of bubble population parameters has also been discussed in the literature. The measurements presented in this section are unique, as far as the author knows, putting together time varying bubble population measurements with time varying propagation parameter measurements for the first time. The significance of these results is the following: Existing theory, specifically that represented by Eq. 2.1, is capable of predicting the *relative variability* of sound propagation parameters in bubbly liquids at resonance, if the bubble population parameters are known. This appears to be the case, despite the fact that the *absolute accuracy* of the theory represented by Eq. 2.1 has not been verified experimentally. A second significant result is this: If given adequate knowledge of the bubble size distribution, the impedance tube apparatus and technique described in this work *does make it possible* to test the absolute accuracy of bubbly liquid sound propagation theory at resonance. This has never before been possible at void fractions above approximately 10^{-4} , but in order to proceed, the development of a new apparatus that produces bubble populations with time invariant statistics, or the development of a co-located bubble sizing instrument will be required.

Case	1	2	3	4	5	6
$\chi (\times 10^{-5})$	5.49 [†]	4.2	33	41	54	270
ℓ (cm)	–	31.5	31.5	31.5	31.5	14.8
$\Delta\ell$ (cm)	–	± 0.2	± 0.2	± 0.2	± 0.2	± 0.2
f (Hz)	–	1585	857.5	810.0	730.0	706.0
Δf (Hz)	–	± 5.000	± 6.875	± 6.125	± 6.000	± 6.125
Δc_{\max} (m/s)	–	± 9.49	± 7.76	± 7.10	± 6.70	± 4.63
$\Delta\chi$ (%)	–	± 3.53	± 3.38	± 3.21	± 3.29	± 4.67

Table 4.1: The table contains the results and the error analysis for the void fraction measurements. [†]For Case 1, χ was estimated from optical measurements.

Case	1	1	2	3	4	5	6
Figure	4.19	4.20	4.23	4.26	4.27	4.28	4.30
$\chi (\times 10^{-5})$	5.49	6.20*	8.00*	33	41	54	270
$c_\ell = c_1$ (m/s)	1455.5	1455.5	1456.5	1457.4	1455.8	1458.0	1455.9
a_{\min} (mm)	0.6033	0.627*	0.625*	0.580*	0.580*	0.580*	0.500*
a_0 (mm)	0.612	0.6365*	0.6742*	0.600*	0.622*	0.638*	0.620*
a_{\max} (mm)	0.620	0.6448*	0.725*	0.750*	0.710*	0.750*	0.800*
s (mm)	0.005	0.005	0.020*	0.031*	0.038*	0.035*	0.10*

Table 4.2: The table contains the parameters used to produce the Figs. 4.28.–4.30. All the physical parameters listed in Table 2.1, except c_ℓ were also used. The presence of the asterisk (*) in a cell indicates that parameter was fitted.

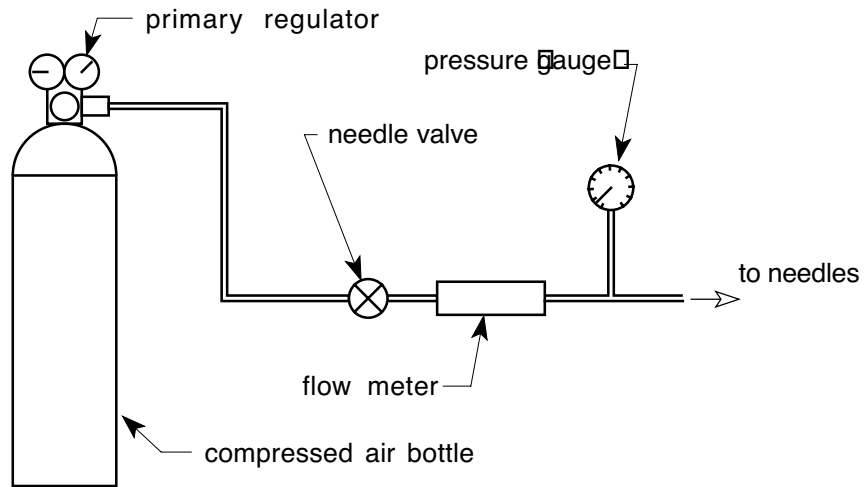


Figure 4.1: A schematic diagram of the air delivery system is shown

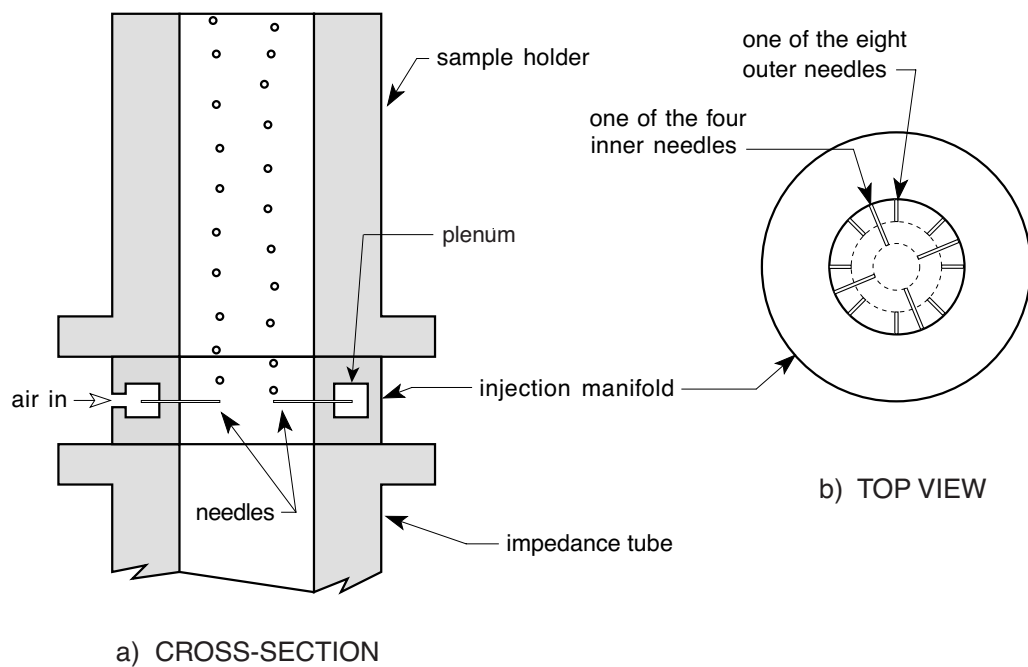


Figure 4.2: A schematic diagram of the bubble injection manifold is shown. Part a) is a cross-sectional view showing the injection manifold mounted between the impedance tube and the sample holder. Two needles are shown making bubbles. Part b) shows a top view of the injection manifold separated from the impedance tube and the sample holder. All twelve needles are in place, forming an inner circle of four and an outer circle of eight.

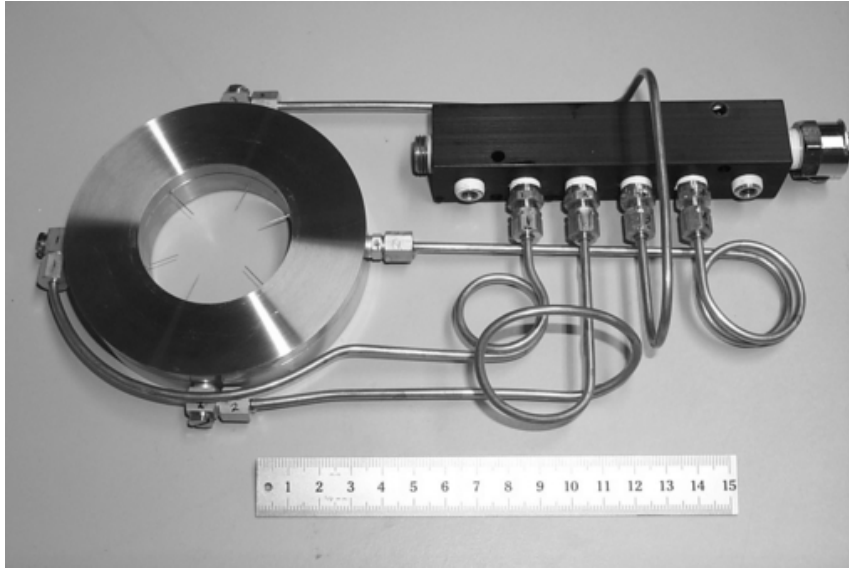


Figure 4.3: The photograph shows the four equal length conduits, made of 3.175 mm diameter copper tubing, which connect the air delivery system to the air injection manifold, insuring an even distribution of air to the plenum. Six 30 gauge needles are shown extending 1.27 cm into the inner diameter of the tube. The scale is 15 cm in length.

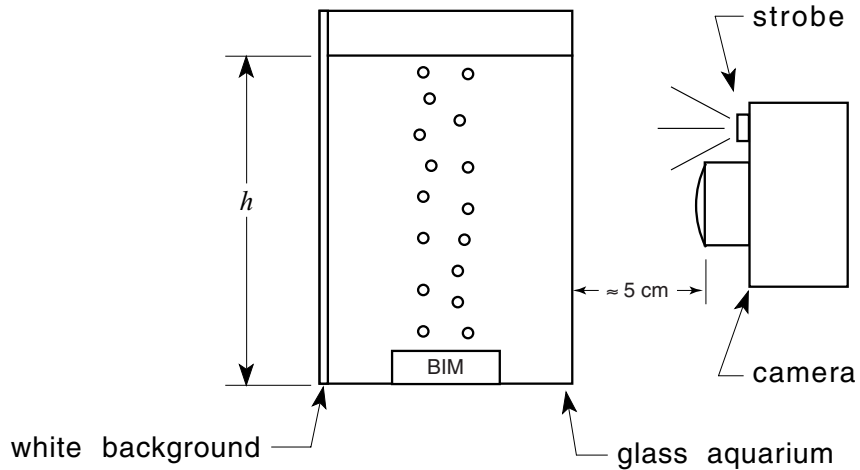


Figure 4.4: A schematic diagram of the bubble size measurement system is shown with the air injection manifold producing bubbles. The height h of the water column is the same as that inside the sample holder during impedance measurements.

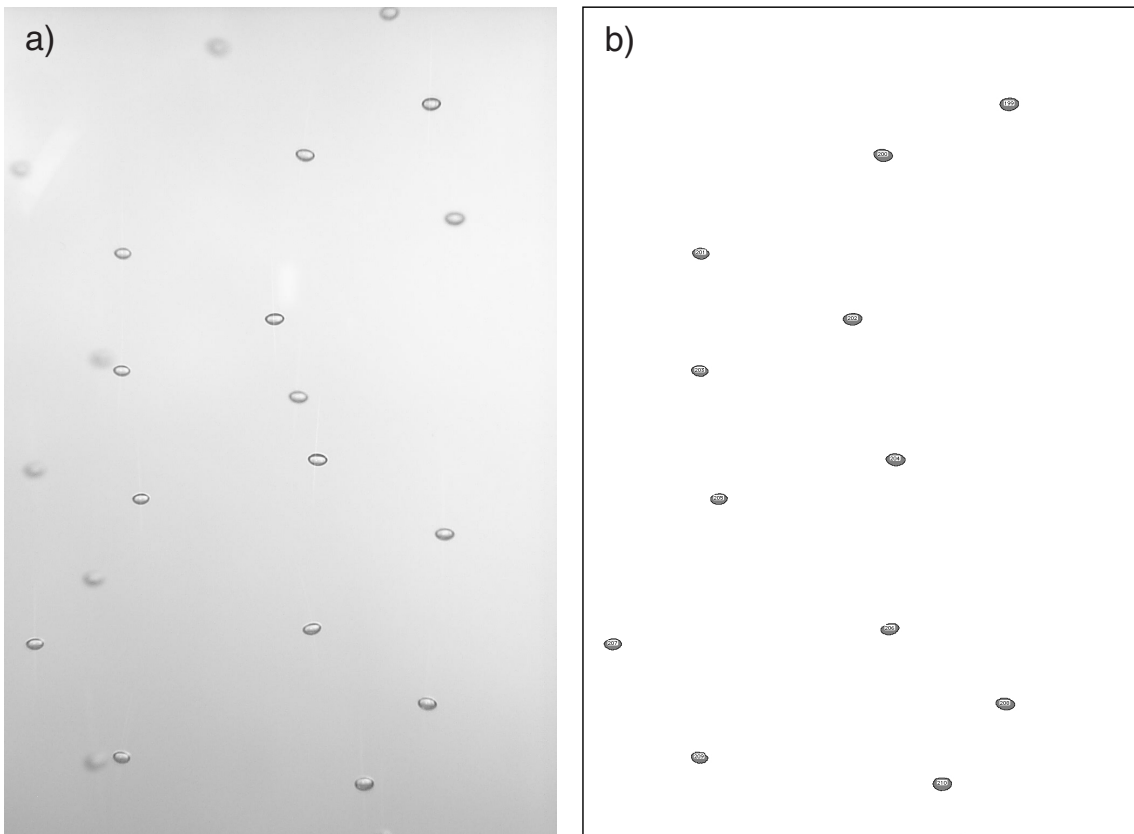


Figure 4.5: A typical image obtained with the bubble size measurement system is shown in a). These bubbles are of a size large enough to exhibit the oblate spheroid shape. The same image after processing is shown in b). Each bubble is outlined and assigned a number and the size data is stored in a file.

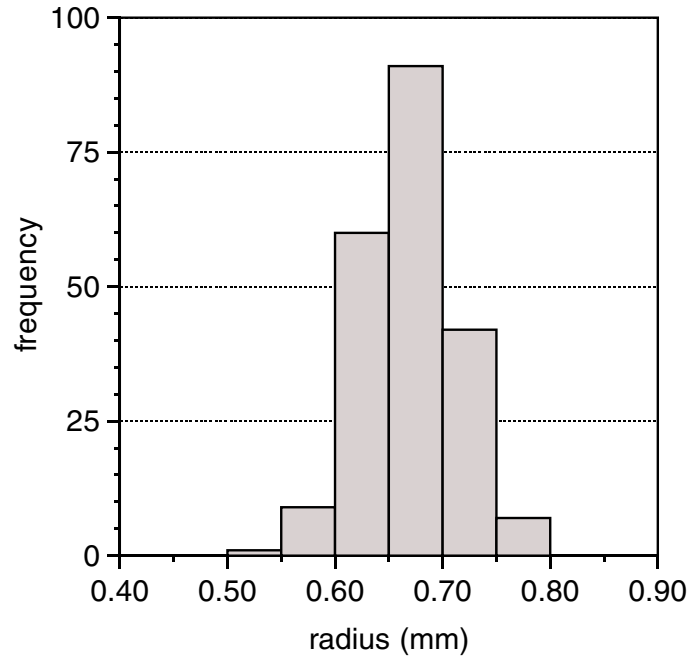


Figure 4.6: The bubble size distribution is shown for the image in Fig. 4.5-b and 19 others like it, based on the oblate spheroid analysis of Eq. 4.2. A total of 210 bubbles were analyzed in this example.

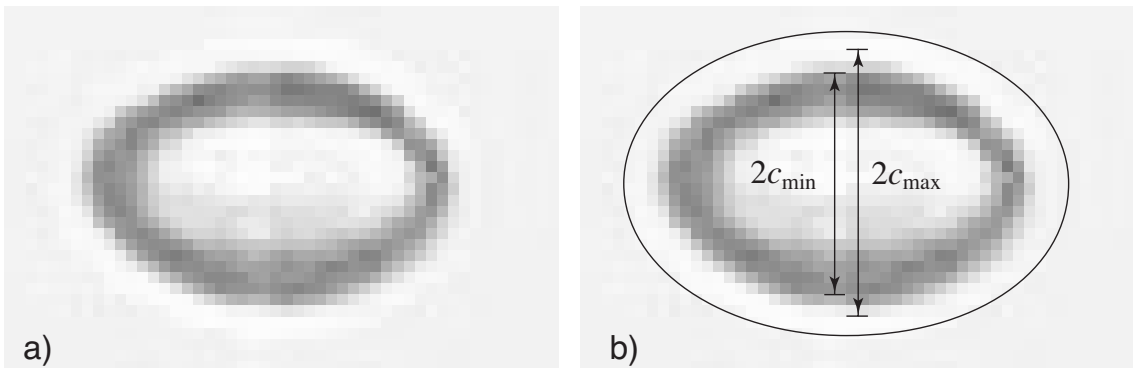


Figure 4.7: An enlarged image of one of the bubbles from Fig. 4.5 is shown in a). Uncertainty due to pixelation is shown in b).

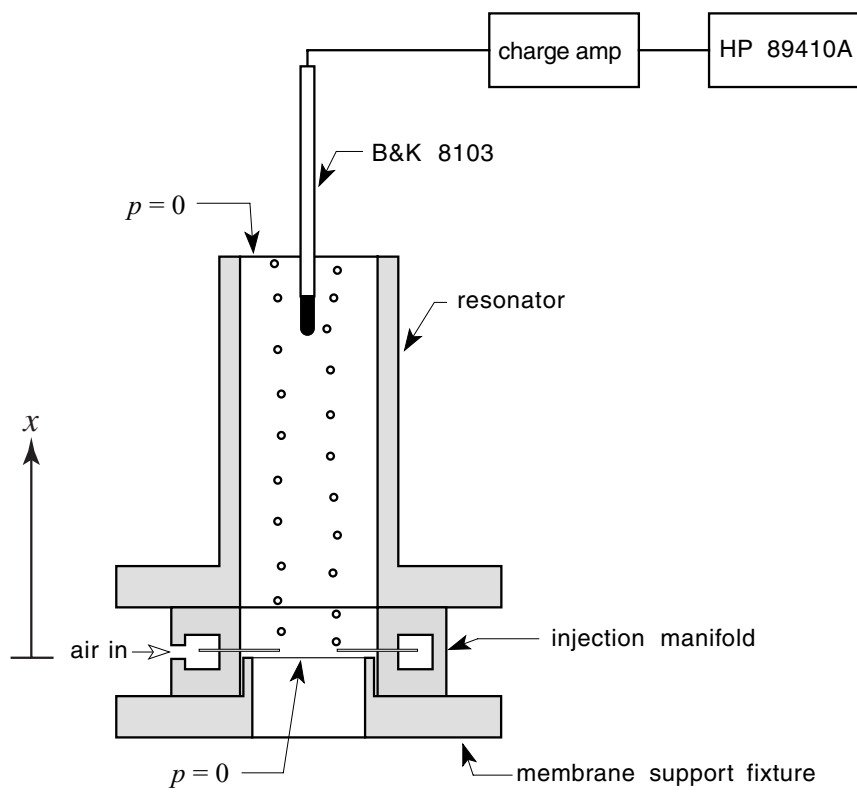


Figure 4.8: A schematic diagram of the void fraction resonator is shown.



Figure 4.9: A photograph is shown of the void fraction resonator with the bubble injection manifold mounted at the bottom of the tube. The scale is 15 cm in length.



Figure 4.10: The void fraction resonator is shown with the hydrophone positioning system attached.

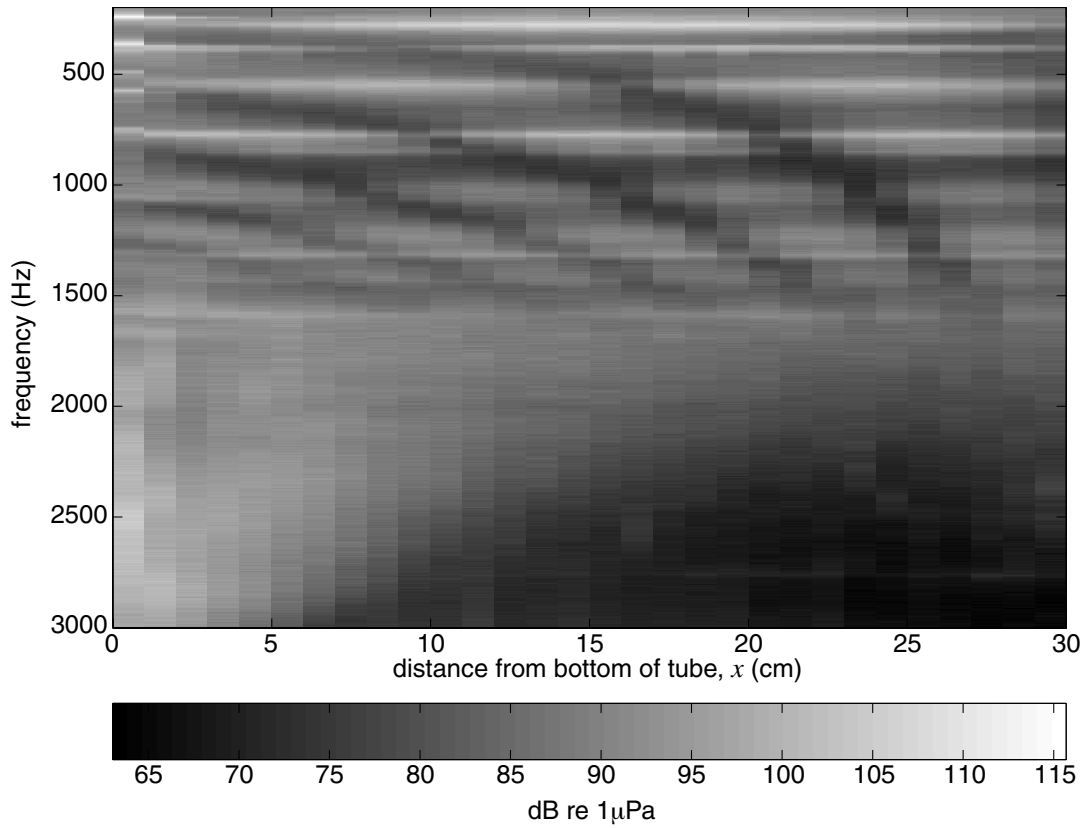


Figure 4.11: The acoustic pressure field measured inside the void fraction resonator is shown for bubbles produced by an airflow of 108ml/min at 21.85 kPa.

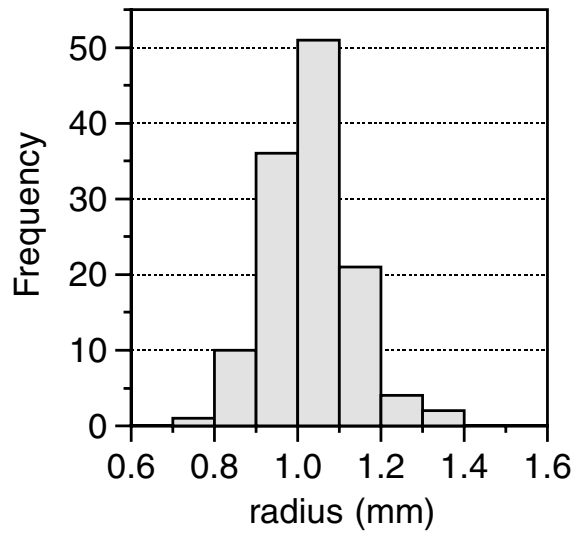


Figure 4.12: The bubble size distribution is shown for the axial scan measurements of Fig. 4.11. The approximate resonance frequency calculated by Eq. 1.15 is 3.1 kHz.

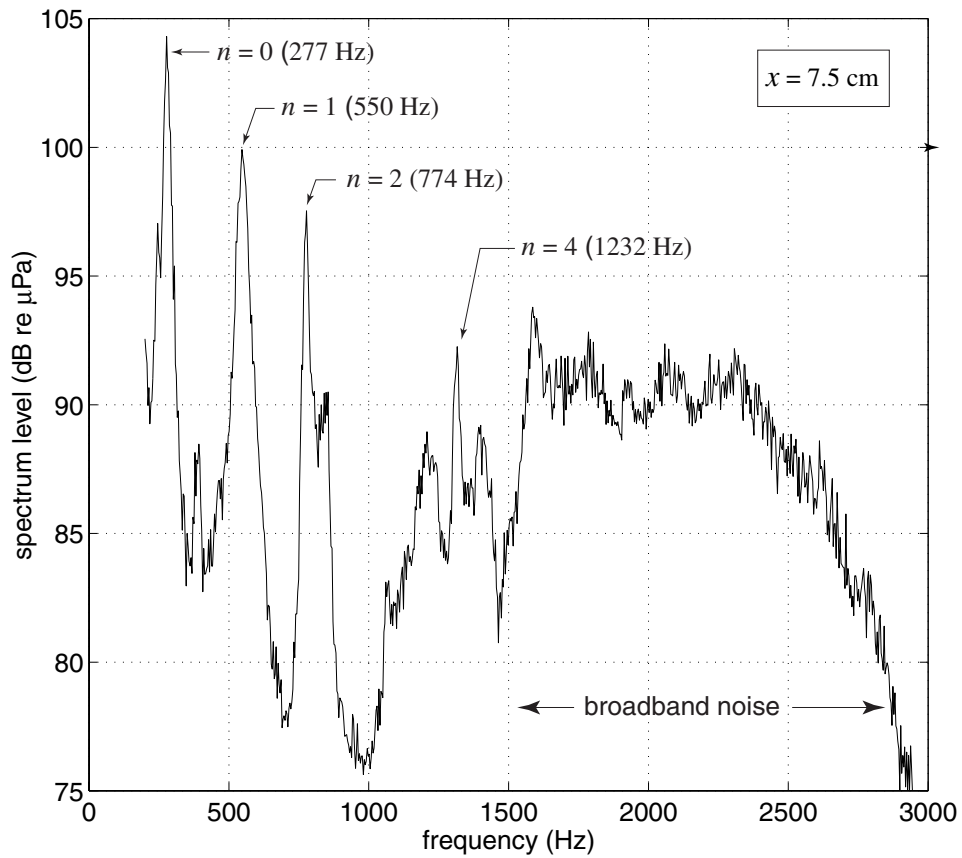


Figure 4.13: A single spectrum obtained from the void fraction resonator at $x = 7.5 \text{ cm}$ is shown. This corresponds to a slice out of Fig. 4.11 at $x = 7.5 \text{ cm}$. The resonance peaks are identified, and the region of bubble generated broadband noise is shown. Above about 2.3 kHz, the spectrum level decreases due to absorption associated with bubble resonance.

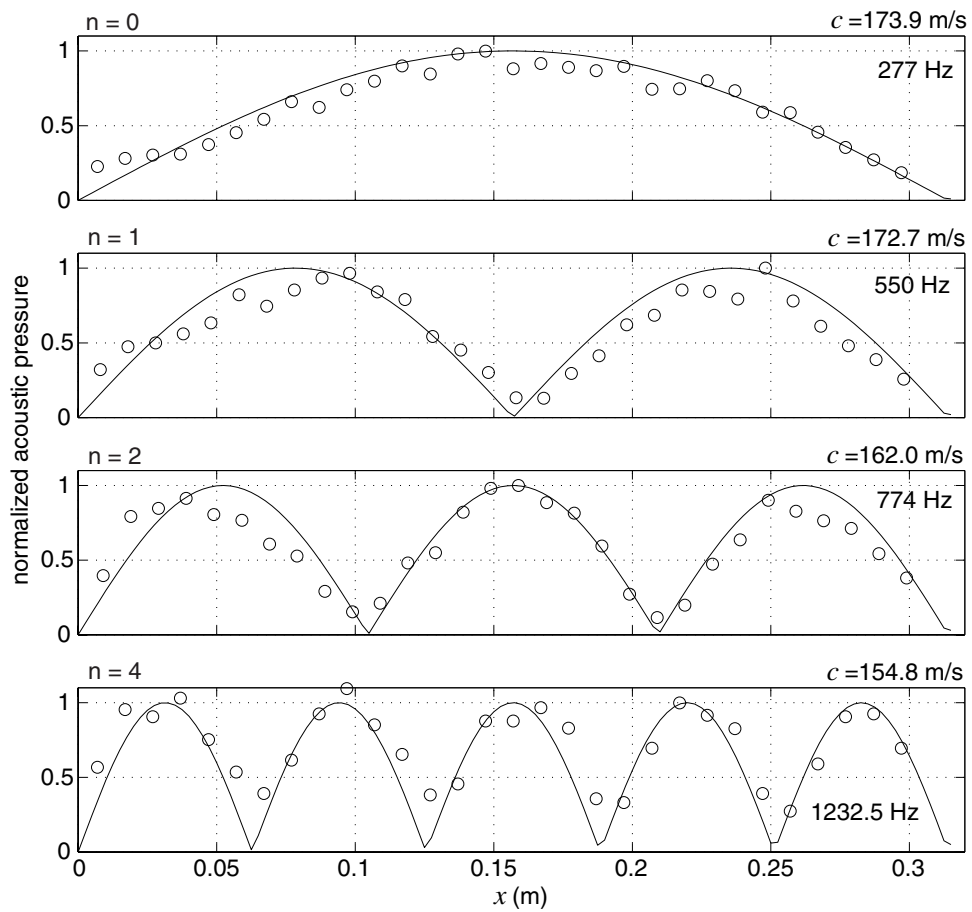


Figure 4.14: The four standing wave patterns corresponding to the resonance frequencies identified in Fig. 4.13 are shown, along with the sound speed obtained from Eq. 4.5. Measurements are shown with open circles and predictions are shown with solid lines.

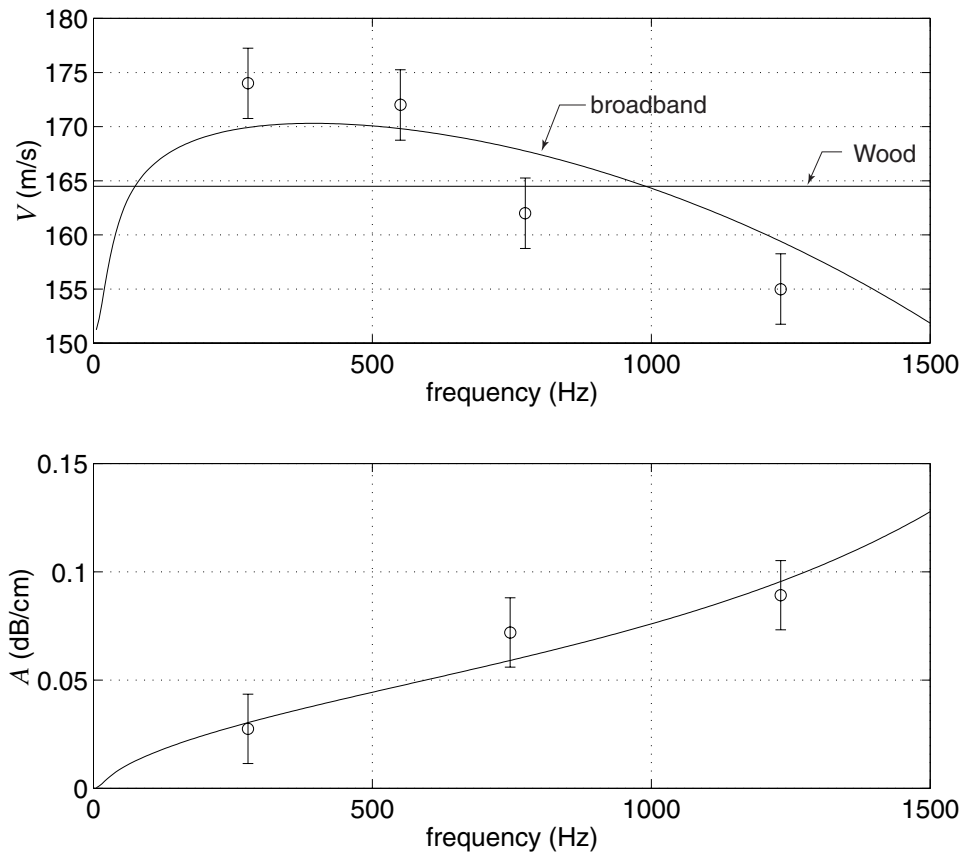


Figure 4.15: Phase speed V and attenuation coefficient A obtained from the void fraction resonator are shown in this figure. Measurements with error bars are shown with open circles and predictions are shown with solid lines.

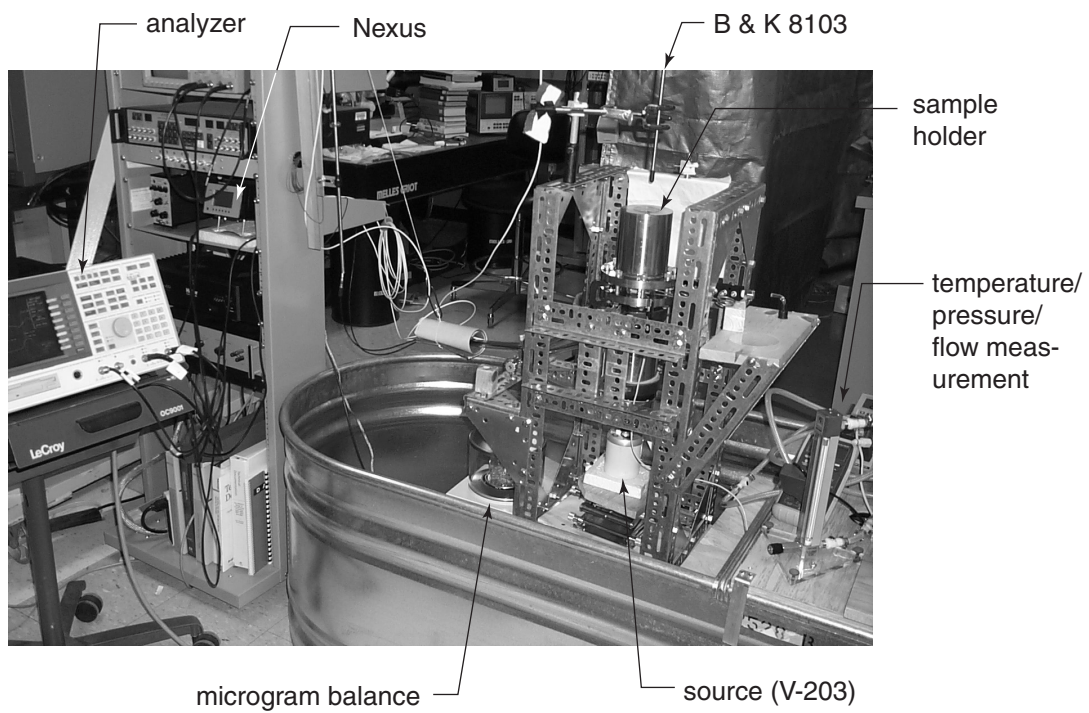


Figure 4.16: A photo of the impedance tube system is shown without the bifilar microscope. The Ling V-203 electrodynamic source appears in the photo, but the Kildare TP-400 was actually used for the measurements in this section.

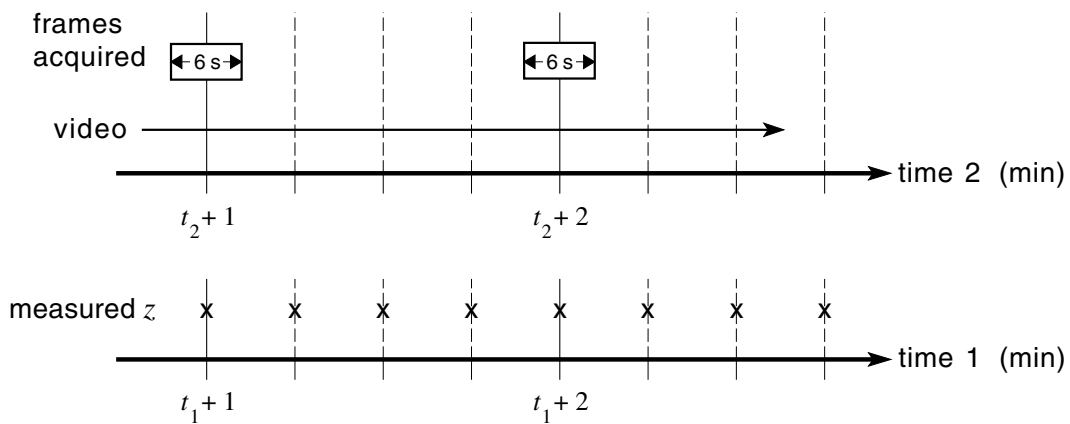


Figure 4.17: Time lines for the instantaneous impedance measurements are shown. Impedance was measured every 15 seconds at times indicated by the symbol “x”. The video recorded continuously, as indicated with the thin horizontal arrow. Individual frames were acquired from the video for six second blocks every minute.

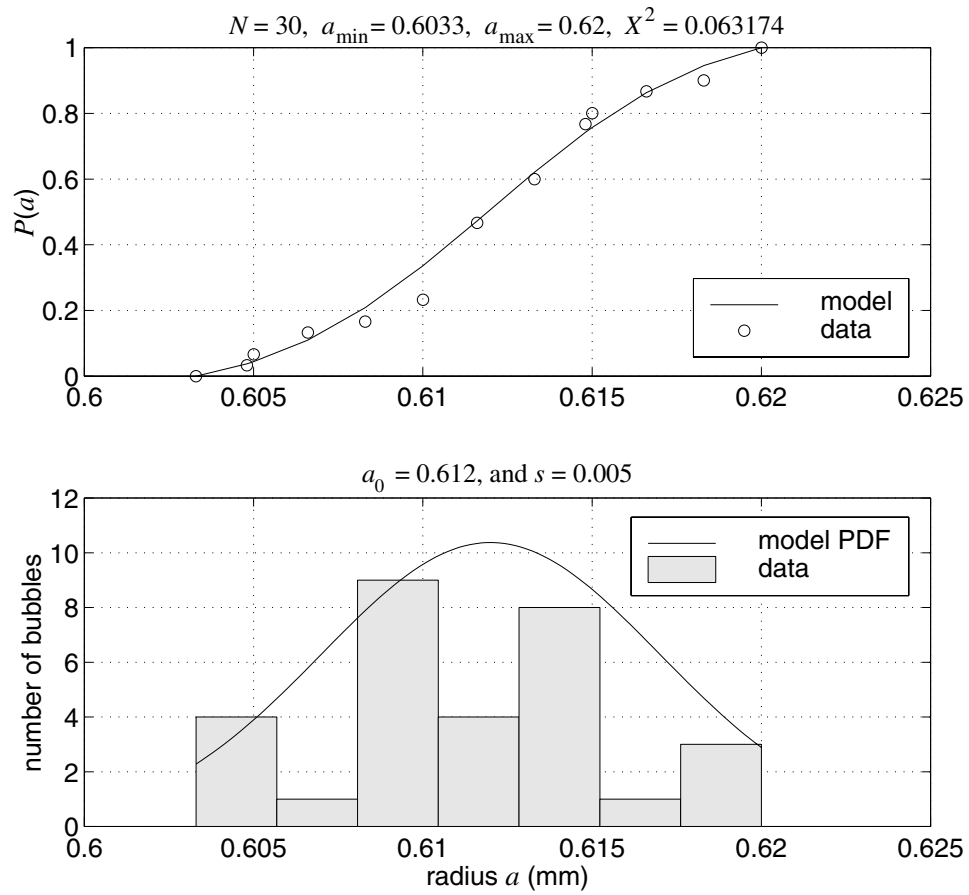


Figure 4.18: Bubble population parameters are shown for Case 1, a single needle.

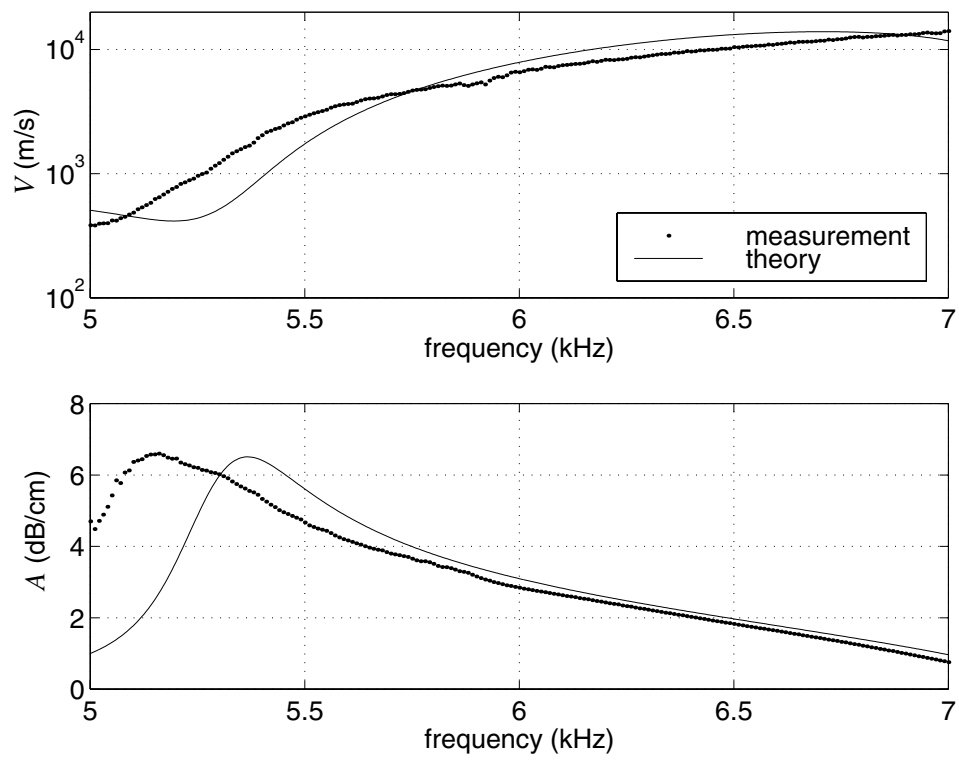


Figure 4.19: Measured and predicted phase speed V and attenuation A for Case 1, using the population parameters from Fig. 4.18.

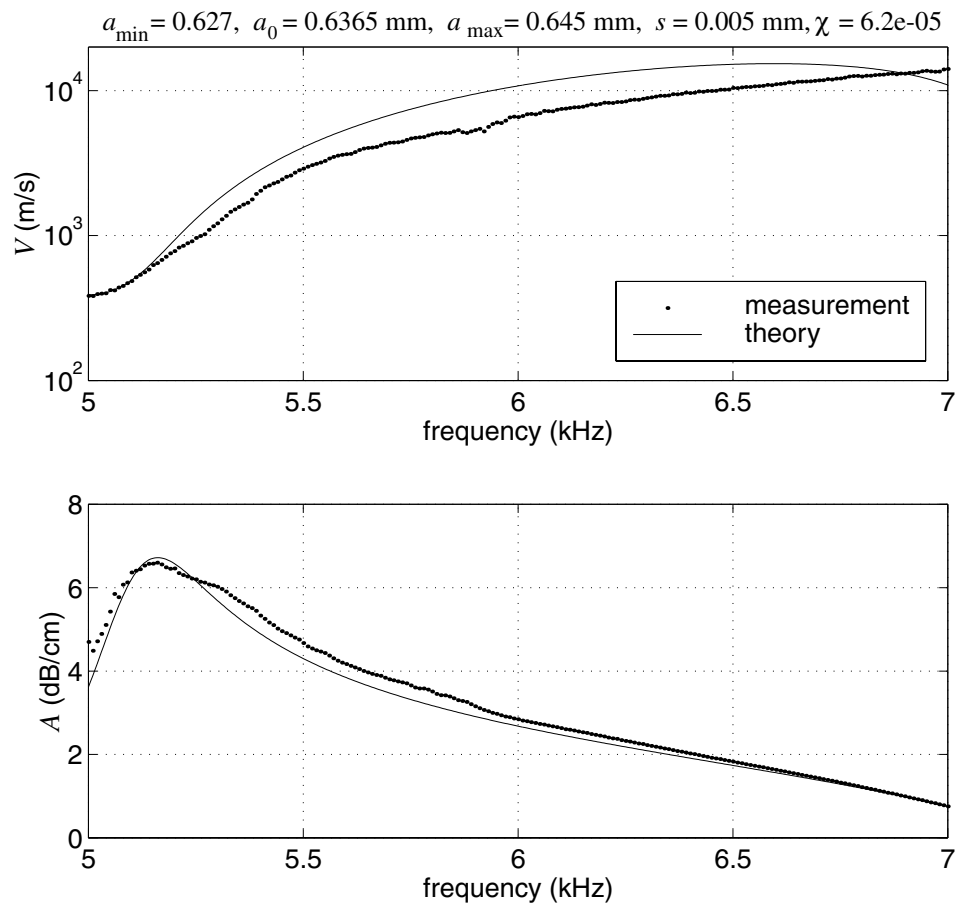


Figure 4.20: The measured data for Case 1 is shown again, but the predicted phase speed V and attenuation A was obtained by adjusting bubble radius.

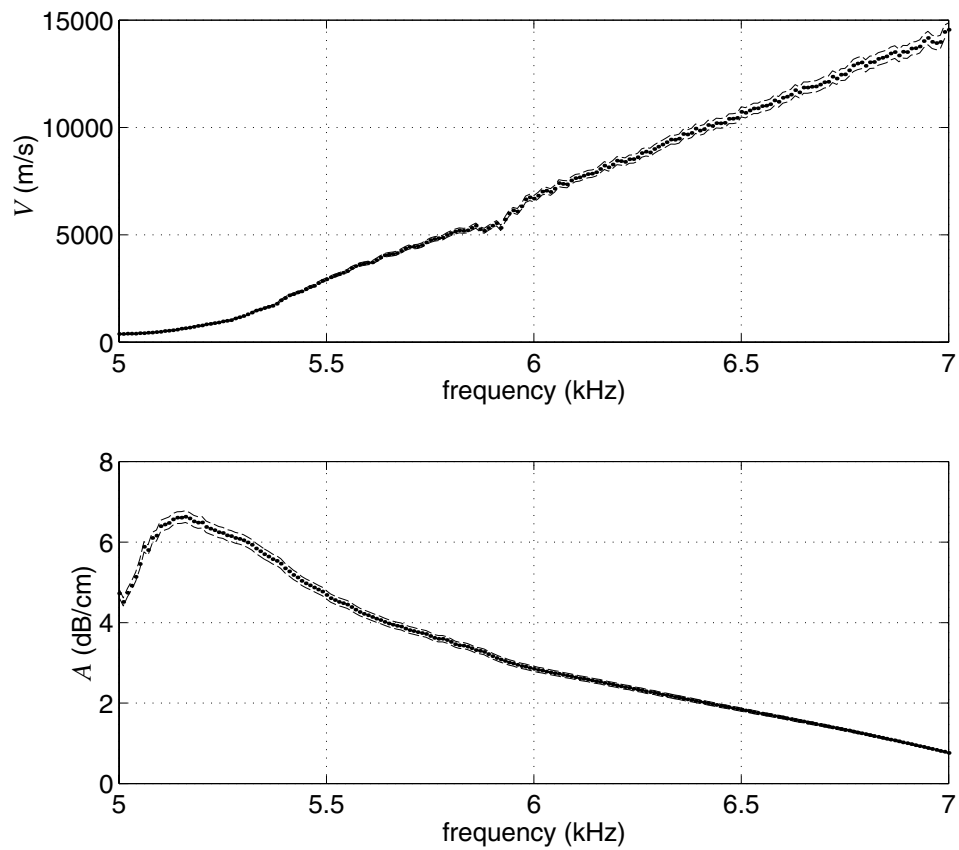


Figure 4.21: The phase speed V and attenuation A data points from Fig. 4.20 are shown with dots, and the range of measurement uncertainty is shown using dashed lines. Note that the phase speed is plotted on a linear scale, in order to make the error range visible.

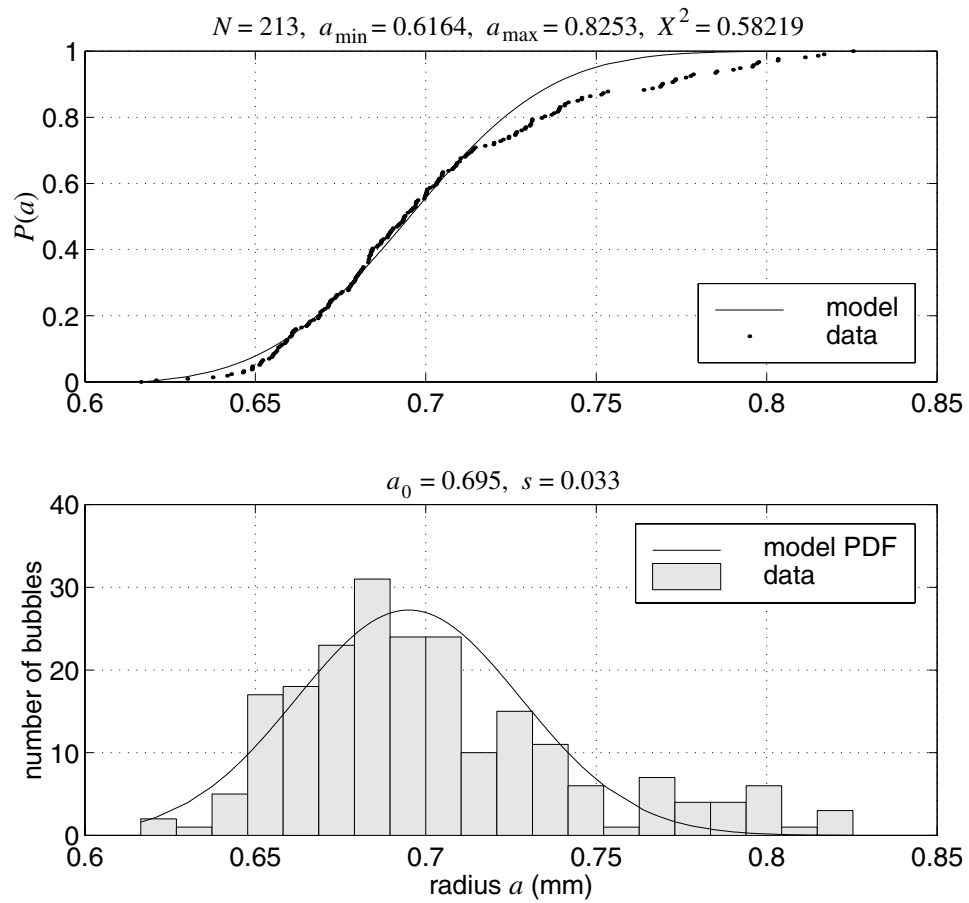


Figure 4.22: Bubble population parameters are shown for Case 2, a single needle installed in the BIM.

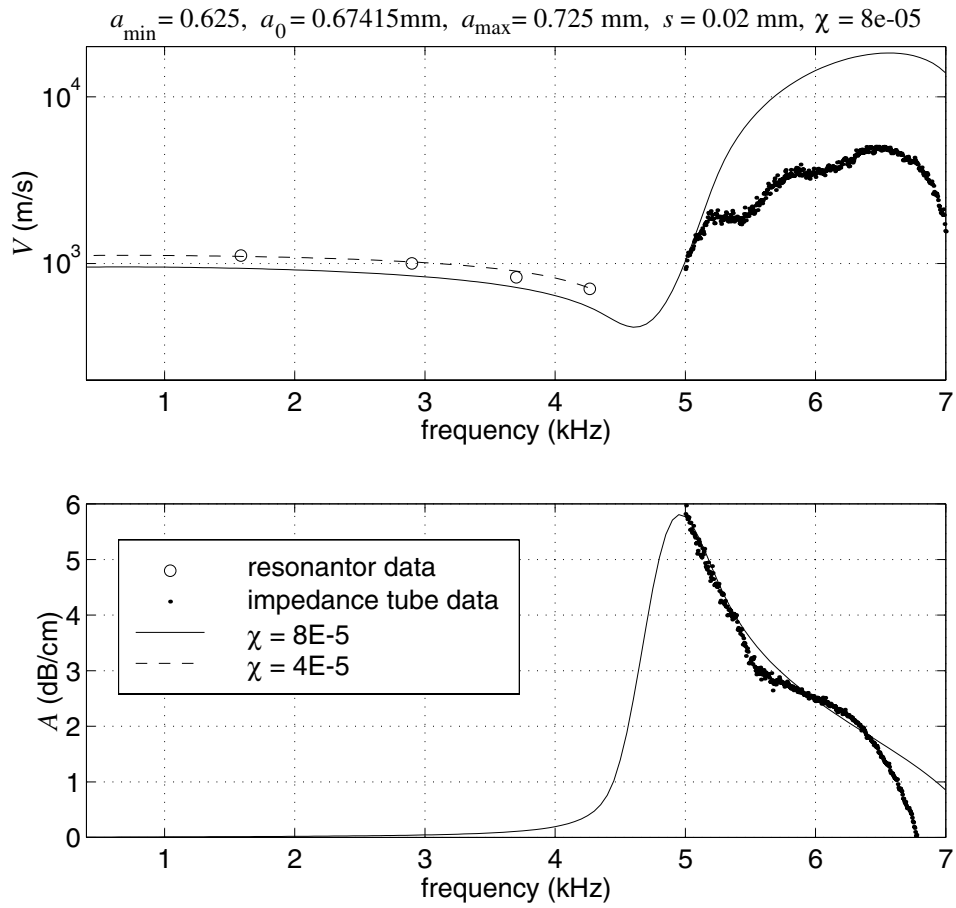


Figure 4.23: The measured data for Case 2 is shown, along with the predicted phase speed V and attenuation A obtained by fitting.

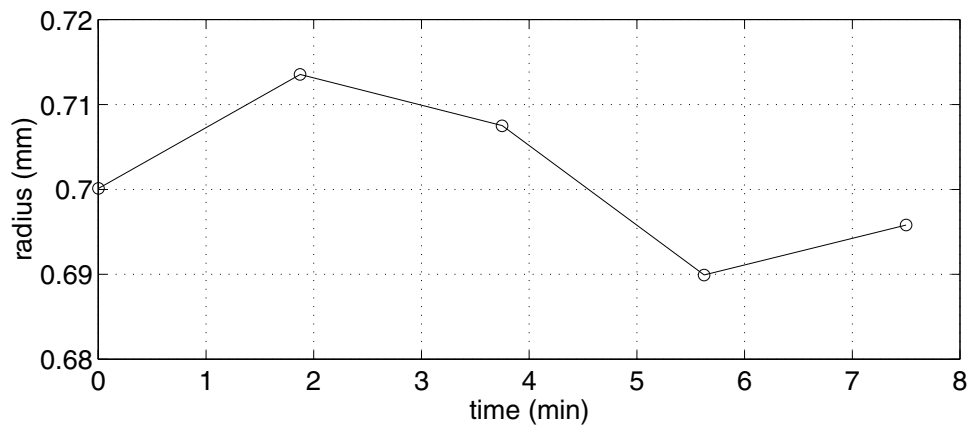


Figure 4.24: A running average of bubble radius versus time for Case 2 bubbles is shown.

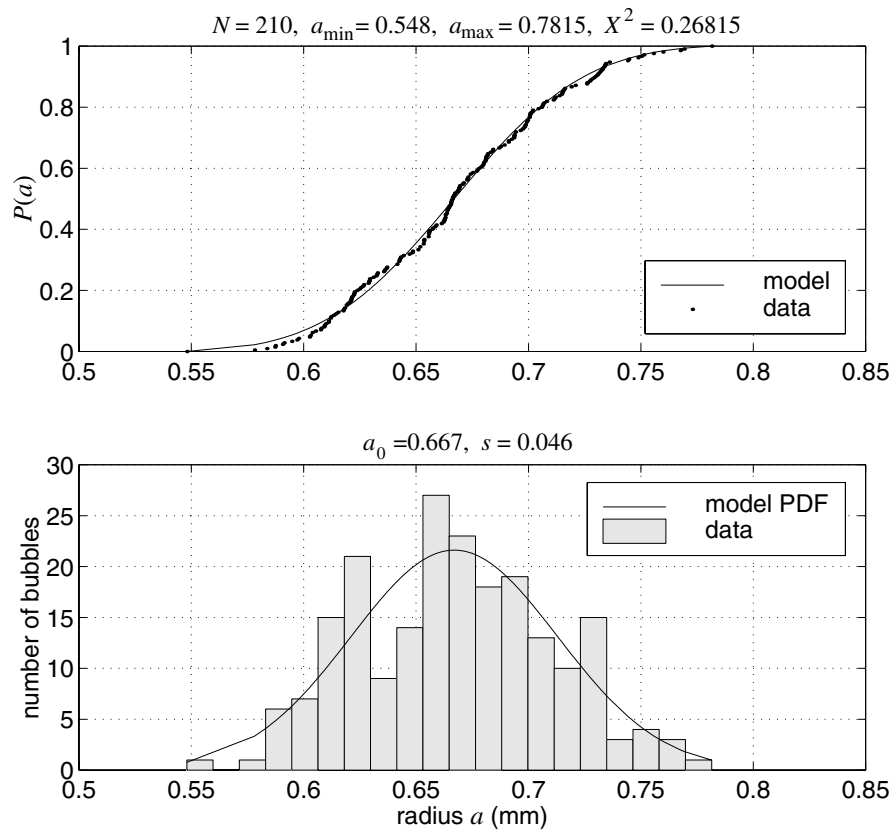


Figure 4.25: Bubble population parameters are shown for Cases 3, 4 and 5. In all three cases, the bubbles were produced by four needles installed in the BIM.

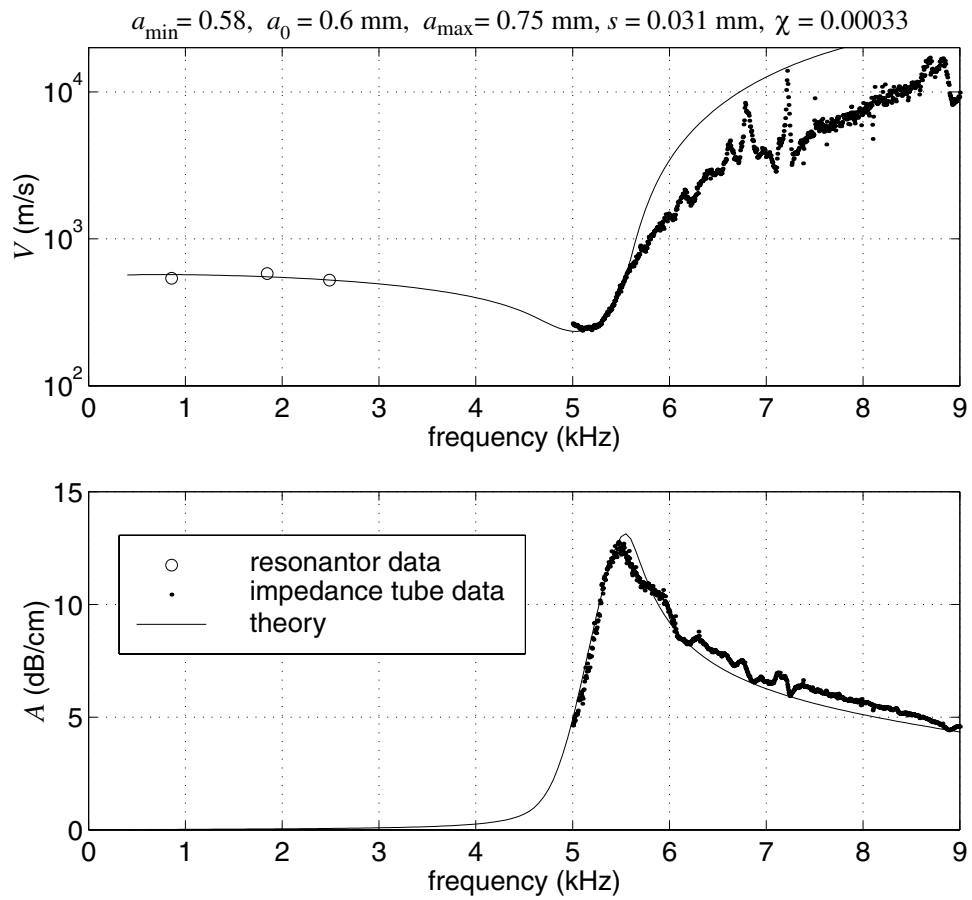


Figure 4.26: The measured data for Case 3 is shown, along with the predicted phase speed V and attenuation A obtained by fitting.

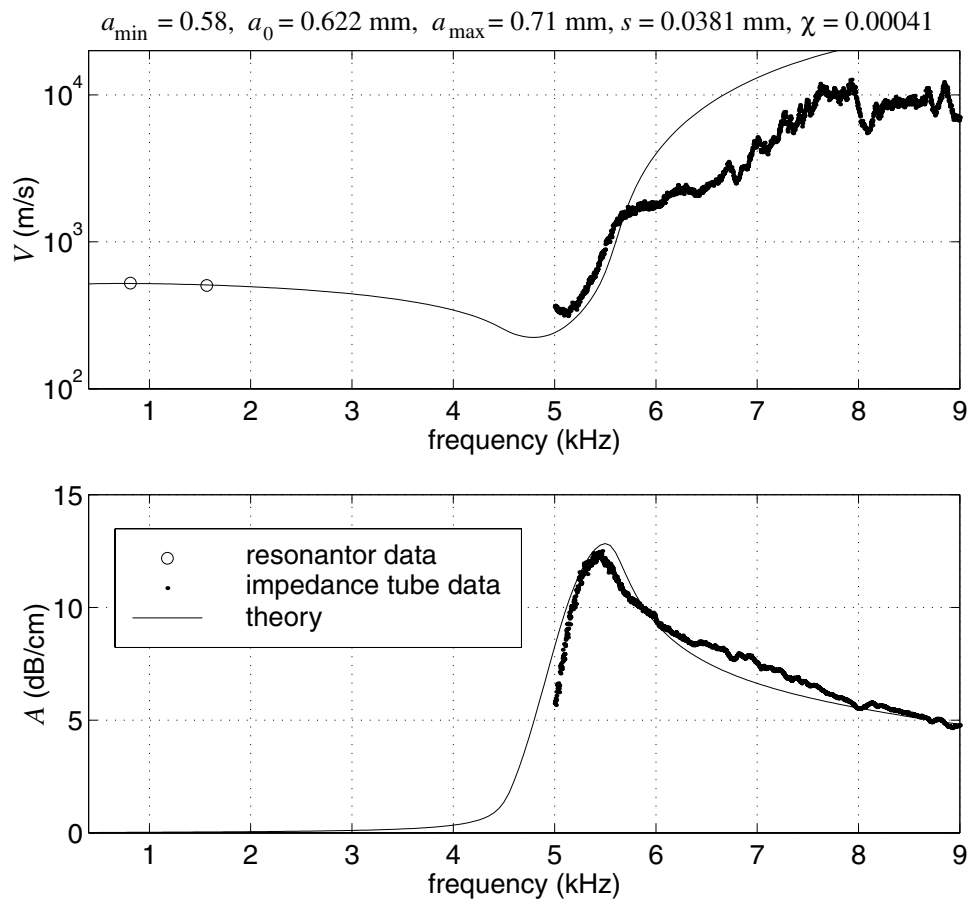


Figure 4.27: The measured data for Case 4 is shown, along with the predicted phase speed V and attenuation A obtained by fitting.

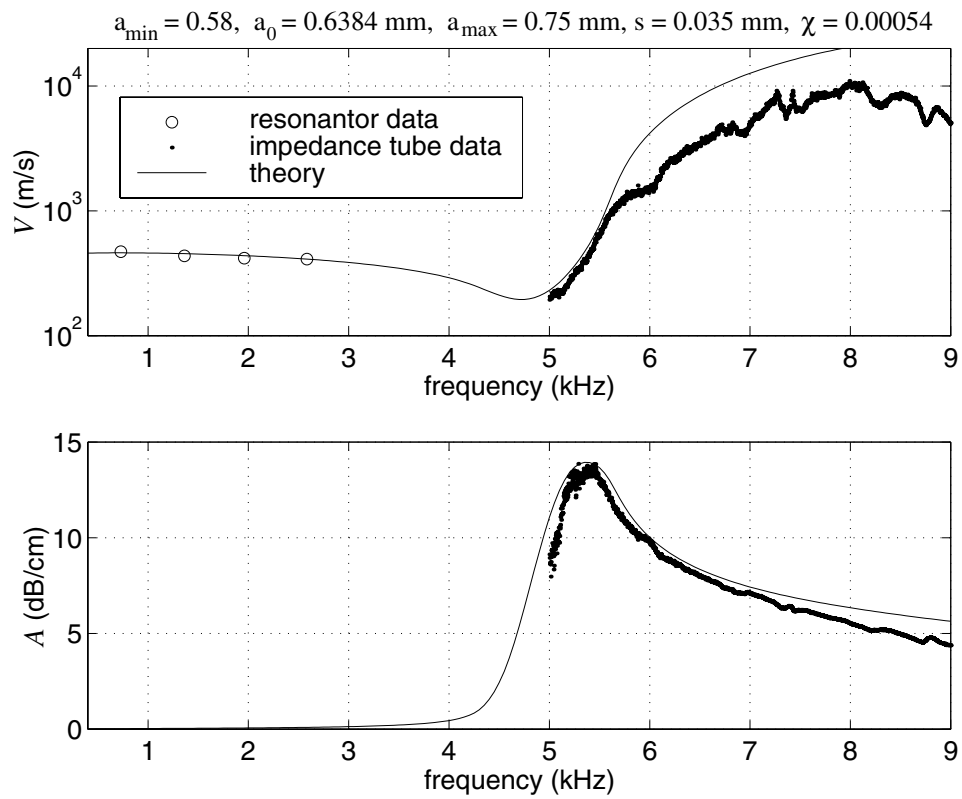


Figure 4.28: The measured data for Case 5 is shown, along with the predicted phase speed V and attenuation A obtained by fitting.

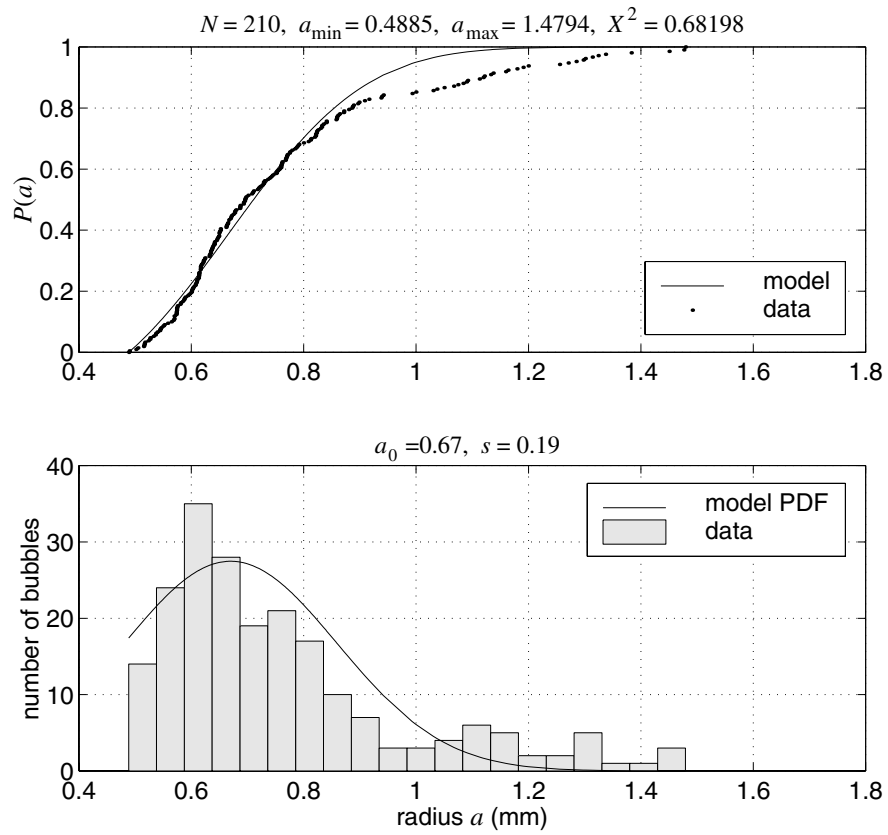


Figure 4.29: Bubble population parameters are shown for Case 3–5, four needles installed in the BIM.

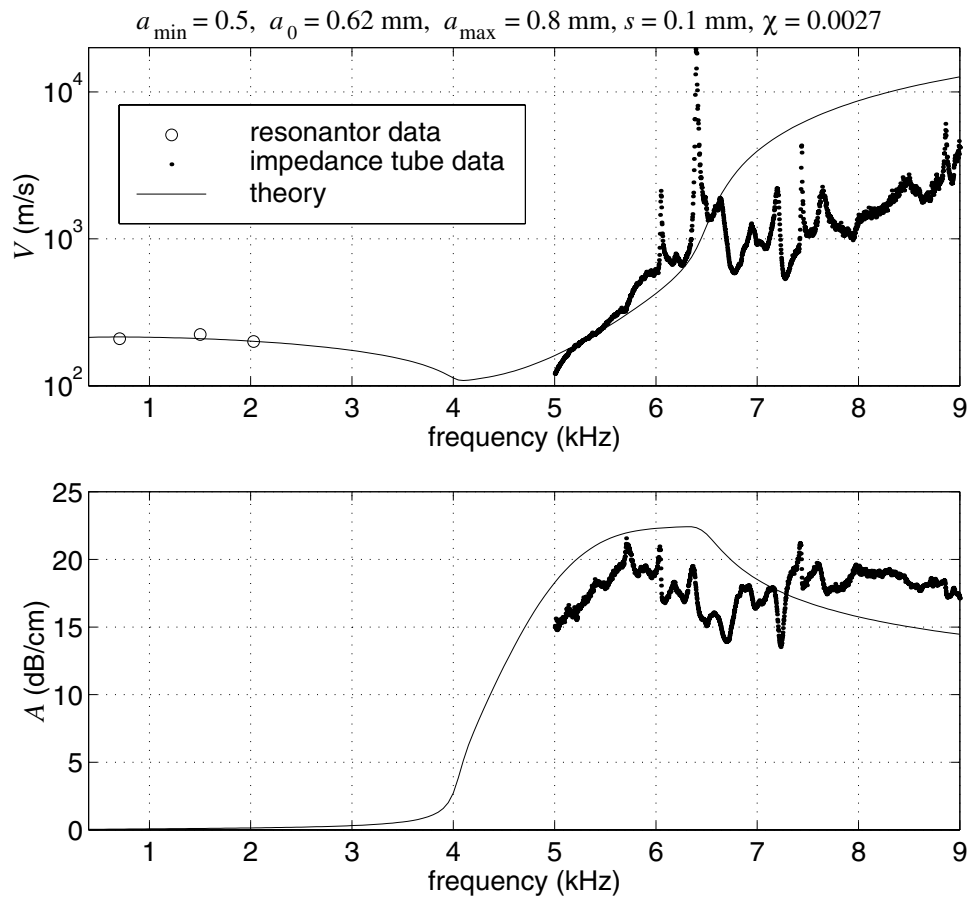


Figure 4.30: The measured data for Case 6 is shown, along with the predicted phase speed V and attenuation A obtained by fitting.

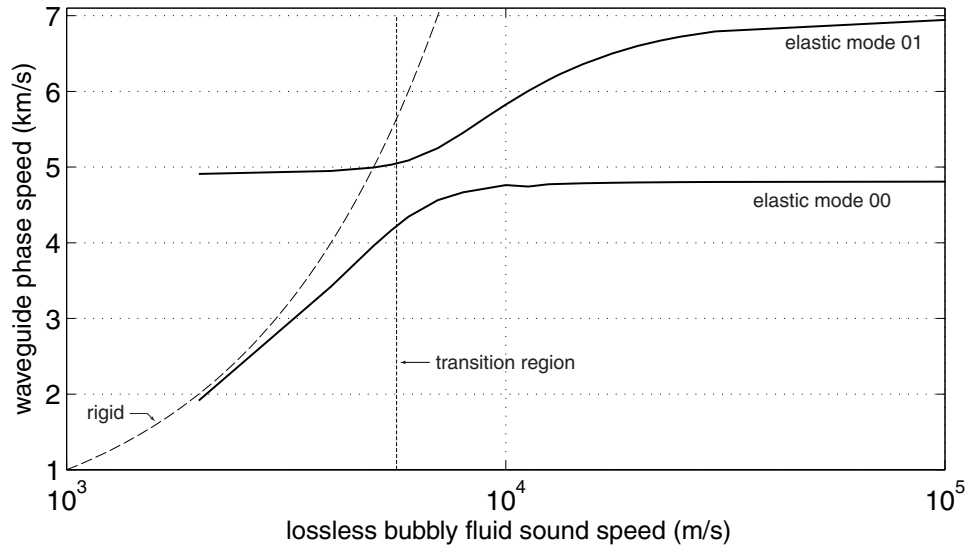


Figure 4.31: Predicted phase speeds in an elastic waveguide are shown for supersonic regime bubbly fluid.

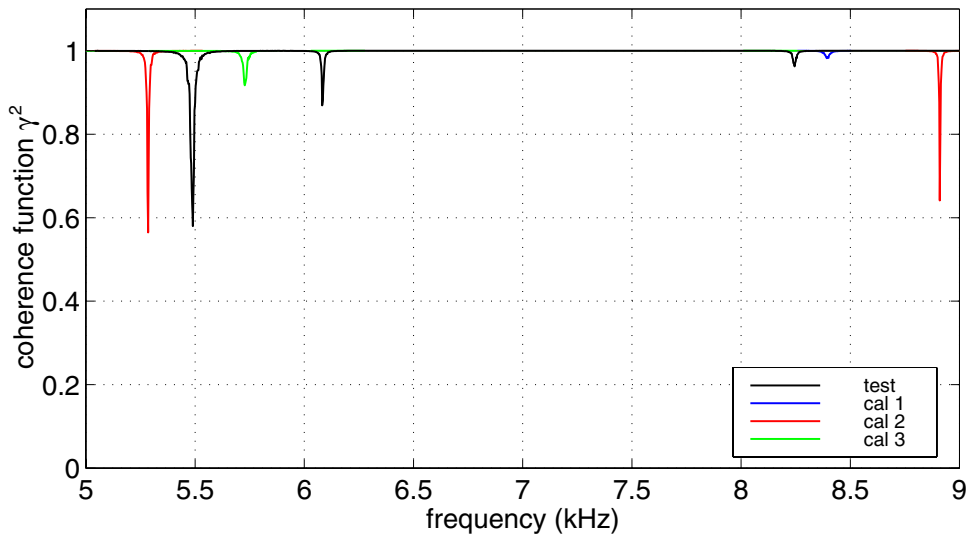


Figure 4.32: The measured coherence function γ^2 is shown for three calibration measurements and a ground truth measurement.

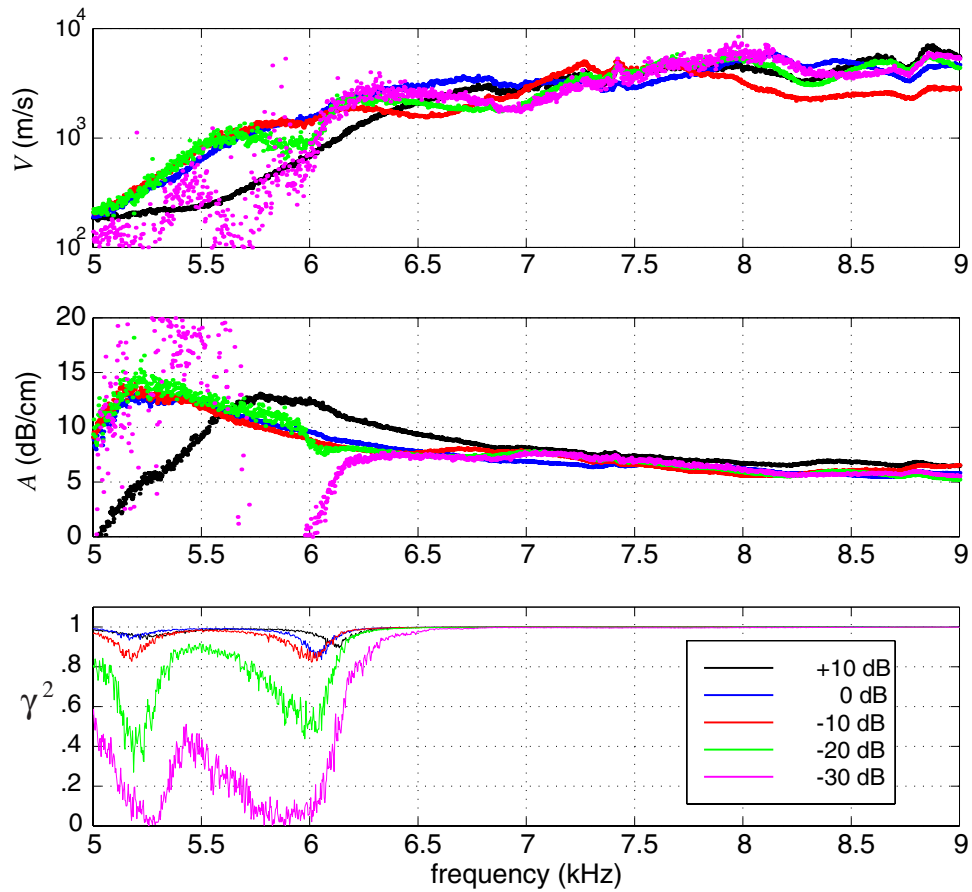


Figure 4.33: The results of the SNR experiment are presented. Phase speed V and attenuation A was measured for five SNRs. The coherence function γ^2 is also shown. The legend applies to all three plots and represents relative change in drive level.

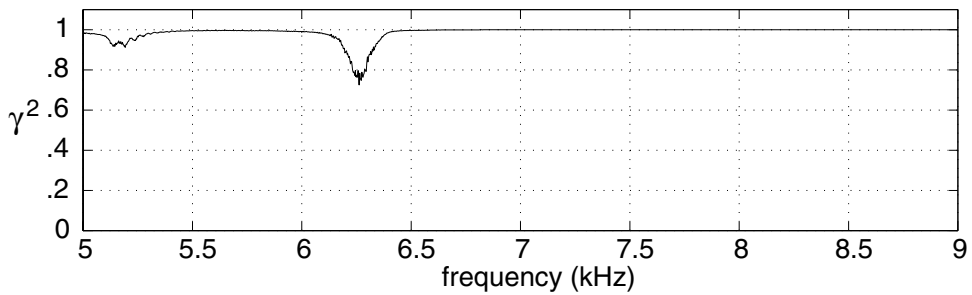


Figure 4.34: The measured coherence function γ^2 is shown for Case 6.

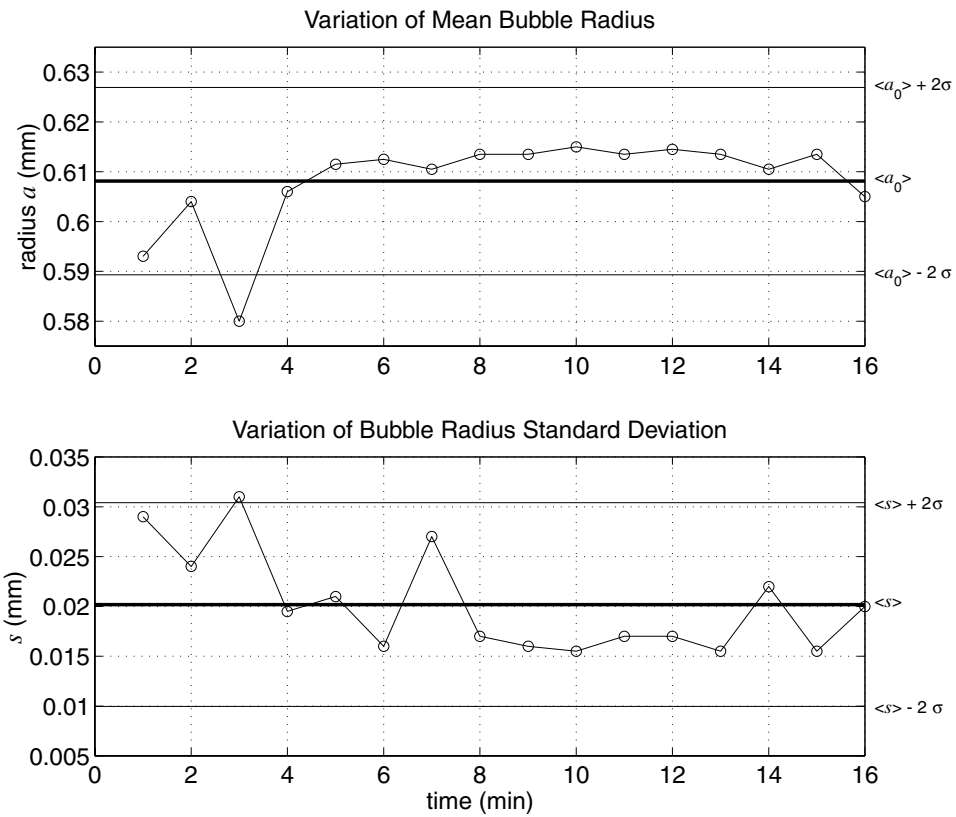


Figure 4.35: Mean bubble radius a_0 and standard deviation s are shown as a function of time. The thick horizontal lines represent the global means, $\langle a_0 \rangle$ and $\langle s \rangle$, and the thin horizontal lines represent two standard deviations above and below the global means.

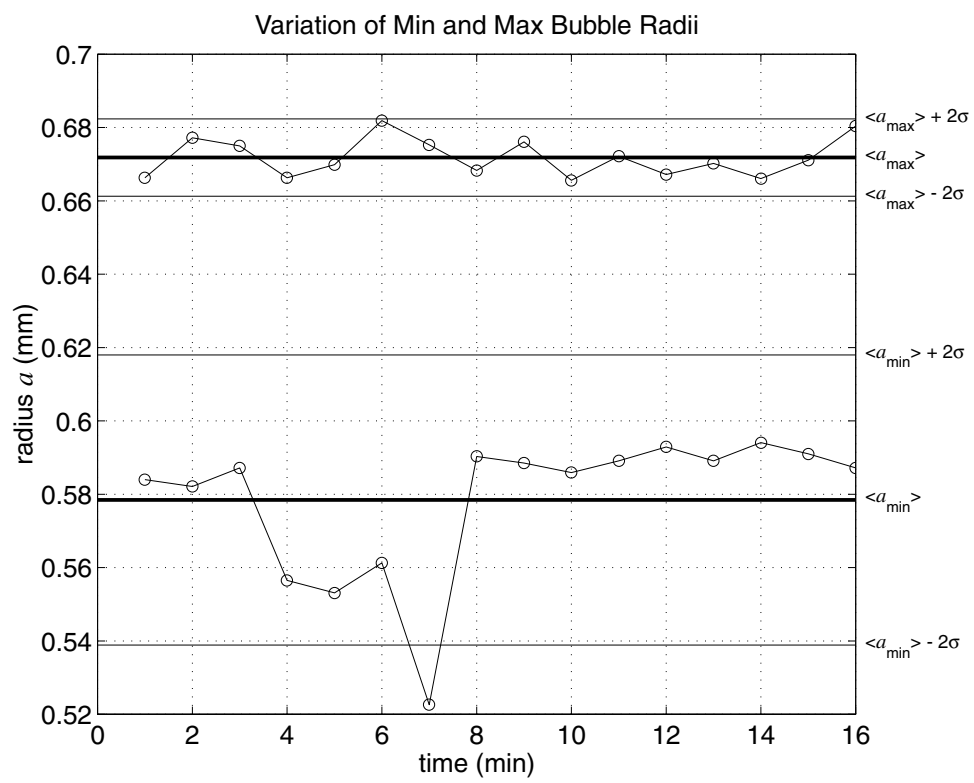


Figure 4.36: Minimum and maximum bubble radius is shown as a function of time.

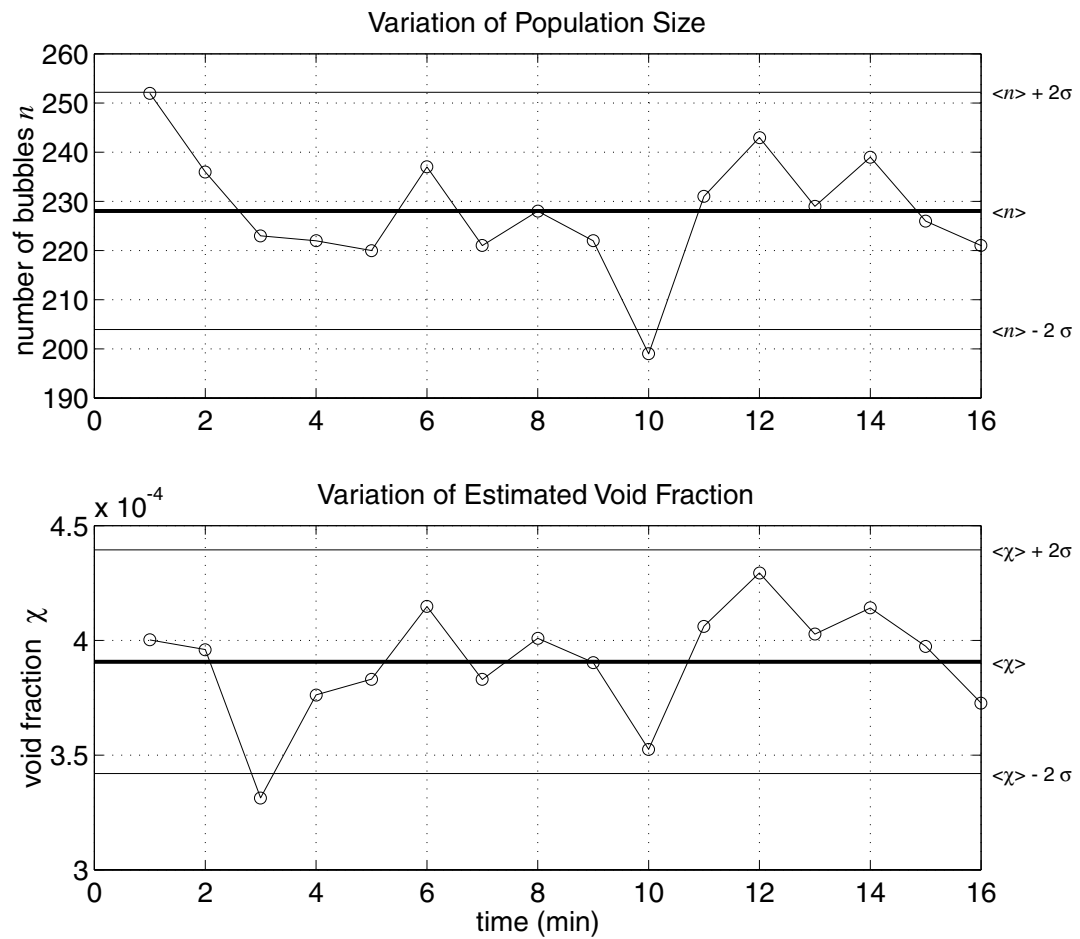


Figure 4.37: Number of bubbles n and optically estimated void fraction χ are shown as a function of time.

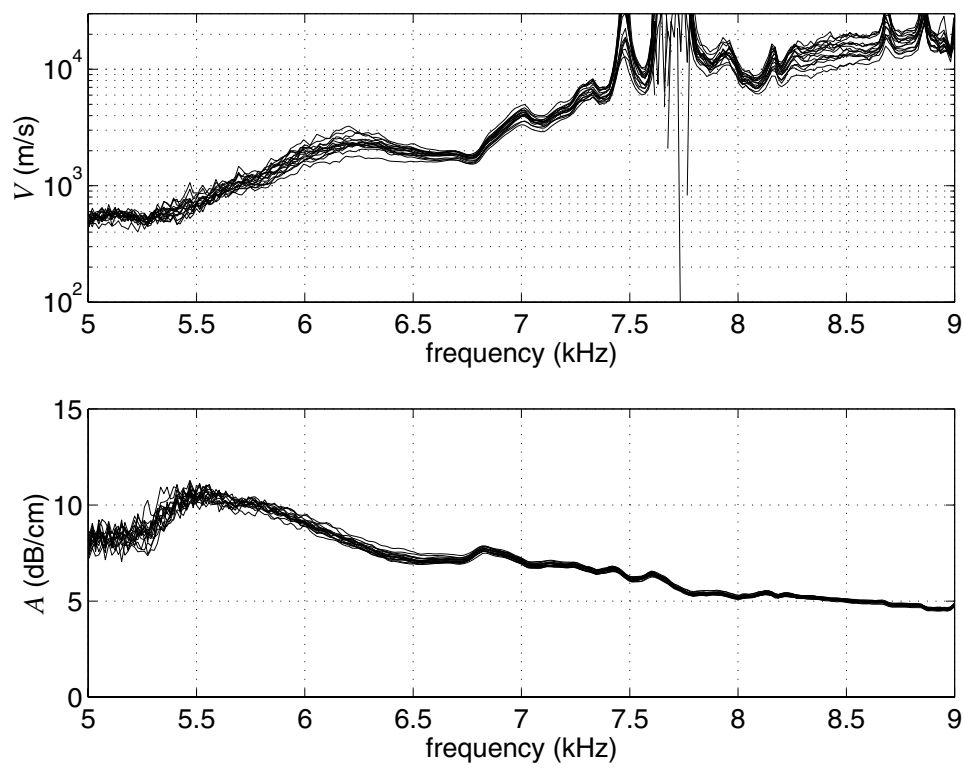


Figure 4.38: Phase speed V and attenuation A is shown for each of the 16 measurements acquired during the instantaneous experiment.

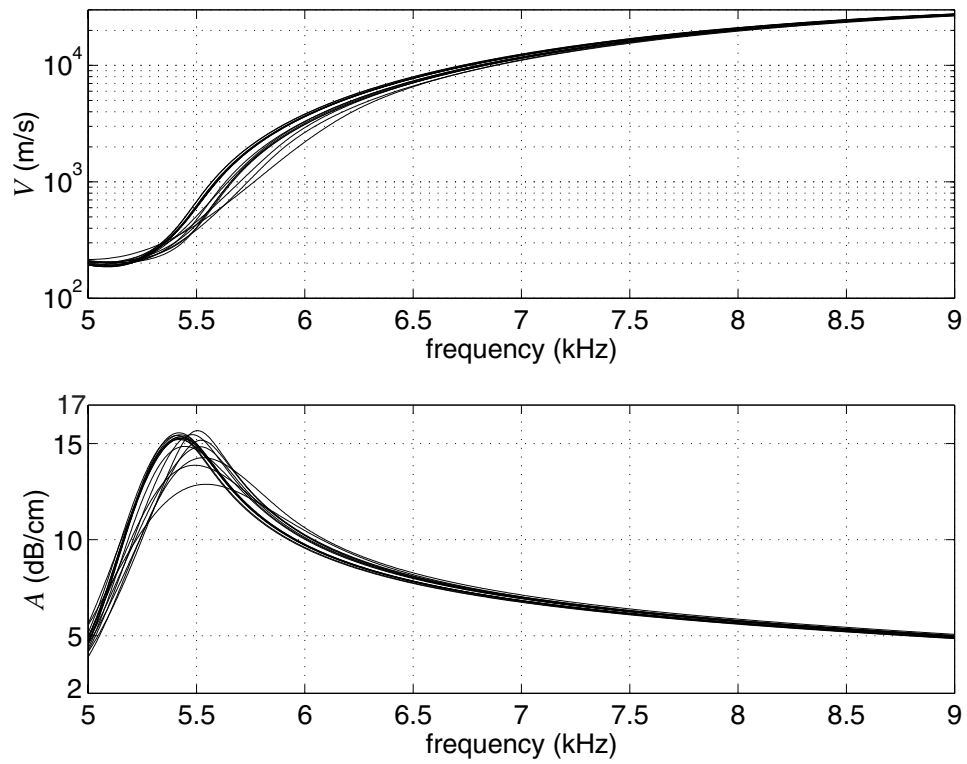


Figure 4.39: Calculated phase speed V and attenuation A from the instantaneous experiment are shown. Refer to the text for details. Note: For comparison, the plots' scales were kept the same as in Fig. 4.38, except the A scale was shifted up 2 dB/cm.

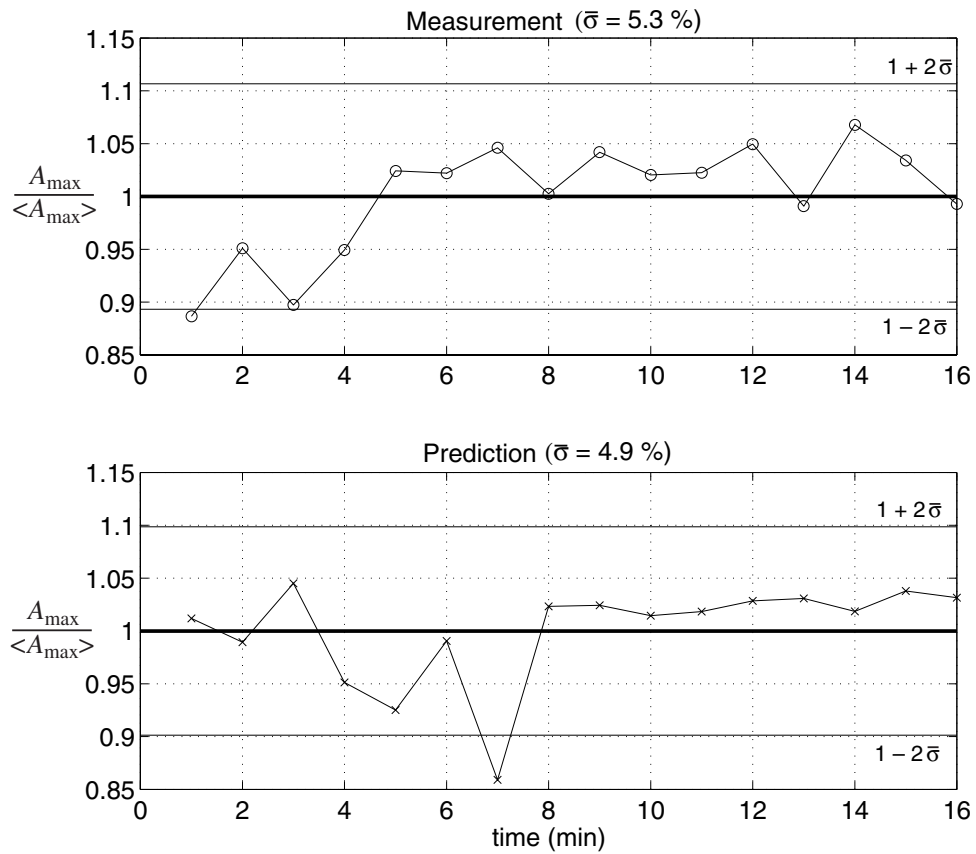


Figure 4.40: Measured and calculated maximum attenuation is shown as a function of time, normalized by the global mean.

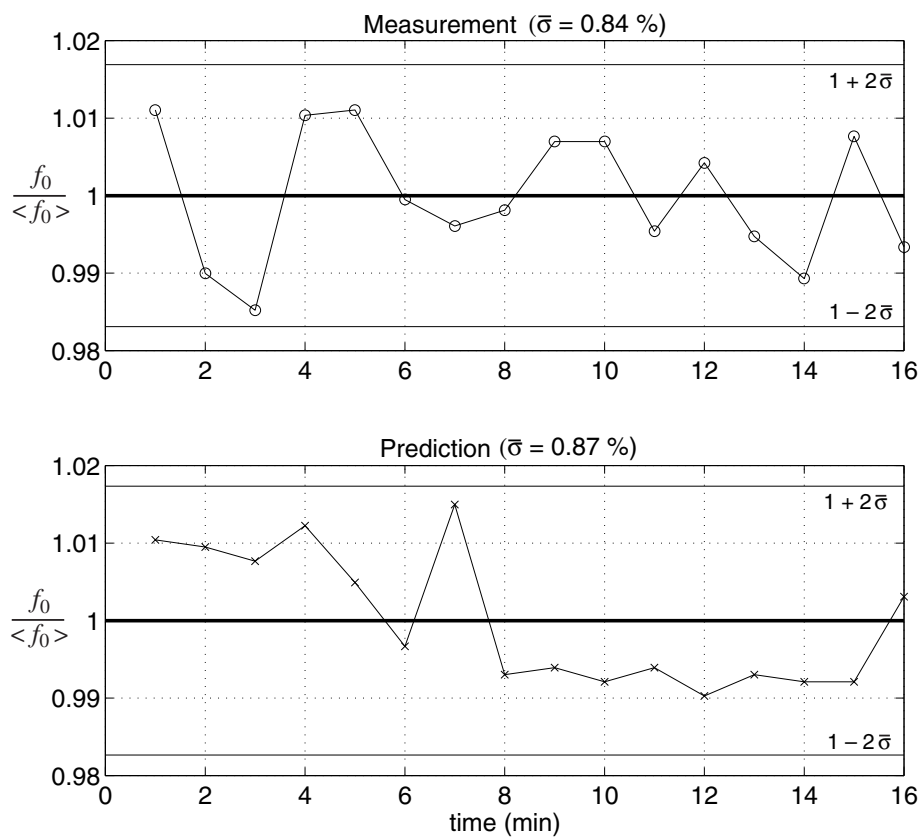


Figure 4.41: Measured and calculated frequency of maximum attenuation is shown as a function of time, normalized by the global mean.

Chapter 5

Scattering from a Bubbly Cylinder

For sufficiently low excitation frequencies, a nonspherical yet acoustically compact bubble cloud can be modeled to first order as a monopole radiator, i.e., as a compressible sphere. If the additional requirement is imposed that all the bubbles are smaller than resonance size, the contents of the cloud can be treated as an effective medium. The cloud's scattering strength depends only on its effective spherical volume and mean void fraction (VF), not the bubble size distribution or cloud shape. Experiments were conducted that verified this hypothesis using freely rising bubble clouds artificially generated in a lake [57]. Certain backscatter features were not initially explained by this partial wave theory [42, 56, 57, 58], but when corrected for the effects of multipath interference between the bubble generator and the rising bubble cloud, a monopole scattering resonance was observed and agreement between the measured and predicted target strength was achieved [29]. Above the first resonance frequency, the cloud was no longer acoustically compact, and the simple "effective monopole" model was not expected to describe the data.

The objective of the experiment presented in this section was to explore the validity of the effective medium approximation for frequencies greater than the first resonance frequency of a scatterer of known shape: a bubbly cylinder. Nicholas *et al.* [23] have shown that acoustic emissions from self-excited bubbly cylinders can be adequately modeled over

a broad frequency range, but this had not been previously demonstrated in a scattering experiment. Measurements of scattering from a bubbly-liquid-filled latex tube are presented and compared to the effective medium scattering theory discussed in Section 2.3. Except for the limiting cases of $VF = 1$ and 0 , these results have only qualitative VF estimation and, therefore, VF is used as the model's only fit parameter. A new method to generate large volumes of nearly monodisperse bubbly fluid is also described.

5.1 Description of the Experiment

The experiment was performed in a large indoor tank at the NUWC Acoustic Test Facility (ATF) in Newport, Rhode Island [126], the week of May 24th, 2000. The tank has the following dimensions: 18 m length \times 12 m width \times 11.4 m depth. No two sides are parallel and the volume of the tank is of 2.366 Mliters. The tank was partially lined with anechoic panels, affixed to the wall behind the projector, and the walls and floor between the projector and the receiver. Equipment was suspended in the water from mobile bridge platforms using the geometry shown in Fig. 5.1. The projector (EDO Western 515-250H), receiver (ITC 8084A), and latex tube were deployed along the projector's acoustic axis using a laser alignment system and an underwater video camera. The latex tube (3 m length, 1.25 cm inner diameter, 0.16 cm wall thickness) was filled with a bubbly fluid via Tygon supply lines and was held in place by thin gauge wire support lines. A schematic of this deployment is shown in Fig. 5.2.

The experimental geometry was archived by recording on tape the video feed from the alignment system at the end of the experiment. Six still images from that video tape are shown in Fig. 5.3. The position of the laser and video camera is shown in Fig. 5.1. The first frame (a) shows a wide angle view from just above the acoustic axis. The laser was projected along the acoustic axis and can be seen illuminating a spot on the back of the projector. The projector was then lifted out of the way revealing the receiver, as seen in (b). In (c), the camera was zoomed in for a close-up, revealing an illuminated spot on the

receiver. The laser was then scanned in a plane parallel to the water surface, illuminating the latex tube just to the right of the receiver, as shown in (d). The laser scan continued, illuminating the latex tube (e) along its length until its end was reached at (f). Also visible in (f) are the fittings which connect the latex scattering section to the Tygon supply lines and one of the wire support lines. Although not shown in the figure, the laser direction was reversed and was scanned all the way to the opposite end of the tube. This revealed that the tube was aligned in a plane parallel to the water surface to within approximately one-half of the tube's radius.

Signals were generated and acquired with ATF in-house systems [127]. A schematic of the computer controlled transmitting and receiving electronics is shown in Fig. 5.4. The incident pulse was a cosine tapered 5-cycle sinusoid, generated with an arbitrary waveform generator. The signal was then amplified with an Instruments Inc. model L-2 wideband power amplifier and sent to the projector. The voltage and current out of the power amplifier could be monitored with an oscilloscope. The hydrophone output was conditioned with a high-input-impedance preamplifier and a 100–100k Hz band-pass filter. The signals from the incident and direct reflected waves were independently acquired with 23-bit A/D conversion using appropriate time gates and gain settings controlled by the computer. The overall system dynamic range was 110 dB. Sixteen pings separated by 0.3 second intervals were averaged in the time domain at discrete frequencies ranging from 5 kHz to 20 kHz, in 200 or 400 Hz increments. This procedure was repeated for five different VFs.

5.2 Mass Production of Microbubbles

The “effective medium” propagation model used to describe the bubbly interior of the scatterer employs a linear mixture rule for the density and the low-frequency limiting form of the dispersive sound speed for the phase velocity [40]. This so-called “Wood limit,” given by Eq. 1.10, requires that all of the bubbles have resonance frequencies that

are much greater than the highest propagation frequency of interest. Moreover, to conduct the experiment, a large volume of the bubbly liquid is required, with a volume-averaged VF that is stationary in space and time, ideally.

To achieve this, a hollow cylinder with porous ceramic walls ($1\mu\text{m}$ pore size) was employed. This was the same type of ceramic cylinder described on page 102. A schematic of the bubbly fluid generator (BFG) is shown in Fig. 5.5. The bubbly liquid was pumped through the center of the ceramic cylinder with a peristaltic pump. The ceramic cylinder was housed in a pressurized container, and a positive air-pressure head was imposed on the outside of the cylinder using the ATF in-house compressed air system. Consequently, air would penetrate the cylinder walls and get sheared off by the interior flow. A degree of control over bubble size is available by controlling the interior flow velocity. Maximum flow rate was used during this experiment to make the bubbles as small as possible. Void fraction was controlled by varying the air pressure head. By using a reservoir and a recirculating “primary” flow path, a large volume of bubbly liquid was produced. After a few minutes at a fixed air pressure and primary flow rate, a steady-state VF was achieved. A portion of the bubbly liquid stream was then diverted through a “secondary” flow circuit that supplied the latex tube scattering target, an imaging cell, or the void fraction resonator.

During the scattering experiments, the velocity of this secondary flow was approximately 1 m/s through the scattering section. Based on optical bubble dissolution rate observations, this velocity was deemed sufficient to pass the bubbly fluid through the scattering section without significant dissolution, yet is acoustically negligible given the fact that the flow trajectory is normal to the incident acoustic propagation vector (i.e., minimal Doppler shift).

The bubble size distribution was measured *a priori* using an in-line imaging cell, a stereo microscope, and diffuse back lighting. Bubble sizes were determined using the image analysis technique discussed in Section 4.2. For the conditions reported below, the distribution was roughly monodisperse and centered between 25–30 μm radius, corre-

sponding to a Minnaert frequency of approximately 133 kHz at 5 m depth. The largest bubble observed was about 38 μm in radius, corresponding to a Minnaert frequency of ≈ 105 kHz. Therefore, the Wood approximation was not compromised, even at the maximum excitation frequency of 20 kHz.

The VF is known for the limiting cases, because only water or air filled the tube. An *a priori* optical VF *estimation* was performed for the maximum non-unity case and it was found to be about 1.5×10^{-3} . The optical technique was based on the acquired images of the bubbles. At these sizes, the bubbles appear spherical, and their volume was calculated from the measured diameter. The effective sampling volume represented by the image and the volume of the bubbles contained in the image were used to estimate the void fraction. For the maximum non-unity case, there were only a few bubbles in each image. For the lower void fraction cases, which turned out to be about two orders of magnitude lower, there were only a few bubbles visible in many frames. The imaged volume technique was deemed too inefficient to use for the low void fraction cases.

After the May 2000 experiments were conducted, an in-line void fraction resonator was installed at the top of the BFG, as shown in Fig. 5.5, in order to monitor the sound speed and/or void fraction of the bubbly fluid being produced. The technique used to do this was described in Section 4.3. Subsequent investigation revealed that the void fraction stability was surprisingly good, but of course depended on the stability of the compressed air supply. In July of 2001, another bubbly fluid scattering experiment was performed at the ATF and the void fraction produced by the BFG was monitored throughout those experiments. Under the assumption¹ that the stability of the ATF house air system was unchanged from the year before, two typical records obtained during the July 2001 experiment are shown in Fig. 5.6. The purpose here is to show the level of stability likely attained during the May 2000 experiments, not to try and classify the actual void fraction of those experiments. The void fraction can certainly be considered an environmental parameter, but for acoustic

¹The ATF air system was not replaced or modified during the 14 months between the two experiments, but was regularly maintained.

experiments, the sound speed in that bubbly fluid is the quantity of interest. Therefore results are plotted in the form of sound speed measured in the resonator, but normalized by the mean for each case. The normalized standard deviations $\bar{\sigma}$ shown on the plots were obtained using Eq. 4.23. In the upper plot, which is from an experiment that ran for about an hour, the overall resonator sound speed variability was about $\pm 5\%$. An initial start-up transient is visible in the first six minutes of the plot. After that, the sound speed variability is lower. Even more stability was achieved in another case, shown in the lower plot, where sound speed variability was only about $\pm 2\%$.

5.3 Experimental Results and Model Comparison

A typical measurement is shown in Fig. 5.7. The incident and reflected pulses were acquired in separately delayed time gates, but the actual time line was reconstructed and is shown for reference. The incident pulse was initiated at time zero and arrived at the hydrophone after 4 milliseconds. The pulse directly reflected from the target returned to the hydrophone at approximately 7 milliseconds, with a shape similar to the incident pulse but lower in amplitude. The energy that arrived after the direct-reflected signal corresponds to the first surface reflection and an indirect target reflection.

For the purpose of model comparison, the back-scattered echo data are presented in the form of peak echo level,

$$EL_{\text{pk}} = 20 \log_{10} \left[\frac{p_{\text{sc}}}{p_{\text{inc}}} \right]_{\text{pp}} + TL, \quad (5.1)$$

where p_{sc} is the scattered acoustic pressure, p_{inc} is the incident acoustic pressure, the subscript pp indicates peak-to-peak pressure values, and TL is a transmission loss correction which accounts for spherical spreading of the incident wave from the hydrophone to the

target. The term TL is given by

$$TL = 20 \log_{10} \left[\frac{PH + HT}{PH} \right], \quad (5.2)$$

where PH is the distance from the projector to the hydrophone, and HT is the distance from the hydrophone to the target. The difference between peak-to-peak and rms-based echo level was typically less than 0.25%, but there is a degree of uncertainty in the exact location of the end of the direct-reflected pulse. Therefore, to eliminate any ambiguity, the peak to peak results were used. The physical parameters used in the following calculations are listed in Table 2.3, except here, c_1 was set to 1480.5 m/s, which was the sound speed in the ATF tank calculated from the measured temperature. The parameters listed in Table 2.3 were obtained from the literature for air and water [96], and the latex rubber [85]. The echo level data presented in Figs. 5.8, 5.9 and 5.11 has an estimated accuracy of ± 0.09 dB and a precision of ± 1 dB. A detailed discussion of this uncertainty and the issue of ping-to-ping variability is presented in Section 5.4.

In order to show the effect of added model complexity, the results will be presented in three stages. In the first case, shown in Fig. 5.8, the data will be compared to a model for continuous plane wave excitation of an infinite fluid cylinder with no shell. The predictions shown are those obtained by least-squares VF fit of Eq. 2.27, with the shell material shear speed set to zero, and the compressive speed and density set to that of the surrounding water. By void fraction fit, the following is implied: The sound speed and density of the inner fluid were obtained from Wood's equation as a function of VF. The VF was varied to minimize the squared error between the model and the data. The best fit void fractions were 1.1×10^{-3} , 1.8×10^{-5} and 1.1×10^{-5} . The two low void fraction cases exhibit fair agreement with this model but the high void fraction case does not. The knees in the high void fraction curve, at 5 and 20 kHz, seem to be occurring close to the predicted frequency, but the echo level is not in agreement.

The next level of complexity is to include the effect of the shell. The shell parameters

were returned to their tabulated values and the model was refitted to the data by again varying VF. These results are displayed in Fig. 5.9. For clarity, only the $\chi = 1.8 \times 10^{-5}$ and $\chi = 1.1 \times 10^{-3}$ cases are shown. For the former case, the no shell model calculation from the previous figure is shown again. The prediction including the shell is also shown and its effect is to increase the echo level slightly. For the high void fraction case, the shell and no shell predictions are both plotted but they are virtually identical. The shell has little effect at the higher void fraction because the scattering strength is dominated by the compressibility of the bubbles. The model still over-predicts the scattering strength for this case, though.

The CW model shown in the previous two plots exhibited a low Q and indicated that only about a cycle and a half would have been required to achieve steady state for the high void fraction case. From Fig. 5.7, it is clear that steady state is not reached for even a cycle. Therefore, the finite length of the incident pulse was accounted for by convolving the CW response with the measured incident pulse using Eq. 2.37. A typical measured incident pulse is shown in the top part of Fig. 5.10. The corresponding back-scattered reflection from the bubbly-liquid-filled latex tube is shown in the lower frame with the reflection predicted by a least-squares VF fit of Eq. 2.37. Good agreement is found. Note that the reflection is not merely an amplitude reduced version of the incident pulse, but has a slightly different shape.

The result of this modeling approach is shown for comparison to the entire data set in Fig. 5.11. In the $\chi = 1$ and $\chi = 0$ cases no fitting was used. For the other three cases, the predictions are those obtained by least-squares void fraction fit. Although Fig. 5.10 was shown first, VFs were actually obtained by fitting the curves in Fig. 5.11.

5.4 Measurement Uncertainty and Ping-to-Ping Variability

The measurements presented in the previous section were subject systematic and random uncertainties which will be discussed in this section. The systematic uncertainty arose pri-

marily from errors in the measurement of acoustic pressure and error in the measurement of the hydrophone to target separation distance. Random uncertainty arose from variation in the scattered signal over time, referred to as ping-to-ping variability. It is believed that this was due to the target characteristics changing over time. The bubbly liquid was of course flowing through the tube during the scattering measurements. Therefore, variation in instantaneous void fraction and perhaps the momentary presence of resonance size bubbles or groups of bubbles could have caused the ping-to-ping variability. No motion of the tube itself was detected visually.

Systematic measurement uncertainty stemmed from at least two sources. 1) Measurement of the lengths PH and HT in Eq. 5.2 were obtained using a measuring tape with an estimated accuracy of ± 1 cm. This leads to an uncertainty in TL of ± 0.026 dB. 2) Measurement of the hydrophone voltage was performed with an accuracy of ± 0.03 dB, according to calibration documentation available at the ATF facility. Assuming the worst case scenario, that these factors would add up in phase,² results in a total estimated systematic measurement uncertainty of ± 0.09 dB.

Unfortunately, individual pings were not stored for the scattering measurements presented in Fig. 5.11, which were obtained in the May 2000 experiment. Therefore absolute statements about the ping-to-ping variability of those measurements can not be made. Individual pings *were* stored for a number of cases in the July 2001 experiments. Since the bubble production, the experimental apparatus, and most of the procedures were similar in the two experiments, the discussion will be based on ping-to-ping variability observed during the July 2001 experiment. The target was a latex tube of the same dimensions used previously. One hundred pings were obtained, separated by 0.7 second intervals, at 15 discrete frequencies from 5 to 75 kHz, in 5 kHz steps. This was repeated for three different void fractions and an air-filled case. In the May 2000 experiments, a constant number of cycles was maintained throughout the frequency range. In the June 2001 experiment,

²For instance, the scattered pulse experiences $+0.03$ dB, the incident pulse experiences -0.03 dB, and another 0.026 dB accumulates from the range error, resulting in: $0.03 - (-0.03) + 0.026 \approx 0.09$ dB.

a constant pulse length in time was maintained, which resulted in a greater number of cycles as the frequency increased. The data is somewhat different in this respect, but the comparison is still useful.

To begin the discussion, the focus will be on a single frequency and void fraction, 15 kHz and $\chi \approx 0.0012$, respectively. All of the 100 incident and scattered pings are shown in Fig. 5.12. The time scales are relative to the beginning of each time gate. The incident pulse is shown in the upper plot and it is very uniform from ping to ping. The direct-reflected pulse is shown in the lower plot, between the markers “a” and “b” on the time axis. Beyond marker “b”, a combination of ring down and surface reflection energy is visible. It is difficult to detect the amplitude variation in this type of plot but the phase variation from ping to ping is clearly visible.

In order to observe the amplitude variation, the rms acoustic pressure of each incident and scattered pulse is shown in Fig. 5.13. Because the pulse length was much longer for the July 2001 data, the pressures shown are rms values, instead of the peak-to-peak values used in the previous section. It can easily be seen that any variation in echo level must be due to variation in the scattered pulse. The range of variation between incident pings is less than 0.01 dB, while the range of variation between scattered pings is almost 4 dB. The variation in echo level is shown in Fig. 5.14 where rms values were used in Eq. 5.1 instead of peak-to-peak. The mean echo level $\langle EL \rangle$ and mean echo level plus and minus the standard deviation, $\langle EL \rangle \pm \sigma$, are also shown. Eqs. 4.21 and 4.22 were used to calculate these quantities. The standard deviation of the echo level was close to 0.6 dB, but the maximum deviation between pings occurred near ping 70 and was more than 2 dB.

The discussion will now be broadened. The ping-to-ping variation observed in the entire data set is presented in Fig. 5.15 using the standard deviation of the echo level $\sigma[EL]$. To orient the reader, the standard deviation shown in Fig. 5.14 is indicated with a small arrow. The data at 5 kHz are difficult to interpret because the reverb noise level during the July 2001 experiment was typically greater than the scattered pressure level at this frequency. Aside from the 5 kHz data, the overall trend is clear, the standard deviation

increases significantly with frequency for the three bubbly fluid cases, while the air-filled case exhibits negligible ping-to-ping variability. The maximum standard deviation was approximately 4 dB at 70 kHz. The maximum deviation between neighboring pings also occurred for the 70 kHz case and was greater than 15 dB. The trend can be explained by noting that the effective medium approximation is less applicable as the frequency increases and the effects of individual bubbles or groups of bubbles play an increasingly important role. It is likely that the instantaneous bubble population statistics were changing from ping to ping, due to bubble production or flow instabilities. This type of variability in laboratory bubble size distributions has already been seen in Chapter 4. It is difficult to detect any trend associated with void fraction for the three bubbly fluid cases.

Now, consider the 5-20 kHz frequency range of Fig. 5.15. The average standard deviation for the 12 data points in that range, excluding the those from the air filled case, is 0.9112 dB. Based on this average standard deviation of the echo level observed in the July 2001 experiments, the estimated measurement precision is approximately ± 1 dB. Therefore the echo level measurements presented in Fig. 5.11 are estimated to have an accuracy of ± 0.09 dB and a precision of ± 1 dB.

5.5 Discussion

After accounting for the finite length of the incident pulse, agreement between measurement and theory is good across the entire range of frequencies and VFs. A peak is seen in Fig. 5.11 at 7 kHz for the $\text{VF} = 1.3 \times 10^{-3}$ case. This corresponds to the first resonance, and agreement between measurement and theory is uniform above and below the resonance. The *a priori* VF estimate of 1.5×10^{-3} corresponds to this case and agrees well with the fitted value. Resonance peaks are also predicted at about 100 Hz for the $\text{VF} = 1$ case and above 20 kHz for each of the lowest VF cases. Unfortunately, the limited experimental frequency range during the May 2000 experiment prevented the observation of a resonance peak in any of the other cases. The high frequency data from the July 2001

experiment was not ready for comparison to theory at the time of this writing.

Scatter in the low frequency data for each of the three lowest VFs is due to the increased difficulty of separating low amplitude reflections from increasing reverberation. As the frequency decreases, the reflection amplitude decreases, *and* the reverb level increases. These two effects conspire to create a frequency dependent, reverb limited noise floor of around -57 dB at 8 kHz, -61 dB at 9 kHz and -65 dB at 10 kHz.

The two limiting cases show somewhat less agreement than the fitted cases. The tube's elasticity dominates the scattering in the $VF = 0$ case. The actual elastic parameters in the tube are at least somewhat frequency dependent and may differ from the single frequency tabulated values that were used. In addition, some residual bubbles could have been present, which would increase the measured echo level. For the $VF = 1$ case, incorrect equalization of tube air pressure may have slightly decreased the tube diameter, and buoyancy of the tube caused a slight upward curve. Both effects would cause over-prediction.

Another limitation of the model used to describe the data is noteworthy. For the infinite length model to be valid, the insonified length L_i of the latex tube should be much greater than the radius R_F of its first Fresnel zone [128]. In the present case L_i is greater than R_F , but at most by a factor of 5 and at least by a factor of 2. The exact degree of error caused by this is uncertain, but numerical tests indicate it should be of order 1 dB. Although finite tube approximations exist, [84] they typically require $L_i \ll R_F$, and are not applicable here.

These results are important for the following reasons: To the author's knowledge, these are the first experimental measurements of acoustic scattering from geometrically well defined bubbly liquid targets, obtained in a well defined environment. These measurements are in agreement with a simple effective medium theory. Despite the lack of independent, precise VF verification, the results support the use of an effective medium for frequencies in excess of the lowest order resonance frequency of the scatterer. This approximation, although successfully employed to describe radiation from bubbly assemblages [18, 21, 23]

has never before been demonstrated in a scattering experiment.

In this experiment, the goal was to produce a bubbly liquid whose acoustic characteristics were stationary with time. Considerable effort was expended toward this goal, yet the variability of the scattering strength of the bubbly liquid cylinder was not negligible. Scattering strength could vary as much as 15 dB in less than a second. The measurements indicated that individual bubble resonance effects were a possible source of this variability, even though the mean bubble resonance frequency was more than five times greater than the maximum excitation frequency. An effective Wood limit scattering behavior may require increased averaging time as the excitation frequency increases above one fifth the mean bubble resonance frequency.

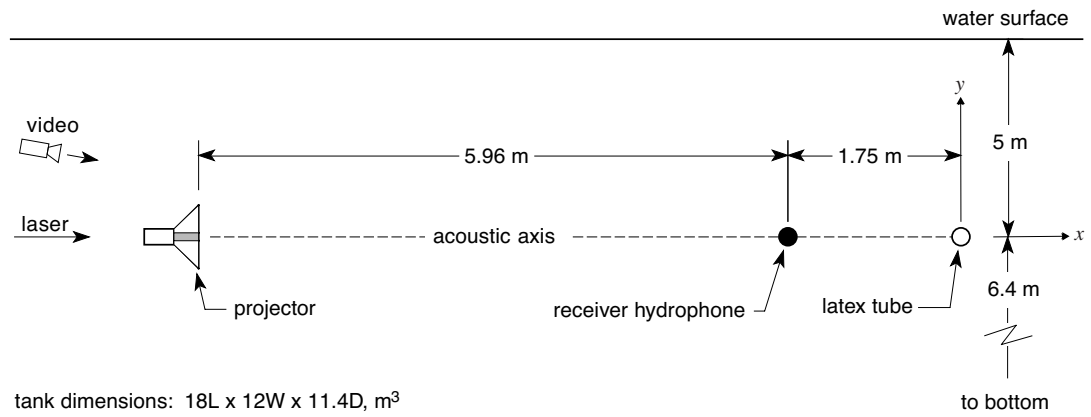


Figure 5.1: Schematic diagram showing a side view of the experimental setup and coordinate axes. The latex tube appears in cross-section, with its length normal to the page.

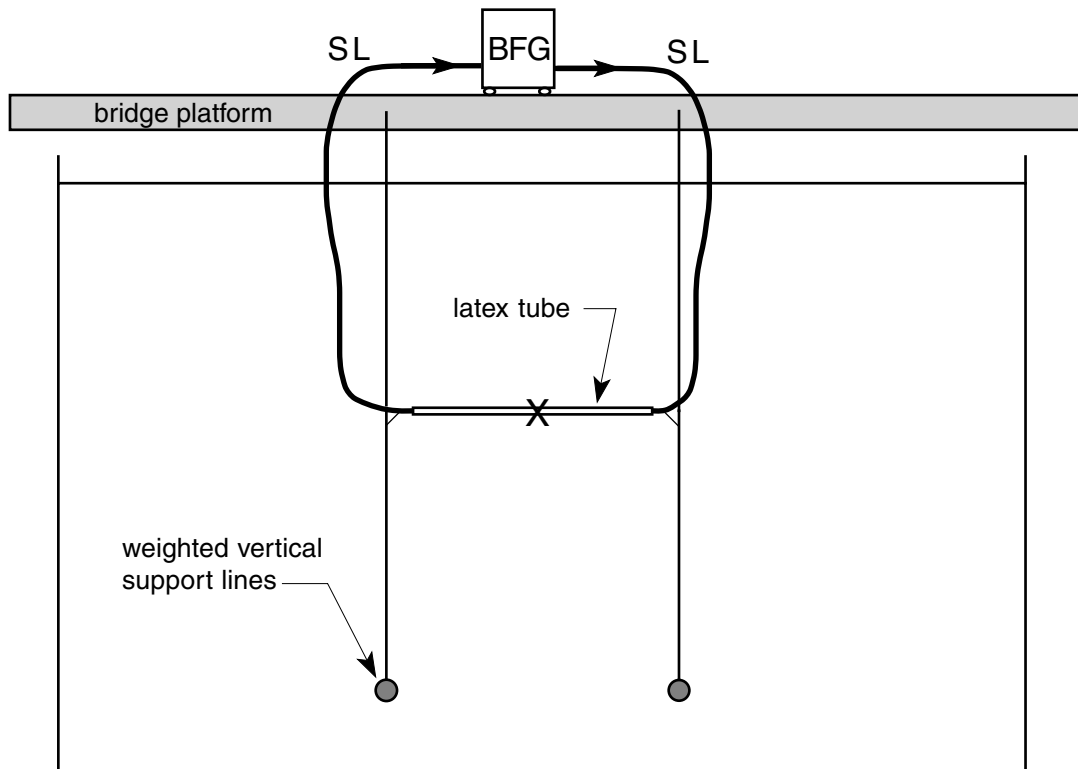


Figure 5.2: Schematic view of the latex tube deployment from a position behind the projector (projector and hydrophone omitted for clarity). The bubbly liquid is generated at BFG and circulated via the supply lines labeled SL. The latex tube is held in place by wire support lines. The letter X marks the acoustic axis, which is normal to the page.

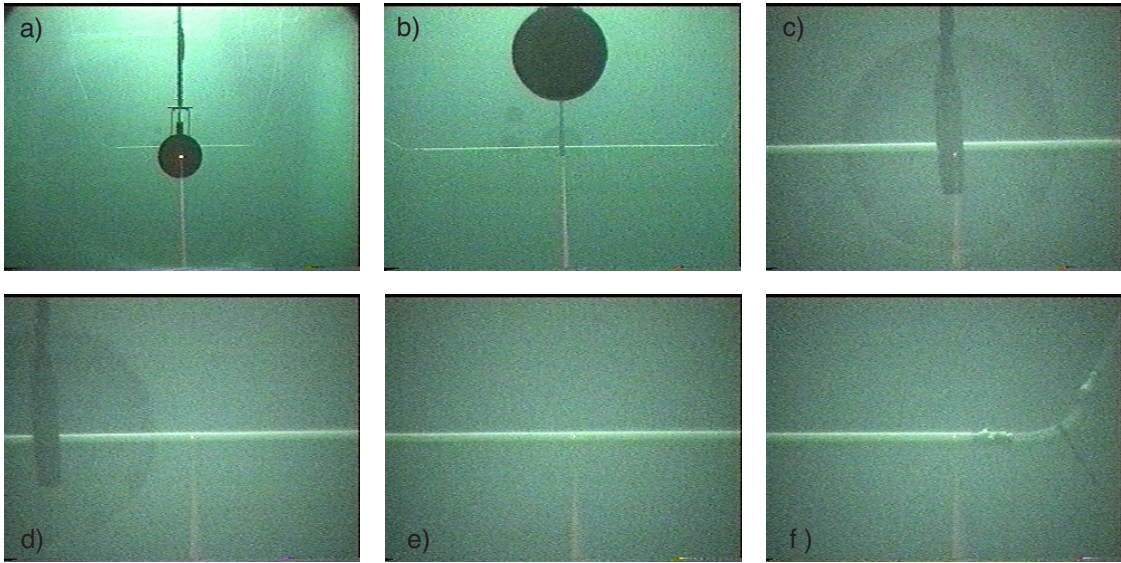


Figure 5.3: Six video frames from the laser alignment system are shown, verifying experimental geometry. See text for details. In the grainy video stills, the tank water looks cloudy, but it was actually clean and clear. A circular viewing port is visible in the tank wall behind the latex tube in b), c) and d).

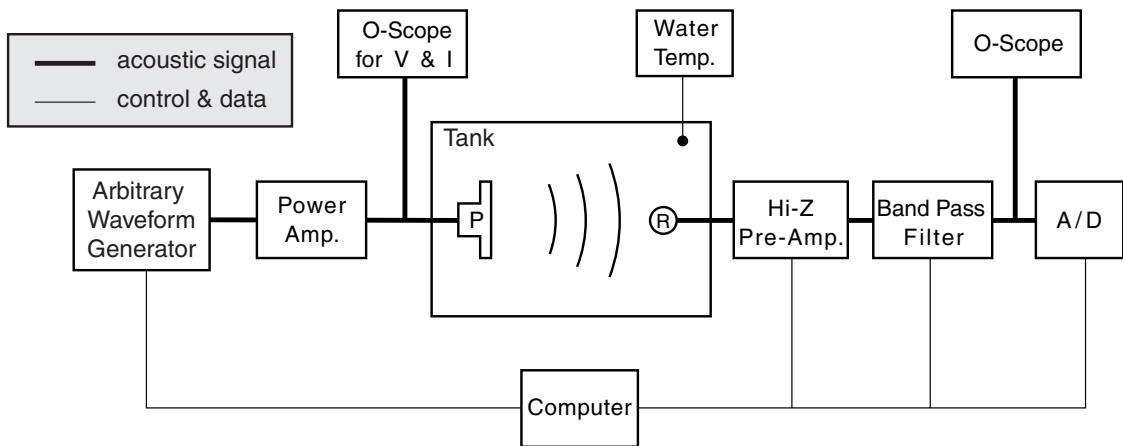


Figure 5.4: A schematic of the transmit and receive electronics used during the scattering experiment is shown. The projector is labeled “P”, the hydrophone receiver is labeled “R” and “A/D” stands for analog-to-digital conversion.

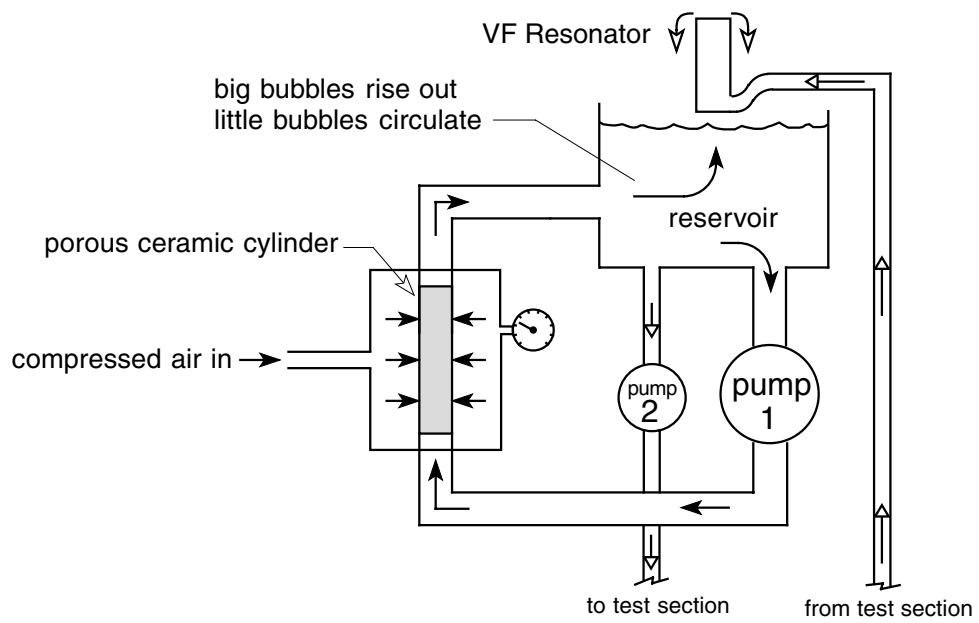


Figure 5.5: A schematic diagram of the bubbly fluid generator is shown. The primary and secondary circuits flow through pumps 1 and 2, respectively. Here “test section” is used to indicate either the latex tube during scattering experiments, or an imaging cell during bubble sizing.

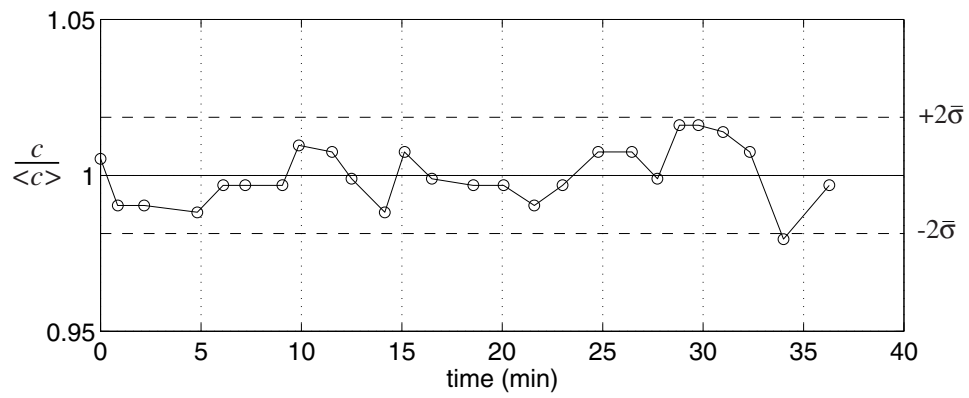
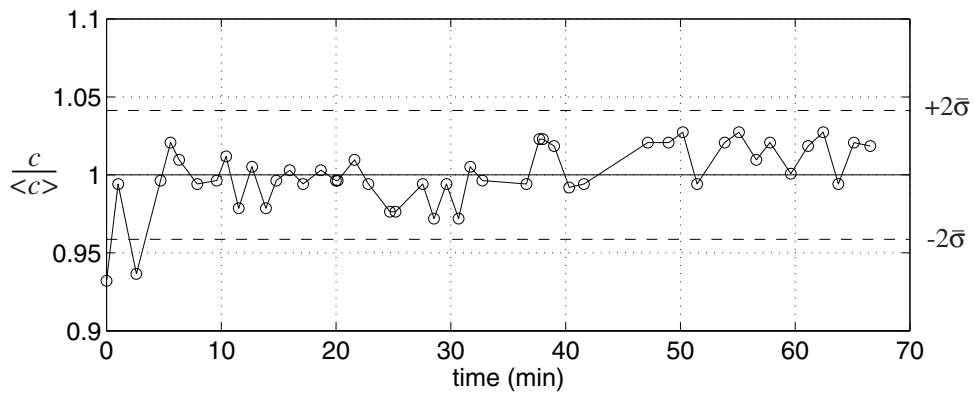


Figure 5.6: Sound speeds measured in the VF resonator for two experimental cases are shown as a function of time.

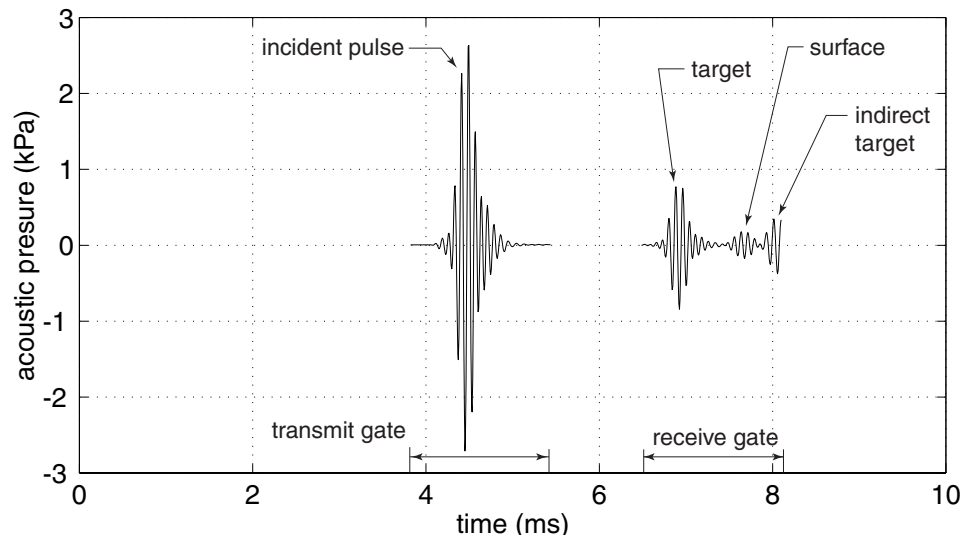


Figure 5.7: A typical measurement showing the incident and scattered waveforms is presented. Various features are identified on the plot. This case is for a frequency of 12 kHz and the highest non-unity void fraction case. The receive gate is plotted at 10 times its actual amplitude, for clarity.

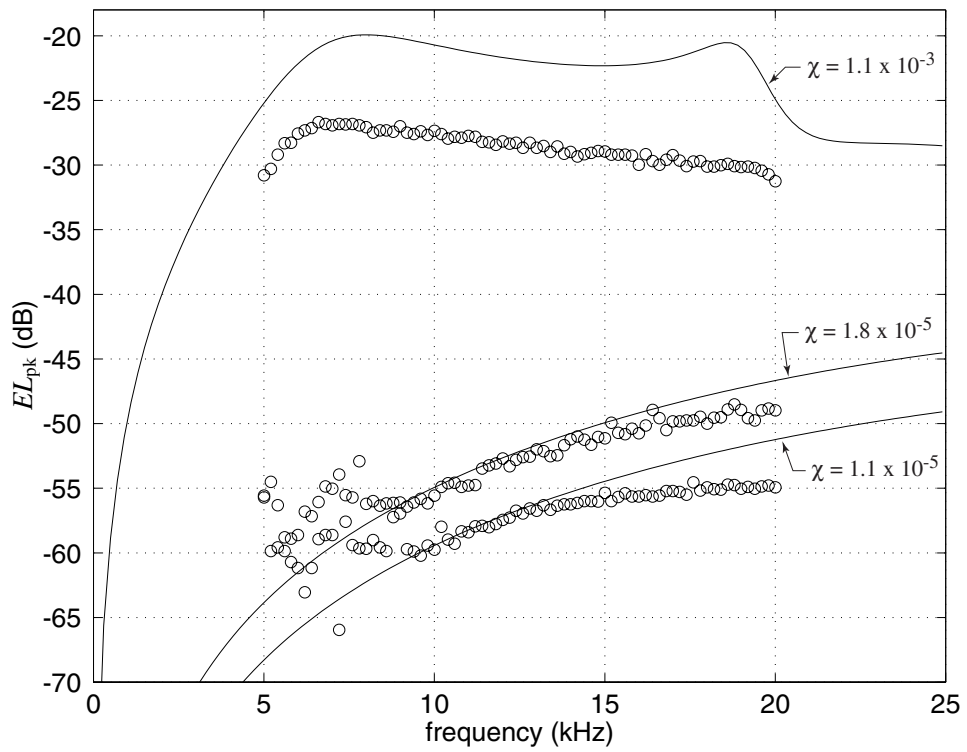


Figure 5.8: Measured scattering from bubbly cylinders (open circles) is shown for three different void fractions χ . Predictions are shown (solid lines) for a CW plane wave fluid cylinder model.

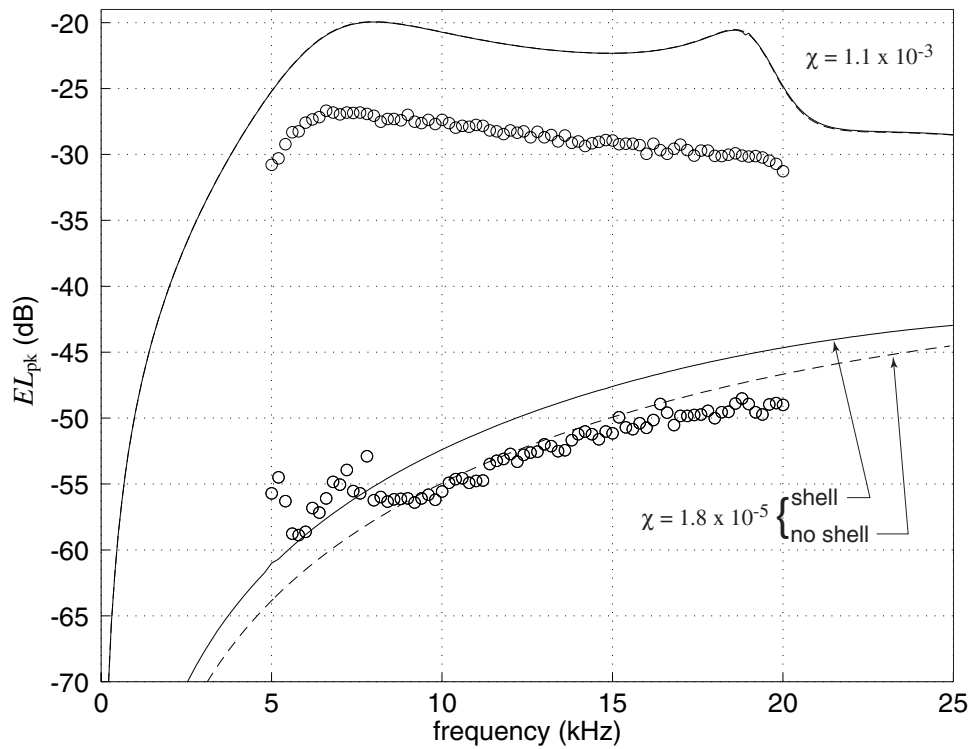


Figure 5.9: The effect of the shell on scattering strength is shown. At low void fractions (lower curve) the shell adds a dB or two to the scattering strength. At higher void fractions, the effect of the shell is barely discernible at the scale shown. The shell (solid line) and no shell (dashed line) cases almost overlay each other.

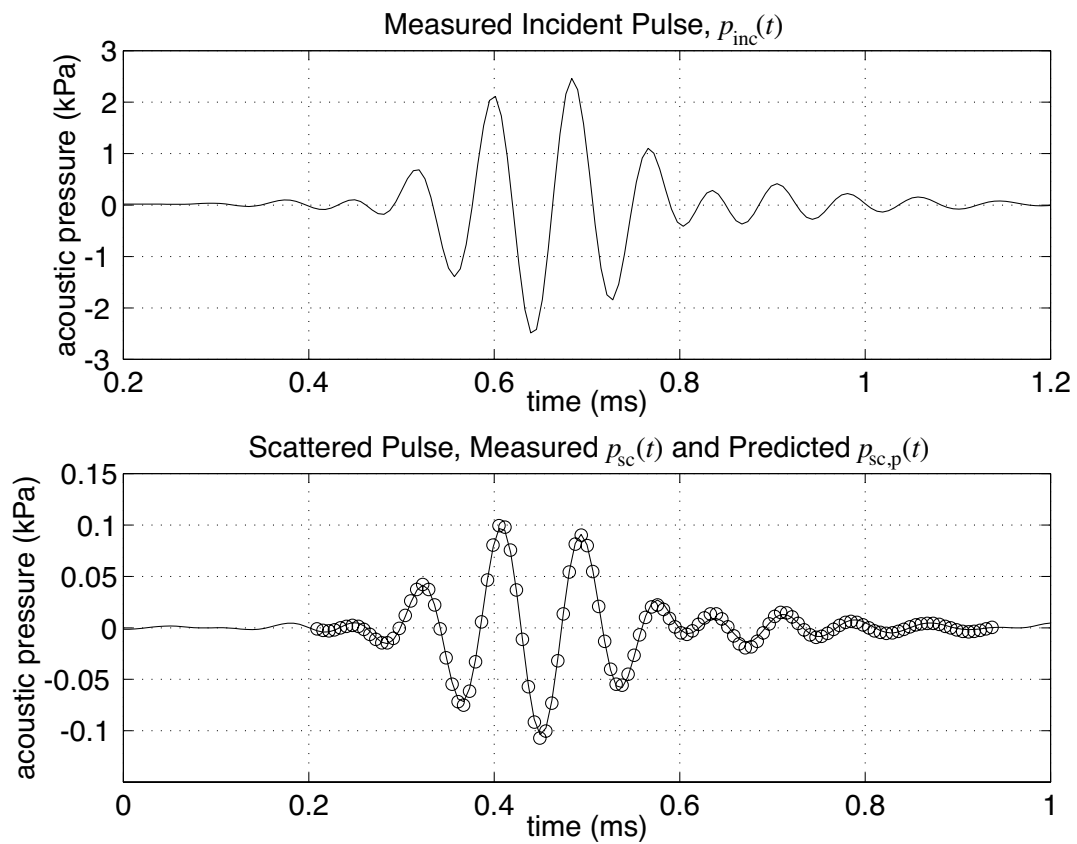


Figure 5.10: A typical pair of measurements, specifically the case corresponding to $\text{VF} = 1.3 \times 10^{-3}$, at 11.2 kHz. Upper plot: measured incident pulse, $p_{\text{inc}}(t)$. Lower plot: measured reflection $p_{\text{sc}}(t)$ shown with a solid line, and predicted reflection $p_{\text{sc,p}}(t)$ shown with open circles.

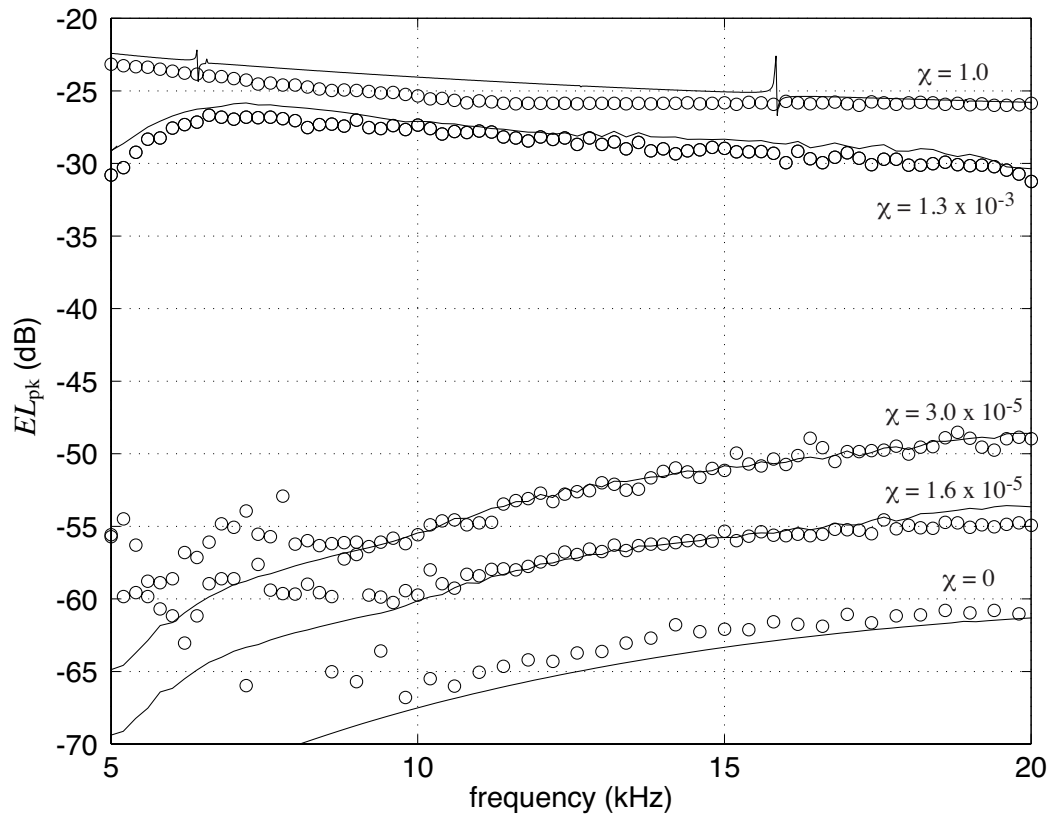


Figure 5.11: Measured (open circles) and predicted (solid lines) peak echo level versus frequency for scattering from the bubbly-liquid-filled latex tube at five different VFs.

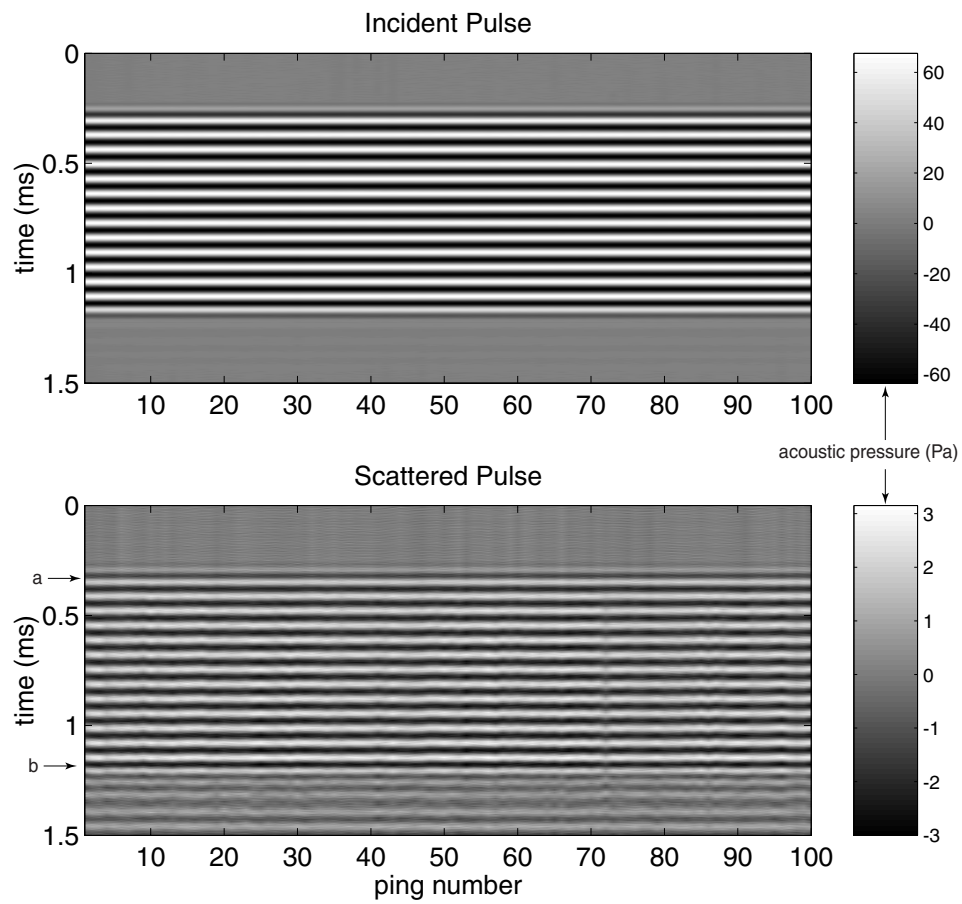


Figure 5.12: One hundred consecutive incident and scattered pings are shown for the 15 kHz and void fraction $\chi \approx 0.0012$ case.

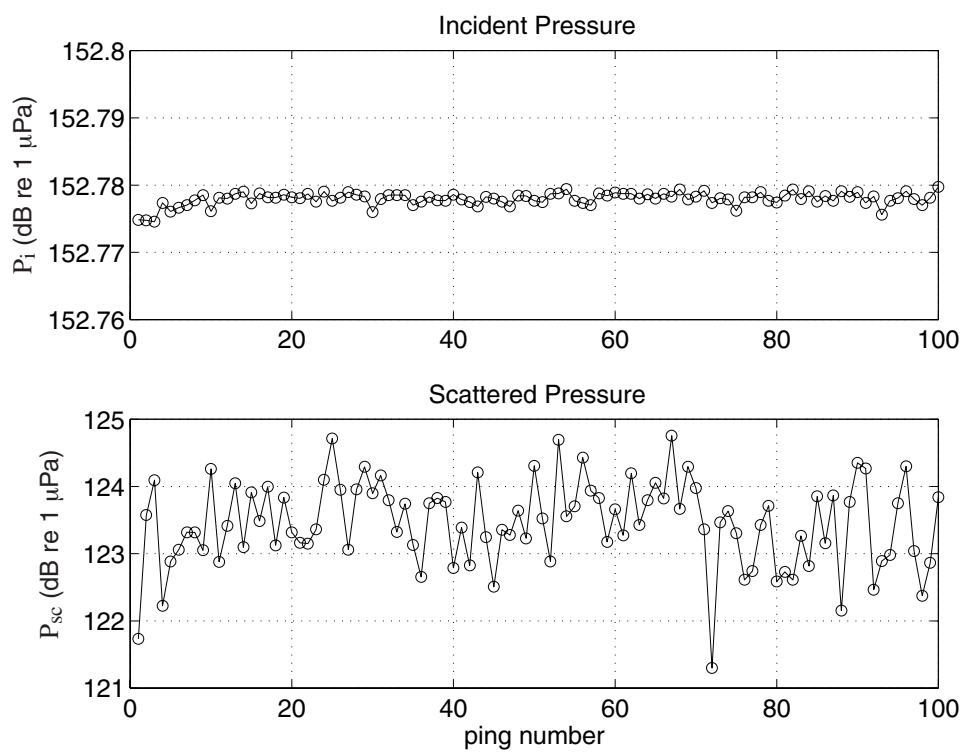


Figure 5.13: The variation in incident and scattered rms acoustic pressure is shown for the 15 kHz data from Fig. 5.12.

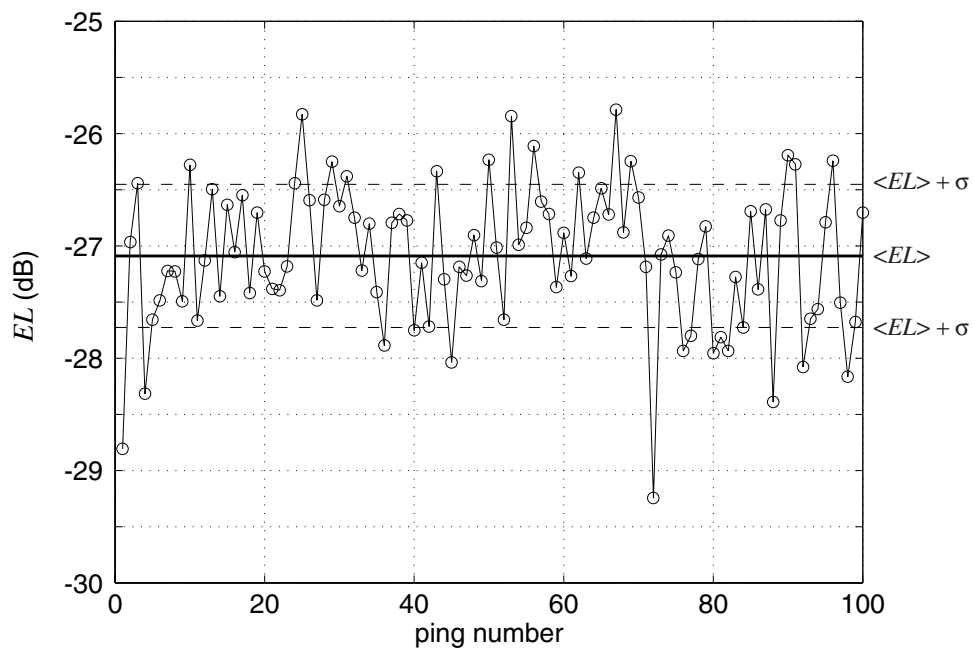


Figure 5.14: The variation in echo level is shown for the 15 kHz data from Fig. 5.12. The mean echo level $\langle EL \rangle$ is shown with a thick solid line, and $\langle EL \rangle \pm \sigma$ are shown with dashed lines.

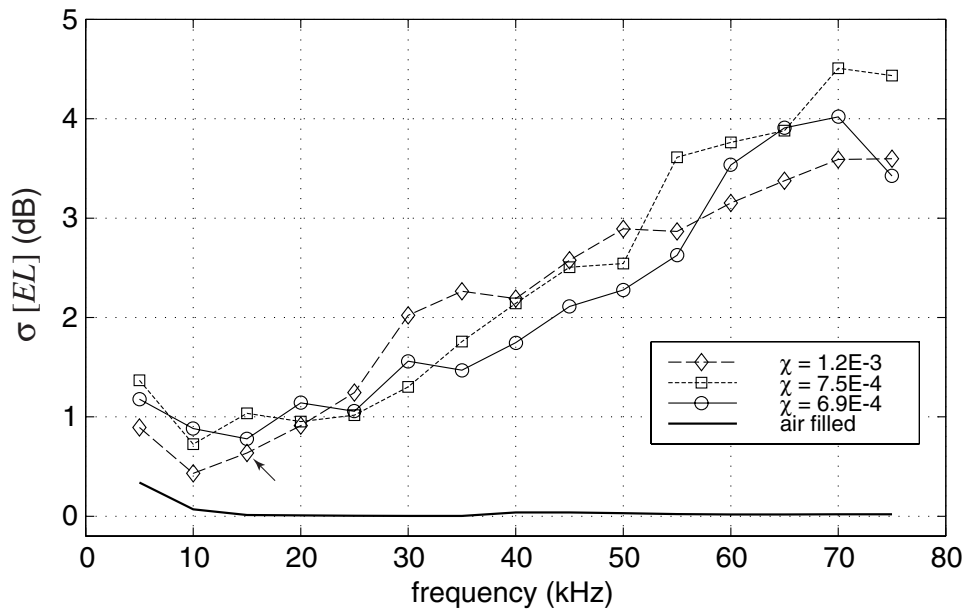


Figure 5.15: The standard deviation of echo level, $\sigma[EL]$, is shown as a function of frequency for three void fractions χ and an air filled tube. The small arrow at 15 kHz indicates the data point corresponding to the standard deviation σ from Fig. 5.14.

Chapter 6

Summary and Conclusions

In this work, the acoustics of bubbly liquid has been investigated. Experiments were conducted which focused on linear plane wave propagation parameters in the frequency range surrounding individual bubble resonance, and on linear scattering from a geometrically well characterized bubble cloud in the form of a bubbly-liquid-filled latex rubber tube. A number of technological innovations were required to make these measurements possible. The main conclusions drawn from the bubbly liquid acoustics measurements and the technological innovations required to obtain them will be summarized below.

6.1 Development of a Water-Filled Impedance Tube System

Because of high attenuation near the individual bubble resonance frequency, traditional time-of-flight and standing wave experimental techniques are not useful for the characterization of propagation parameters in bubbly liquids at void fractions greater than approximately 2×10^{-4} . An impedance tube technique was successfully developed to investigate this regime. The impedance tube itself utilizes the two-sensor transfer function method which yields a measurement of the specific acoustic impedance of a sample material at a range of frequencies. Such devices are common for use in airborne acoustics, but a number of practical difficulties have made them much rarer for use in waterborne acous-

tics. Through the use of an elastic waveguide propagation model, and the development of acoustically hard pressure sensors, these practical difficulties were overcome. The resulting instrument is capable of making impedance measurements in water over the 5–9 kHz frequency range, has a dynamic range of over 5 orders of magnitude, and yields an average measurement uncertainty of 2.2%. These performance criteria put this instrument in a class by itself in comparison to other devices reported in the open literature. A simple modification of the standard technique allows the frequency range to be extended down to 1 kHz, and indicates that future implementations of the system can be scaled up or down in size for a further increase in frequency range.

6.2 Propagation Measurements Near Resonance

The impedance tube system was used to measure the phase speed and attenuation in fluids composed of air bubbles and pure water for a range of void fractions between 6.2×10^{-5} and 2.7×10^{-3} . The bubble size distributions were centered around 0.62 mm in radius. The void fraction and size distribution parameters were obtained from secondary measurements done just prior to or just after the measurement of impedance. It was found that the bubble population statistics were not stationary in time. They were in fact changing during the experiments, even though the observable bubble production controls were stationary in time. Despite this discrepancy, it was found that the theory discussed in Section 2.1 could be used to describe measurements near resonance. In order to do so, some of the bubble population parameters were used to fit the theory to the measurements. This fitting was well within the uncertainty of the population parameter measurements and yielded good agreement between theory and observation near resonance for both phase speed and attenuation. Above resonance, the theory over predicted the observed phase speed, however, it was determined that the inversion technique used to obtain the phase speed and attenuation from the impedance measurements was not appropriate for use when the phase speed rose above approximately 2000 m/s. Therefore, further use of the

impedance tube technique for investigation of the supersonic regime above resonance will require additional work on the inversion process.

In a second round of experiments, the *variability* of both the bubble population statistics and the propagation parameters were investigated. The population statistics measurements and impedance measurements were still done in succession, but here, the time scales of the two sets of measurements were put into synchronization. It was found that Eq. 2.1 could indeed predict the *relative variability* of the propagation parameters at resonance frequency, specifically the peak attenuation and the frequency at which it occurred. This is the case despite the fact that the *absolute accuracy* of Eq. 2.1 has not been experimentally verified. Another general conclusion drawn from these results is the following: Observation of acoustical parameters in bubbly liquids must be done on the same time scale as observation of the associated bubble population parameters.

Finally, these results indicate that the *absolute accuracy* of Eq. 2.1 and of other competing theories can be verified near resonance using the existing impedance tube system. In order to do this, a co-located instrument to simultaneously measure bubble population statistics must be developed, or more stable bubble production equipment must be designed. A less invasive bubble delivery system would also be useful. A scheme utilizing acoustic levitation far away from the frequency of interest may be possible. Alternatively, a bubble stabilizing gel could be used to eliminate the time variability and invasiveness of the needles entirely. At the present time, it appears that the viscoelasticity of this gel (which holds the bubbles in place) has little effect on the response of bubbles in this size range. In either case, the resolution and accuracy of the sizing apparatus must be increased by an order of magnitude over the present system, and the number of bubbles observed per unit time should also be increased by an order of magnitude.

One last result that was not fully investigated in the present work should be reiterated. Evidence of an excitation energy level dependent phase speed and attenuation was observed during the impedance tube measurements. Other possible sources of this effect could not, however, be ruled out. Such nonlinear behavior could have significant prac-

tical consequences. For example, a sonar searching for mines in the presence of bubble clouds could easily exploit this behavior. The bubble clouds surrounding the mine would exhibit an excitation level dependent target strength. This could be used to distinguish them from a mine, which most likely would not have an excitation level dependent target strength. One can envision a detection scheme in which objects with excitation level dependent features were assigned a color different from those without. Subsequent display of this information on a plan-position-indicator would allow a sonar operator to visually localize the mine and perhaps classify it. Of course automated detection, localization and classification schemes could be utilized as well. In any case, this effect certainly warrants further study.

6.3 Scattering Measurements

Observations were obtained of the scattering of acoustic waves from a bubbly-liquid-filled latex tube. These measurements are the first of their kind, in which scattering observations from a geometrically well characterized bubbly fluid target were obtained in a well characterized acoustic environment. In order to make these experiments possible a new device was developed that created a large volume of microbubble-filled liquid. It was found that an effective medium description of the bubbly fluid could be used, in conjunction with a classical scattering formulation described in Section 2.3, to predict scattering at frequencies up to three times the lowest resonance frequency of the structure and one-fifth the mean bubble resonance frequency. Previously, this effective scattering model had only been verified up to the lowest resonance frequency.

In situ void fraction measurement was not available for these measurements and therefore void fraction was used as the model's only fit parameter. Good agreement between the time averaged results and theory was achieved, but considerable amount of ping-to-ping variability was observed. The scattering strength could change by as much as 15 dB between successive pings and significant variability was observed throughout the exper-

imental frequency range. Well below individual bubble resonance, this variability could have been caused by rogue bubbles much larger than average size, or more interestingly, by groups of bubbles travelling together and exhibiting collective oscillation resonance effects. The level of variability was observed to increase as the individual bubble resonance frequency was approached, thereby suggesting that individual bubble effects were also playing a role. The evidence suggests that the effective medium model may continue to be valid as the excitation frequency is increased relative to the individual bubble resonance frequency, but additional averaging may be required. Future scattering experiments of this kind would benefit greatly from true in situ bubble population parameter measurement.

Appendix A

Experimental Verification of Wood's Equation

In this appendix, data from two different low frequency bubbly liquid sound speed experiments will be discussed. Both experiments utilized standing wave tubes. The first experiment was conducted at BU by the author and relied on an organ pipe model of the system to deduce sound speed from measured resonance frequencies. In addition to providing a quick and easy measurement of bubbly liquid sound speed, this experiment was developed to be a lecture demonstration device. The second experiment was performed by Ruggles [46] and was designed for very accurate measurements of sound speed at very low frequencies, where a small amount of dispersion is present. Ruggles obtained sound speed by measuring a half wavelength inferred from the positions of neighboring nulls in the standing wave field.

BU Lecture Demonstration VF Resonator

As an introduction to experimental bubble acoustics at the very beginning of this work, an experiment was conducted to investigate the low frequency propagation regime characterized by Wood's Equation [40]. This experiment was also constructed as an acoustics

of bubbly liquid demonstration apparatus for an education in acoustics demonstration session at the Norfolk ASA meeting in 1998 [68]. Finally, this experiment served as a proving ground for the development of the low frequency void fraction resonators that were used in Chapters 4 and 5. The work reported here is very similar to that reported in Section 4.3, but the key difference was that the void fraction of the fluid of interest was measured using a non-acoustic method, and therefore could be used to verify Wood's equation. The version of Wood's equation that was considered was that given by Eq. 1.10, and repeated here for convenience:

$$\frac{1}{c_{mlf}^2} = \frac{(1 - \chi)^2}{c_\ell^2} + \frac{\chi^2}{c_g^2} + \chi(1 - \chi) \frac{\rho_g^2 c_g^2 + \rho_\ell^2 c_\ell^2}{\rho_\ell \rho_g c_\ell^2 c_g^2}, \quad (\text{A.1})$$

The apparatus was closely related to that discussed in Section 4.3 and shown in Fig. 4.8, but with the following differences. The resonator tube was 0.6 m in length and made of PVC pipe, 5.2 cm in diameter. A different type of needle injection manifold was used. It consisted of twelve 22-gauge needles embedded in an epoxy filled PVC fitting that attached to the bottom of the resonator tube. The needles were positioned in a vertical orientation and therefore released air bubbles directly upward. A small mechanical float was positioned at the top of the tube, such that it floated on the upper surface of the water. The float was attached to a pointer which indicated the height of the water surface on a centimeter scale. In this way, the overall length of the water column in the tube could be measured to an accuracy of about 0.5 mm. The length is related to the void fraction by $\chi = \Delta\ell/(\ell + \Delta\ell)$. These details are shown in Fig. A.1, which also shows additional apparatus used in the lecture demonstration, specifically sound reinforcement for public address.

Just as in Section 4.3, the bubbles breaking off the needles excited the normal modes of the tube, and the resonance frequencies could be observed using a hydrophone and a spectrum analyzer. The airflow rate was set, and the void fraction measured using the float. A spectrum was acquired and from the resonance frequencies, a sound speed was

calculated as detailed in Section 4.3. This was repeated for several void fractions ranging from about 0.1% to 2%. A single spectrum is shown in Fig. A.2-a for the case of 0.4% void fraction. A waterfall plot of all the spectra obtained in the experiment is shown in Fig. A.2-b. In Chapter 4, the sound speed at each frequency was used to calculate the dispersive sound speed as the resonance frequency was approached from below. In this case, the resonance frequency was high enough to render dispersion negligible, and the slope of the resonance frequency versus mode number curve was used to obtain a spatially and frequency averaged sound speed. The slight variation of void fraction with depth over the 0.5 meter column length was ignored. The elastic waveguide effects were calculated and found to be of order 1% and also ignored.

The results of the data reduction and the comparison to theory are shown in Fig. A.3. Good agreement is found between the measured and predicted sound speeds at void fractions above 0.3%. Below this void fraction, the number of bubbles in the tube at any given time was few, and they were not evenly positioned out throughout the length of the tube, leading to non-homogeneous conditions inside the waveguide. The effective medium theory breaks down under such conditions and no longer describes the system. In order to go to lower void fractions, a different bubble injection scheme would be required. These results confirmed that Wood's Equation could be used to determine void fraction from low frequency bubbly fluid sound speed, which itself had been determined from the measurement of resonance frequencies inside a one-dimensional waveguide.

As mentioned previously, the apparatus described in this section was also used as a lecture demonstration. When the hydrophone output is amplified and broadcast through a public address system, the normal modes of the column can be detected as low frequency tonal sounds superimposed on a background of noise. The dependency of sound speed on void fraction can actually be heard in real time, as it is expressed in the pitch of the normal modes. Changing the flow rate from 0.1% to 2% over a few seconds results in the sound speed in the tube changing from approximately 300 m/s to 100 m/s over the same time scale, and hence the pitch of the sound is changed from about 150 Hz to 50 Hz,

which is an octave and a half. This is easily detected by ear, but because the frequencies are relatively low, a large speaker is required to reproduce the sound. The overtones can still be heard if only a small speaker is available, but the demonstration is more effective with a large speaker. The flow rate can be cycled up and down, and interesting sounds can be made by playing with the flow rate in this way. The spectra of these sounds can be seen in real time on the signal analyzer, with the peaks shifting up and down with the flow rate. Ideally, a waterfall plot can be displayed showing a brief history, like that shown in Fig. A.2-b. This demonstration has been given a number of times and has been very successful in impressing observers ranging from elementary school students to deans of large research universities. Although certainly more complicated to carry out, this a fine alternative to the often used glass of beer demonstration.

Very Low Frequency Data of Ruggles

It has been mentioned previously that Wood's limit is a low frequency approximation which predicts dispersionless propagation. In fact, there is a small amount of dispersion all the way down to zero frequency. In 1986, Ruggles [46] conducted an experiment to investigate this and indeed found dispersion which was well described by a theory put forth in the same paper and later fully detailed in his dissertation [129]. By 1989, Commander and Prosperetti [33], henceforth referred to as C & P, had put together a rigorous broadband theory and published a summary of experimental work to compare with their theory. They decided not to include Ruggles' data, claiming that Ruggles' own theory failed to describe his attenuation measurements, and that it appeared the culprit was poor control of the bubble production.

Ruggles' own theory, however, did a very good job of predicting the low frequency dispersion that he observed. The theory of C & P, which also appears to do a good job at low frequencies, was not compared to either Ruggles' data or theory. It turns out that C & P also does a very good job of describing the low frequency data of Ruggles, except it does so at a slightly different void fraction than that reported by Ruggles. The measurements

of Ruggles and the theory of C & P (Eq. 2.10) are shown in Fig. A.4 for two different void fractions and bubble sizes. Very good agreement is seen between measurement and theory for both cases but best fit void fractions were used to produce these curves, not the void fractions reported by Ruggles. The upper curve was produced with $\chi = 1.625\%$, but Ruggles reported $\chi = 2.01\%$. The lower curve was produced with $\chi = 2.28\%$, but Ruggles reported $\chi = 2.98\%$. When used as input to Eq. 2.1, the void fractions reported by Ruggles did not yield good agreement between the data and the C & P theory. Ruggles' original figure is not shown here, but the same data is described equally well by Ruggles' theory using the void fractions he reported. This discrepancy remains a curiosity and a mystery. It is uncanny that the dispersion is predicted so well by both theories, but the absolute value is represented incorrectly by at least one of the theories. Most likely, additional experimentation will be necessary to sort this out. In any case, the Wood limit sound speed is also shown in Fig. A.4 and it is seen to be within 3% of the measured values. The deviation is worse as the frequency goes down, but above 50 Hz, the Wood limit sound speed is a good approximation of the actual sound speed.

Although it plays a minor role here, the following information is included for completeness. Ruggles reported average bubble sizes for the two data sets shown in Fig. A.4. Those bubble sizes, $\bar{a}_1 = 1.2$ mm and $\bar{a}_2 = 1.5$ mm, are included in the figure. They were also used as input to Eq. 2.10 for the theoretical calculations shown in the figure.

Demonstration Apparatus

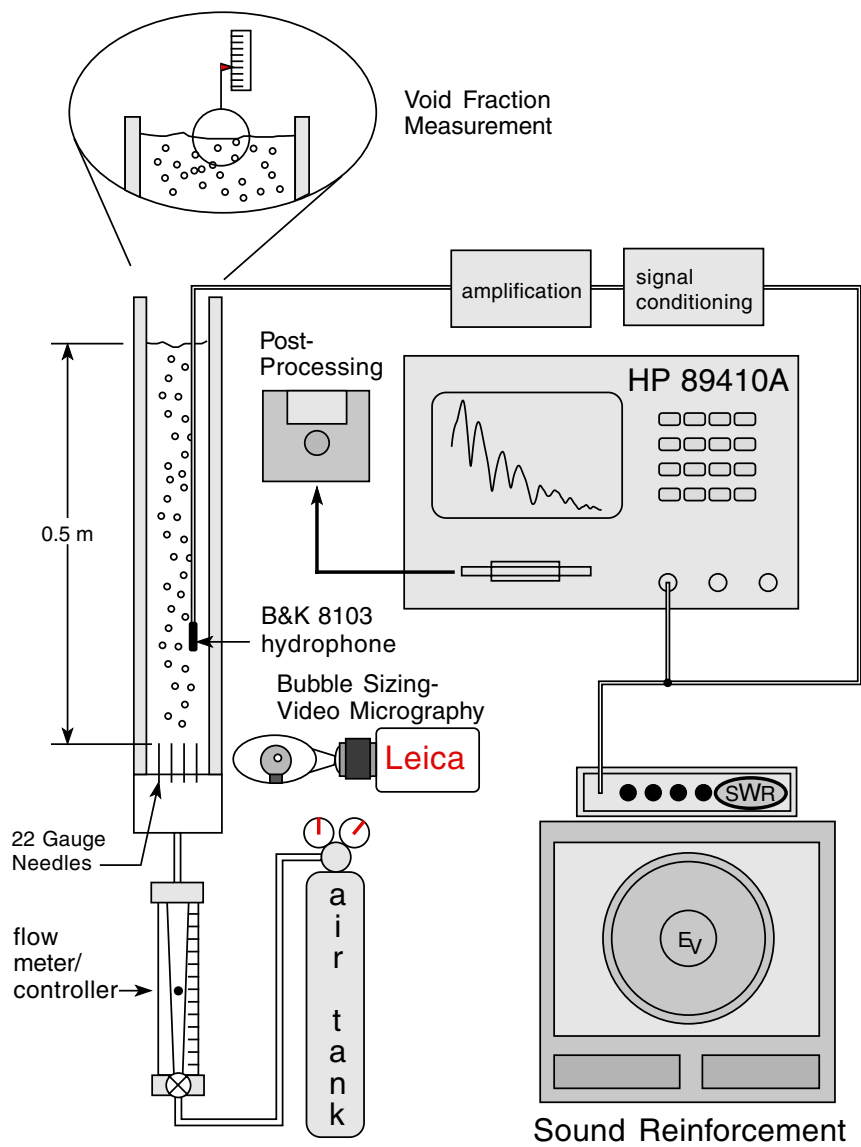


Figure A.1: A schematic diagram of the demonstration apparatus is shown.

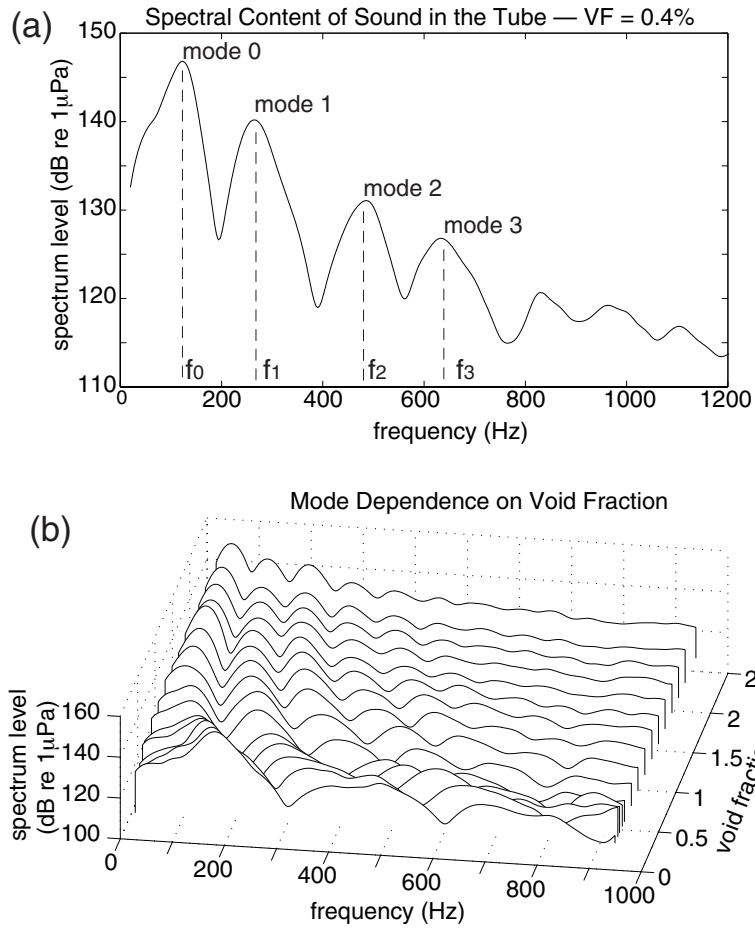


Figure A.2: A single spectra from the 0.4% void fraction case is shown in (a) where the individual modes have been identified. A waterfall plot of all the experimental spectra is shown in (b). Sound speeds obtained from these spectra are shown in Fig. A.3.

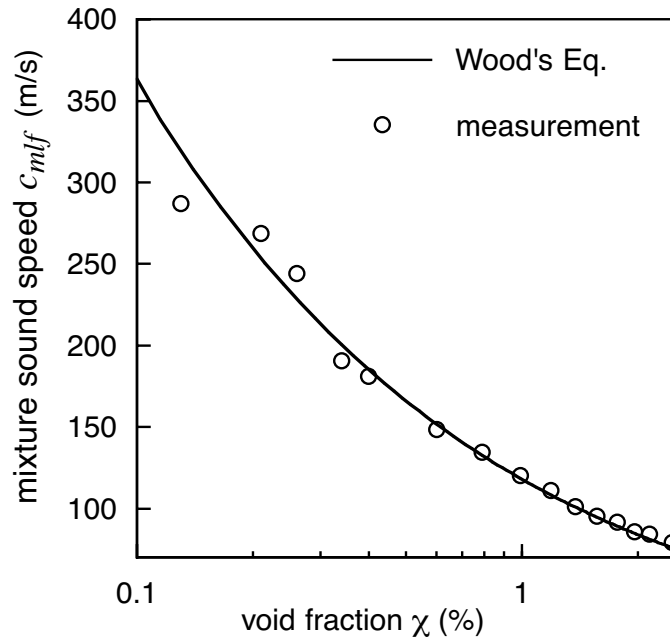


Figure A.3: Experimental verification of Wood's Equation.

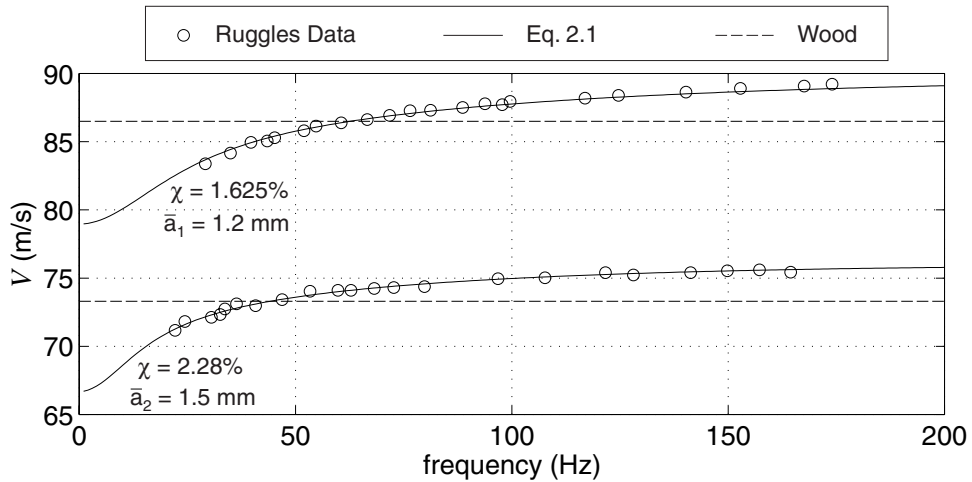


Figure A.4: Ruggles data from Fig. 5.2.2 of [129] is shown along with the predictions of Eq. 2.1 for two best fit void fractions, $\chi = 1.625\%$ and $\chi = 2.28\%$. The dashed horizontal lines represent the Wood limit sound speed at the same void fractions. Ruggles reported $\chi = 2.01\%$ and $\chi = 2.98\%$ for the upper and lower data, respectively.

Appendix B

High Mechanical Input Impedance Hydrophones

The TFM standard [99] calls for flush, wall mounted pressure sensors that do not perturb the acoustic field. This means the sensor and the wall must have similar acoustic impedances. The sensor must also be significantly decoupled from acoustic wall motions. Fulfillment of these requirements in an air-filled tube is not difficult, but it becomes a serious issue in a water filled tube due to the relatively high specific acoustic impedance of water. No appropriate commercially available sensors were found, so the hydrophones had to be custom made.

The initial design, designated BU-250-10, utilized a PZT disc¹ as the sensing element which was installed in a 1.27 cm diameter aluminum housing shown in Fig. B.1-a. The hydrophone is inserted in a match-drilled hole in the impedance tube wall, and sealed with double o-rings. In order to couple with the fluid medium in the tube, but remain decoupled from wall motion, the PZT disc was mounted on a Corprene backing and encapsulated with a water-impedance matched potting material called Sylgard 170.² Despite meeting

¹PZT dimensions: 0.635 cm diameter \times 0.254 cm thick. Supplier: Piezo Kinetics Inc.; P.O. Box 756; Bellefonte, PA 16823; (814) 355-1594

²Supplier: Dow Corning Corporation; Midland, Michigan 48686-0994; USA

the geometric requirements, this hydrophone altered the acoustic conditions in the tube, as shown in Fig. B.2-a. The plot shows the frequency response in the tube prior to drilling the holes for the hydrophones, and the same measurement performed after the hydrophones were installed. The shape and location of several features have changed. First, several resonance frequencies have shifted, indicating a frequency dependent boundary condition change. Second, the low frequency response has decreased, indicating a frequency dependent increase of damping. This indicates the sensors have a significantly lower acoustic impedance than the tube wall, rendering them unusable in the present system.

Based on the first design, using the same sensing element, a new phone was designed and is shown in Fig. B.1-b. This design was designated BU-2502. The PZT disc is now sandwiched between a stainless steel window and a stainless steel backing, in order to provide high input impedance in the radial direction. (See Fig. 3.4 for coordinate system.) Previous elastic waveguide modeling indicated the wall motions are primarily perpendicular to this direction, so the PZT element was decoupled from this motion by layering three 0.01 mm thick mica sheets between the steel and PZT on both sides. The mica is a hard glass-like material, so it does not decrease the impedance in the radial direction. These shear layers slip relative to one another and therefore decouple transverse motions. This effectively isolates the sensing element from most acoustically induced wall motions. The effectiveness of the new phone design is shown in Fig. B.2-b. The before and after responses are very similar, except for slightly increased damping at certain frequencies. This was deemed acceptable and the design was adopted for use in the TFM.

The mechanical drawings for the acoustically hard hydrophone housing are given in Figs. B.3 and B.4 and an assembly drawing is shown in Fig. B.5. This hydrophone design was named BU-2502, and two units were produced. The housing was machined out of 304L grade stainless steel. After completion of the housing, 40 gauge wire leads were attached to the ceramic element of the type mentioned above. The PZT element and the mica layers were then installed between the cap and the base. The housing was designed such that upon threading the cap and the base together, the mica/PZT sandwich would

be in slight compression, thus putting it in acoustic contact with the steel window, and thus the water in the impedance tube. The leads from the PZT element were connected to a twisted pair of 28 gauge conductors. The positive electrical connection was made with the red member of the twisted pair and was attached to the upper face of the PZT element, with respect to the orientation shown in Fig. B.1-b. The twisted pair was in turn surrounded by a 100% coverage foil shield layer and a copper drain wire. The cable assembly was completed with a PVC jacket. In order to isolate the hydrophone signal from electrical noise, the drain wire was electrically connected to the hydrophone housing. At the other end of the cable, the positive (red) lead was connected to the pin of a BNC plug, and the negative (black) lead was connected along with the drain wire to the base of the BNC plug, putting the shield in contact with electrical ground, but only at the dry end of the hydrophone. This is essential to isolating the signal from noise. If the shield is put into contact with electrical ground at the hydrophone as well, a ground loop can be created. The cable was then potted into the cavity in the base of the hydrophone housing using Sylgard. Unfortunately, the potting has subsequently detached from the hydrophone housing, and it is no longer hermetically sealed against moisture. The cap of the hydrophone is sealed, but in order to operate the hydrophone with the cable end submerged, an alternative method for water proofing was used. The hydrophone cable was inserted into a 1/2" i.d. Tygon tube, which was clamped to the hydrophone housing. This provides effective waterproofing down to the length of the cable.

Since these hydrophones will perhaps be used for some time to come, electrical input impedance curves for both units are included in Figs. B.6 and B.7. Although the hydrophone sensitivity is not directly needed for use in the Transfer Function Method, the sensitivity of these hydrophones was measured using a substitution method within the impedance tube. An 8103 was used to measure a pressure spectrum, and then a BU-250-10 was placed in the same position for another pressure spectrum measurement. Physical differences between the 8103 and the BU-250-10 result in the technique providing only an approximate calibration, intended to provide the basic sensitivity level, not an absolute

wideband calibration, such as would be obtained from a free field calibration. The voltage sensitivity curve for the BU-250-10, serial number 1 is shown in Figs. B.8, along with sensitivity curves for the B & K 8103 and the Dapco needle hydrophone used in the radial scan measurements shown in section 3.6.1. The charge sensitivity curves for 2 later units, BU-250-10-4 and -5 are shown in Fig. B.9. Sensitivity curves for the hard hydrophones, BU-2502 are not available, but have been used at exactly the same amplification levels as the BU-250-10 units, and therefore should have quite similar sensitivities. Certainly, the PZT element is of the same material and size in both models.

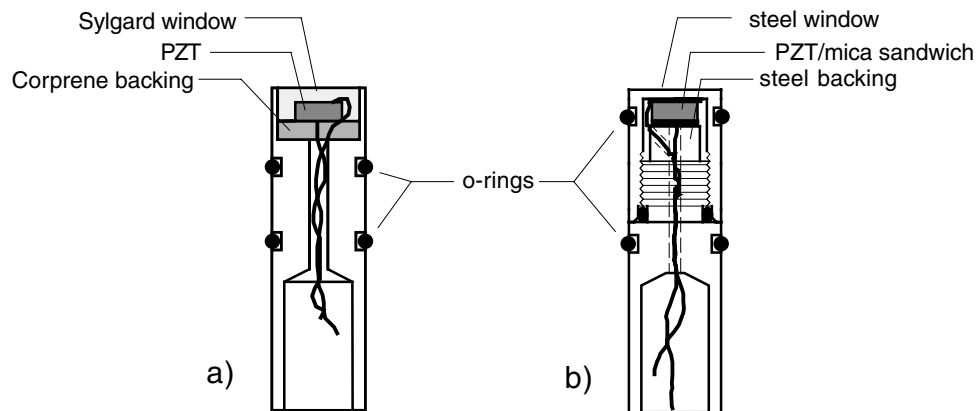


Figure B.1: a) Cross-sectional view of original custom hydrophone, BU-250-10, which proved too great an impedance mismatch with the tube wall. b) Redesigned high mechanical-input-impedance hydrophone, BU-2502.

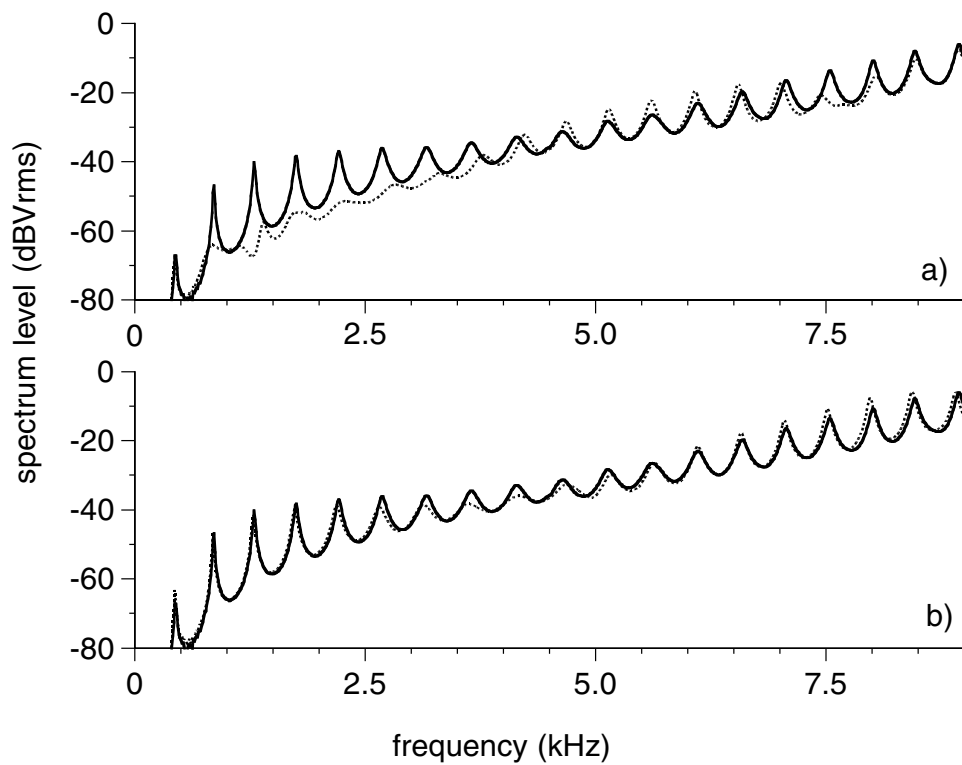
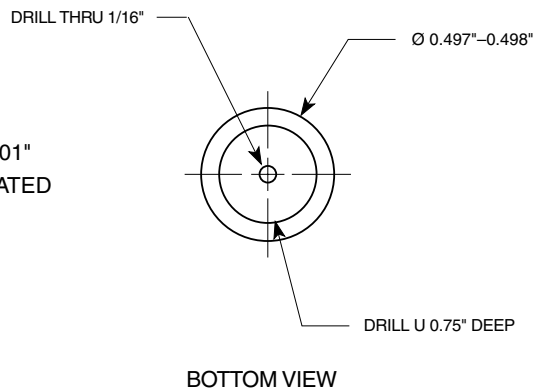
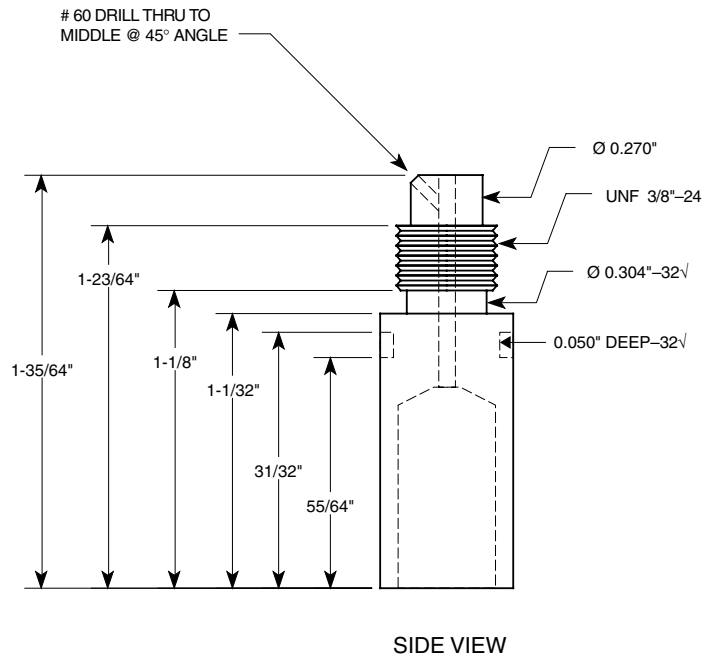


Figure B.2: a) Frequency response before (solid line) and after (dotted line) installation of original custom hydrophone. Note frequency shifts throughout range, and severely reduced response from 1500–4000 Hz. b) Frequency response before (solid line) and after (dotted line) installation of high impedance hydrophone.

BU-2502 — HYDROPHONE CASE



ALL TOLERANCES +/- 0.001"
UNLESS OTHERWISE STATED

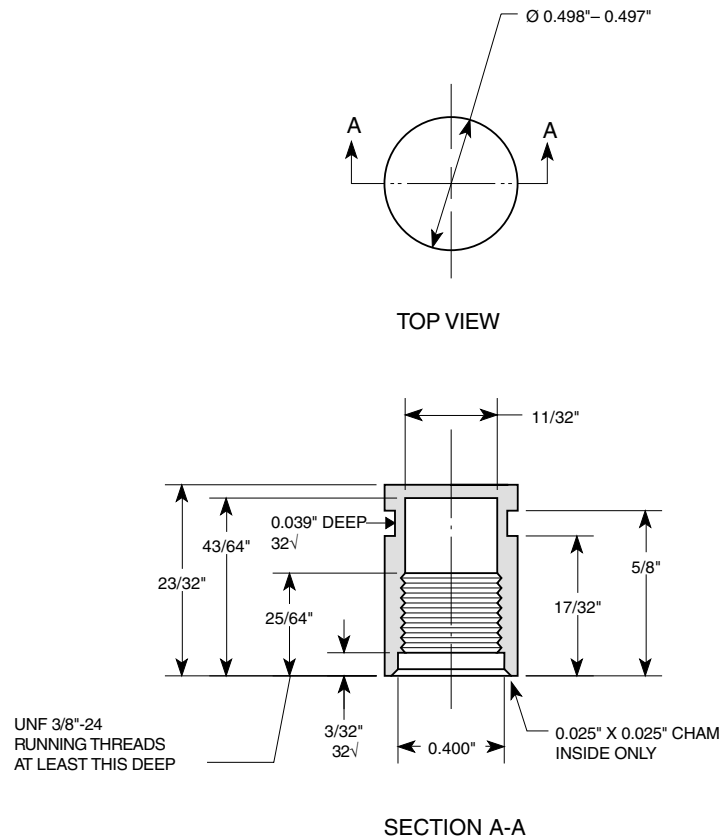
NEED TWO PIECES

SCALE: 2:1
Material: 304SS
Preston Wilson
353-4854

CHARGE TO:
REQ. NO. 593111

Figure B.3: A facsimile of the mechanical drawing used to make the high mechanical input impedance hydrophone BU-2502 is shown. This is part 1 of a 3 part drawing.

BU-2502 — HYDROPHONE CAP



ALL TOLERANCES $\pm 0.001''$ UNLESS OTHERWISE STATED

NEED TWO PIECES

SCALE: 2:1

Material: 304 SS

Preston Wilson

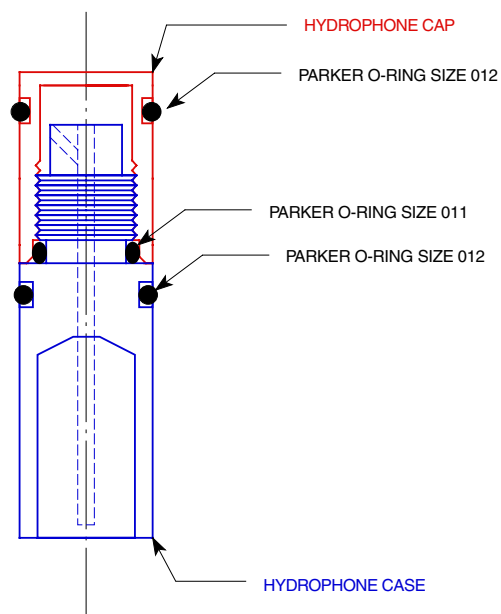
353-4854

CHARGE TO:

REQ. NO. 593111

Figure B.4: A facsimile of the mechanical drawing used to make the high mechanical input impedance hydrophone BU-2502 is shown. This is part 2 of a 3 part drawing.

BU-2502 — ASSEMBLY DRAWING



SCALE: 2:1
Preston Wilson
353-4854
CHARGE TO:
REQ. NO. 593111

Figure B.5: A facsimile of the mechanical drawing used to make the high mechanical input impedance hydrophone BU-2502 is shown. This is part 3 of a 3 part drawing.

performed by:
Preston Wilson
psw@bu.edu

Electrical Input Impedance — BU2502-1 (in water)
performed on HP 89410A

Oct. 14, 1999
PACLAB
BU Aero/Mech
Rm 409

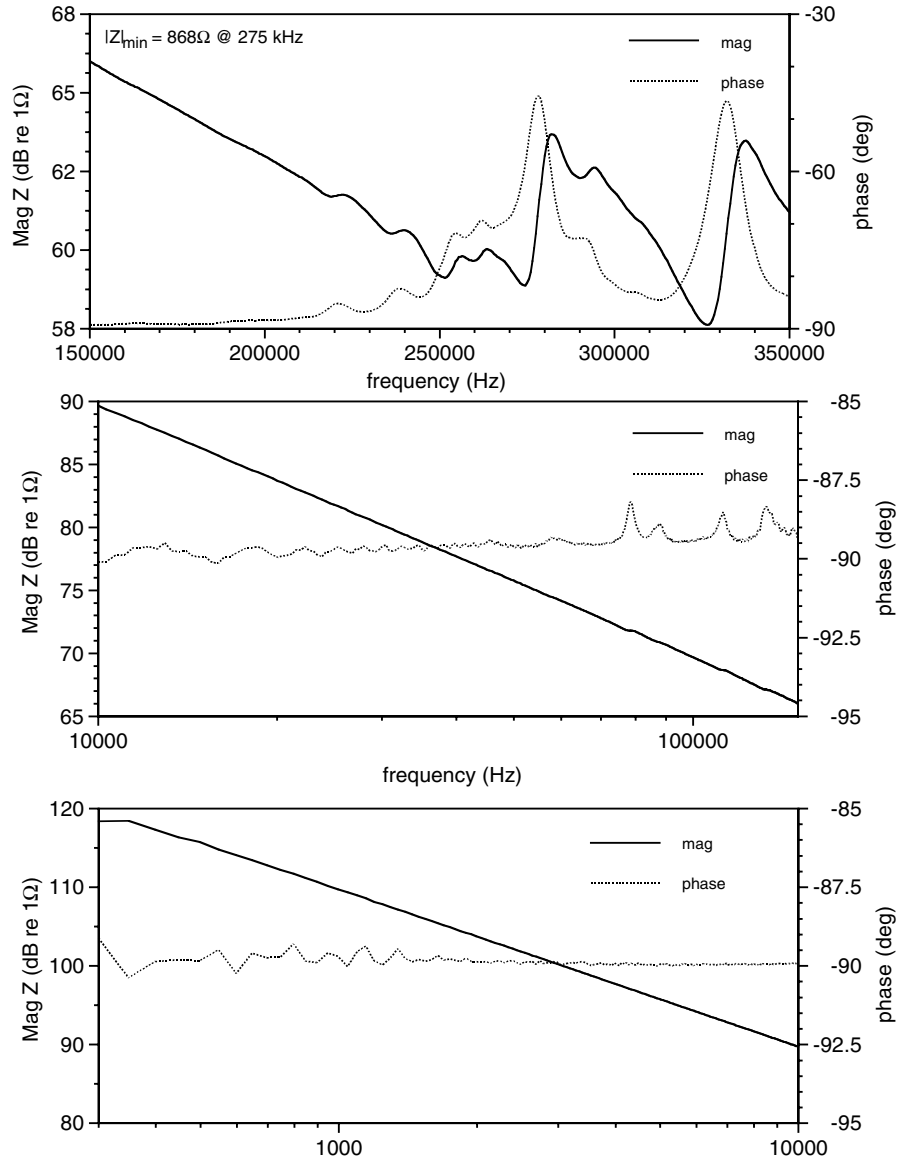


Figure B.6: A measurement of the electrical input impedance of the BU-2502 hydrophone, Serial Number 1 is shown.

performed by:
Preston Wilson
psw@bu.edu

Electrical Input Impedance — BU2502-2 (in water)
performed on HP 89410A

Oct. 14, 1999
PACLAB
BU Aero/Mech
Rm 409

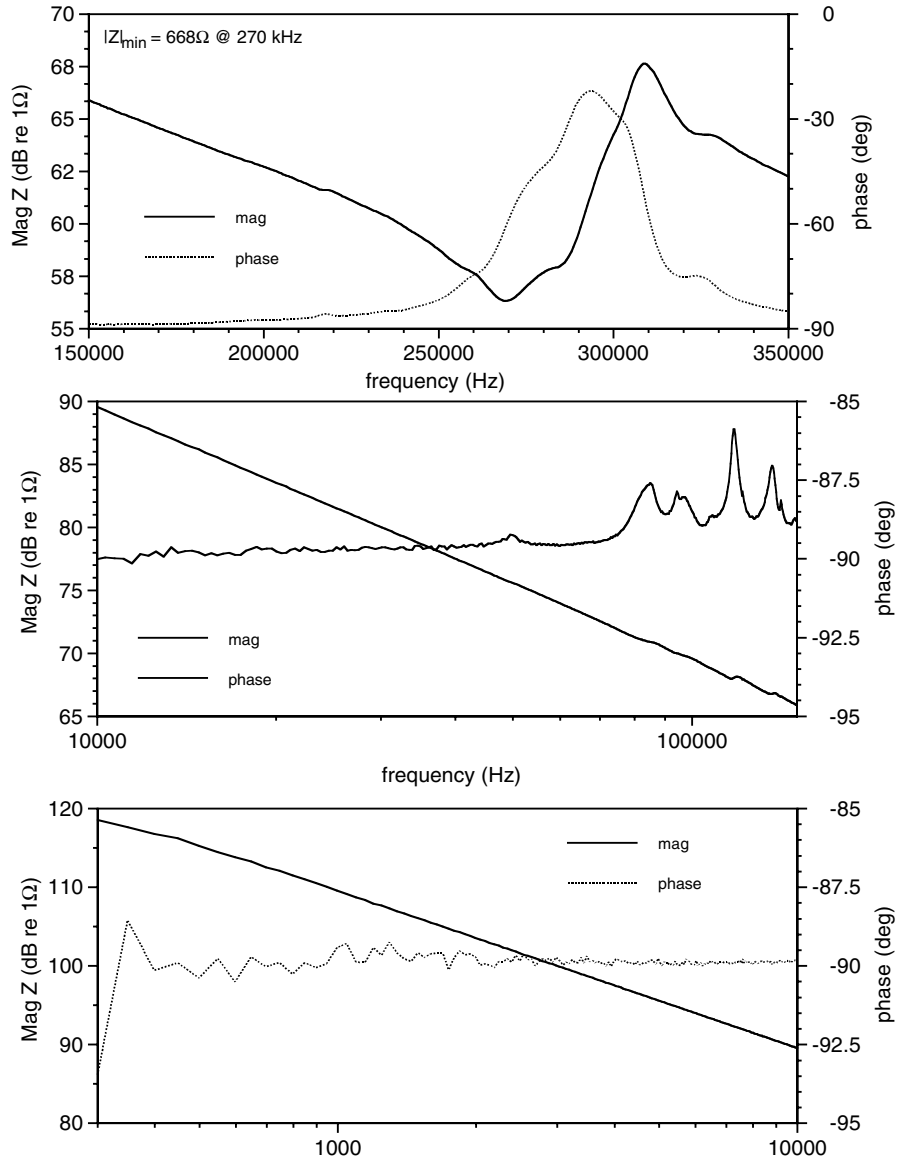
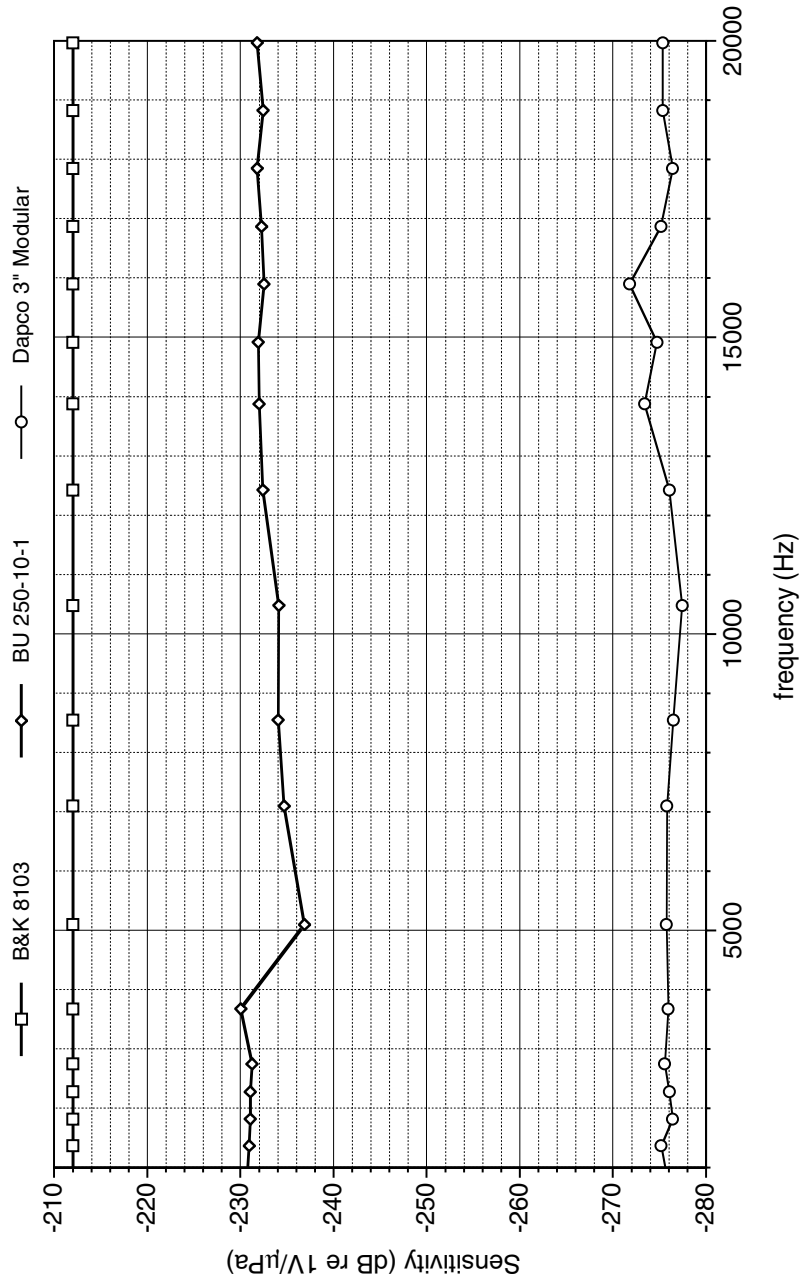


Figure B.7: A measurement of the electrical input impedance of the BU-2502 hydrophone, Serial Number 2 is shown.

Hydrophone Calibration by Standing Wave Substitution Method

Standard: B&K 8103 s/n 2071686 Facility: 4 1/2" Tube Depth: 16 cm
 Water Temp: 22 °C Source: Ling V-203 Drive Level: 1.01 Vrms
 Data Acquisition: Nexus/TDS 420A (full BW-1MΩ)

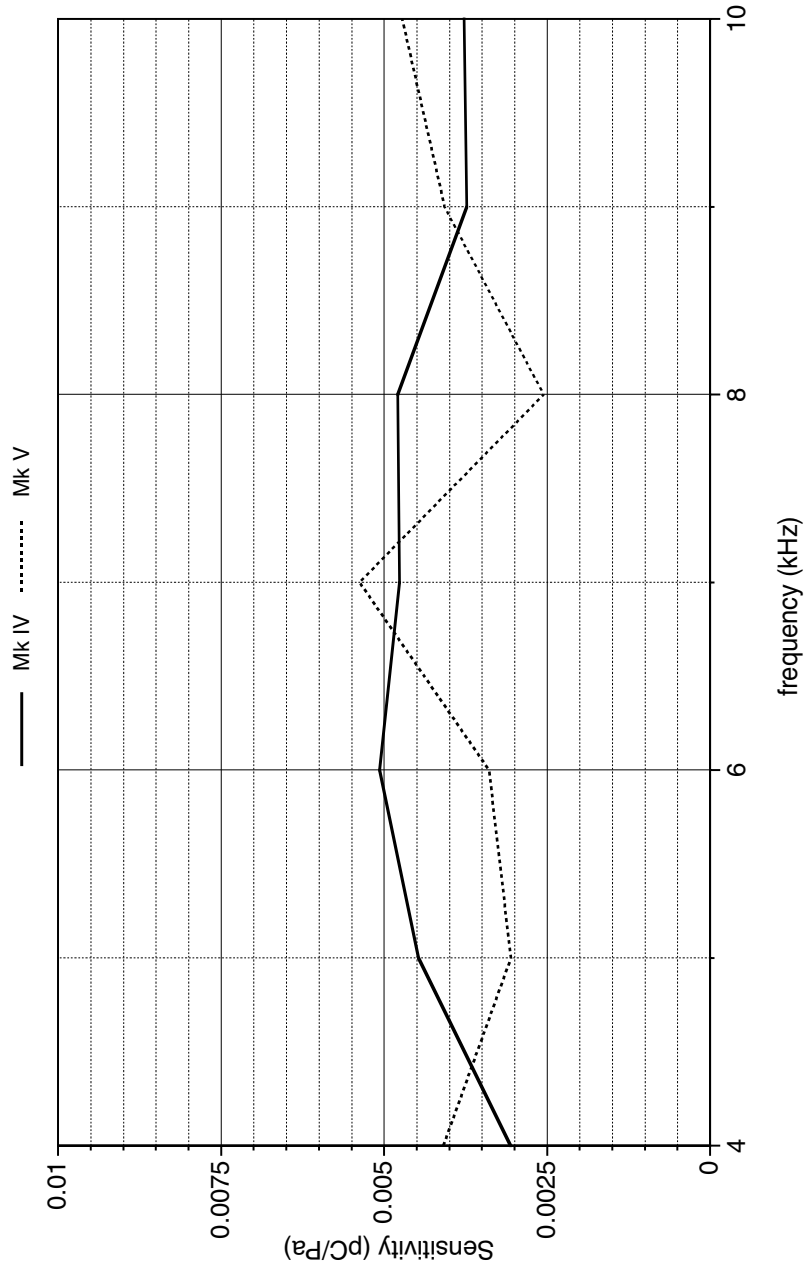


Calibration Performed by:
 Preston Wilson
 psw@bu.edu

9/17/98
 BU:PACLAB

Figure B.8: Sensitivity of three hydrophones used in this work. The curve for the 8103 was not measured in house, but represents the data provided by the supplier.

Hydrophone Calibration by Standing Wave Substitution Method
 Standard: B&K 8103 s/n 2071686 Facility: 4 1/2" Tube Depth: # 1&2 pos.
 Water Temp: 23.5 °C Source: TP/400 Drive Level: various
 Data Acquisition: Nexus/2635/TDS460



Calibration Performed by:
 Preston Wilson
 psw@bu.edu

9/03/99
 BU:PACLAB

Figure B.9: Measured charge sensitivity of BU 250-10 hydrophones, Mark IV and V.

Appendix C

Initial Cross-Calibration Procedure

In order to compensate for the complex response inequality between the two sensors, the TFM standard document [99] prescribes a cross-calibration procedure which requires a “non-reflecting” termination. This was physically unrealizable in the existing and foreseen deployment scenarios, therefore a different procedure was utilized at the beginning of this work, and herein described.

Equation 3.41 for the complex reflection coefficient used in TFM is repeated here

$$R(f) = \frac{H_{12}(f) - e^{-iks}}{e^{iks} - H_{12}(f)} e^{+i2k\ell}, \quad (\text{C.1})$$

where $H_{12}(f) = \bar{H}_{12}(f)/H_c(f)$. \bar{H}_{12} is the actual measurement made during an impedance run, and H_c is the cross-calibration factor obtained from the standard cross-calibration procedure. This procedure results in an accurate absolute measurement, requiring no further calibration.

Instead of obtaining $H_c(f)$ in the forward manner,¹ it was obtained in a reverse manner utilizing a known impedance termination, and hence a known reflection coefficient

¹“Forward manner” indicates without comparison to some known impedance.

$R(f)$. The air-water surface is undoubtedly the most well known impedance reference obtainable in a water filled impedance tube, so it was used. \bar{H}_{12} was measured with an air termination and H_c was calculated from C.1 using,

$$R(f) = R = \frac{z_{\text{air}}(T) - z_{\text{water}}(T)}{z_{\text{air}}(T) + z_{\text{water}}(T)}, \quad (\text{C.2})$$

where $z_x(T)$ indicates temperature dependent tabulated values for specific acoustic impedance. A typical value obtained in the laboratory was $R = -0.999$.

There is a serious flaw in this technique. Obviously, the pressure release termination creates a strong standing wave pattern in the tube. At a certain frequency, a half wavelength exists between the first sensor and the interface. At different frequency, a half wavelength exists between the second sensor and the interface. At each offending frequency, one sensor is co-located with a pressure node and the calibration fails. Qualitatively, there is no calibration information available at these points. Quantitatively, \bar{H}_{12} suffers a singularity at these points.

Away from these frequencies, H_c is fairly smooth. See for example Fig. C.1. With this in mind, a temporary fix was to extrapolate the actual function by manually smoothing out the singularities in H_c . This worked fairly well, but as can be seen in Figs. 3.21 and 3.22 for example, some real and very necessary information was certainly lost, which leads to the areas of uncertainty. This issue was solved by the adoption of the TMTC technique described in Section 3.7.3.

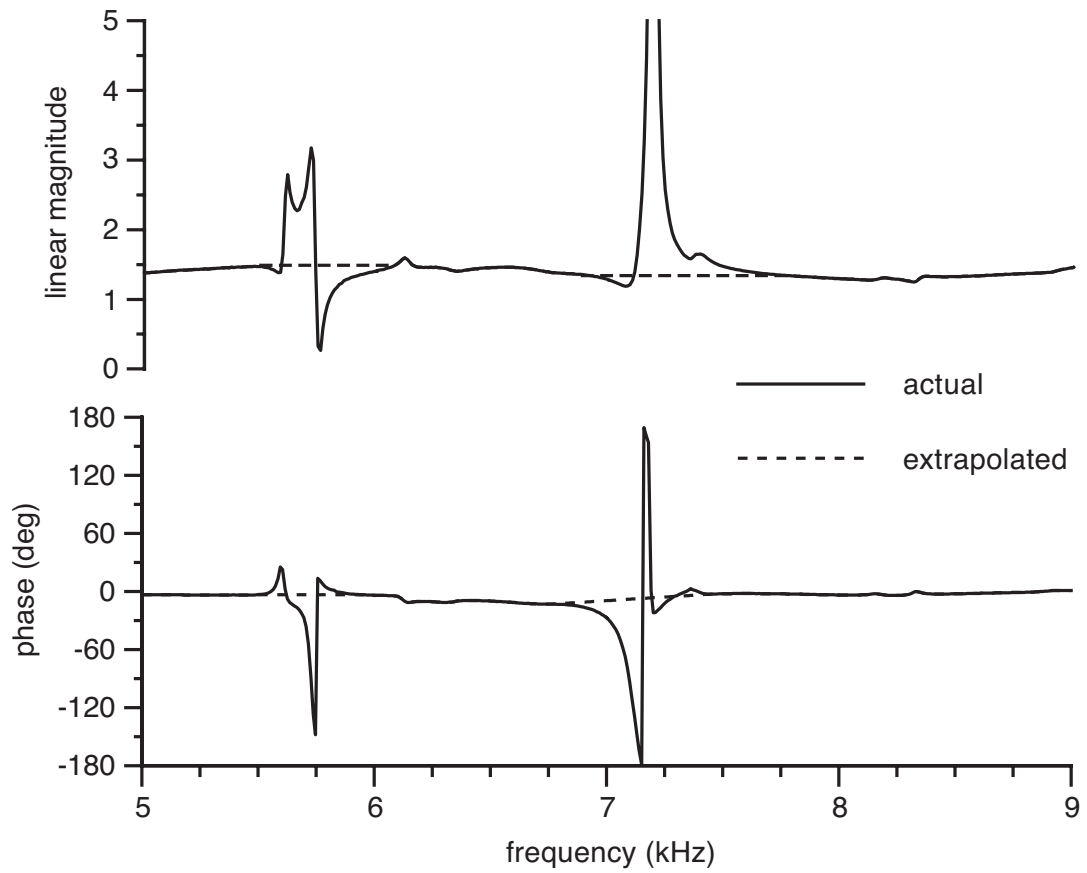


Figure C.1: The hydrophone cross-calibration function H_c , obtained in the reverse fashion described in the text.

Appendix D

Single Needle Bubble Population Statistics

The bubble population parameters that go along with the short-time impedance experiment are contained in this section. These plots represent the results of the detailed single needle bubble size measurement experiment discussed in Sections 4.2 and 4.4.2. This painstaking experiment and subsequent image analysis was conducted by Eun-Joo Park. All-in-all she analyzed the size of about 3,200 individual bubbles. Two photographs of the measurement system are shown in Figs. D.1 and D.2. The Canon video camera is seen in the foreground of the photo. The BIM is seen through the glass wall of the aquarium, and is held together with c-clamps. The length reference scale is also visible. If you look closely, to the left of the scale a few bubbles can be seen rising up. A typical image is shown in Fig. D.3. A typical surface of minimization is shown in Fig. D.4. Finally the statistical fitting plots for all 16 events are shown in Figs. D.5 through D.20. The NIH Image macro used by EJ to partially automate the image analysis is given on page 283. The experiment log written by EJ is shown on page 284. Finally, an error analysis of the size measurement is given on page 285.

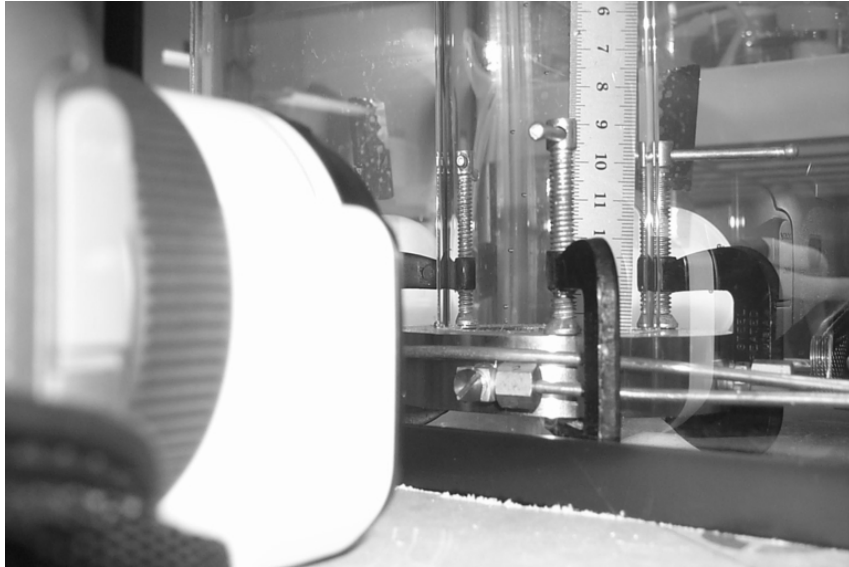


Figure D.1: A photograph of the single needle bubble experiment apparatus is shown.

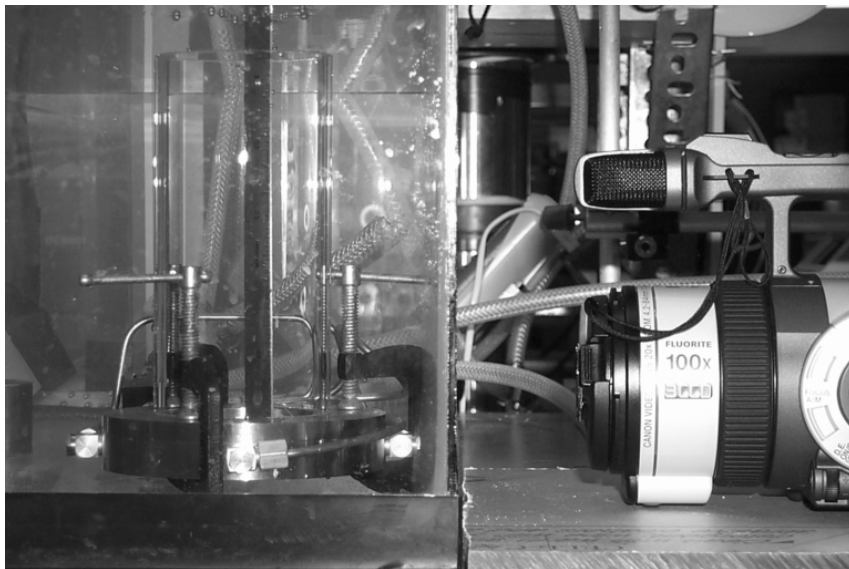


Figure D.2: A different view of the single needle bubble experiment apparatus is shown.

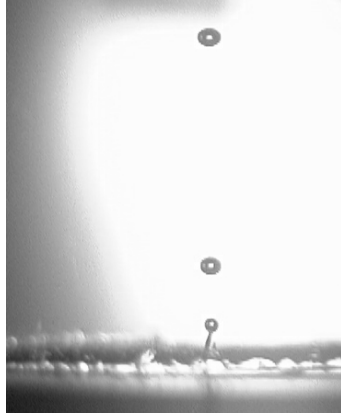


Figure D.3: A typical unprocessed image from the single needle bubble experiment is shown. This is frame 01:02:24.

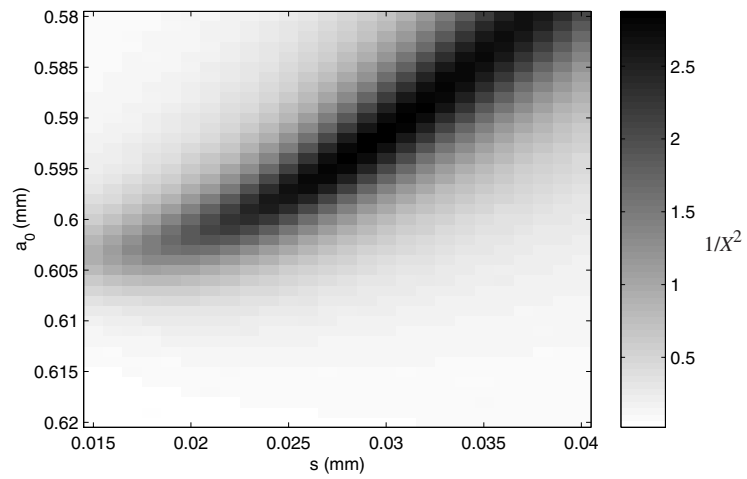


Figure D.4: A typical surface of minimization used for fitting the bubble size distribution parameters is shown. This goes along with Fig. D.5. Although X^2 was actually minimized, the plot is shown for $1/X^2$ because visualization is easier in this format.

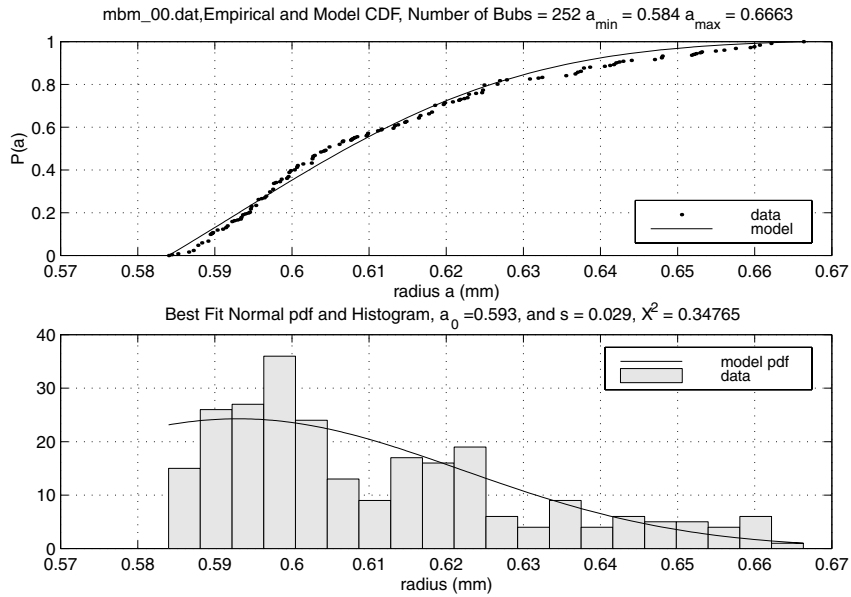


Figure D.5: Minute 1 statistics are shown. For archival purposes, the data file name is included in the upper plot title.

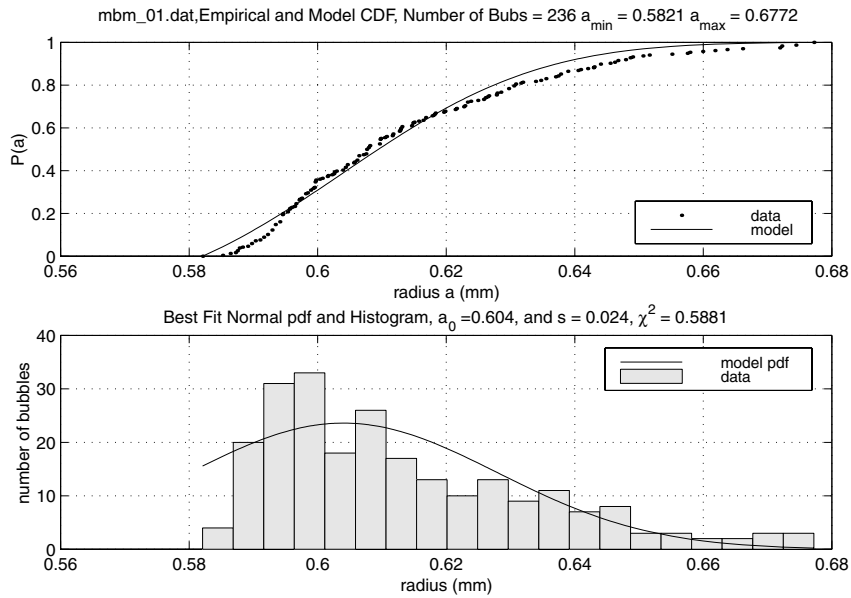


Figure D.6: Minute 2

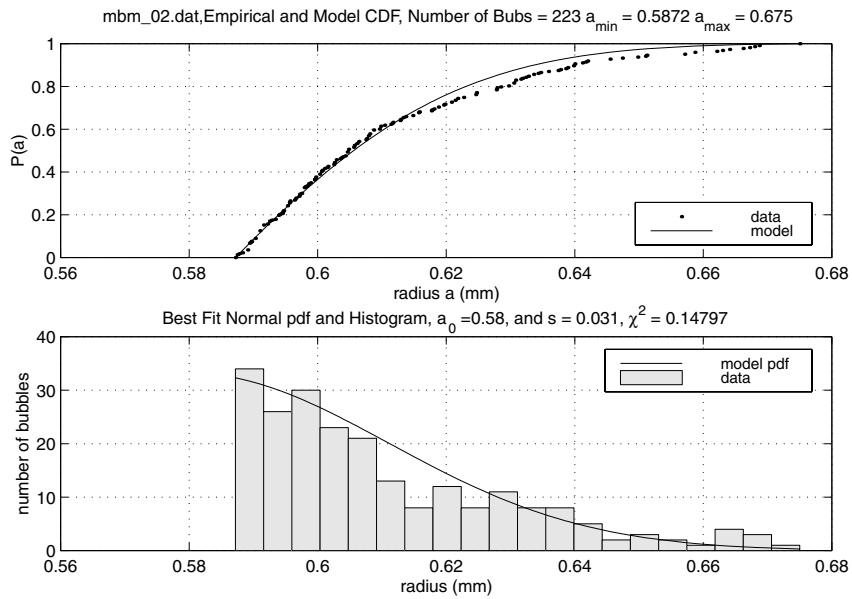


Figure D.7: Minute 3

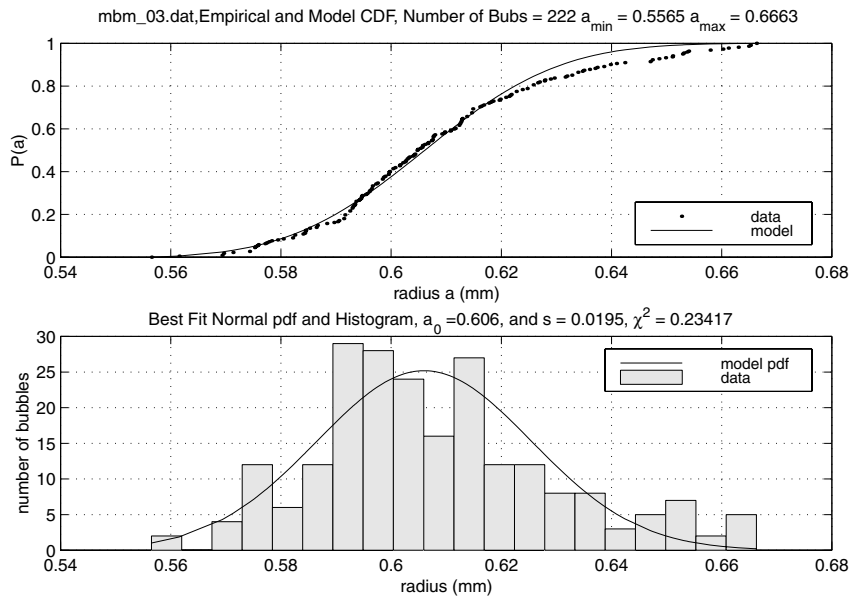


Figure D.8: Minute 4

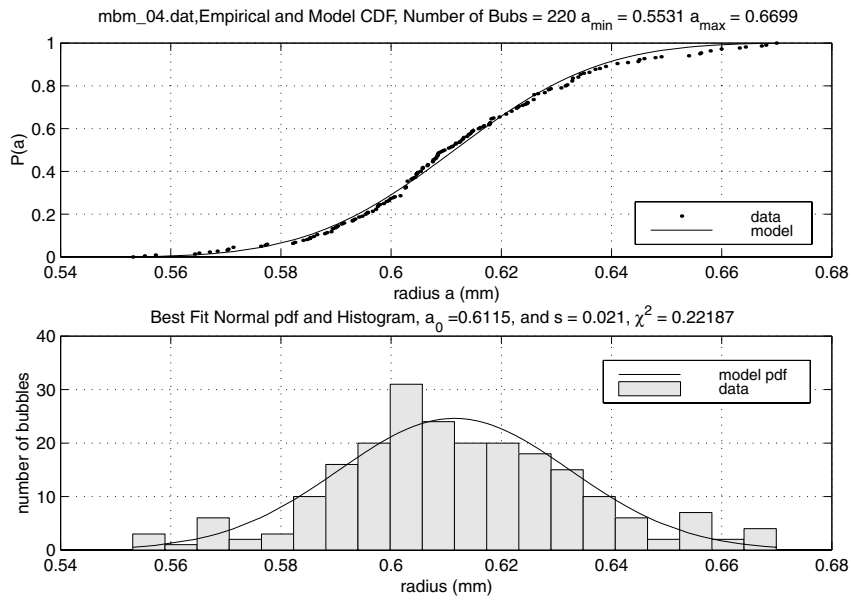


Figure D.9: Minute 5

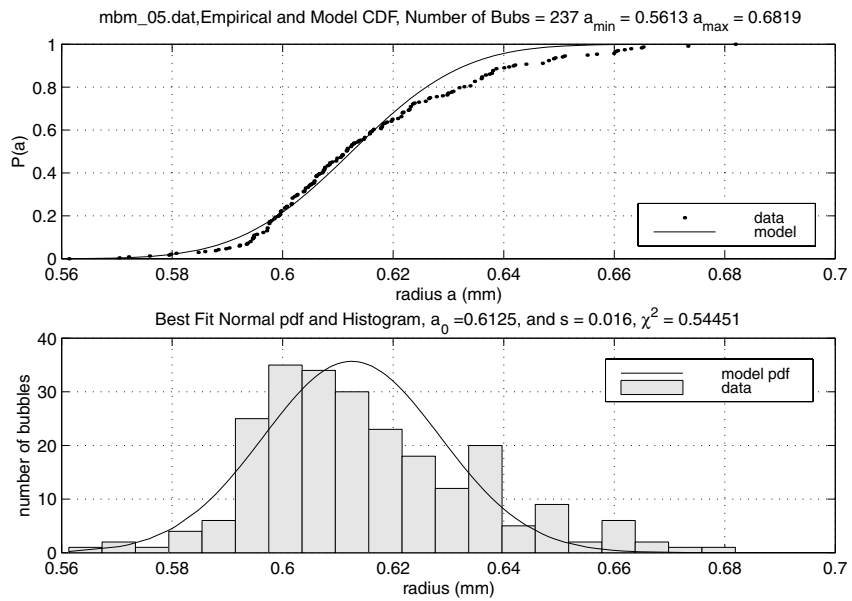


Figure D.10: Minute 6

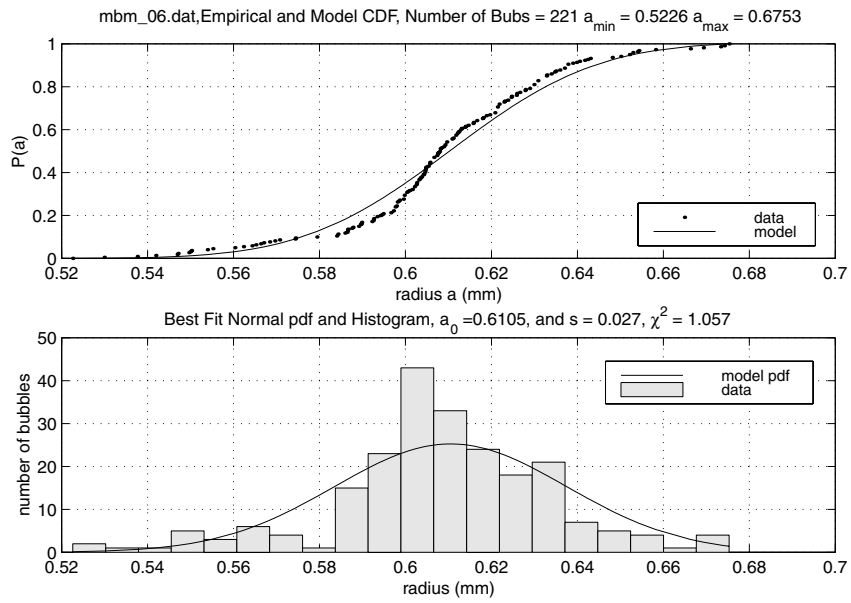


Figure D.11: Minute 7

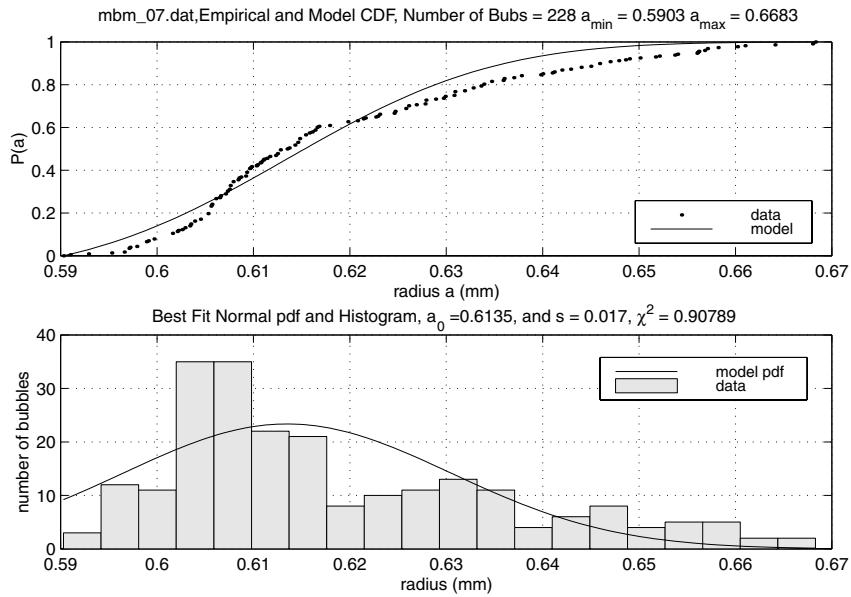


Figure D.12: Minute 8

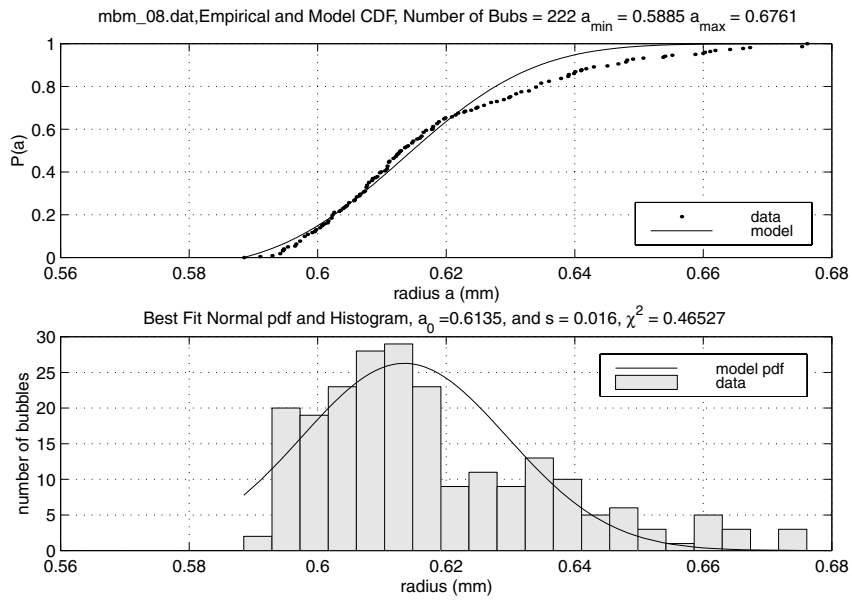


Figure D.13: Minute 9

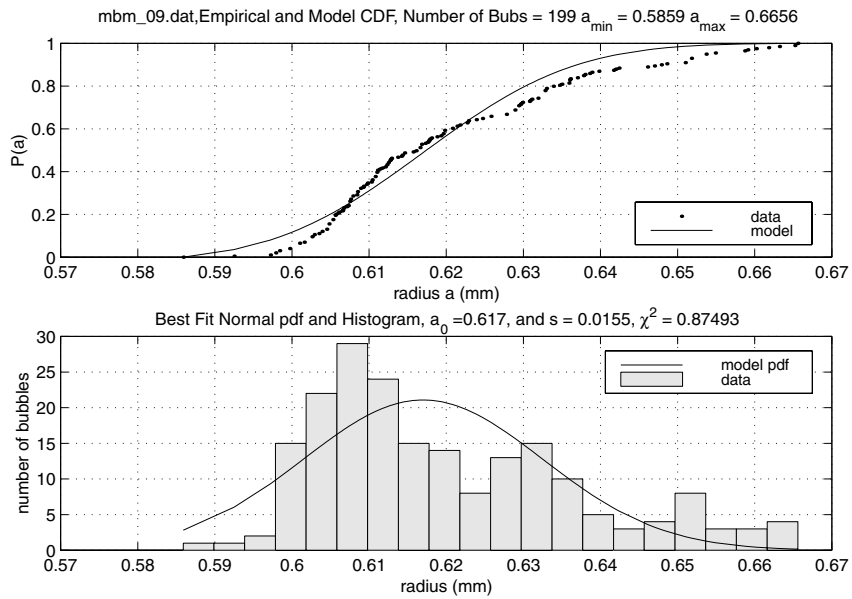


Figure D.14: Minute 10

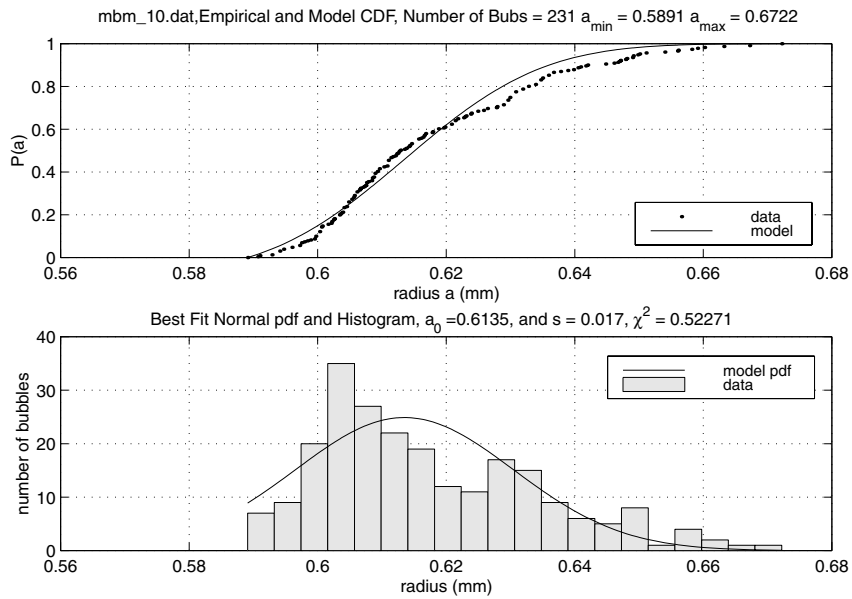


Figure D.15: Minute 11

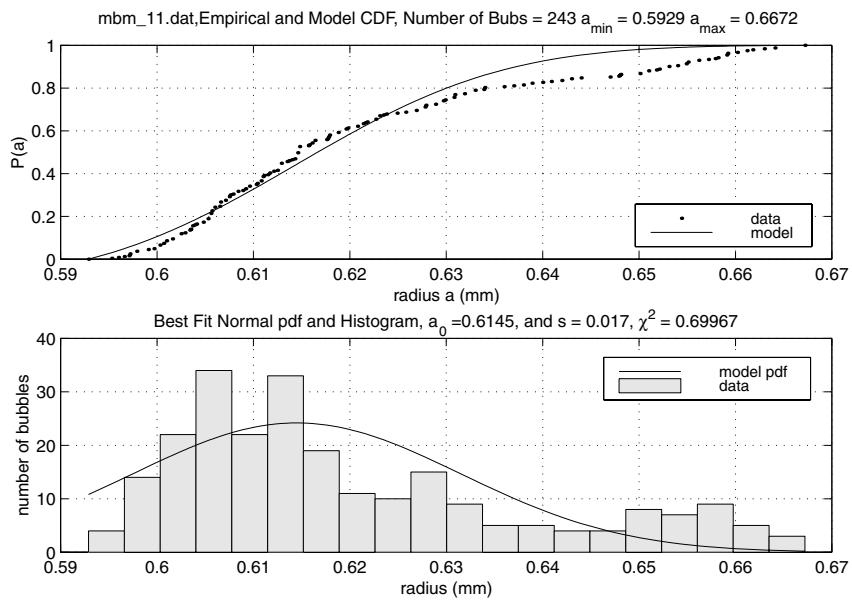


Figure D.16: Minute 12

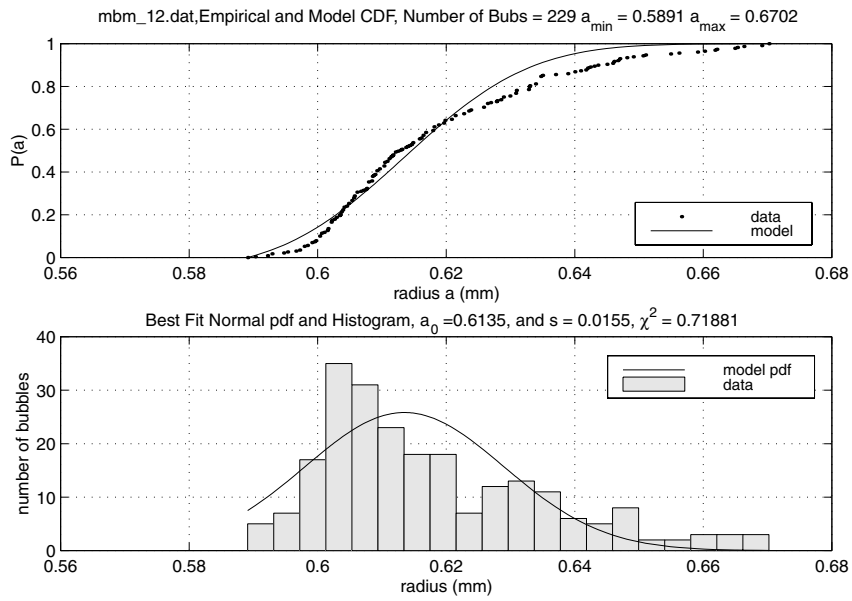


Figure D.17: Minute 13

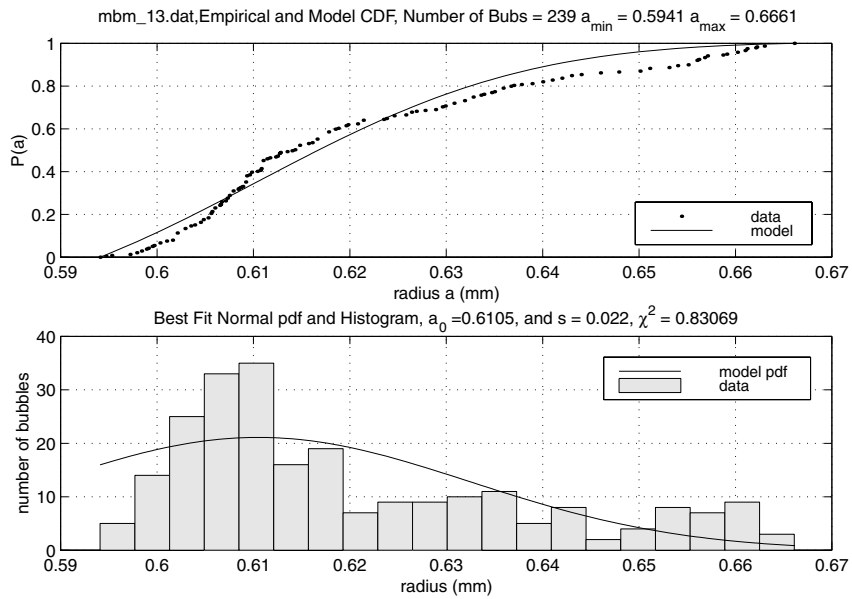


Figure D.18: Minute 14

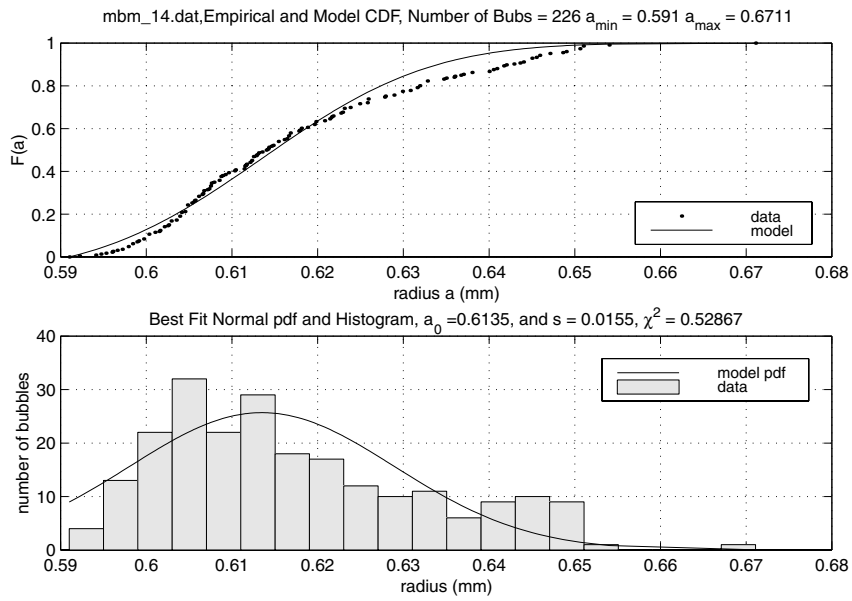


Figure D.19: Minute 15

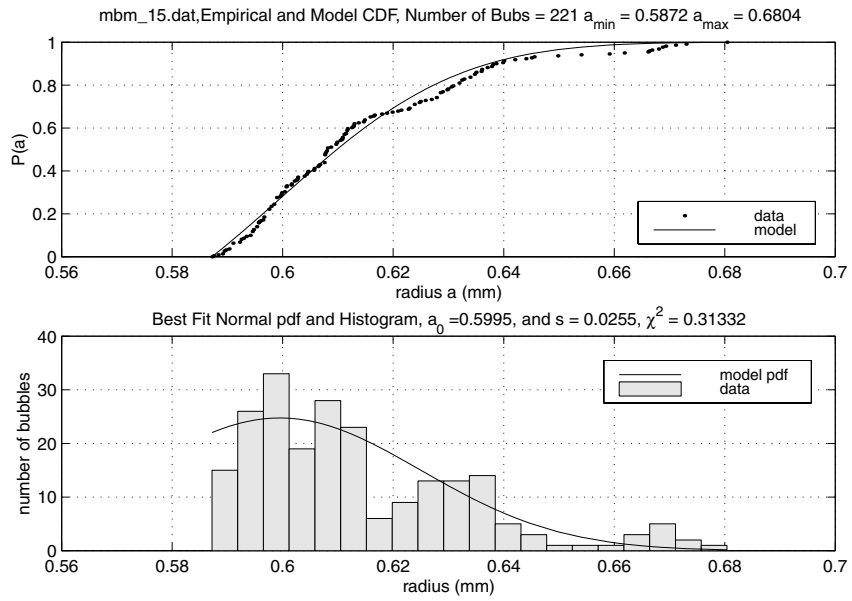


Figure D.20: Minute 16

NIH Image Macro

```
macro 'Analyze Particles [1]';
var
  i:integer;
begin
  for i:=1 to 40 do begin
    Open('',i:3);
    MakeRoi(209,20,100,341);
    SubtractBackground('1D Vertical',50);
    SetThreshold(33);
    MakeRoi(209,22,100,336);
    MakeBinary;
    SetBinaryCount(3);
    Dilate;
    Dilate;
    Erode;
    Erode;
    SetScale(18.0625,'mm');
    MakeRoi(209,22,100,336);
    SetParticleSize(320,9000);
    SetOptions('Major,Minor');
    AnalyzeParticles('label','outline','ignore');
    save;
    close;
  end;
  ShowResults;
end;
```


Single Needle Bubble Sizing Experiment Log

< Measuring bubble size distribution with single needle >

1. Pressure : $P_s(\text{source}) = 20 \text{ kPa}$
 $P_1(\text{pressure gauge}) = 3.3 \text{ kPa}$
 $FR(\text{Flow-Rate}) = \#11(\text{ about } 2.1 \text{ ml/min})$
[Glimont flowmeter,tube size 200, glass float]
2. Temperature : $T = 22.99 (22.98\sim 23.00) \text{ in Celsius}$
 $T_w(\text{temperature of water}) = 22 \text{ in Celsius}$
3. Camera : Model = Canon Digital Camcorder GL1
Mode = manual
Shutter speed = 1/15000 [1/60 for scale recording]
FO = 1.8
light gain = 12dB
4. Light : Source = NCL150 cold light source (Volpi)
Waveguide = gooseneck waveguide (Twin arms ,Volpi)
5. Setup picture : P0002220.jpg & P0002221.jpg
6. Picture of bubbles : 'mbmaabbcc.jpg' in 'ataamin' folder
~~~~~  
aa : minute at the clip (it started from 00.)  
bb : Second at the clip  
cc : number of frame  
ex) 'mbm035707.jpg' in 'at03min' folder means  
7th frame of the picture captured at 3min 57 sec.
7. Used software : NIH Image for MAC (with macro 'AP')

## Error Analysis

The error analysis procedure for this experiment was the same as that which was presented in Section 4.2. Bubble measurement is always full of tradeoffs. Length resolution comes at the expense of field-of-view. Both of these quantities come at the expense of sample rate. In this experiment, sample rate was the driving requirement, so resolution and field-of-view were sacrificed. The resolution of the digital video camera was  $640 \times 480$  pixels. In comparison, the resolution of the digital still camera was  $1536 \times 1024$ . So despite having only two bubbles in the field of view, the overall uncertainty is greater in this case.

For the bubble sizes used in this experiment, the oblate spheroid shape was again appropriate. For the typical bubble size, the minor axis pixelation was  $2c_{\min} = 16$  pixels, and  $2c_{\min} = 20$  pixels. The major axis pixelation was  $2b_{\min} = 20$  and  $2b_{\max} = 24$  pixels. The scale value was  $l_{\text{ref}} = 154 \pm 3$  pixels/cm. Using Eq. 4.2 one finds the uncertainty in the measured bubble radius for this size range is  $\pm 11\%$ .

## Appendix E

# Matlab Scripts

In this section, several of the Matlab scripts that were used to perform calculations for this dissertation will be presented for archival purposes. They are listed below in the order in which they were used in the main body of the dissertation.

### Complex Sound Speed in Bubbly Fluid: Evaluation of Eq. 2.1 for Delta Function Bubble Size Distribution

```
function [kmr,kmi,V,A,wo] = complex_k_cgs(f,c,vf,a,mu)

% This follows the paper by Commander and Prosperetti in
% JASA Vol 85, No.2, Feb 1989, eqns 27-41
%
% Inputs:
% f - frequency vector
% c - sound speed in outer medium (m/s)
% vf - void fraction (absolute number - NOT percentage)
% a - average bubble radius in cloud (m)
% mu - viscosity of bubbly medium (cP or 1/100th of cgs unit Poise)
%                                     [usually 1 for clean water]
%
% Outputs:
% kmr - real wave number vector (1/cm)
% kmi - imaginary wave number vector (1/cm)
% V - real phase velocity vector (cm/s)
% A - attenuation (dB/cm)
```

```

% wo - resonance frequency of cloud (rad/s) [bubble's resonance frequency]
%
% Last modified: 16 Nov 2000

w = 2*pi.*f; % Angular frequency (rad/s)

c = c*100; % Sound speed in liquid - convert to cgs (cm/s)
a = a*100; % Average bubble radius - convert to cgs (cm)
n = 3*vf/(4*pi*a^3); % Number of bubbles per unit volume(mL)
gamma = 1.4; % Ratio of specific heats
D = .208; % Gas thermal diffusivity (cm^2/s) (cf Leighton % p184)
chi = D./(w.*a.*a); % Variable in phi

phi = (3.*gamma)./(1-3.*(gamma-1).*i.*chi.*...
((i./chi).^0.5 .* coth((i./chi).^0.5) - 1));

rho = 0.998; % Liquid density (g/cm^3)
sigma = 72.5; % Surface tension (dyne/cm)
p_inf = 1013250; % Equilibrium pressure in the liquid (dyne/cm^2)
po = p_inf + 2*sigma/a; % Incident pressure amplitude

% Natural frequency of bubble cloud
wosqrd = ((po/(rho*a^2)).*(real(phi) - (2*sigma/(a*po))));
wo = sqrt(wosqrd);

mu = mu/100; % Viscosity converted from cP to Poise (cgs unit)

% Damping factor
b = 2*mu/(rho*a^2) + (po./(2*w.*rho*a^2)).*imag(phi) + (a.*w.^2)./(2*c);

kmsqrd = (w./c).^2 + (4.*pi.*w.^2.*a.*n.*(wo.^2-w.^2))./...
((wo.^2-w.^2).^2 + (2.*b.*w).^2) - i.*((8.*pi.*w.^3.*a.*b.*n)./...
((wo.^2-w.^2).^2 + (2.*b.*w).^2));

km = sqrt(kmsqrd);

kmr = real(km); % Output variable - real part of wave number
kmi = -imag(km); % Output variable - imaginary part of wave number

c_over_cm_sqrd = 1 + ((4*pi*c^2*n*a)./(wo.^2 - w.^2 + 2*i*b.*w));

c_over_cm = sqrt(c_over_cm_sqrd);
u = real(c_over_cm);
v = -imag(c_over_cm);

```

```

% Phase speed (cm/s) - Output variable
V = c./u;

% Attenuation (db/cm) - Output variable
A = 20*log10(exp(1)).*(w.*v./c);
%A = 100*A/(20*log10(exp(1))); %A calculated in dB/cm -> convert to 1/m

```

## Complex Sound Speed in Bubbly Fluid: Evaluation of Eq. 2.1 for Discrete Bubble Size Distribution

```

function [kmr,kmi,V,A,wo] = complex_k_cgs_dist(f,c,a,n,mu)

% This follows the paper by Commander and Prosperetti in
% JASA Vol 85, No.2, Feb 1989, eqns 27-41
%
% Inputs:
% f - frequency vector
% c - sound speed in outer medium (m/s)
% a - vector containing discrete bubble radii (cm)
%     n - vector containing number of bubbles/mililiter for
%         each discrete size in a. Must add up to give vf
%         a and n must be same length
% mu - viscosity of bubbly medium (cP or 1/100th of cgs unit Poise)
%       [usually 1 for clean water]
%
% Outputs:
% kmr - real wave number vector (1/cm)
% kmi - imaginary wave number vector (1/cm)
% V - real phase velocity vector (cm/s)
% A - attenuation (dB/cm)
% wo - resonance frequency of cloud (rad/s) [bubble's resoance frequency]
%
% Last modified: 16 Nov 2000

w = 2*pi.*f; % Angular frequency (rad/s)
c = c*100; % Sound speed in liquid - convert to cgs (cm/s)
gamma = 1.4; % Ratio of specific heats
D = .208; % Gas thermal diffusivity (cm^2/s) (cf Leighton, p.184)
rho = 0.998; % Liquid density (g/cm^3)
sigma = 72.5; % Surface tension (dyne/cm)
p_inf = 1013250; % Equilibrium pressure in the liquid (dyne/cm^2)

```

```

mu = mu/100; % Viscosity converted from cP to Poise (cgs unit)

for j=1:length(a),
chi(j,:) = D./(w.*a(j).*a(j)); % Variable in phi
phi(j,:) = (3.*gamma)./(1-3.*(gamma-1).*i.*chi(j,).*((i./chi(j,))...
.^0.5 .*coth((i./chi(j,)).^0.5) - 1));
po(j) = p_inf + 2*sigma/a(j); % Incident pressure amplitude
% Natural frequency of bubble at equilibrium radius a_i
wosqrd(j,:) = ((po(j)/(rho*a(j)^2)).*(real(phi(j,))...
- (2*sigma/(a(j)*po(j))))); wo(j,:) = sqrt(wosqrd(j,:));
% Damping factor
b(j,:) = 2*mu/(rho*a(j)^2) + (po(j)./(2.*w.*rho*a(j)^2))...
.*imag(phi(j,)) + (a(j).*w.^2)./(2*c);
% calculate wave number
kmsqrd(j,:) = 4.*pi.*w.^2.*a(j).*n(j)./(wo(j,).^2-w.^2+2.*i.*b(j,).*w);
% calculate complex wave speed
c_over_cm_sqrd(j,:) = ((4*pi*c^2*n(j)*a(j))./(wo(j,).^2...
- w.^2 + 2*i*b(j,).*w)); end

% prepare outputs
if length(a) == 1
kmsqrd = (w./c).^2 + kmsqrd;
c_over_cm_sqrd = 1 + c_over_cm_sqrd;
else
kmsqrd = (w./c).^2 + sum(kmsqrd);
c_over_cm_sqrd = 1 + sum(c_over_cm_sqrd);
end

km = sqrt(kmsqrd);
kmr = real(km); % Output variable - real part of wave number
kmi = -imag(km); % Output variable - imaginary part of wave number
c_over_cm = sqrt(c_over_cm_sqrd);
u = real(c_over_cm);
v = -imag(c_over_cm);

% Phase speed (cm/s) - Output variable
V = c./u;

% Attenuation (db/cm) - Output variable
A = 20*log10(exp(1)).*(w.*v./c);
%A = 100*A/(20*log10(exp(1))); %A calculated in dB/cm -> convert to 1/m

```

## Complex Sound Speed in Bubbly Fluid: Evaluation of Eq. 2.1 for Continuous Bubble Size Distribution

A Matlab function must also be created to calculate the probability density function  $\varphi(a)$ . This function should be titled `CnP_kernal` and placed within the argument of the function `adaptsim`, which is an adaptive Simpson's rule quadrature routine [80].

```
% This follows the paper by Commander and Prosperetti in
% JASA Vol 85, No.2, Feb 1989, eqns 27-41
%
% Inputs:
% f - frequency vector
% c - sound speed in outer medium (m/s)
% mu - viscosity of bubbly medium (cP or 1/100th of cgs unit Poise)
%           [usually 1 for clean water]
%
% Outputs:
% kmr - real wave number vector (1/cm)
% kmi - imaginary wave number vector (1/cm)
% V - real phase velocity vector (cm/s)
% A - attenuation (dB/cm)
% wo - resonance frequency of cloud (rad/s) [bubble's resoance frequency]
%
% Last modified: 16 Nov 2000
f=logspace(3,4.3,100);
c=1481;
mu=1;

w = 2*pi.*f; % Angular frequency (rad/s)
c = c*100; % Sound speed in liquid - convert to cgs (cm/s)
gamma = 1.4; % Ratio of specific heats
D = .208; % Gas thermal diffusivity (m^2/s) (cf Leighton, p.184)
rho = 1; % Liquid density (g/cm^3)
sigma = 72.5; % Surface tension (dyne/cm)
p_inf = 1013250; % Equilibrium pressure in the liquid (dyne/cm^2)
mu = mu/100; % Viscosity converted from cP to Poise (cgs unit)

kmsqrd=ones(1,length(f));
c_over_cm_sqrd=ones(1,length(f));
for j=1:length(w),
    int =
adaptsim('CnP_kernal',0.090,0.110,[0.00001],[],D,w(j),...
%           start radius (cm)/^^^^ ^^^\_finish radius (cm)
        gamma,sigma,p_inf,rho,c,mu);
```

```

kmsqrd(j) = (w(j)./c).^2 + int*4*pi.*w(j).*w(j);
c_over_cm_sqrd(j) = 1 + int.*4*pi*c*c;
end

km = sqrt(kmsqrd);
kmr = real(km); % Output variable - real part of wave number
kmi = -imag(km); % Output variable - imaginary part of wave number
c_over_cm = sqrt(c_over_cm_sqrd);
u = real(c_over_cm);
v = -imag(c_over_cm);

% Phase speed (m/s) - Output variable
V = c./u./100;

% Attenuation (db/cm) - Output variable
A = 20*log10(exp(1)).*(w.*v./c);
%A = 100*A/(20*log10(exp(1))); %A calculated in dB/cm -> convert to 1/m

```

## Scattering from a Fluid Cylinder with an Elastic Shell: Evaluation of Eq. 2.27

This first script calls several other functions: `elascylscat`, `getb`, `H_prime`, `J_prime`, `N_prime`, `J_double_prime` and `N_double_prime`, which are listed immediately following.

```

% Script calculates scattered field from infinite fluid immersed,
% elastic shelled, fluid filled cylinder.
%
% From Doolittle and Uberall, JASA 39(2),p.273,Eq.(2b)
%
% Outputs:
%
%           Psc = scattered field in units of Po

% INPUTS:

Po=1;           % incident plane wave pressure (Pa)
r=1.75;        % radial position coordinate (m),
               % (can be array, if f is not)
theta=pi;      % azimuthal angle (radians, 0 = forward scatter
               % direction, pi=back)
f=100:20:20000; % frequency of interest (Hz, can be array, if r is not)

```



```

% fluid 1 properties (host fluid):
c1=1480.5;      % sound speed of fluid 1, host fluid (m/s)
rho1=998;      % density of fluid 1, host fluid (kg/m^3)

% material 2 properties (elastic shell material):
lam=1.9497e9;  % Lam constant (lambda) for elastic shell material
mu=4.3e5;     % Lam constant (mu) for elastic shell material
rho2=970;     % density of elas. shell material 2, host fluid (kg/m^3)

% fluid 3 properties (inner fluid):

c3=343;      % internal sound speed (fluid 3) (m/s)
rho3=1.21*1.5; % density of internal fluid 3, by mixture eq. (kg/m^3)

% shell dimentions:
a=0.008019;  % shell outer radius (m)
b=0.00635;  % shell inner radius (m)

Psc=elascylscat(Po,r,theta,f,c1,rho1,lam,mu,rho2,c3,rho3,a,b);

EL=log10(abs(Psc)./Po).*20;
hold,plot(f./1000,EL),hold
title('Echo Level from Elastic Shelled Fluid Cylinder')
xlabel('frequency (kHz)')
ylabel('Echo Level (dB)')

function [Psc]=elascylscat(Po,r,theta,f,c1,rho1,lam,mu,rho2,c3,rho3,a,b)

% Fuction calculates scattered field from infinite fluid immersed,
% elastic shelled, fluid filled cylinder.
%
% From Doolittle and berall, JASA 39(2),p.273,Eq.(2b)
%
% Passed Quantities, Input:
%
%     Po = incident plane wave pressure
%     r = radial position of receiver (can be array, if f is not)
%     theta = azimuthal angle of receiver (radians)
%     f = frequency of interest (Hz, can be array, if r is not)
%
% fluid 1 properties (host fluid):
%
```

```

%      c1 = sound speed of fluid 1, host fluid (m/s)
%      rho1 = density of fluid 1, host fluid (kg/m^3)
%
% material 2 properties (elastic shell material):
%
%      lam = Lam constant (lambda) for elastic shell material
%      mu = Lam constant (mu) for elastic shell material
%      rho2 = density of elastic shell material 2, host fluid (kg/m^3)
%
% fluid 3 properties (inner fluid):
%
%      c3 = sound speed of fluid 3, internal fluid (m/s)
%      rho3 = density of fluid 3, host fluid (kg/m^3)
%
% shell dimentions:
%
%      a = shell outer radius (m)
%      b = shell inner radius (m)
%
% Passed Quantities, Outputs:
%
%      Psc = scattered field in units of Po

% Internal Parameters to be set by user:
N=2;      % number of iterations (3 is good up to f=22kHz)

% Internal calculations:
c1 = sqrt((lam + 2*mu)/rho2)   % longitudinal wave speed in shell
ct = sqrt(mu/rho2)- i.*(0)     % transverse wave speed in shell
w = f.*2*pi;                  % circular frequency (rad/s)
k1=w./c1;                     % wave number in fluid 1
kl=w./cl;                     % longitudinal wave number in shell 2
kt=w./ct;                     % transverse wave number in shell 2
k3=w./c3;                     % wave number in fluid 3

%figure(4),subplot(2,1,1),plot(real(k3)),subplot(2,1,2),plot(imag(k3))

k1r=k1.*r;                    % argument for Hankel function

if size(r)==1                 % If calculation is for a single radius (vector of
    % frequencies) do this:
[BH,IERR]=BESSELH(0,k1r); % these two lines do n = 0
Psc=BH.*getb(0,k1,kt,kl,k3,rho1,rho3,lam,mu,a,b,w);
    for n = 1:1:N,% these do n = 1 thru N

```

```

n,tic
  [BH,IERR]=BESSELH(n,k1r);

ptemp=BH.*cos(n*theta).*(i^n).*2.*getb(n,k1,kt,kl,k3,rho1,...
      rho3,lam,mu,a,b,w);
  Psc=Psc+ptemp;
toc
  end
elseif size(f)==1 % if calculation is for a single frequency (vector
                  % of radii), do this:
[BH,IERR]=BESSELH(0,k1r);% these two lines do n = 0
Psc=BH.*getb(0,k1,kt,kl,k3,rho1,rho3,lam,mu,a,b,w);
  for n = 1:1:N,% these do n = 1 thru N
    [BH,IERR(n+1)]=BESSELH(n,k1r);

ptemp=BH.*cos(n*theta).*(i^n).*2.*getb(n,k1,kt,kl,k3,rho1,...
      rho3,lam,mu,a,b,w);
  Psc=Psc+ptemp;
  end
else
Psc=0;
end

Psc=Psc.*Po;

% send flag if error was detected
IERR=sum(IERR);
if IERR > 0
IERR
end

function [bn] = getb(n,k1,kt,kl,k3,rho1,rho3,lam,mu,a,b,w)

% Fuction calculates term b_n from Doolittle and berall,
% JASA 39(2),p.273,Eq.(2b)
% This function is called by the function "elascylscat.m"

wsq=w.*w;

x1=k1.*a;
xl=kl.*a;
xt=kt.*a;

```

```

y3=k3.*b;
yl=kl.*b;
yt=kt.*b;

alph=zeros(6,6,length(w)); % initialize 3-D array, a 6x6 matrix for each
                             % frequency bin. The 6x6 portion contains the
                             % alpha's on page 274 of the paper

alph(1,1,:) = besselh(n,x1).*a^2.*(-1);
alph(1,2,:) =
(J_double_prime(n,x1).*(x1.^2).*2*mu)...
    -(besselj(n,x1).*(x1.^2).*lam);
alph(1,3,:) = (N_double_prime(n,x1).*(x1.^2).*2*mu)...
    -(bessely(n,x1).*(x1.^2).*lam);
alph(1,4,:) = (besselj(n,xt)-J_prime(n,xt).*xt).*2*n*mu;
alph(1,5,:) = (bessely(n,xt)-N_prime(n,xt).*xt).*2*n*mu;

alph(2,1,:) = H_prime(n,x1).*x1.*(-1);
alph(2,2,:) = J_prime(n,x1).*x1.*wsq.*rho1*(-1);
alph(2,3,:) = N_prime(n,x1).*x1.*wsq.*rho1*(-1);
alph(2,4,:) = besselj(n,xt).*wsq.*rho1*n;
alph(2,5,:) = bessely(n,xt).*wsq.*rho1*n;

alph(3,2,:) = (J_prime(n,x1).*x1-besselj(n,x1)).*2*n;
alph(3,3,:) = (N_prime(n,x1).*x1-bessely(n,x1)).*2*n;
alph(3,4,:) = J_prime(n,xt).*xt-J_double_prime(n,xt).*(xt.^2)...
    -besselj(n,xt).*n^2;
alph(3,5,:) = N_prime(n,xt).*xt-N_double_prime(n,xt).*(xt.^2)...
    -bessely(n,xt).*n^2;

alph(4,2,:) = (J_double_prime(n,yl).*(yl.^2).*2*mu)...
    -(besselj(n,yl).*(yl.^2).*lam);
alph(4,3,:) = (N_double_prime(n,yl).*(yl.^2).*2*mu)...
    -(bessely(n,yl).*(yl.^2).*lam);
alph(4,4,:) = (besselj(n,yt)-J_prime(n,yt).*yt).*2*n*mu; alph(4,5,:) =
    (bessely(n,yt)-N_prime(n,yt).*yt).*2*n*mu;
alph(4,6,:) = besselj(n,y3).*(-b^2);

alph(5,2,:) = J_prime(n,yl).*yl.*wsq.*(-rho3);
alph(5,3,:) = N_prime(n,yl).*yl.*wsq.*(-rho3);
alph(5,4,:) = besselj(n,yt).*wsq.*n*rho3;
alph(5,5,:) = bessely(n,yt).*wsq.*n*rho3;
alph(5,6,:) = J_prime(n,y3).*(-y3);

```

```

alph(6,2,:) = (J_prime(n,y1).*y1-besselj(n,y1)).*2*n;
alph(6,3,:) = (N_prime(n,y1).*y1-bessely(n,y1)).*2*n;
alph(6,4,:) = J_prime(n,yt).*yt-J_double_prime(n,yt).*(yt.^2)...
              -besselj(n,yt).*n^2;

alph(6,5,:) =
N_prime(n,yt).*yt-N_double_prime(n,yt).*(yt.^2)-bessely(n,yt).*n^2;

% the following calculates the determinant of the alpha matrix
% for each
frequency for i=1:length(w),
D(i)=det(alph(:,:,i));
end

% Here we form the matrix in eq. 9b out of the first matrix
% by replacing the beta
alph(1,1:)=besselj(n,x1).*a^2; % this is beta_1 from eq. 9b, page 274
alph(2,1:)=J_prime(n,x1).*x1; % this is beta_2 from eq. 9b, page 274

for i=1:length(w),
bn(i)=det(alph(:,:,i))/D(i);
end

function ans = H_prime(m,arg)

% function to calculate the first derivated of the Hankel function
% of the first kind.
%
% pass index m and argument arg.
%
% returns the value of d[H_m(x)]/dx evaluated at x = arg.
% arg can be an array.

if m == 0
ans=besselh(1,arg).*(-1);
else
ans=(besselh(m-1,arg)-besselh(m+1,arg)).*0.5;
end

```

```

function ans = J_prime(m,arg)

% function to calculate the first derivated of the Bessel function.
% pass index m and argument arg.
%
% returns the value of d[J_m(x)]/dx evaluated at x = arg.
% arg can be an array.

if m == 0
ans=besselj(1,arg).*(-1);
else
    ans=(besselj(m-1,arg)-besselj(m+1,arg)).*0.5;
end

function ans = N_prime(m,arg)

% function to calculate the first derivated of the Neumann function.
% pass index m and argument "arg".
%
% returns the value of d[J_m(x)]/dx evaluated at x = "arg".
% arg can be an array.

if m == 0
ans=bessely(1,arg).*(-1);
else
    ans=(bessely(m-1,arg)-bessely(m+1,arg)).*0.5;
end

function ans = J_double_prime(m,arg)

% function to calculate the second derivated of the Bessel function.
% pass index m and argument arg.
%
% returns the value of d[J_m(x)]^2/dx^2 evaluated at x = arg.
% arg can be an array.

ans=(besselj(m-2,arg) - besselj(m,arg).*2 + besselj(m+2,arg))./4;

```

```

function ans = N_double_prime(m,arg)

% function to calculate the second derivated of the Bessel function.
% pass index m and argument arg.
%
% returns the value of  $d[N_m(x)]^2/dx^2$  evaluated at  $x = \text{arg}$ .
% arg can be an array.

ans=(bessely(m-2,arg) - bessely(m,arg).*2 + bessely(m+2,arg))./4;

```

## Elastic Waveguide Propagation: Evaluation of Eq. 3.72

```

% Script to calculate elastic waveguide phase speeds from
% Lafleur and Shields, JASA 97(3):1434-1445
%
% Maps out Cphase vs. Frequency by displaying the
% zero contour of Eq. 5
%
% Good for getting a quick idea of how the system behaves.
%
% Set C0m: the phase speeds that you are interested in observing

% C1 = intrinsic velocity of sound in fluid (m/s)
% Cc = compressional velocity of sound in solid (m/s)
% Cs = shear velocity of sound in solid (m/s)
%
% b = inner radius of cylinder (m)
% d = outer radius of cylinder (m)
% pl = density of liquid
% pw = density of cylinder wall material
%
% w = angular frequency (rad/s) - CAN BE AN ARRAY!!
% C0m = phase velocity of axisymmetric wave in system (m/s)

% Input Parameters
C0m = 1000:5:8000; % Here, set sound speed range of interest. (m/s)
fmax = 7500; % max value frequency (Hz)
fmin = 6500; % start value frequency (Hz)
N = 3; % number of frequency steps

% load material parameter file
props_res_BF_Steel_Big

```

```

% Calculations
wf=2*pi*fmax; % final frequency
w0=2*pi*fmin; % initial frequency

dw=(wf-w0)/(N-1);

for n=1:N
n
w=(n-1)*dw + w0;
f(n)=w/2/pi;

sum(n,:) = LandS_eqsolvr(C0m,w,C1,Cc,Cs,b,d,pl,pw);
if n ==1
tic
elseif n ==2
t=toc
time_till_end_in_min = (t*N-2*t)/60
end
end

%k1b=(f.*2.*pi).*b./C1;
contour(f,C0m,sum',[0 0])
ylabel('phase speed (m/s)')
xlabel('frequency (Hz)')
grid
colormap black
toc/60

```

## Impedance Measurement: Evaluation of Eq. 3.93

```

% script for 2mic3cal technique
% using mass removal system for calibration
%
% Inputs
load X01102801.ASC % measurement file
load X01102802.ASC % cal file 1
load X01102803.ASC % cal file 2
load X01102804.ASC % cal file 3

c=1455.3; % sound speed in tube (from null frequency) (m/s)
rho = rhotemp_NIST(23.25)/1000; % denisty of water (g/ml)

```



```

m1=192.252+0.005; % mass of water removed for each calibration (g)
m2=20.751;
m3=22.621;

turns = 2.231;          % number of turns on Gaetner
dh=(turns*0.1/0.985)*1e-3 % depth of water below top of tube (m)
dbim = 1.281/100;      % length of bim (m)

% Parameters
r=0.051775/2;          % radius of sample holder (m)
ell=0.14-dh-dbim;     % effective length of sample holder (m)

% Calculations
dV1=m1/rho; % volume of fluid removed in between 1st and 2nd run (ml)
dV2=m2/rho; % volume of fluid removed in between 2nd and 3rd run (ml)
dV3=m3/rho; % volume of fluid removed in between 3rd and 4th run (ml)

f=X01102801(:,1);     % creates frequency vector out of data

yprime=X01102802(:,2)+i.*X01102802(:,3); % converts complex data
ydubprime=X01102803(:,2)+i.*X01102803(:,3);
ytripprime=X01102804(:,2)+i.*X01102804(:,3);
t1=X01102801(:,2)+i.*X01102801(:,3);

% calculates complex k
eps = 0.0001; % loss parameter for thermal and viscous losses in tube
w = 2*pi.*f; % circular frequency (rad/sec)
k_loss = (1 + (1-i).*(sqrt(2).*eps./r).*sqrt(c./w)).*w.*w./c./c;
k = sqrt(k_loss);
%k=2*pi.*f./c; % lossless wave number (1/m)

d1 = ell-(dV1*1e-6/pi/r/r); % length of termination for each
% calibration measurement (m)
d2 = ell-((dV1+dV2)*1e-6/pi/r/r); % the 1e-6 changes the ml to cubic
% meters
d3 = ell-((dV1+dV2+dV3)*1e-6/pi/r/r);
d_test = ell;

z1 = tan(k.*d1).*i; % theoretical calibration value/normalized by rho-c
z2 = tan(k.*d2).*i;
z3 = tan(k.*d3).*i;

y = t1; % doing the transmission line test case

```

```

A=z1.*z3.*(yprime-ytripprime).(y-ydubprime);
B=z1.*z2.*(ydubprime-yprime).(y-ytripprime);
C=z2.*z3.*(ytripprime-ydubprime).(y-yprime);
D=z3.*(ydubprime-yprime).(ytripprime-y);
E=z1.*(ytripprime-ydubprime).(yprime-y);
F=z2.*(yprime-ytripprime).(ydubprime-y);

z=(A+B+C)./(D+E+F);

z_predict = i.*tan((k).*d_test); % predicted value for this case

subplot(2,1,1)
semilogy(f./1000,abs(z),'.',f./1000,abs(z_predict))
grid

subplot(2,1,2)
plot(f./1000,angle(z).*(360/2/pi),'.',f./1000,...
      angle(z_predict).*(360/2/pi))
grid

```

# Bibliography

- [1] A. Mallock. The damping of sound by frothy liquids. *Proceedings of The Royal Society, Series A*, 84(A 572):391–395, 1910.
- [2] Robert John Strutt. *Life of John William Strutt, Third Baron Rayleigh, O. M., F. R. S.* University of Wisconsin Press, Madison, 1968.
- [3] Lord Rayleigh. On the pressure developed in a liquid during the collapse of a spherical cavity. *Philosophical Magazine*, 34:94–98, 1917.
- [4] M. Minnaert. On musical air-bubbles and the sounds of running water. *The London, Edinburgh and Dublin Philosophical Magazine and Journal of Science, Series 7*, 16:235–248, 1933.
- [5] Clayton Crowe, Martin Sommerfeld, and Yutaka Tsuji. *Multiphase Flows with Droplets and Particles*. CRC Press, Boca Raton, 1998.
- [6] LeAnn E. Faidley and J. Adin Mann III. Development of a model for acoustic liquid manipulation created by a phased array. *The Journal of the Acoustical Society of America*, 109(5):2363 (A), 2001.
- [7] H. B. Karplus. The velocity of sound in a liquid containing gas bubbles. Technical Report C00-248, Armour Research Foundation of Illinois Institute of Technology, June 11, 1958.
- [8] Herman Medwin and Clarence S. Clay. *Fundamentals of Acoustical Oceanography*. Academic Press, Boston, 1998.
- [9] Naval Sea Systems Command. *Underwater Ship Husbandry Manual*, 1995. NAVSEA Publication S0600-AA-PRP-050.
- [10] Gordon M. Wenz. Acoustic ambient noise in the ocean: spectra and sources. *The Journal of the Acoustical Society of America*, 34(12):1936–1956, 1962.
- [11] Bryan R. Kerman. Underwater sound generation by breaking wind waves. *The Journal of the Acoustical Society of America*, 75(1):149–165, 1984.
- [12] Herman Medwin and Matthew M. Beaky. Bubble sources of the Knudsen sea noise spectra. *The Journal of the Acoustical Society of America*, 86(3):1124–1130, 1989.

- [13] Robert Urick. *Ambient Noise in the Sea*. Peninsula, Los Altos, 1986. (Originally published by Department of the Navy, Washington, D.C., 1984).
- [14] W. M. Carey and M. P. Bradley. Low-frequency ocean surface noise sources. *The Journal of the Acoustical Society of America*, 78(Suppl. 1):S1 (A), 1985.
- [15] A. Prosperetti. Bubble-related ambient noise in the ocean. *The Journal of the Acoustical Society of America*, 78(Suppl. 1):S2 (A), 1985.
- [16] William M. Carey and David Browning. Low frequency ocean ambient noise: Measurements and theory. In B. R. Kerman, editor, *Sea Surface Sound*, pages 361–376. Kluwer, Boston, 1988.
- [17] William M. Carey and James W. Fitzgerald. Low frequency noise from breaking waves. In B. R. Kerman, editor, *Natural Physical Sources of Underwater Sound*, pages 277–304. Kluwer, Boston, 1993.
- [18] W. M. Carey, J. W. Fitzgerald, E. C. Monahan, and Q. Wang. Measurement of the sound produced by a tipping trough with fresh and salt water. *The Journal of the Acoustical Society of America*, 93:3178–3192, 1993.
- [19] Andrea Prosperetti. Bubble dynamics in oceanic ambient noise. In B. R. Kerman, editor, *Sea Surface Sound*, pages 151–171. Kluwer, Boston, 1988.
- [20] A. Prosperetti, N. Q. Lu, and H. S. Kim. Active and passive acoustic behavior of bubble clouds at the ocean’s surface. *The Journal of the Acoustical Society of America*, 93(6):3117–3127, 1993.
- [21] A. R. Kolaini, R. A. Roy, L. A. Crum, and Y. Mao. Low-frequency underwater sound generation by impacting transient cylindrical water jets. *The Journal of the Acoustical Society of America*, 94:2809–2820, 1993.
- [22] Ali R. Kolaini, Ronald A. Roy, and David L. Gardner. Low-frequency acoustic emissions in fresh and salt water. *The Journal of the Acoustical Society of America*, 96(3):1766–1772, 1994.
- [23] M. Nicholas, R. A. Roy, L. A. Crum, H. Oğuz, and A. Prosperetti. Sound emissions by a laboratory bubble cloud. *The Journal of the Acoustical Society of America*, 95(6):3171–3182, 1994.
- [24] Vernon M. Albers. *Underwater Acoustics Handbook II*. Pennsylvania State University Press, University Park, 1965.
- [25] D. C. Blanchard and A. H. Woodcock. Bubble formation and modification in the sea and its meteorological significance. *Tellus*, 9(2):145–158, 1957.
- [26] Edward C. Monahan and Mingzhi Lu. Acoustically relevant bubble assemblages and their dependence on meteorological parameters. *IEEE Journal of Oceanic Engineering*, 15(4):340–349, 1990.

- [27] S. A. Thorpe. On the clouds of bubbles formed by breaking wind-waves in deep water, and their role in air-sea gas transfer. *Philosophical Transactions of the Royal Society of London, A*, 304:155–210, 1982.
- [28] S. A. Thorpe. The effect of Langmuir circulation on the distribution of submerged bubbles caused by breaking wind waves. *Journal of Fluid Mechanics*, 142:151–170, 1984.
- [29] Andrew D. Gephart. Acoustic scattering from compact bubble clouds. M.S. Thesis, Boston University, 1999.
- [30] P. Wille, D. Geyer, L. Ginzkey, and E. Schunk. Measurements of wind dependent acoustic transmission loss in shallow water under breaking wave conditions. In Harold M. Merklinger, editor, *Progress in Underwater Acoustics*, pages 501–508. Plenum Press, New York, 1986.
- [31] William R. Turner. Abnormal attenuation in Chesapeake Bay waters. *The Journal of the Acoustical Society of America*, 60(6):1300–1308, 1976.
- [32] Stanley A. Cheyne, Carl T. Stebbings, and Ronald A. Roy. Phase velocity measurements in bubbly liquids using a fiber optic laser interferometer. *The Journal of the Acoustical Society of America*, 97(3):1621–1624, 1995.
- [33] Kerry W. Commander and Andrea Prosperetti. Linear pressure waves in bubbly liquids: Comparison between theory and experiments. *The Journal of the Acoustical Society of America*, 85(2):732–746, 1989.
- [34] Ferren Macintyre. On reconciling optical and acoustical bubble spectra in the mixed layer. In E. C. Monahan and G. MacNiocaill, editors, *Oceanic Whitecaps and Their Role in Air-Sea Exchange Processes*, pages 75–94. D. Reidel, 1986.
- [35] Roman E. Glazman. Effects of adsorbed films on gas bubble radial oscillations. *The Journal of the Acoustical Society of America*, 74(3):980–986, 1983.
- [36] Roman E. Glazman. Damping of bubble oscillations induced by transport of surfactants between the adsorbed film and the bulk solution. *The Journal of the Acoustical Society of America*, 76(3):890–896, 1984.
- [37] Roman E. Glazman. Acoustical properties of bubbly liquid contaminated by surface-active solutes. In *Multiple Scattering of Waves in Random Media and Random Rough Surfaces*, pages 399–407. Penn. State Univ. Press, 1985.
- [38] Gregory J. Orris and Michael Nicholas. Collective oscillations of fresh and salt water bubble plumes. *The Journal of the Acoustical Society of America*, 107(2):771–787, 2000.
- [39] T. G. Leighton. *The Acoustic Bubble*. Academic Press, London, 1994.
- [40] A. B. Wood. *A Textbook of Sound*. MacMillan, New York, 1st edition, 1930.

- [41] William M. Carey. A derivation of sonic speed relationships for bubbly liquids. unpublished notes, Boston University, 1997.
- [42] William M. Carey and Ronald A. Roy. Sound scattering from microbubble distributions near the sea surface. In D. D. Ellis, J. R. Preston, and H. G. Urban, editors, *Ocean Reverberation*, pages 25–44. Kluwer Academic, Dordrecht, Netherlands, 1993.
- [43] Din-Yu Hsieh and Milton S. Plesset. On the propagation of sound in a liquid containing gas bubbles. *The Physics of Fluids*, 4(8):970–975, 1961.
- [44] Andrea Prosperetti. The thermal behavior of oscillating gas bubbles. *Journal of Fluid Mechanics*, 222:587–616, 1991.
- [45] A. Crespo. Sound and shock waves in liquids containing bubbles. *The Physics of Fluids*, 12(11):2274–2282, 1969.
- [46] A. E. Ruggles, H. A. Scarton, and R. T. Lahey Jr. An investigation of the propagation of pressure perturbations in bubbly air/water flows. In H. H. Safwat, J. Braun, and U. S. Rohatgi, editors, *First International Multiphase Fluid Transients Symposium*, pages 1–9, New York, 1986. American Society of Mechanical Engineers.
- [47] Walter Kuhl, Erwin Meyer, Hermann Oberst, Eugen Skudrzyk, and Konrad Tamm. *Sound Absorption and Sound Absorbers in Water. (Dynamic Properties of Rubber and Rubberlike Substances in the Acoustic Frequency Region)*, volume 1. Dept. of the Navy Bureau of Ships, Washington, D.C., 1947. a. k. a. NavShips 900164, Translation by Charles E. Mongan, Jr., June, 1947.
- [48] Edward Gick Richardson and Erwin Meyer. *Technical Aspects of Sound*, volume 2. Elsevier Pub. Co., Amsterdam, New York, 1st edition, 1953.
- [49] Leslie L. Foldy. The multiple scattering of waves. *Physical Review*, 67(3 and 4):107–119, 1945.
- [50] E. L. Carstensen and L. L. Foldy. Propagation of sound through a liquid containing bubbles. *The Journal of the Acoustical Society of America*, 19(3):481–501, 1947.
- [51] O. J. Whitfield and M. S. Howe. The generation of sound by two-phase nozzle flows and its relevance to excess noise of jet engines. *Journal of Fluid Mechanics*, 75(3):553–576, 1976.
- [52] Russel E. Caflisch, Michael J. Miksis, Geroge C. Papanicolaou, and Lu Ting. Effective equations for wave propagation in bubbly liquids. *Journal of Fluid Mechanics*, 153:259–273, 1985.
- [53] L. van Wijngaarden. On the equations of motion for mixtures of liquid and gas bubbles. *Journal of Fluid Mechanics*, 33(3):465–474, 1968.
- [54] A. Prosperetti, L. A. Crum, and K. W. Commander. Nonlinear bubble dynamics. *The Journal of the Acoustical Society of America*, 83:502–513, 1988.

- [55] Joseph B. Keller and Michael Miksis. Bubble oscillations of large amplitude. *The Journal of the Acoustical Society of America*, 68(2):628–633, 1980.
- [56] Jeffery A. Schindall. *Acoustic Scattering from Compact Bubble Clouds*. Ph.D. Dissertation, The University of Mississippi, 1995.
- [57] Ronald A. Roy, William Carey, Michael Nicholas, Jeffrey Schindall, and Lawrence A. Crum. Low-frequency scattering from submerged bubble clouds. *The Journal of the Acoustical Society of America*, 92(5):2993–2996, 1992.
- [58] William M. Carey and Ronald A. Roy. The low frequency radiation and scattering of sound from bubbly mixtures near the sea surface. In L. Bjørnø, editor, *The 2nd European Conference on Underwater Acoustics*, pages 207–212, Luxembourg, 1994. European Commission.
- [59] Victor C. Anderson. Sound scattering from a fluid sphere. *The Journal of the Acoustical Society of America*, 22(4):426–431, 1950.
- [60] Philip McCord Morse and K. Uno Ingard. *Theoretical Acoustics*. Princeton University Press, Princeton, N.J., 1986.
- [61] S. N. Rzhevkin. *A Course of Lectures On the Theory of Sound*. Pergamon Press, Oxford, New York, 1963.
- [62] L. A. Crum, J. A. Schindall, R. A. Roy, and W. M. Carey. Low-frequency resonance backscatter from near-surface bubble clouds. In *NATO Symposium on Low-Frequency Active Sonar*, volume B9.1-9.16, Lerici, Italy, 1993. SAACLANTCEN.
- [63] R. A. Roy, J. A. Schindall, W. M. Carey, and L. A. Crum. Can near-surface bubble clouds and plumes lead to anomalous perturbations in low-frequency sea-surface scattering? In L. Bjørnø, editor, *The 2nd European Conference on Underwater Acoustics*, pages 195–202, Luxembourg, 1994. European Commission.
- [64] Edward Silberman. Sound velocity and attenuation in bubbly mixtures measured in standing wave tubes. *The Journal of the Acoustical Society of America*, 29(8):925–933, 1957.
- [65] I. J. Campbell and A. S. Pitcher. Flow of air-water mixtures. In *Symposium at Admiralty Research Laboratory*, Middlesex, England, 1954.
- [66] Frederick W. Gibson. Measurement of the effect of air bubbles on the speed of sound in water. *The Journal of the Acoustical Society of America*, 48(5):1195–1197, 1970.
- [67] G. Costigan and P. B. Whalley. Measurements of the speed of sound in air-water flows. *Chemical Engineering Journal*, 66:131–135, 1997.
- [68] Preston S. Wilson, Ronald A. Roy, and William M. Carey. An audible demonstration of low-frequency sound propagation in bubble water. *The Journal of the Acoustical Society of America*, 104(3, Pt. 2):1792, 1998.

- [69] N. I. Semenov and S. I. Kosterin. Results of studying the speed of sound in moving gas-liquid system. *Teploenergetica*, 11:46–51, 1964.
- [70] Francis E. Fox, Stanley R. Curley, and Glenn S. Larson. Phase velocity and absorption measurements in water containing air bubbles. *The Journal of the Acoustical Society of America*, 27(3):534–539, 1955.
- [71] I. S. Kol'tsova, L. O. Krynskii, I. G. Mikhalov, and I. E. Pokrovskaya. Attenuation of ultrasonic waves in low-viscosity liquids containing gas bubbles. *Soviet Physics Acoustics*, 25:409–413, 1979.
- [72] J. D. Macpherson. The effect of gas bubbles on sound propagation in water. *Proceedings of The Royal Society of London Section B*, 70:85–92, 1957.
- [73] C. Feuillade. The attenuation and dispersion of sound in water containing multiply interacting air bubbles. *The Journal of the Acoustical Society of America*, 99(6):3412–3430, 1996.
- [74] V. K. Varadan, V. V. Varadan, and Y. Ma. A propagator model for scattering of acoustic waves by bubbles in water. *The Journal of the Acoustical Society of America*, 78(5):1879–1881, 1985.
- [75] M. S. Howe. On the kinetic theory of wave propagation in random media. *Philosophical Transactions of the Royal Society of London*, 274 A:523–549, 1973.
- [76] Peter H. Dahl. Bubble clouds and thier transport within the surf zone as measured with a distributed array of upward-looking sonars. *The Journal of the Acoustical Society of America*, 109(1):133–142, 2001.
- [77] B. E. McDonald. Echoes from vertically striated subresonant bubble clouds: A model for ocean surface reverberation. *The Journal of the Acoustical Society of America*, 89:617–622, 1991.
- [78] Frank S. Henyey. Acoustic scattering from ocean microbubble plumes in the 100 hz to 2 khz region. *The Journal of the Acoustical Society of America*, 90:399–405, 1991.
- [79] Merran Evans, N. A. J. Hastings, and J. Brian Peacock. *Statistical Distributions*. Wiley, New York, 3rd edition, 2000.
- [80] Walter Gander and Walter Gautschi. Adaptive quadrature-revisited. Technical Report 306, Institute für Wissenschaftliches Rechnen, Eidgenössische Technische Hochschule Zürich, August 1998.
- [81] J. D. Achenbach. *Wave Propagation in Elastic Solids*. North-Holland Pub. Co. Elsevier Science Publishers, Amsterdam,, 1st pbk. edition, 1975.
- [82] R. D. Doolittle and H. Überall. Sound scattering by elastic cylindrical shells. *The Journal of the Acoustical Society of America*, 39(2):272–275, 1966.



- [83] A. E. H. Love. *A Treatise On the Mathematical Theory of Elasticity*. Dover Publications, New York, 4th edition, 1944.
- [84] T. K. Stanton. Sound scattering by cylinders of finite length. I. Fluid cylinders. *The Journal of the Acoustical Society of America*, 83(1):55–63, 1988.
- [85] J. Brandrup, E. H. Immergut, and E. A. Grulke, editors. *Polymer Handbook*. Wiley, New York, 4th edition, 1999.
- [86] Scott S. Corbett III. A two-hydrophone technique for measuring the complex reflectivity of materials in water-filled tubes. M. S. Thesis, Pennsylvania State University, 1983.
- [87] John I. Dunlop. Measurement of acoustic attenuation in marine sediments by impedance tube. *The Journal of the Acoustical Society of America*, 91(1):460–469, 1992.
- [88] Debra M. Kenney. A short water-filled pulse tube for the measurement of the acoustic properties of materials at low frequencies. Technical Report NSWCCD-TR-97/029, Naval Surface Warfare Center, Carderock Division, 1997.
- [89] Gerald A. Sabin. Acoustic-impedance measurements at high hydrostatic pressures. *The Journal of the Acoustical Society of America*, 40(6):1345–1353, 1966.
- [90] J. L. Lastinger. Acoustic characteristics of woods at high hydrostatic pressure. *The Journal of the Acoustical Society of America*, 47(1 (Part 2)):285–289, 1970.
- [91] J. L. Lastinger. The acoustical properties of water-saturated fibrous metal. *The Journal of the Acoustical Society of America*, 52(5 (Part 2)):1465–1470, 1972.
- [92] Walter Kuhl, Hermann Oberst, and Eugen Skudrzyk. Impulsverfahren zur messung der reflexion von wasserschallabsorbern in rohren. *Acustica*, 3:421–433, 1953.
- [93] Michale S. Hughes, Alexander L. Klibanov, Jon N. Marsh, James G. Miller, and Gary H. Brandenburger. Broadband time-domain reflectometry measurement of attenuation and phase velocity in highly attenuating suspensions with application to the ultrasound contrast medium Albunex<sup>®</sup>. *The Journal of the Acoustical Society of America*, 108(2):813–820, 2000.
- [94] Leo L. Beranek. *Acoustical Measurements*. Acoustical Society of America, Woodbury, NY, revised edition, 1988.
- [95] Allan D. Pierce. *Acoustics: An Introduction to Its Physical Principles and Applications*. Acoustical Society of America, Woodbury, NY, 1994.
- [96] Lawrence E. Kinsler, Austin R. Frey, Alan B. Coppens, and James V. Sanders. *Fundamentals of Acoustics*. Wiley, New York, 3rd edition, 1982.

- [97] American Society for Testing and Materials, West Conshohocken, PA. *Standard test method for impedance and absorption of acoustical materials by the impedance tube method*, 1995. ASTM Designation: C 384-95.
- [98] David T. Blackstock. *Fundamentals of Physical Acoustics*. Wiley, New York, 2000.
- [99] American Society for Testing and Materials, West Conshohocken, PA. *Standard test method for impedance and absorption of acoustical materials using a tube, two microphones, and a digital frequency analysis system*, 1990. ASTM Designation: E 1050-90.
- [100] J. Y. Chung and D. A. Blaser. Transfer function method of measuring in-duct acoustic properties. I. Theory. *The Journal of the Acoustical Society of America*, 68(3):907–913, 1980.
- [101] Athanasios Papoulis. *Probability, Random Variables, and Stochastic Processes*. McGraw-Hill, New York, 2nd edition, 1984.
- [102] W. T. Chu. Transfer function technique for impedance and absorption measurements in an impedance tube using a single microphone. *The Journal of the Acoustical Society of America*, 80(2):555–560, 1986.
- [103] A. B. Wood. *A Textbook of Sound*. G. Bell and Sons, London, 2nd edition, 1941.
- [104] William J. Jacobi. Propagation of sound waves along liquid cylinders. *The Journal of the Acoustical Society of America*, 21(2):120–127, 1949.
- [105] T. C. Lin and G. W. Morgan. Wave propagation through fluid contained in a cylindrical, elastic shell. *The Journal of the Acoustical Society of America*, 28(6):1165–1176, 1956.
- [106] Vincent A. Del Grosso. Analysis of multimode acoustic propagation in liquid cylinders with realistic boundary conditions—application to sound speed and absorption measurements. *Acustica*, 24(6):299–311, 1971.
- [107] L. Dwyann Lafleur and F. Douglas Shields. Low-frequency propagation modes in a liquid-filled elastic tube waveguide. *The Journal of the Acoustical Society of America*, 97(3):1435–1445, 1995.
- [108] Paul A. Hwang, Ronald A. Roy, and Lawrence A. Crum. Artificial bubble cloud targets for underwater acoustic remote sensing. *Journal of Atmospheric and Oceanic Technology*, 12(6):1287–1302, 1995.
- [109] Harold Levine and Julian Schwinger. On the radiation of sound from an unflanged circular pipe. *Physical Review*, 73(4):383–406, 1948.
- [110] Lord Rayleigh. *Theory of Sound*, volume 2. Dover, New York, 2nd edition, 1945.
- [111] A. N. Norris and I. C. Sheng. Acoustic radiation from a circular pipe with an infinite flange. *Journal of Sound and Vibration*, 135(1):85–93, 1989.

- [112] Noritane Chiba and Yuji Takahashi. Generation of micro air bubbles of uniform size in water. In *Third International Symposium on Cavitation*, pages 91–94, Grenoble, France, 1998.
- [113] V. Gibiat and F. Laloë. Acoustical impedance measurements by the two-microphone-three-calibration (TMTC) method. *The Journal of the Acoustical Society of America*, 88(6):2533–2545, 1990.
- [114] A. F. Seybert and Benjamin Soenarko. Error analysis of spectral estimates with application to the measurement of acoustic parameters using random sound fields in ducts. *The Journal of the Acoustical Society of America*, 69(4):1190–1199, 1981.
- [115] Hans Bodén and Mats Åbom. Influence of errors on the two-microphone method for measuring acoustic properties in ducts. *The Journal of the Acoustical Society of America*, 79(2):541–549, 1986.
- [116] W. T. Chu. Extension of the two-microphone transfer function method for impedance tube measurements. *The Journal of the Acoustical Society of America*, 80(1):347–348, 1986.
- [117] W. T. Chu. Further experimental studies on the transfer-function technique for impedance tube measurements. *The Journal of the Acoustical Society of America*, 83(6):2255–2260, 1988.
- [118] Mats Åbom and Hans Bodén. Error analysis of two-microphone measurements in ducts with flow. *The Journal of the Acoustical Society of America*, 83(6):2429–2438, 1988.
- [119] Julius S. Bendat and Allan G. Piersol. *Engineering Applications of Correlation and Spectral Analysis*. J. Wiley, New York, 2nd edition, 1993.
- [120] E. W. Lemmon, M.O. McLinden, and D.G. Friend. Thermophysical properties of fluid systems. In W.G. Mallard and P.J. Linstrom, editors, *NIST Chemistry WebBook*. National Institute of Standards and Technology, Gaithersburg MD, 2000. NIST Standard Reference Database Number 69.
- [121] Ajit Jillavenkatesa, Stanley J. Dapkunas, and Lin-Sien H. Lum. *Particle Size Characterization*. U. S. Government Printing Office, Washington D.C., 2001.
- [122] John C. Russ. *The Image Processing Handbook*. CRC Press, Boca Raton, 2nd edition, 1995.
- [123] John C. Russ. *Computer-Assisted Microscopy : The Measurement and Analysis of Images*. Plenum Press, New York, 1990.
- [124] Julius S. Bendat and Allan G. Piersol. *Random Data: Analysis and Measurement Procedures*. Wiley-Interscience, New York, 1971.

- [125] Jean-Pierre Dalmont and Anne-Marie Bruneau. Acoustic impedance measurement: Plane-wave mode and first helical mode contributions. *The Journal of the Acoustical Society of America*, 91(5):3026–3033, 1992.
- [126] W. Boober. Naval undersea warfare center newport division acoustic test facility, 2000. <http://www.npt.nuwc.navy.mil/ATF8211/index.html>.
- [127] W. Boober. Naval undersea warfare center newport division acoustic test facility, 2000. <http://www.npt.nuwc.navy.mil/ATF8211/funct/index.html>.
- [128] D. T. DiPerna and T. K. Stanton. Fresnel zone effects in the scattering of sound by cylinders of various lengths. *The Journal of the Acoustical Society of America*, 90(6):3348–3355, 1991.
- [129] Arthur E. Ruggles. *The Propagation of Pressure Perturbations in Bubbly Air/Water Flows*. Ph.D. Dissertation, Rensselaer Polytechnic Institute, 1987.

# Vita

Preston Scot “Pepper” Wilson was born in Gary, Indiana on July 11, 1968, the only child of Mickey E. and Helen Wilson. The family moved to Houston, Texas in 1973, where Preston attended Clear Lake High School and graduated in 1986. The following fall he entered The University of Texas at Austin. His summers were spent as an intern at Johnson Space Center, working for Rockwell Space Operations Corporation. The first two years, Preston’s advisor was Dr. Ilene Busch-Vishniac and the last two years, his advisor was Dr. Mark Hamilton. He was awarded the Bachelor of Science degree in Mechanical Engineering from UT in December of 1990.

In the spring of 1991, Preston entered The Graduate School at The University of Texas at Austin to study acoustics in the Department of Mechanical Engineering under Dr. Janet Ellzey and Dr. Mark Hamilton. He began working at Applied Research Laboratories, The University of Texas at Austin on February 11, 1991, where he conducted research under Dr. Thomas Muir. Preston was awarded the Master of Science degree in May of 1994 and went on to work at ARL:UT as a research engineer for Tom Muir until July of 1997. He entered the Ph.D. program at Boston University in the Aerospace and Mechanical Engineering Department in August of 1997. A brief curriculum vitae follows on the next page.

Permanent Address: 16319 Heatherdale; Houston, Texas 77059

This dissertation was typeset with L<sup>A</sup>T<sub>E</sub>X by the author.

## CURRICULUM VITAE: Preston Scot Wilson

1/3/2002

**Address:** 399 Massachusetts Ave., Apt.1; Boston, MA 02115

**Telephone:** 617-267-9147; **email:** psw@bu.edu

### EDUCATION

**Ph.D. Mechanical Engineering, 1/2002**

**Boston University**

Advisors: R. A. Roy, W. M. Carey, M. S. Howe  
and J. G. McDaniel

Dissertation title: *Sound Propagation and  
Scattering in Bubbly Liquids*

**M.S. Mechanical Engineering, 5/1994**

**The University of Texas at Austin**

Advisors: J. Ellzey, T. G. Muir, M. F. Hamilton

Thesis title: *The Combustive Sound Source*

**B.S. Mechanical Engineering, 12/1990**

**The University of Texas at Austin**

Advisors: I. Busch-Vishniac, M. F. Hamilton  
Tech. Area: Mechanical Systems and Design

### HONORS AND AWARDS

- ASA Student Paper Award in UW (5/2001)
- Fitzgerald Award, Boston University College of Engineering, 2001
- ASA/NCPA/ONR Physical Acoustics Summer School Fellowship, 2000
- B.U. Graduate Teaching Fellowship, Spring 2000
- Dean's Award for Dissert. Research, BU College of Engineering, Science Day 1999
- Department of Mechanical Engineering Scholarship, UT Austin (1987)
- NASA Johnson Space Center Employee Scholarship (1987-1991)
- UT Austin College of Engineering Honors Program (1986-1990)

### SECURITY CLEARANCE

U.S. Citizen, clearance is currently inactive.  
1991–1997: Secret U.S. & Secret NATO

### RESEARCH AND WORK EXPERIENCE

**9/97–Present: Research Assistant**

Dept. of Aersp. and Mech. Eng., Boston Univ.  
Supervisor: R. A. Roy

**2/94–8/97: Research Engineering Associate**

Applied Research Laboratories, The University of  
Texas at Austin  
Supervisor: T. G. Muir

**2/91–1/94: Research Engineering / Scientific  
Assistant**

Applied Research Laboratories, The University of  
Texas at Austin  
Supervisor: T. G. Muir

**Summers 1988–1990: Summer Intern**

Rockwell Space Operations Corporation, Johnson  
Space Center, Houston, TX  
Supervisor: Daniel Gerik

### PROFESSIONAL AFFILIATIONS

**Member:** The Acoustical Society of America,

Student Council Rep. to PA TC (2000–2001)

**Engineer-in-training:** Official precursor to P.E.  
license in the State of Texas

### SELECTED TECHNICAL PAPERS

- P. S. Wilson, R. A. Roy, and W. M. Carey "Acoustic scattering from a bubbly-liquid-filled compliant tube," *Acoustics Research Letters Online* **2**, Oct. 2001.
- R. A. Roy, P. S. Wilson and W. M. Carey, "Characterization of bubbly fluids using a water filled sound hard impedance tube and the transfer function technique", *Proc. Fifth Conf. Underwater Acoust., ECUA 2000*, P. Chevert and M.E. Zakarius, Eds., 2000.
- D. E. Smith, P. S. Wilson and T. G. Muir, *et al.* "Measurement and localization of interface wave reflections from a buried target", *JASA* **103** (5) Pt.1, May 1998.
- P. S. Wilson, J. L. Ellzey and T. G. Muir, "Experimental investigation of the Combustive Sound Source", *IEEE Journal of Ocean Engineering*, Vol.20, No.4, Oct. 1995.

### SOLUTIONS MANUAL

- P. S. Wilson and M. S. Howe, *Mathematical Methods for Mechanical Sciences—Model Answers*, Cambridge University Press, submitted for publication December, 2000.

### SELECTED PUBLISHED ABSTRACTS

- P. S. Wilson, R. A. Roy and W. M. Carey, "Acoustic Scattering from an elastic tube filled with bubbly fluid.", *JASA* **108** (5) Pt.2, Nov. 2000.
- P. S. Wilson, R. A. Roy and W. M. Carey, "Measurement of the complex impedance of a bubbly fluid in the vicinity of the bubble resonance frequency.", *JASA* **106** (4) Pt.2, Oct. 1999.
- R. A. Roy, P. S. Wilson and W. M. Carey, "An audible demonstration of low-frequency sound propagation in bubbly water", *JASA* **104** (3) Pt.2, Sept. 1998.
- P. S. Wilson and T. G. Muir, "Development of combustive sound source for array and towed deployment", *JASA* **100** (4) Pt.2, Oct. 1996.
- E. Smith, P. S. Wilson, J. A. Behrens and T. G. Muir, "A seismic interface wave transducer", *JASA* **98** (5) Pt.2, Nov. 1995.
- P. S. Wilson, T. G. Muir, J. A. Behrens and J. L. Ellzey, "Applications of the combustive sound source", *JASA* **97** (5) Pt.2, May 1995.
- E. Smith, A. Atchley, J. A. Behrens, P. S. Wilson, B. T. Wolz and T. G. Muir, "Scattering of seismic interface waves from point like obstacles in unconsolidated sediments", *JASA* **96** (5) Pt.2, Nov. 1994.